FACULTY
OF MATHEMATICS
AND PHYSICS
Charles University

DOCTORAL THESIS

Vojtěch Sidorin

Shell-like structures in the ISM: Observation versus simulations

Astronomical Institute of Charles University

Supervisor of the doctoral thesis: Prof. RNDr. Jan Palouš, DrSc.
Study programme: Physics
Study branch: Theoretical Physics, Astronomy and Astrophysics (4F1)

Prague 2016

I declare that I carried out this doctoral thesis independently, and only with the cited sources, literature and other professional sources.

I understand that my work relates to the rights and obligations under the Act No. 121/2000 Sb., the Copyright Act, as amended, in particular the fact that the Charles University in Prague has the right to conclude a license agreement on the use of this work as a school work pursuant to Section 60 subsection 1 of the Copyright Act.

In Prague

In relation to this thesis and my PhD study, I would like to thank to the following people:

— *Jan Palouš* for his support of my PhD study, for his suggestions how to proceed with my research, and for his thorough review of this thesis.

— *Kevin Douglas* for his significant help in the early phases of my research into the bubble N107, especially for his suggestions how to analyse radio observations.

— *Richard Wünsch* and *Soňa Ehlerová* for the discussions about various topics related to my research, for the programs they provided me to do my work, and for their help with reviewing this thesis.

Title: Shell-like structures in the ISM: Observation versus simulations

Author: Vojtěch Sidorin (vojtech.sidorin@gmail.com)[1]

Department: Astronomical Institute of Charles University[2]

Supervisor: Prof. RNDr. Jan Palouš, DrSc. (palous@asu.cas.cz), Astronomical Institute of the Czech Academy of Sciences[3]

Abstract: Shell-like structures are objects found in large numbers in the interstellar medium (ISM). They usually appear as bubbles or segments of bubbles and are believed to result from the deposition of mass and energy into the ISM by stars, gamma-ray bursts, or high-velocity clouds. Interstellar turbulence may play a role in their creation too. These structures influence the dynamics of the ISM and are also linked to star formation. In this thesis, I review our current knowledge of the ISM, interstellar turbulence, and shell-like structures in the ISM. Then I present the research into the GLIMPSE bubble N107 conducted in collaboration with my colleagues. N107 is a dusty shell-like structure found in our Galaxy. We explored its atomic, molecular, and radio-continuum components; derived its distance (3.6 kpc), size (radius of 12 pc), and expansion velocity ($8\,\mathrm{km\,s^{-1}}$); and identified 49 associated molecular clumps. Using numerical simulations, we estimated the conditions under which N107 formed and concluded it is probably 1 Myr to 2.25 Myr old. Finally, I describe the code Quickclump that I developed. It is an automated tool that identifies clumps in three-dimensional data. Quickclump was inspired by another clump-finding code called DENDROFIND. Shell-like structures are often associated with molecular clouds and Quickclump can decompose those clouds into individual clumps.

Keywords: ISM: bubbles – ISM: general – ISM: GLIMPSE bubble N107 – methods: data analysis – turbulence

---

[1] `http://galaxy.asu.cas.cz/~vosidorin`

[2] `http://astro.mff.cuni.cz`

[3] `http://www.asu.cas.cz`

Contents

Introduction

This thesis summarises the work I have done during my PhD study. It deals with shell-like structures in the interstellar medium (ISM) and related topics, and builds on my previous research published in my master's thesis (Sidorin, 2008).

Shell-like structures are objects found in large numbers in our Galaxy as well as in other galaxies. They are believed to result from the deposition of mass and energy into the ISM by stars (radiation, winds, supernovae) or gamma-ray bursts (GRBs), or from collisions of high-velocity clouds with the Galactic disk. Interstellar turbulence could play a role in their formation too. Shell-like structures are typically expanding, ranging in size from a few parsecs to several hundred parsecs. Most of them appear as bubbles filled with a low-density hot gas, or shells with an apparently empty interior. Sometimes they form shapes resembling arcs, filaments, or chimneys. They have an extensive influence on the structure and dynamics of the ISM, and are also linked to star formation.

The thesis is organised into three chapters. Chapter 1 *Reviews* contains three concise reviews that give introduction to the ISM, interstellar turbulence, and shell-like structures in the ISM.

Chapter 2 *GLIMPSE bubble N107* presents a detailed study of the GLIMPSE bubble N107 – a shell-like structure discovered in the infrared emission of dust in the disk of our Galaxy. The study combines an observational analysis with numerical simulations of the bubble formation. The chapter contains a full reprint of the paper Sidorin et al. (2014) followed by additional material that was not included in the paper.

Chapter 3 *Quickclump* describes the computer program Quickclump that I wrote during my PhD study. It is an automated, fast, and accurate clump-finding tool that identifies clumps in three-dimensional datacubes, typically containing observations of interstellar clouds. It was inspired by another clump-finding code, DENDROFIND (Wünsch et al., 2012), which I used to identify molecular clumps associated with the bubble N107. Shell-like structures in the ISM are often associated with complexes of molecular clouds. A clump-finding code like Quickclump can help with the analysis of those clouds by decomposing them into individual clumps.

Chapter 1

Reviews

This chapter contains three concise reviews related to shell-like structures in the interstellar medium (ISM).

Section 1.1 *Interstellar medium* briefly summarises our current knowledge of the ISM. It describes the various components of the ISM, mainly from the observational point of view.

Section 1.2 *Turbulence in the interstellar medium* reviews the turbulent dynamics of the ISM from both the observational and theoretical point of view. Interstellar turbulence is currently a very active field of research, yet it is not satisfactorily understood. It may be responsible for the creation of some shell-like structures, and expanding shells in turn provide power for interstellar turbulence.

Section 1.3 *Shell-like structures in the interstellar medium* reviews the properties, possible origin, and dynamics of shell-like structures – objects found in large numbers in the ISM all over our Galaxy. The section also discusses the impact those structures have on their surroundings. A case study of one medium-size shell, the GLIMPSE bubble N107, is given in Chap. 2.

1.1 Interstellar medium

The interstellar medium (ISM) is the matter found between stellar systems. It is a highly dynamic and turbulent environment that serves as the reservoir of material from which new stars are born. Stars in turn return energy and matter, enriched with heavier elements, back into the ISM. The ISM is comprised of gas, dust, high-energy cosmic rays, and the interstellar radiation field. It is also pervaded by interstellar magnetic fields.

Our Galaxy – the Milky Way – contains abundance of the ISM. According to our current knowledge, the Milky Way is a barred spiral galaxy with a central bulge, a disk with prominent spiral arms, and a low-density halo (Bland-Hawthorn & Gerhard, 2016). Figure 1.1 shows the appearance of the Milky Way as we believe it would look like when viewed face-on. The ISM is mostly concentrated in the disk and accounts for about 10% to 15% of the total disk mass (Ferrière, 2001). Of the total ISM mass, 99% is in the form of gas, 1% is in the form of dust. A typical density of the ISM in the Galactic disk is about 1 gas atom per cm^3 and 100 dust grains per km^3.

First in situ observation of the interstellar medium. Until recently, we had only indirect observations of the ISM. The first in situ observation of the ISM was done by the space probe Voyager 1 (Gurnett et al., 2013). The probe was launched in 1977. In 2004, it crossed the termination shock – the place where the solar wind slows down to subsonic speeds and its kinetic energy is thermalised. In 2012, after 35 years of flight, it crossed the heliopause and entered the nearby interstellar space as the first human-made spacecraft. Later, the data acquired by Voyager 1 were used to analyse interstellar turbulence (Burlaga et al., 2015, see also Sect. 1.2.9).

1.1.1 Basic characteristics of interstellar gas

Interstellar space was long considered empty. The existence of interstellar gas was originally deduced from observations of interstellar absorption lines. In 1904, Hartmann noticed that one calcium absorption line in the spectrum of the binary star δ Orionis (Mintaka) behaved differently than other lines. It did not exhibit the periodic displacements caused by the orbital motion of the star. He concluded that

> *“. . . at some point in space in the line of sight between the Sun and δ Orionis there is a cloud which produces that absorption. . . ”*

Observations that followed showed that the ISM is distributed not only in dense clouds, but also in a diffuse form all over our Galaxy. The most abundant element in the ISM is hydrogen, which comprises about 90.8% of the ISM by number of

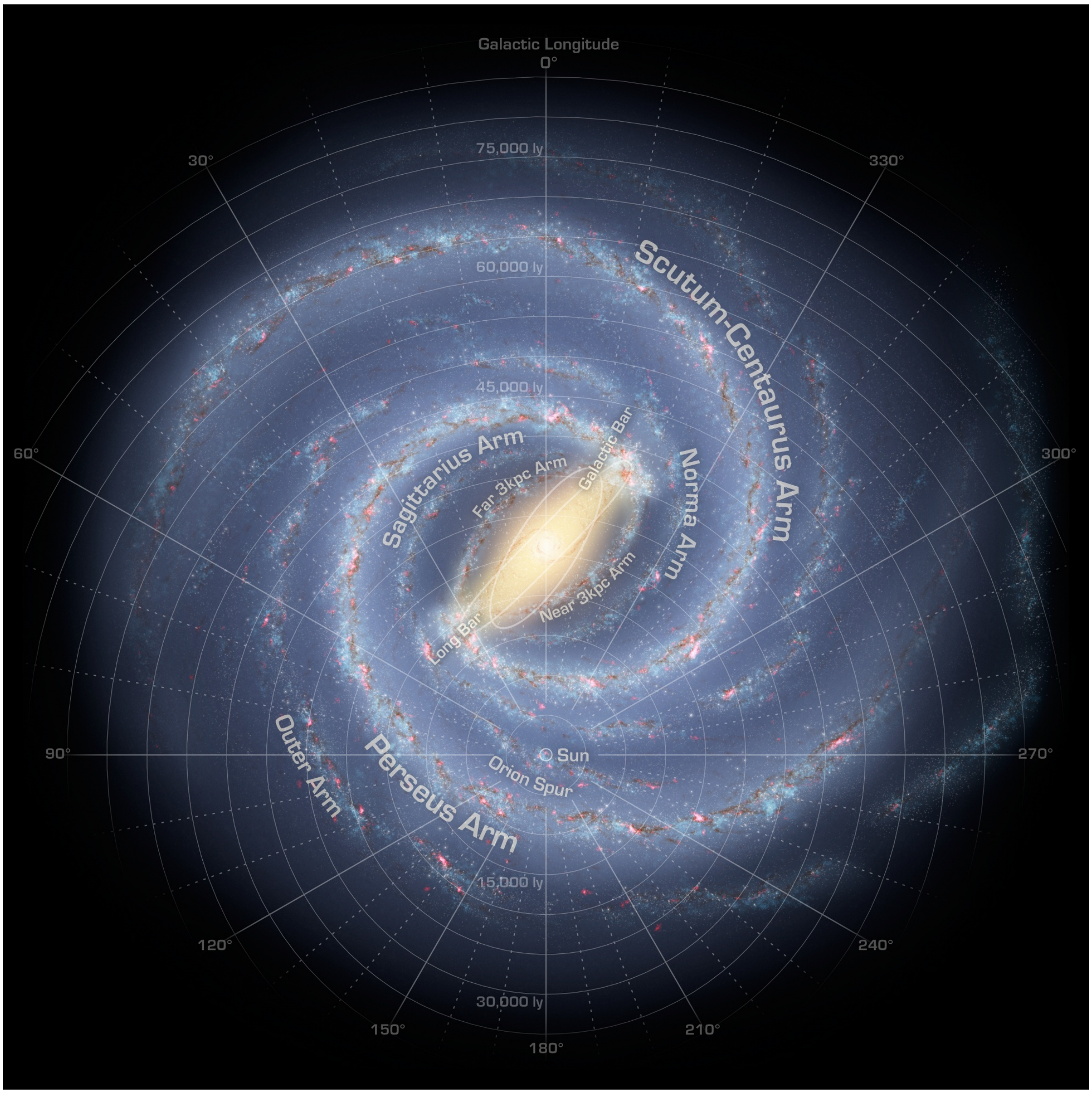

Figure 1.1: Artist's concept of the Milky Way galaxy as we believe it would look like when viewed face-on. (Courtesy NASA/JPL-Caltech/R. Hurt, `http://www.spitzer.caltech.edu/images/1928-ssc2008-10b1-The-Milky-Way-Galaxy-Annotated-`)

Table 1.1: Relative abundances (by number of atoms) of elements from hydrogen to oxygen in the interstellar gas towards ζ Ophiuchi. For comparison, ratios to solar abundances are also given. The depletion of heavier elements in interstellar gas is believed to be caused by their condensation into dust grains. (Karttunen et al., 2007).

Element	Symbol	Interstellar abundance	$\frac{\text{Interstellar abundance}}{\text{Solar abundance}}$
1 Hydrogen	H	1 000 000	1.00
2 Helium	He	85 000	≈ 1
3 Lithium	Li	5.1×10^{-5}	0.034
4 Beryllium	Be	$<7.0 \times 10^{-5}$	<5.8
5 Boron	B	7.4×10^{-5}	0.016
6 Carbon	C	74	0.20
7 Nitrogen	N	21	0.19
8 Oxygen	O	172	0.26

Table 1.2: Properties of the five basic components of interstellar gas (Ferrière, 2001). T is the mean temperature, n is the mean number density of hydrogen nuclei, and M is the total estimated mass of a given component in the Milky Way.

Component		$\frac{T}{\mathrm{K}}$	$\frac{n}{\mathrm{cm}^{-3}}$	$\frac{M}{10^9\,M_\odot}$
Molecular clouds	(Fig. 1.2)	10–20	10^2–10^6	$\approx$1.3–2.5
Cold neutral medium	(Fig. 1.3)	50–100	20–50	$\gtrsim 6.0$
Warm neutral medium		6000–10 000	0.2–0.5	
Warm ionised medium	(Fig. 1.5)	≈ 8000	0.2–0.5	$\gtrsim 1.6$
Hot ionised medium	(Fig. 1.6)	$\approx 10^6$	≈ 0.0065	(not given)

atoms (70.4% by mass). It is followed by helium, which comprises about 9.1% of the ISM by number of atoms (28.1% by mass). Heavier elements, called *metals* in astrophysics, are significantly less abundant and comprise the remainder of about 0.12% by number of atoms (1.5% by mass) (Ferrière, 2001, adopted from Spitzer, 1978). Most heavier atoms in the ISM are believed to be condensed into dust grains (Ferrière, 2001; Draine, 2003). When locked in a dust grain, atoms do not produce the same absorption and emission lines as when they are free. That explains why the observed abundances of metals in the gaseous phase are lower than the abundances in the solar atmosphere (Table 1.1).

Interstellar gas can be divided into five basic components (Table 1.2) (Ferrière, 2001): molecular clouds, cold neutral medium (CNM), warm neutral medium (WNM), warm ionised medium (WIM), and hot ionised medium (HIM).

Table 1.3: Selected CO lines that are commonly used to observe the molecule in the ISM. (`http://www.nist.gov/pml/data/molspec.cfm`)

Specie	Transition	Frequency	Wavelength in vacuum
$^{12}C^{16}O$	$J = 1–0$	115.271 GHz	2.60 mm
$^{12}C^{16}O$	$J = 2–1$	230.538 GHz	1.30 mm
$^{13}C^{16}O$	$J = 1–0$	110.201 GHz	2.72 mm
$^{12}C^{18}O$	$J = 1–0$	109.782 GHz	2.73 mm

Molecular clouds are the coldest and densest component of the ISM. Their mean temperature can be as low as 10 K and the mean number density of hydrogen nuclei up to $10^6\,\mathrm{cm}^{-3}$. Neutral atomic gas occupies most of the volume of the Galactic disk and exists there in the cold (CNM, $T \approx 50\,\mathrm{K}$ to 100 K) and warm (WNM, $T \approx 6000\,\mathrm{K}$ to 10 000 K) phase. The thickness of the atomic disk is about 200 pc. The WIM can be found either in well-defined H II regions around massive stars, or in a diffuse form all over the Galaxy. It reaches temperatures of about 8000 K. The HIM is the hottest and the most rarefied component with temperatures reaching 10^6 K and number densities of hydrogen nuclei less than $0.01\,\mathrm{cm}^{-3}$. The HIM fills the Galactic halo and the cavities in the ISM created by stellar winds and supernova explosions. The Local Bubble, which surrounds our Solar System, is one such cavity filled with the HIM.

To explain the coexistence of multiple phases of the ISM, Field et al. (1969) introduced a two-phase model. The model assumes that the ISM is heated by cosmic rays and consists of two gas phases: cold, with a temperature $T < 300\,\mathrm{K}$, and warm, with a temperature $T \approx 10^4\,\mathrm{K}$. These phases are assumed to be thermally stable and in pressure equilibrium. The model was later extended by McKee & Ostriker (1977) with a third hot phase. In the three-phase model, most of the space is filled with a hot ionised medium (HIM, $n \approx 10^{-3}\,\mathrm{cm}^{-3}$, $T \approx 10^6\,\mathrm{K}$), presumably originating in supernova explosions. The hot medium filling factor is estimated at about 0.7 to 0.8. Embedded in the hot medium are clouds of cold neutral medium (CNM, $n \approx 10^2\,\mathrm{cm}^{-3}$, $T \approx 10^2\,\mathrm{K}$) with a filling factor of about 0.02 to 0.04. These clouds are then surrounded by a warm medium ($T \approx 8000\,\mathrm{K}$) with a filling factor of about 0.2. The warm medium in the model includes the WNM and WIM. For a review of the multiphase models of the ISM see McKee (1995).

1.1.2 Molecular clouds

Molecular clouds represent the densest and coolest component of the ISM. With the mean temperatures as low as 10 K and the mean densities of hydrogen nuclei reaching $10^6\,\mathrm{cm}^{-3}$, these are the places where new stars are born. The physical

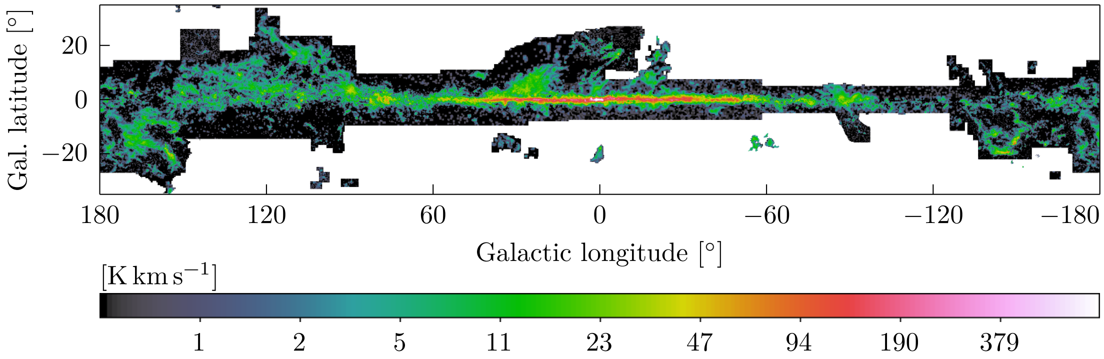

Figure 1.2: Molecular clouds near the Galactic disk as seen in the ^{12}CO ($J = 1{-}0$) emission line at 2.60 mm. The intensity is integrated over the radial velocity channels. (The image data were provided by the composite survey of the Galactic CO by Dame et al., 2001, using 37 original data sets; see the paper for the complete list of references).

conditions in these clouds allow the formation of various molecules. As of August 2016, almost 200 different molecules have been detected in the ISM or circumstellar shells.[1] Most of them have only a few atoms, but molecules as large as fullerenes C_{60} or C_{70} have also been detected.

The most abundant molecule in the ISM is the hydrogen molecule H_2. The first observational evidence of its presence in the ISM was provided by Carruthers (1970). When analysing data acquired during a rocket experiment, he found an ultraviolet (UV) H_2 absorption band in the spectrum of the star ξ Persei. Hydrogen molecules are believed to form on the surface of dust grains (Hollenbach & Salpeter, 1971). Dust also helps to shield molecules in dense clouds against stellar UV radiation (Schlegel et al., 1998; Ferrière, 2001).

Molecular clouds are opaque at optical wavelengths. They can be, however, observed well at radio wavelengths. As the H_2 molecule has no suitable spectral lines at radio wavelengths, molecular clouds are usually observed in radio emission of other molecules, e.g. CO (Fig. 1.2). The CO molecule is the second most abundant molecule in the ISM. It has radio spectral lines originating in its rotational transitions (Table 1.3). A practical example of how a CO line can be used to explore a molecular cloud is given in Chap. 2.

The matter within molecular clouds is not distributed homogeneously; it forms a hierarchical structure (e.g. Larson, 1981; Ferrière, 2001; Bergin & Tafalla, 2007). Clouds consist of denser condensations called *clumps*, which in turn contain *cores* – the densest, coldest, and the most compact parts of molecular clouds (Table 1.4). The cores are believed to be the very places where new stars are born. The hierarchical structure of clouds suggests that turbulence plays an important role in their

---

[1] Molecules in space: `http://www.astro.uni-koeln.de/cdms/molecules`

Table 1.4: Approximate observed properties of molecular clouds, clumps, and cores as given by Bergin & Tafalla (2007, Table 1). The crossing time is defined as the object's half-size divided by the Gaussian dispersion in internal velocity (Elmegreen, 2000).

	Clouds	Clumps	Cores
Mass ($M_\odot$)	10^3–10^4	50–500	0.5–5
Size (pc)	2–15	0.3–3	0.03–0.2
Mean density (cm^{-3})	50–500	10^3–10^4	10^4–10^5
Internal velocity dispersion ($\mathrm{km\,s}^{-1}$)	2–5	0.3–3	0.1–0.3
Crossing time (Myr)	2–4	≈1	0.5–1
Temperature (K)	≈10	10–20	8–12

formation (Elmegreen & Scalo, 2004). Another indicator suggesting turbulence is acting in molecular clouds is the discrepancy between the observed internal velocity dispersions and thermal speeds (Larson, 1981). The thermal speed in a cloud with $T < 20\,\mathrm{K}$ is $\sqrt{3kT/m_{\mathrm{H}_2}} < 0.5\,\mathrm{km\,s}^{-1}$. This is markedly less than the typically observed velocity dispersion of $1\,\mathrm{km\,s}^{-1}$ to $5\,\mathrm{km\,s}^{-1}$ (Scoville et al., 1987). A more detailed review of interstellar turbulence is given in Sect. 1.2.

Compared with the neutral atomic medium, molecular matter is confined more to the Galactic plane. Near the Sun, the vertical distribution of molecular matter can be approximated by a Gaussian function (Ferrière, 2001)

$$\langle n_\mathrm{m}\rangle(Z) = n_0 \exp\left[-\left(\frac{Z}{H_\mathrm{m}}\right)^2\right], \tag{1.1}$$

where $\langle n_\mathrm{m}\rangle$ is the space-averaged vertical distribution of the number density of hydrogen nuclei in molecular form, and Z is the vertical distance from the centre of the Galactic plane. The estimate of Clemens et al. (1988) gives $n_0 = 0.58\,\mathrm{cm}^{-3}$ and $H_\mathrm{m} = 81\,\mathrm{pc}$. The estimate of Bronfman et al. (1988) gives $n_0 = 0.53\,\mathrm{cm}^{-3}$ and $H_\mathrm{m} = 71\,\mathrm{pc}$.[2]

1.1.3 Neutral atomic medium

As our Solar System is located in the disk of the Milky Way Galaxy, it is difficult to see the overall structure of the Galaxy. Interstellar extinction makes it even impossible to see far in the optical domain in the direction of the Galactic disk. A breakthrough came in 1951, when Ewen & Purcell and Muller & Oort observed for the first time the 21 cm line emitted by interstellar H I gas. Soon, the H I line

---

[2] I take the values of the parameters n_0 and H_m from Ferrière (2001). According to a comment in the paper, the values are rescaled to the Galactocentric radius of the Sun of 8.5 kpc. That explains why they are slightly different than in the original papers.

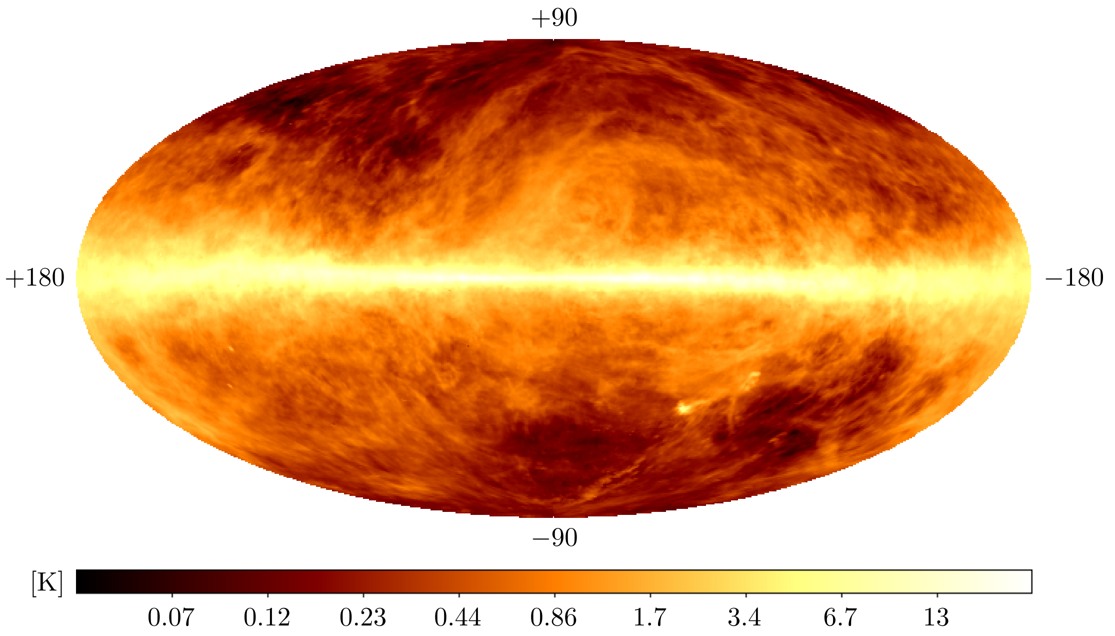

Figure 1.3: Sky in the H I line emission (21 cm) tracing the CNM and WNM in our Galaxy; Hammer projection, Galactic coordinates centred at the Galactic centre. The Magellanic Clouds can be seen as the bright smudges in the lower right segment. Shown is the average brightness temperature in the interval of radial velocities of ±250 km s^{-1}. (The image was made from the data provided by the Leiden/Argentine/Bonn Survey of Galactic H I , Kalberla et al., 2005.)

proved to be an extremely useful tracer of the neutral atomic medium and the structure of our Galaxy.

The H I line has several advantages for observations of the interstellar atomic gas in our Galaxy. First, it suffers almost no interstellar extinction, since it is a radio line. Second, the line is optically thin in virtually all directions. And third, the line is naturally extremely narrow. We can thus see even the most remote parts of our Galaxy, and from the Doppler shift accurately derive the radial velocity of the emitting gas. Surveys of neutral hydrogen revealed that the Milky Way is a spiral galaxy, similar to the Andromeda Galaxy, and that it has a rich reservoir of the ISM. The surveys also showed that the ISM is highly inhomogeneous with lots of structures. Among the most common features found in the ISM are shell-like structures studied in this thesis. A full-sky image in the H I line is shown in Fig. 1.3.

Neutral hydrogen emits at 21 cm due to the forbidden transition of the proton–electron spin orientation. The difference between the higher energy level with parallel spins and the lower energy level with antiparallel spins is 9.4×10^{-25} J, or equivalently 5.9×10^{-6} eV. A jump from the higher level to the lower level generates a photon with a wavelength of 21 cm, or equivalently a frequency of

1420 MHz. Since this hyperfine transition is forbidden, its probability is very small: only $2.9 \times 10^{-15}\,\mathrm{s}^{-1}$. The mean lifetime is therefore very large: about 10 Myr. The large lifetime means that the line is naturally very narrow. On the other hand, we need a large amount of hydrogen for the H I line to be detectable. This is why it had not been observed in a laboratory before being detected in the ISM.

In the optically-thin limit, which is a reasonable assumption for most observations of interstellar H I gas, the H I line intensity can be transformed into the H I particle column density N_H with the equation (Rohlfs & Wilson, 2004, Eq. 12.17)

$$\frac{N_\mathrm{H}}{\mathrm{cm}^{-2}} = 1.822 \times 10^{18} \int_{-\infty}^{+\infty} \left(\frac{T_\mathrm{b}(v)}{\mathrm{K}}\right) \left(\frac{\mathrm{d}v}{\mathrm{km\,s^{-1}}}\right), \tag{1.2}$$

where T_b is the main beam brightness temperature, and v is the radial velocity.

The H I line can also be observed in absorption, when a bright radio continuum source, e.g. a quasar or a supernova remnant, is present in the background. While H I emission spectra trace both the CNM and WNM, absorption spectra are biased towards the CNM (Dickey & Lockman, 1990, Fig. 2). The CNM has a typical temperature of 50 K to 100 K and is found in discrete clouds. The WNM has a typical temperature of 6000 K to 10 000 K and is found in a more diffuse form (Ferrière, 2001). These two phases are thermally stable and have comparable thermal pressures (Field et al., 1969; Goldsmith et al., 1969; Wolfire et al., 1995; Ferrière, 2001). Their coexistence is explained by the shape of the cooling function. It has a peak around 100 K, corresponding to the fine-structure line of C II at 158 µm, then it rises steeply around 8000 K due to the Lyα line (Wolfire et al., 1995; Ferrière, 2001).

The space-averaged vertical distribution of the Galactic H I gas $\langle n_\mathrm{H\,I} \rangle$ in the Galactocentric radial interval $3.5\,\mathrm{kpc} < R < R_\odot$ can be approximated as (Ferrière, 2001, based on Dickey & Lockman, 1990, Sect. 6.2)

$$\begin{aligned}\langle n_\mathrm{H\,I} \rangle = (0.57\,\mathrm{cm}^{-3}) \Bigg\{ 0.70 \exp\left[-\left(\frac{Z}{127\,\mathrm{pc}}\right)^2\right] + 0.19 \exp\left[-\left(\frac{Z}{318\,\mathrm{pc}}\right)^2\right] \\ + 0.11 \exp\left[-\frac{|Z|}{403\,\mathrm{pc}}\right] \Bigg\}.\end{aligned} \tag{1.3}$$

1.1.4 H II regions and diffuse warm ionised medium

The warm ionised medium (WIM) in our Galaxy is found in two different forms: in a more compact form in H II regions, and in a diffuse form.

H II regions, sometimes referred to as *classical* H II regions, are regions of ionised hydrogen formed around young OB stars. These massive stars emit enough UV radiation to ionise large amounts of hydrogen in their vicinity. This ionised hydrogen can then be observed as an emission nebula. In a homogeneous medium, H II regions would be perfectly spherical with a radius of the Strömgren sphere (Kuiper et al., 1937; Strömgren, 1939; equation adopted from Ferrière, 2001, based on Spitzer, 1978):

$$r_{\mathrm{S}} = (30\,\mathrm{pc}) \left[\left(\frac{N_{\mathrm{LyC}}}{10^{48}\,\mathrm{s}^{-1}} \right) \left(\frac{\mathrm{cm}^{-3}}{n_{\mathrm{H}}} \right) \left(\frac{\mathrm{cm}^{-3}}{n_{\mathrm{e}}} \right) \right]^{1/3}, \tag{1.4}$$

where N_{LyC} is the total number of Lyman continuum photons emitted by the ionising source per unit time. Lyman continuum photons are photons with an energy higher than 13.6 eV, or equivalently a wavelength shorter than 912 Å, capable of ionising hydrogen atoms. n_{H} is the number density of free protons; and n_{e} is the number density of free electrons.

The ISM is, however, hardly homogeneous enough to form perfectly spherical H II regions. Most of the observed H II regions have irregular shapes, often open in the direction of the least dense medium. An example of an H II region is the Orion Nebula (M42), or the Rosette Nebula (Caldwell 49) shown in Fig. 1.4.

A typical temperature in an H II region, about 8000 K (Spitzer, 1978; Ferrière, 2001), is higher than that of the ambient medium. The higher temperature, together with the ionisation of the gas, cause a raise in pressure. This leads to the expansion of the H II region. If the expansion is supersonic with respect to the ambient medium, a shock wave will form. This shock wave will then collect and compress the ambient medium in a shell surrounding the ionised gas. The collected medium can become gravitationally unstable and form a new generation of stars. This mechanism of star formation, triggered by an expanding H II region, is called *collect-and-collapse*. A more detailed description of the collect-and-collapse process, together with other mechanisms of triggered star formation, is given in Sect. 1.3.5.

Ionised hydrogen emits strongly in the Balmer line series, namely in the red Hα line. It also emits continuum emission that originates in thermal movements of free electrons, i.e. *free-free radiation*. At optical wavelengths, the continuum emission is too weak to be observed. It can be, however, well observed at radio wavelengths.

The diffuse WIM can be found in every direction in the sky (Ferrière, 2001). It concentrates towards the Galactic disk. Its typical temperature, about 8000 K (Reynolds, 1985), is comparable to the temperature in H II regions. There is an ongoing debate about the energy source that keeps the diffuse gas warm and ionised. A possible source could be O stars. Some fraction of their ionising radiation may perhaps escape from the H II regions surrounding them and provide energy for the diffuse WIM (Reynolds, 1984; Ferrière, 2001).

Figure 1.4: Rosette Nebula – a large H II region in our Galaxy – shown here in Hα emission. (The image is based on the data obtained as part of The INT Photometric H-Alpha Survey of the Northern Galactic Plane, Drew et al., 2005, prepared by Nick Wright, University College London, on behalf of the IPHAS Collaboration; retrieved from `https://commons.wikimedia.org/wiki/File:Rosette_nebula_s.jpg`.)

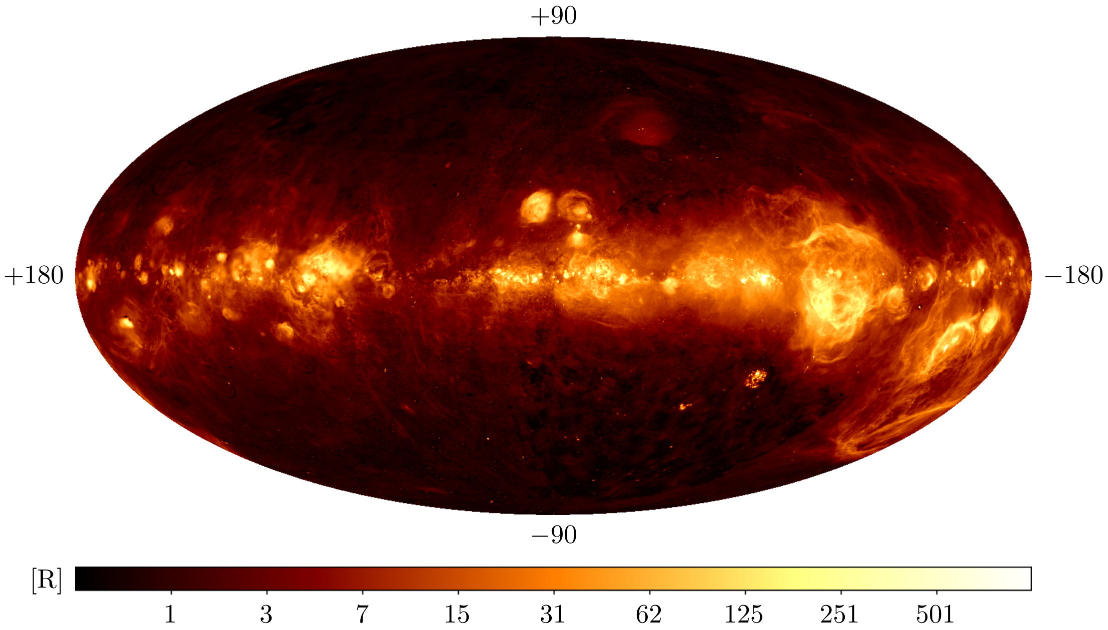

Figure 1.5: Sky in the Hα line emission (656 nm) tracing the WIM in our Galaxy; Hammer projection, Galactic coordinates centred at the Galactic centre. The image unit is rayleigh. (The image uses the data provided by the composite full-sky Hα map by Finkbeiner, 2003, which is based on three original data sets: The Virginia Tech Spectral line Survey, `http://www.phys.vt.edu/~halpha/`; The Southern H-Alpha Sky Survey, Gaustad et al., 2001; and The Wisconsin H-Alpha Mapper Northern Sky Survey, Reynolds et al., 2002.)

Near the Sun, the space-averaged number density of free electrons $\langle n_\mathrm{e}\rangle$, corresponding to the distribution of the WIM, can be approximated as (Reynolds, 1991)

$$\langle n_\mathrm{e}\rangle(Z) = \underbrace{(0.015\,\mathrm{cm}^{-3})\exp\left(-\frac{|Z|}{70\,\mathrm{pc}}\right)}_{\text{H II regions}} + \underbrace{(0.025\,\mathrm{cm}^{-3})\exp\left(-\frac{|Z|}{900\,\mathrm{pc}}\right)}_{\text{diffuse WIM}}, \tag{1.5}$$

where the first term represents the contribution from H II regions, and the second term represents the contribution from the diffuse WIM.

A full-sky image in the Hα line, tracing the WIM in our Galaxy, is shown in Fig. 1.5.

1.1.5 Hot ionised medium

The hot ionised medium (HIM) is a very hot, rarefied, ionised gas that pervades our Galaxy. It fills the Galactic halo, where it forms the Galactic corona, and can be

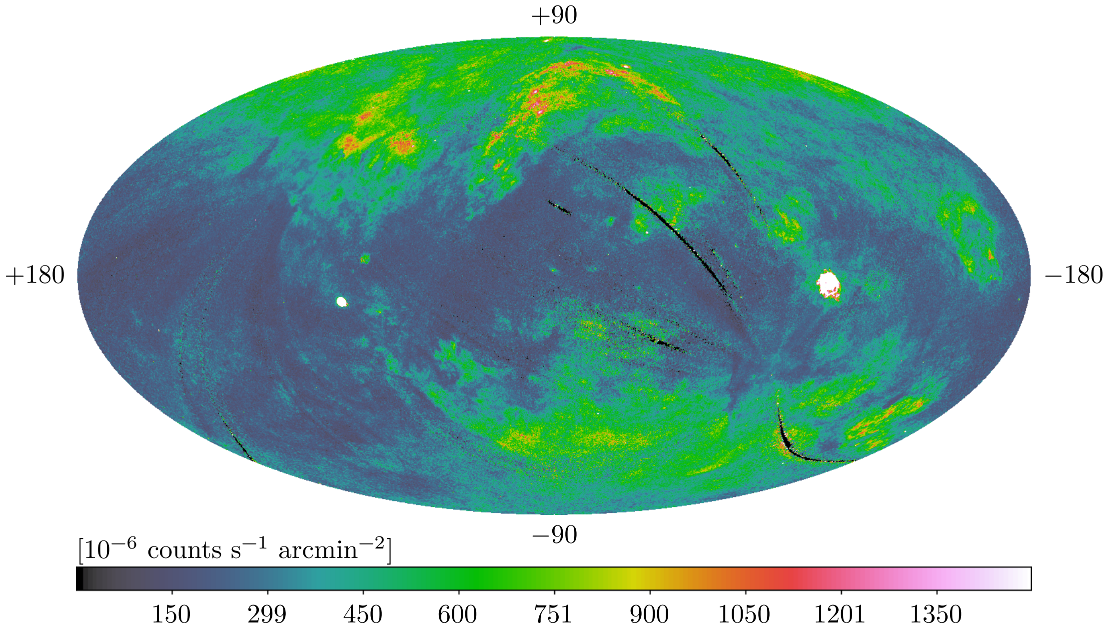

Figure 1.6: Sky in soft X-ray continuum emission (0.25 keV) tracing the HIM in our Galaxy; Hammer projection, Galactic coordinates centred at the Galactic centre. Most of the flux originates probably in the Local Bubble. The increase in flux towards the poles is due to the hot gas in the Galactic corona. (ROSAT X-Ray All-Sky Survey, `http://www.xray.mpe.mpg.de/cgi-bin/rosat/rosat-survey`, Snowden et al., 1997)

also found inside large shells and superbubbles throughout the Galaxy. For example it fills the Local Bubble.

The existence of the HIM and the Galactic corona was proposed by Spitzer (1956) to explain the presence of spiral arms and high-latitude clouds in our Galaxy. He argued that a hot rarefied medium should pervade the Galaxy to establish a pressure equilibrium that would allow the formation of those structures. He also believed that some of the observed radio noise originates in the corona. The existence of the HIM was confirmed later by the discovery of absorption lines of highly ionised metals in stellar spectra. Observations with the Copernicus satellite revealed broad UV absorption lines of oxygen (O VI), nitrogen (N V), and other ions (Jenkins et al., 1973; Jenkins & Meloy, 1974; York, 1977). Observations of soft X-ray background continuum emission also confirmed the existence of the HIM (Williamson et al., 1974).

A typical temperature of the HIM is about 10^6 K, and a typical number density of hydrogen nuclei is about $0.0065\,\mathrm{cm}^{-3}$. The thermal pressure of the HIM in the Local Bubble is about 3 to 15 times higher than that of the neutral medium (Ferrière, 2001). It is believed that the hot gas is generated primarily by supernova explosions, with some contribution from winds of massive stars (McKee & Ostriker, 1977; McKee, 1995; Ferrière, 2001).

The HIM can be traced with soft X-ray continuum emission (Fig. 1.6). The hot gas in the Local Bubble, which surrounds our Solar System, is probably the source of most of the observed total soft X-ray flux (Cox & Reynolds, 1987). The Galactic corona presents itself as an increase in the flux towards the Galactic poles.

1.1.6 Planetary nebulae

Planetary nebulae are expanding shells of ionised gas around small hot blue stars. In the late phase of stellar evolution, during the red giant phase, stars with the main sequence masses of roughly $0.8\,M_\odot$ to $8\,M_\odot$ expel their atmospheres (Maciel et al., 2009). The remaining hot core of the original star then ionises the expelled gas, which starts glowing. Planetary nebulae are relatively short-lived objects, lasting only tens of thousands of years. Then they disperse into the ambient ISM, enriching it with heavier elements that were produced in the progenitor star.

Compared to H II regions, planetary nebulae are more symmetrical and expand faster. When planetary nebulae were first observed in the late 18th and early 19th century, some of them resembled faint planets in the telescopes then available. Hence the name planetary nebula, which is in fact a misnomer.

1.1.7 Supernovae

Supernovae are violent explosions associated with the final stage of evolution of some stars. They have a profound effect on the ISM, affecting its chemical composition, structure, and dynamics. The matter ejected in the explosion enriches the ISM with heavier elements created in the core of the progenitor star. The explosion creates a low density cavity filled with the HIM and surrounded by an expanding shock wave (Fig. 1.8). As the shock wave moves through the ambient medium, it collects the medium in an expanding shell. The shell later cools down, fragments and may form molecular clouds, which in turn can start forming a new generation of stars (McCray & Kafatos, 1987). This is one of the variants of propagated, or triggered, star formation (see Sect. 1.3.5). When the shock hits a pre-existing condensation, it can trigger star formation there. This is another variant of triggered star formation. The shock further supplies kinetic energy into the ISM, driving interstellar turbulence (see Sect. 1.2.7). Supernovae are also believed to be an important source of cosmic rays (Ferrière, 2001).

Historically, supernovae have been divided into two basic groups based on the presence (type II) or absence (type I) of hydrogen lines in their spectra (Fig. 1.7). However, a more physical classification would be based on the type of the progenitor star (Cappellaro & Turatto, 2001): Type Ia supernovae are believed to originate in

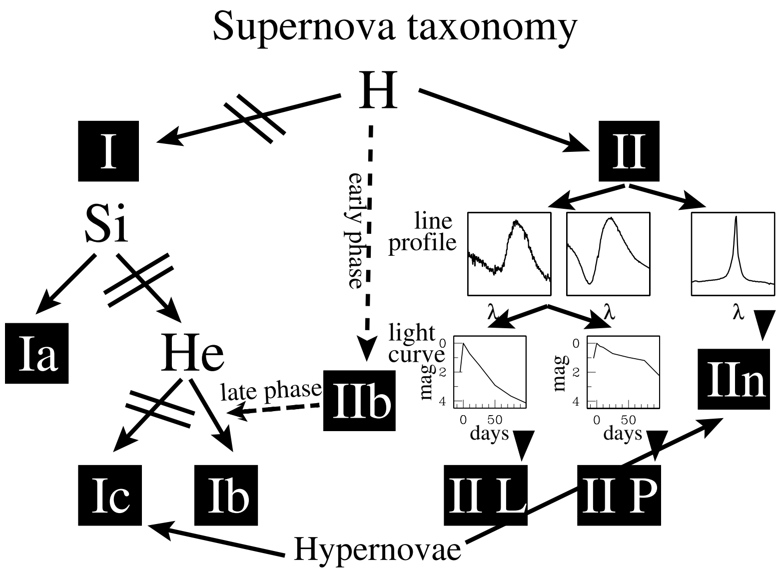

Figure 1.7: Supernova taxonomy based on the observational properties. The main division is based on the presence (type II) or absence (type I) of hydrogen lines in the spectra. (Cappellaro & Turatto, 2001, Fig. 2, retrieved from arXiv:astro-ph/0012455)

the thermonuclear explosion of a low-mass star. They are thought to result from binary stellar systems, where a white dwarf accretes mass from its companion. When the white dwarf's mass surpasses the Chandrasekhar limit, which is about $1.38\,M_\odot$, the star undergoes a thermonuclear explosion (Woosley & Weaver, 1986; Mazzali et al., 2007). On the other hand, type Ib, Ic, and II supernovae are believed to originate in the collapse of a massive star's core. The progenitors of the core-collapse supernovae are believed to be stars with the main sequence mass over $9\,M_\odot$ (Heger et al., 2003).

The total supernova rate in our Galaxy is estimated at about one explosion per 48 yr (Ferrière, 2001, based on Cappellaro et al., 1997). Tammann et al. (1994) give a comparable rate of one explosion per (40 ± 10) yr. The total energy released in a supernova explosion, regardless of its type, is estimated at 10^{51} erg (Chevalier, 1977; Woosley & Weaver, 1986). The shock wave created during the explosion moves with a velocity of $(1 \text{ to } 2) \times 10^{7}\,\mathrm{m\,s^{-1}}$ (Schawinski et al., 2008).

The structure resulting from a supernova explosion is called *supernova remnant*. As of 2014, over 290 supernova remnants have been discovered in our Galaxy (Green, 2014, online catalogue[3]). An example is the Crab Nebula shown in Fig. 1.8. Only a fraction of the discovered remnants is visible at optical wavelengths; most of them are detected at radio wavelengths, which do not suffer from interstellar extinction. At radio wavelengths, the remnants emit synchrotron radiation – continuum emission

---

[3] Catalogue of supernova remnants: `https://www.mrao.cam.ac.uk/surveys/snrs/`

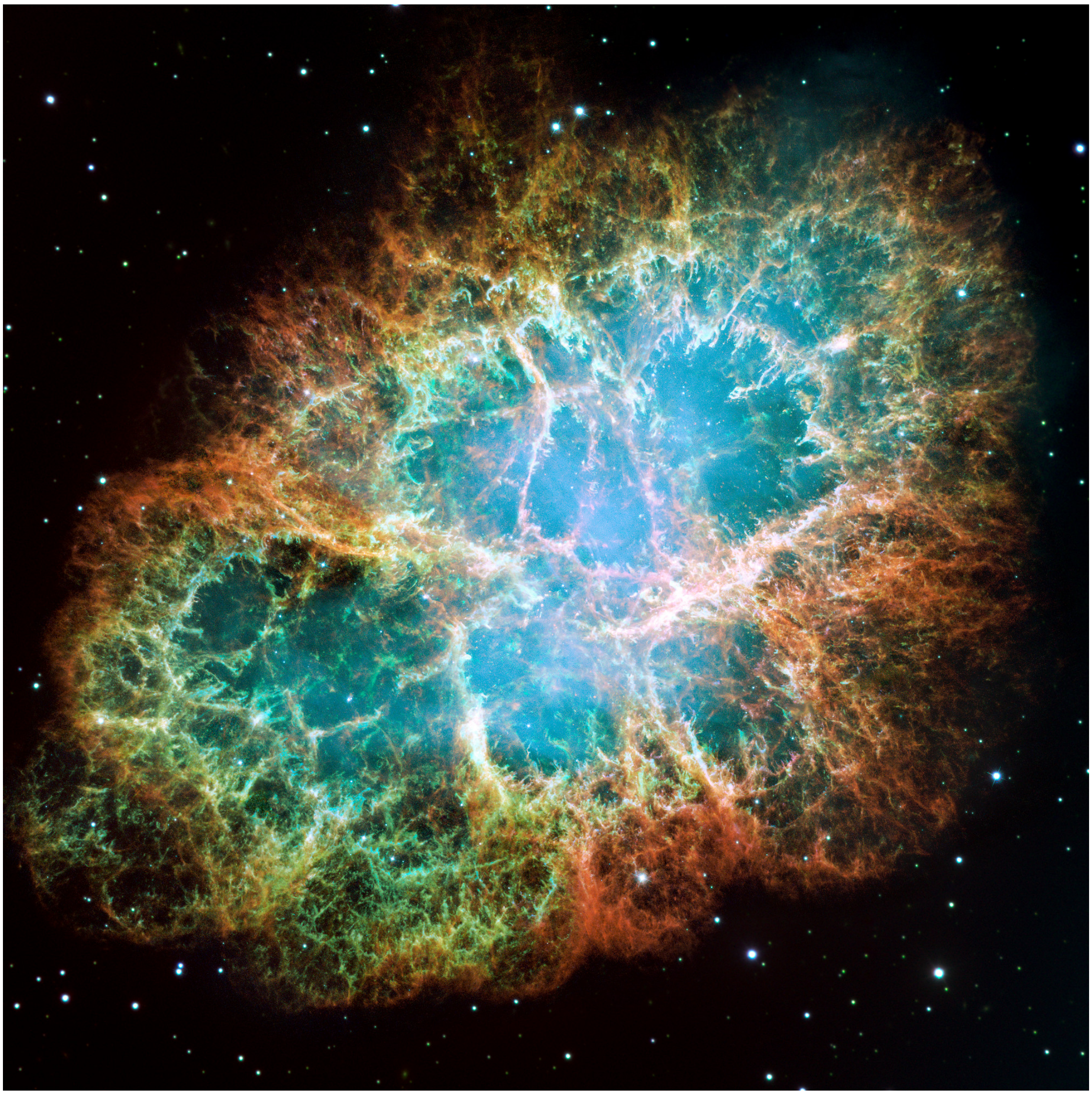

Figure 1.8: Crab Nebula (M1) – a supernova remnant in the constellation Taurus. It was created by a supernova that exploded in 1054. The remnant is a highly turbulent environment with lots of complex filamentary structures created by hydrodynamic instabilities (primarily Rayleigh-Taylor and Kelvin-Helmholtz). Supernovae are thought to be a major source of energy for turbulence in the Galactic disk. (NASA, ESA, J. Hester and A. Loll, Arizona State University, 2005)

that originates in relativistic electrons moving in their magnetic fields (Berezhko & Völk, 2004; Reynolds, 2008). The radio emission has a power-law spectrum with a typical spectral index around −0.5 (average value in the catalogue of Green, 2014). Contrary to that, the theoretical spectral index for a classical H II region in the optically thin limit is −0.1 (Condon & Ransom, 2010), and the usually observed values are around 0 or more (Verschuur & Kellermann, 1988; Rohlfs & Wilson, 1996). Thus, the radio spectral index can be used to distinguish supernova remnants from classical H II regions. A practical demonstration of determining the spectral index is given in Sect. 2.1.2.5.

Supernova remnants can be divided into three basic groups (NASA online[4], Weiler & Sramek, 1988). The first group has a shell-like structure, e.g. Cassiopeia A. The second group has a pulsar wind nebula inside, e.g. the Crab Nebula in Fig. 1.8. The pulsar supplies additional energy into the remnant by injecting relativistic electrons into its surroundings. The third group are composite remnants that combine features of both the shell-like and Crab-like remnants.

Multiple supernova explosions occurring close to each other in space and time can create a very large cavity with a size reaching several hundred parsecs (Tenorio-Tagle & Bodenheimer, 1988). Such a cavity, called *superbubble* or *remnant supershell*, can then be observed as an H I shell or hole. I note that not all supershells need to be created by supernovae (see Sect. 1.3.2).

1.1.8 Cosmic rays

Cosmic rays are high-energy charged particles travelling in the ISM. They constantly bombard Earth, where they interact with the atmosphere and cause secondary particle showers. Most of the particles are hydrogen nuclei (protons), about 10% are helium nuclei (alpha particles), about 1% are heavier nuclei, and about 2% are electrons; positrons and antiprotons have also been detected (Ferrière, 2001, and the citations therein).

Most cosmic-ray particles have an energy below 10^9 eV, but particles with an energy over 10^{20} eV have been detected as well. At energies below 10^9 eV, the flux of cosmic rays is strongly modulated by the solar wind (Ferrière, 2001). At energies higher than 10^9 eV, the flux decreases as a piecewise power law (Fig. 1.9). The power-law index varies between about −2.5 and −3.3, depending on the energy range and the type of particles (Ferrière, 2001). Cosmic rays with an energy below about 10^{17} eV are thought to originate primarily in our Galaxy, while those with higher energies are probably of an extragalactic origin (Hörandel, 2008).

---

[4] NASA on supernova remnants: http://imagine.gsfc.nasa.gov/science/objects/supernova_remnants.html

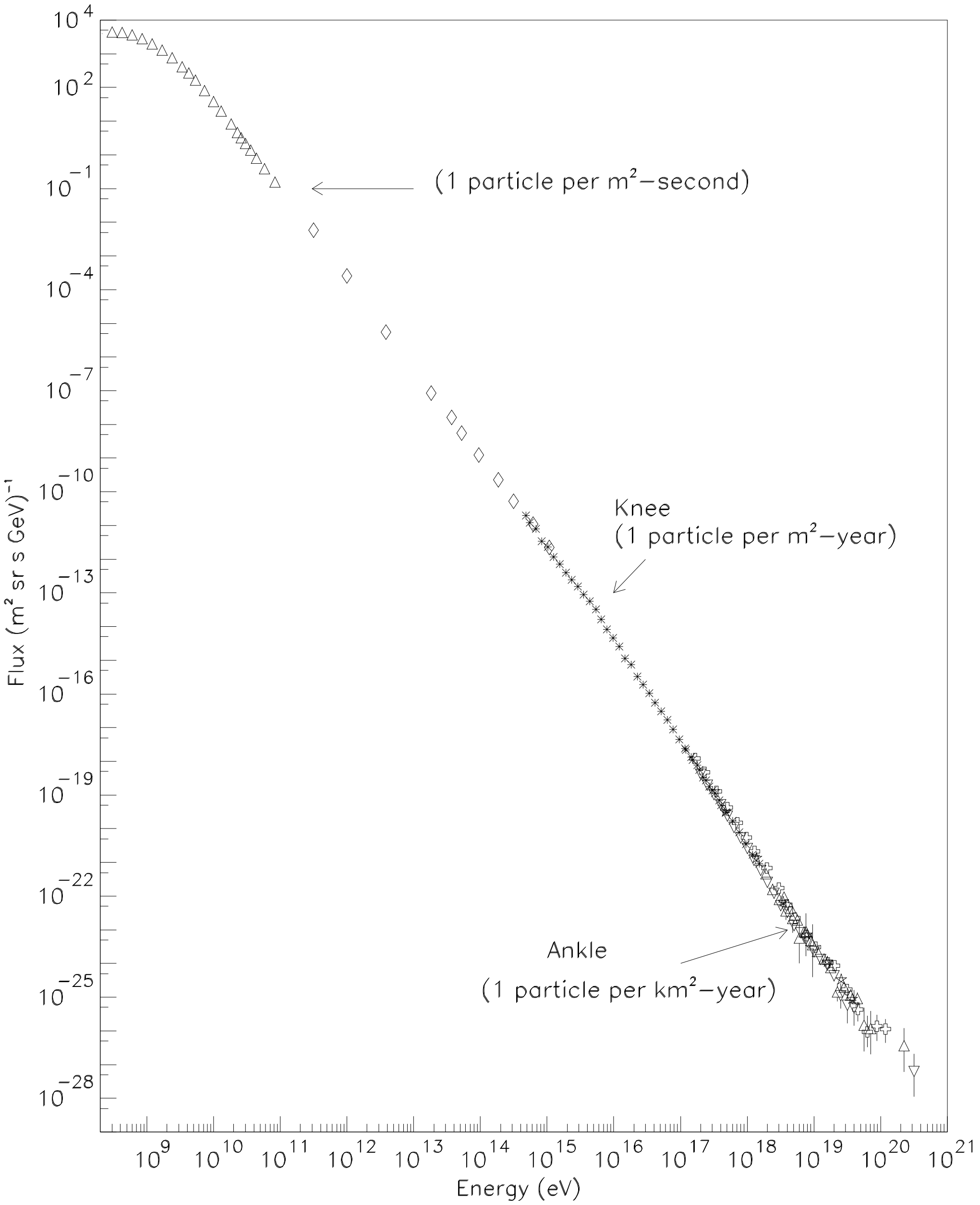

Figure 1.9: Energy spectrum of cosmic rays reaching Earth. The various symbols show measurements from different experiments. (Bhattacharjee, 2000, Fig. 1, retrieved from arXiv:astro-ph/9811011v2, edited)

The energy density of cosmic rays near the Sun is estimated at about $1\,\mathrm{eV\,cm^{-3}}$ (Hörandel, 2008). This is a few times more than the energy density of the visible star light ($\approx 0.3\,\mathrm{eV\,cm^{-3}}$), the Galactic magnetic field ($\approx 0.25\,\mathrm{eV\,cm^{-3}}$), or the cosmic microwave background ($\approx 0.25\,\mathrm{eV\,cm^{-3}}$) (Hörandel, 2008). The estimated pressure of cosmic rays near the Sun is about $10^{-12}\,\mathrm{dyn\,cm^{-2}}$, which is comparable to the pressures of other ISM constituents there, namely magnetic field and gas (Ferrière, 1998).

The Solar System is located inside the Local Bubble. It is, however, not directly embedded in its HIM, but in a warm interstellar cloud. Therefore, the energy density and pressure of cosmic rays given above for the solar vicinity could represent typical conditions for the warm phase of the ISM (Ferrière, 2001).

The possible primary sources of the Galactic cosmic rays include supernova explosions and flares of late-type stars (Simpson, 1983; Meyer, 1985; Ferrière, 2001). After the energetic charged particles are released by primary sources, they are probably further accelerated in the turbulent ISM by the second-order Fermi acceleration, or in supernova shocks by the first-order Fermi acceleration (Ferrière, 2001).

As cosmic rays are electrically charged, their motion is affected by the interstellar magnetic field. Cosmic rays are estimated to spend typically several million years travelling across the Galaxy, trapped in its magnetic field. Simpson & Garcia-Munoz (1988) estimated their mean lifetime at 15 Myr. During that lifetime, the particles travel a distance many times the size of the Milky Way.[5] Their trajectories are therefore strongly affected by the magnetic field, which hinders the direction of their original source. After spending millions of years travelling in the ISM, cosmic rays may lose their kinetic energy in collisions with interstellar gas or, alternatively, they can escape the Galaxy (Rasmussen & Peters, 1975; Jokipii, 1976; Ferrière, 2001).

1.1.9 Interstellar magnetic field

The existence of the Galactic magnetic field was first suggested by the discovery that starlight is subtly linearly polarised (Hall, 1949; Hiltner, 1949a,b). The observed degree of polarisation reaches typically a few percent. It is caused by the selective extinction of asymmetric dust grains aligned by the Galactic magnetic field (Davis & Greenstein, 1951). Those grains tend to rotate around their short axis and align that axis along magnetic field lines. Thus, their long axis tends to be aligned in the direction perpendicular to the field lines. Dust grains preferentially absorb

---

[5] Let us give a rough estimate: Assume that cosmic-rays travel at a speed close to the speed of light, say $10^8\,\mathrm{m\,s^{-1}}$, and that our Galaxy is about 30 kpc in diameter (`http://imagine.gsfc.nasa.gov/features/cosmic/milkyway_info.html`). Then, during the lifetime of 15 Myr, a cosmic-ray particle will travel a distance of about 150 times the diameter of our Galaxy.

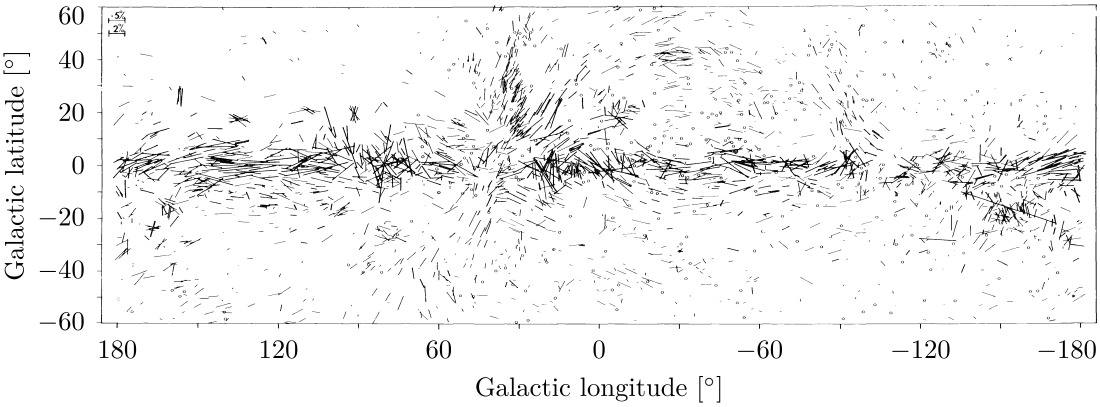

Figure 1.10: Observed polarisation of starlight. The dashes indicate the direction and the degree of polarisation. The scale is shown in the top left corner. Stars with polarisation smaller than 0.6% are represented by thinner dashes, stars with polarisation greater than or equal to 0.6% are represented by thicker dashes. Stars with polarisation smaller than 0.08% are shown as small circles. (Mathewson & Ford, 1970, Fig. Ia)

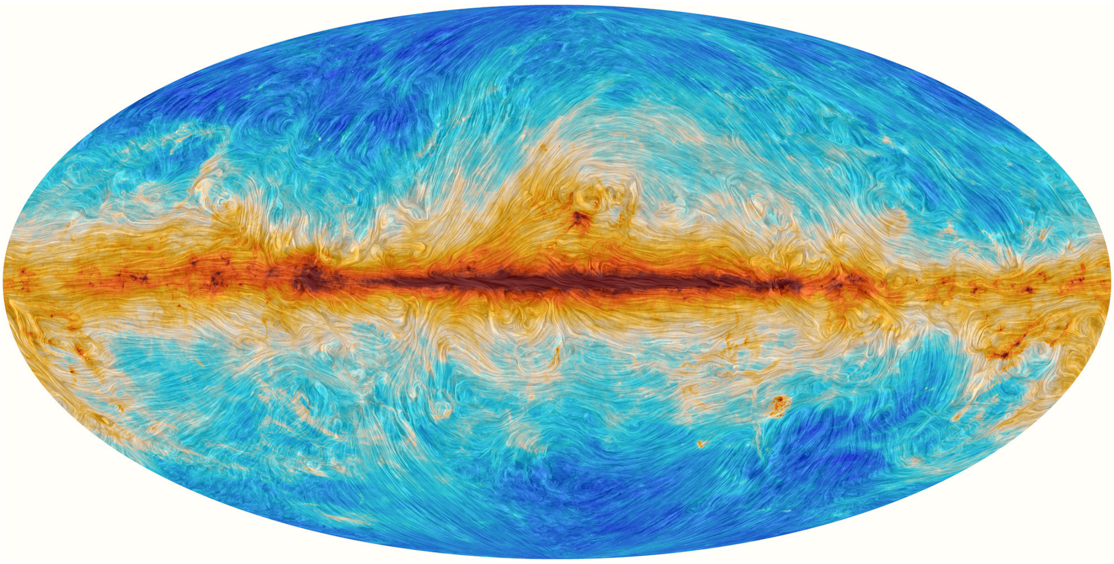

Figure 1.11: Polarised emission from Milky Way dust as observed by the Planck satellite. The colour scale represents the total intensity of dust emission, while the texture indicates the direction of magnetic field lines. (ESA and the Planck Collaboration 2015, Id 334841, `http://www.esa.int/spaceinimages/Images/2015/02/Polarised_emission_from_Milky_Way_dust`)

and scatter the component of light with the polarisation vector parallel to their long axis. Therefore, the passing light becomes partially polarised in the direction parallel to the interstellar magnetic field. The first large-scale survey of starlight polarisation, revealing the global structure of the Galactic magnetic field, was compiled by Mathewson & Ford (1970) (Fig. 1.10).

Another means of probing the structure of the interstellar magnetic field is the polarisation of submillimetre dust emission (Planck Collaboration et al., 2015). Figure 1.11 shows a full-sky image of polarised dust emission as observed by ESA's Planck space observatory[6].

The strength of the interstellar magnetic field can be estimated from the Zeeman splitting of spectral lines (e.g. of the H I line), from the Faraday rotation of linearly polarised radio signals, or from the synchrotron emission of relativistic electrons. The interstellar magnetic field in our Galaxy has an estimated typical strength of a few µG (Ferrière, 2001). For comparison, the magnetic field of the Earth has about 0.3 G at the equator; and the field of the Sun has about 1 G in quiet regions and $\propto 10^3$ G in sunspots.

Even though it is relatively weak, the Galactic magnetic field contributes significantly to the total pressure in the ISM. The magnetic pressure in the vicinity of the Sun is estimated at about $10^{-12}\,\mathrm{dyn\,cm^{-2}}$, which is comparable to the pressures of gas or cosmic rays there (Ferrière, 2001).

The Galactic magnetic field also plays an important role in interstellar magnetohydrodynamic turbulence, which is discussed in Sect. 1.2.

1.1.10 Interstellar dust

The presence of dust in interstellar space was discovered thanks to the effects it has on starlight. When studying the distribution of Galactic open star clusters, Trumpler (1930b) noticed that the diameters of the more distant ones seemed systematically larger. He also noticed a discrepancy between colour indices and spectral types of stars. More distant stars seemed redder. To explain that, he concluded that within the Milky Way Galaxy light is subject to selective absorption. In a following study, Trumpler (1930a) suggested that it is interstellar dust what causes this selective absorption.

The total attenuation of light, when it passes through a medium, is given by the combined effect of absorption and scattering. It is referred to as *extinction*. Even though dust represents only about 1% of the mass of the ISM, it is the dominant cause of interstellar extinction (Ferrière, 2001). The contribution from gas is negligible. The mean extinction curve for the dust in our Galaxy is shown in Fig. 1.12.

---

[6] Planck space observatory: `http://sci.esa.int/planck/`

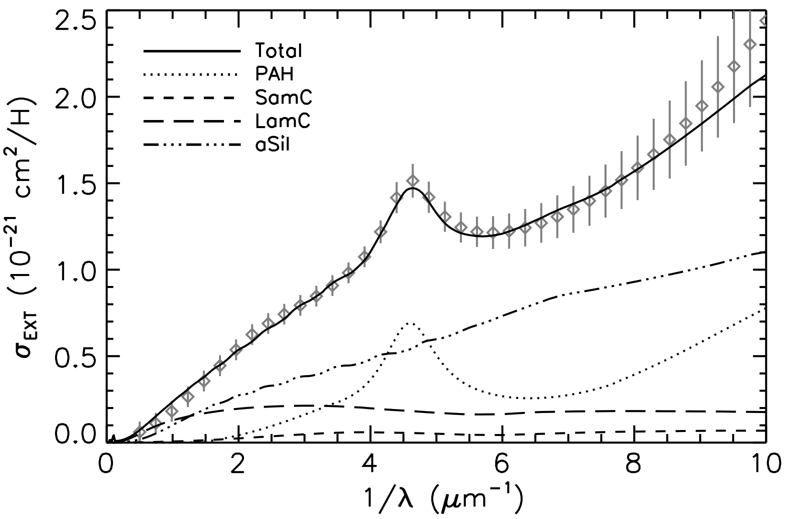

Figure 1.12: Mean dust extinction curve for our Galaxy. The grey diamonds show the extinction as given by the observation-based model of Fitzpatrick (1999) for $R_{\rm V} \equiv A_{\rm V}/E_{\rm B-V} = 3.1$. The black lines show synthetic curves generated by the code DustEM for various types of dust: PAHs, small amorphous carbon grains (SamC), large amorphous carbon grains (LamC), and amorphous silicate grains (aSil). (Compiègne et al., 2011, Fig. 4, retrieved from arXiv:1010.2769v1 [astro-ph.GA])

The dust column density is well correlated with the hydrogen column density, so the densest concentrations of dust are associated with molecular clouds (Schlegel et al., 1998; Ferrière, 2001). Dust clouds can be observed both as dark nebulae, when they lie in front of a brighter background, or as reflection nebulae, when they are illuminated by a nearby bright star.

Dust grains are believed to be nonspherical in shape and tend to align themselves with the Galactic magnetic field. This causes the observed polarisation of starlight and the polarisation of thermal dust emission (Figs. 1.10 and 1.11). The grains have a typical size of less than 1 µm (Draine, 2003), which is comparable to the size of a particle in cigarette smoke. The typical temperature of dust grains with a size greater than about 0.01 µm is 15 K to 20 K (Draine, 2003). Their thermal emission has therefore a peak at far-infrared wavelengths between 140 µm and 200 µm (Fig. 1.13). Indeed, far-infrared emission is a good tracer of interstellar dust. A full-sky image in a broadband filter centred at 100 µm is shown in Fig. 1.14.

Very small grains radiate also nonthermally, as they can be heated to high non-equilibrium temperatures by absorbing a single photon (Draine, 2003). For example, polycyclic aromatic hydrocarbons (PAHs) have strong emission features at wavelengths around 10 µm (Fig. 1.13). The emission of very small grains is a good tracer of photodissociation regions (PDRs) around stars with strong UV radiation (Fig. 1.19).

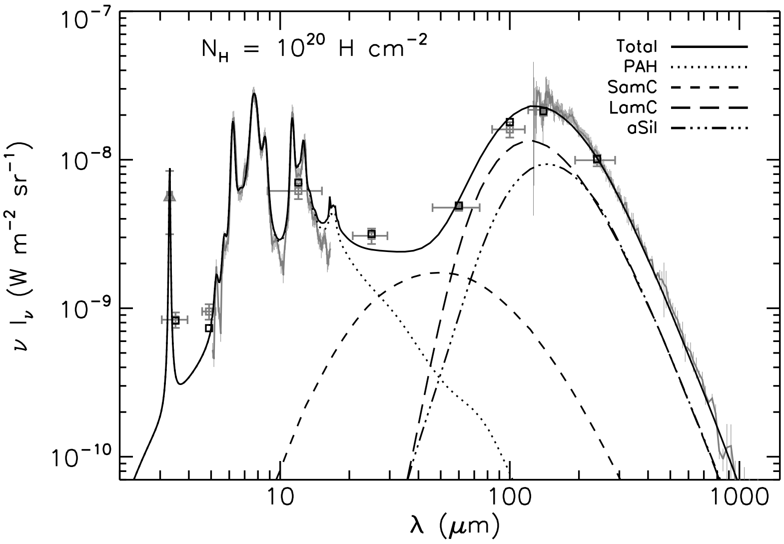

Figure 1.13: Emission spectrum of dust in our Galaxy, normalised to the hydrogen column density of 10^{20} cm^{-2}. The grey symbols and curves show the observed emission from various instruments. The black lines show synthetic spectra generated by the code DustEM for various types of dust. The acronyms are the same as in Fig. 1.12. (Compiègne et al., 2011, Fig. 2, retrieved from arXiv:1010.2769v1 [astro-ph.GA])

Most of the dust in our Galaxy is believed to have formed in atmospheres of late type stars and in planetary nebulae, where densities are high enough and temperatures low enough for gas to condense into dust grains (Ferrière, 2001). This mechanism of dust formation is, however, too slow to explain its observed presence in early galaxies (Bertoldi et al., 2003; Watson et al., 2015). Supernovae are therefore believed to be another source. Both simulations (e.g. Nozawa et al., 2003) and observations (e.g. Bouchet et al., 2006; Indebetouw et al., 2014) suggest they can produce large amounts of dust, and possibly supply that dust into the ISM. Dust seems to form also around massive stars before they turn into supernovae, as is suggested by the dusty envelopes found around massive stars by the *Spitzer* Space Telescope (Gvaramadze et al., 2010; Wachter et al., 2010).

Recommended video. For a review of interstellar dust, with emphasis on the mechanisms of dust formation, I recommend the video *Rosseland Lecture 2015 – Making, baking and breaking: Dust in the interstellar medium* by Anja C. Andersen, available at `https://youtu.be/Zqx1C4XNLbw`.

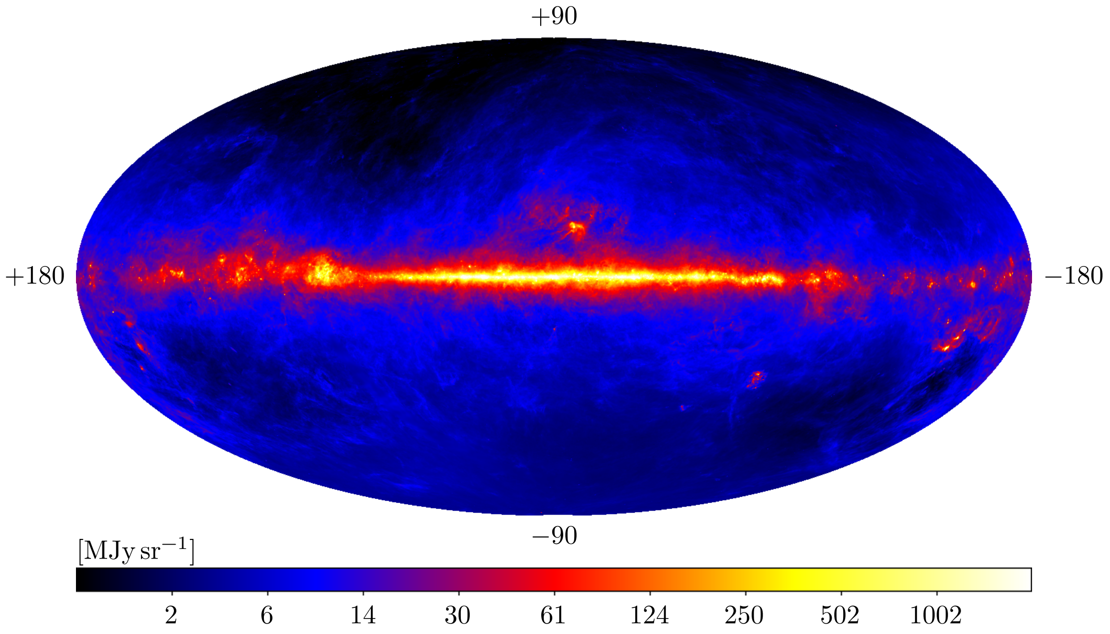

Figure 1.14: Sky in infrared continuum emission at 100 µm tracing dust in our Galaxy; Hammer projection, Galactic coordinates centred at the Galactic centre. (The observation was made by the IRAS – Infrared Astronomical Satellite, Neugebauer et al., 1984. The image data were provided by the IRIS data release – Improved Reprocessing of the IRAS Survey, Miville-Deschênes & Lagache, 2005.)

Figure 1.15: *The Starry Night* by Vincent van Gogh (1889). The whorls in the sky seem to be more than just fine art. An analysis of Aragón et al. (2006) showed that the luminance fluctuations in the painting compares well with the predictions of Kolmogorov for turbulent flows (see Sect. 1.2.5). Van Gogh was somehow able to capture the properties of turbulence surprisingly well in this famous painting.

1.2 Turbulence in the interstellar medium

Turbulence is a chaotic flow that occurs when the flow velocity surpasses a certain value. Turbulent flows are characterised by irregularity, vorticity, and increased rates of dissipation and diffusion. Energy and momentum exchange between fluid elements is significantly faster in turbulent flows than in laminar ones. Even though we can observe turbulence almost everywhere around us, it is still not fully understood. Turbulence, namely the existence of a smooth solution to the Navier-Stokes equations, is one of the Millennium Prize Problems[7] that were stated in 2000 by the Clay Mathematics Institute. The fascination with turbulence can

---

[7] Millennium Prize Problems: `http://www.claymath.org/millennium-problems`

be found even in fine art. Painting *The Starry Night* (Fig. 1.15) by Dutch artist Vincent van Gogh features patterns typical for turbulent flows. Indeed, the analysis of the painting by Aragón et al. (2006) showed that Van Gogh captured turbulence with exceptionally good mathematical precision.

1.2.1 Basic equations of fluid dynamics

The motion of fluids is studied by fluid dynamics, sometimes also called hydrodynamics. Fluid dynamics is built on four basic equations. Three equations describe conservation laws for momentum, mass, and internal energy; and one equation, the equation of state, describes a relation between thermodynamic variables.

Conservation of momentum. The conservation of momentum of a fluid element is given by the Cauchy momentum equation

$$\varrho \frac{\mathrm{D}\mathbf{u}}{\mathrm{D}t} = \nabla \cdot \sigma + \mathbf{f}, \tag{1.6}$$

where ϱ is the fluid density, $\mathbf{u}$ is the flow velocity, σ is the Cauchy stress tensor, and $\mathbf{f}$ represents the density of all body forces. A body force is a force acting on each fluid element. A typical example of a body force is gravity (external or self-gravity), or magnetic field as described in Sect. 1.2.4. $\mathrm{D}\mathbf{u}/\mathrm{D}t$ represents the material derivative of the fluid velocity field, i.e. the derivative in the reference frame comoving with the fluid element. It can be expanded as

$$\frac{\mathrm{D}\mathbf{u}}{\mathrm{D}t} = \frac{\partial \mathbf{u}}{\partial t} + (\mathbf{u} \cdot \nabla)\mathbf{u}. \tag{1.7}$$

For an incompressible Newtonian fluid, the Cauchy stress tensor σ can be expressed as

$$\sigma_{ij} = -p\delta_{ij} + \mu \left(\frac{\partial u_i}{\partial x_j} + \frac{\partial u_j}{\partial x_i} \right), \tag{1.8}$$

where p is the fluid pressure, and μ is the fluid dynamic viscosity. Dynamic viscosity is the measure of a fluid's resistance to shear flows. Using Eqs. 1.7 and 1.8, the Cauchy momentum equation 1.6 can be rewritten in the form of the Navier-Stokes equations

$$\varrho \left(\frac{\partial \mathbf{u}}{\partial t} + (\mathbf{u} \cdot \nabla)\mathbf{u} \right) = -\nabla p + \mu \Delta \mathbf{u} + \mathbf{f}. \tag{1.9}$$

The Navier-Stokes equations describe the conservation of momentum for an incompressible Newtonian fluid.

The ratio of inertial forces to viscous forces is given by the Reynolds number

$$\mathrm{Re} = \frac{\varrho \mathbf{u} L}{\mu} = \frac{\mathbf{u} L}{\nu}, \tag{1.10}$$

where L is a characteristic length of the system (e.g. a pipe's diameter), and $\nu = \mu/\varrho$ is the fluid kinematic viscosity. The same Reynolds number of two incompressible flows suggests they will exhibit the same flow patterns. Although there is no theory relating turbulence to the Reynolds number, experiments and numerical simulations show that turbulent flows start usually appearing at Reynolds numbers over 4000 (Morrison, 2013).

The advection term $(\mathbf{u} \cdot \nabla)\mathbf{u}$ in Eq. 1.9 causes that, at large Reynolds numbers, solutions of the equation are unstable to finite perturbations. It is this term where hydrodynamic turbulence originates.

Conservation of mass. The conservation of mass is given by the continuity equation

$$\frac{\partial \varrho}{\partial t} + \nabla \cdot (\varrho \mathbf{u}) = 0, \tag{1.11}$$

which in the case of an incompressible flow reduces to

$$\nabla \cdot \mathbf{u} = 0. \tag{1.12}$$

Conservation of internal energy. The conservation of internal energy is given by the equation (Fitzpatrick, 2012)

$$\varrho \frac{\mathrm{D}e}{\mathrm{D}t} = -p \nabla \cdot \mathbf{u} + \chi + \nabla \cdot (\kappa \nabla T), \tag{1.13}$$

where e is the internal energy; χ is the viscous dissipation function, i.e. the rate of heat generation due to viscosity; κ is the thermal conductivity; and T is the temperature. This equation says that the internal energy of a fluid element changes as the combined result of work done by pressure as the element volume changes, heating due to viscous dissipation, and heat conduction.

Equation of state. The relation between thermodynamic state variables is given by an equation of state. In the case of ideal gas, the equation of state has the form

$$p = \frac{\varrho R T}{M}, \tag{1.14}$$

where $R \approx 8.31\,\mathrm{J\,mol^{-1}\,K^{-1}}$ is the gas constant, and M is the molar mass.

1.2.2 Reynolds-averaged Navier-Stokes equations

Turbulence can be viewed as local fluctuations of quantities. *Reynolds decomposition* is a technique to separate their average and fluctuating components (Reynolds, 1895). Let

$$\mathbf{u} = \overline{\mathbf{u}} + \mathbf{u}', \quad p = \overline{p} + p', \quad \mathbf{f} = \overline{\mathbf{f}} + \mathbf{f}', \tag{1.15}$$

where $\overline{\mathbf{u}}$, $\overline{p}$, and $\overline{\mathbf{f}}$ are the time-averaged means, and $\mathbf{u}'$, p', and $\mathbf{f}'$ are the local fluctuations, which satisfy

$$\overline{\mathbf{u}'} = \overline{p'} = \overline{\mathbf{f}'} = 0. \tag{1.16}$$

If we substitute the decomposed quantities from Eq. 1.15 into the continuity equation 1.12, and take the time average of the whole equation, we get

$$\nabla \cdot \overline{\mathbf{u}} = 0 \qquad \text{and} \qquad \nabla \cdot \mathbf{u}' = 0. \tag{1.17}$$

Substituting the decomposed quantities from Eq. 1.15 into the Navier-Stokes equations 1.9, and taking the time average of the equations results in the Reynolds-averaged Navier-Stokes equations (RANS) (adopted from McDonough, 2007)

$$\varrho \nabla \cdot \overline{\mathbf{u}}^2 + \nabla \cdot \mathsf{R} = -\nabla \overline{p} + \mu \Delta \overline{\mathbf{u}} + \overline{\mathbf{f}}, \tag{1.18}$$

where $\mathsf{R} = \varrho \overline{\mathbf{u}'^2}$ is the Reynolds stress tensor that represents the force action of the fluid due to the turbulent fluctuations. RANS describe approximate time-averaged solutions to the Navier-Stokes equations.

1.2.3 Vorticity equation

The vorticity is defined as

$$\omega = \nabla \times \mathbf{u}. \tag{1.19}$$

It is the curl of the flow velocity and is a measure of the local fluid circulation. If we take the curl of the Navier-Stokes equations 1.9, assuming incompressible fluid, and assuming $\nabla \times \mathbf{f} = 0$ (i.e. $\mathbf{f}$ is an irrotational field, e.g. gravity), we get the vorticity-transport equation (Morrison, 2013)

$$\frac{\partial \omega}{\partial t} + (\mathbf{u} \cdot \nabla)\omega = (\omega \cdot \nabla)\mathbf{u} + \nu \Delta \omega. \tag{1.20}$$

This equation describes the evolution of the fluid vorticity. The term $(\omega \cdot \nabla)\mathbf{u}$ is the source of the vortex stretching (deformation of vortices occurring in three dimensions).

1.2.4 Magnetohydrodynamic equations

The dynamics of electrically conducting fluids is studied by magnetohydrodynamics (MHD). To take into account the interaction of a fluid with an electromagnetic field, we need to include the Lorentz force in the Navier-Stokes equations 1.9. The Lorentz force density is given by the equation

$$\mathbf{f}_{\mathrm{L}} = q(\mathbf{E} + \mathbf{u} \times \mathbf{B}), \tag{1.21}$$

where q is the charge density, $\mathbf{E}$ is the electric field, $\mathbf{u}$ is the fluid velocity, and $\mathbf{B}$ is the magnetic field. Let us assume a fluid that is quasineutral, but electrically conducting. An example of such a fluid is plasma. The Lorentz force density then reduces to

$$\mathbf{f}_{\mathrm{L}} = \mathbf{j} \times \mathbf{B}, \tag{1.22}$$

where $\mathbf{j} = q\mathbf{u}$ is the electric current density. Using Ampere's law, and still assuming quasineutrality, we can further expand the Lorentz force as

$$\mathbf{j} \times \mathbf{B} = \frac{(\nabla \times \mathbf{B}) \times \mathbf{B}}{\mu_0} = \frac{(\mathbf{B} \cdot \nabla)\mathbf{B}}{\mu_0} - \nabla \left(\frac{B^2}{2\mu_0} \right), \tag{1.23}$$

where μ_0 is the vacuum permeability. The term $\frac{(\mathbf{B} \cdot \nabla)\mathbf{B}}{\mu_0}$ is the magnetic tension force, more precisely the magnetic tension gradient with the unit of force density; and the term $\frac{B^2}{2\mu_0}$ is the magnetic pressure. If we now include the Lorentz force as given in Eq. 1.23 in the Navier-Stokes equations 1.9, we get the MHD momentum equation

$$\varrho \left(\frac{\partial \mathbf{u}}{\partial t} + (\mathbf{u} \cdot \nabla)\mathbf{u} \right) = -\nabla p + \mu \Delta \mathbf{u} + \frac{(\mathbf{B} \cdot \nabla)\mathbf{B}}{\mu_0} - \nabla \left(\frac{B^2}{2\mu_0} \right) + \mathbf{f}. \tag{1.24}$$

The coupling of the magnetic field and the velocity field is described by the MHD induction equation. It follows from Maxwell's equations, Ohm's law, and the assumption of fluid quasineutrality. The MHD induction equation can be written in the form

$$\frac{\partial \mathbf{B}}{\partial t} = \nabla \times (\mathbf{u} \times \mathbf{B}) + \eta \Delta \mathbf{B}, \tag{1.25}$$

where $\eta = (\mu_0 \gamma)^{-1}$ is the magnetic diffusivity, sometimes also called the electrical resistivity; and γ is the electrical conductivity of the fluid. In the case of *ideal* MHD, the magnetic diffusivity η is zero, which makes the diffusive term $\eta \Delta \mathbf{B}$ also zero. The magnetic field is then so tightly coupled with the fluid that it is said to be *frozen* into the fluid.

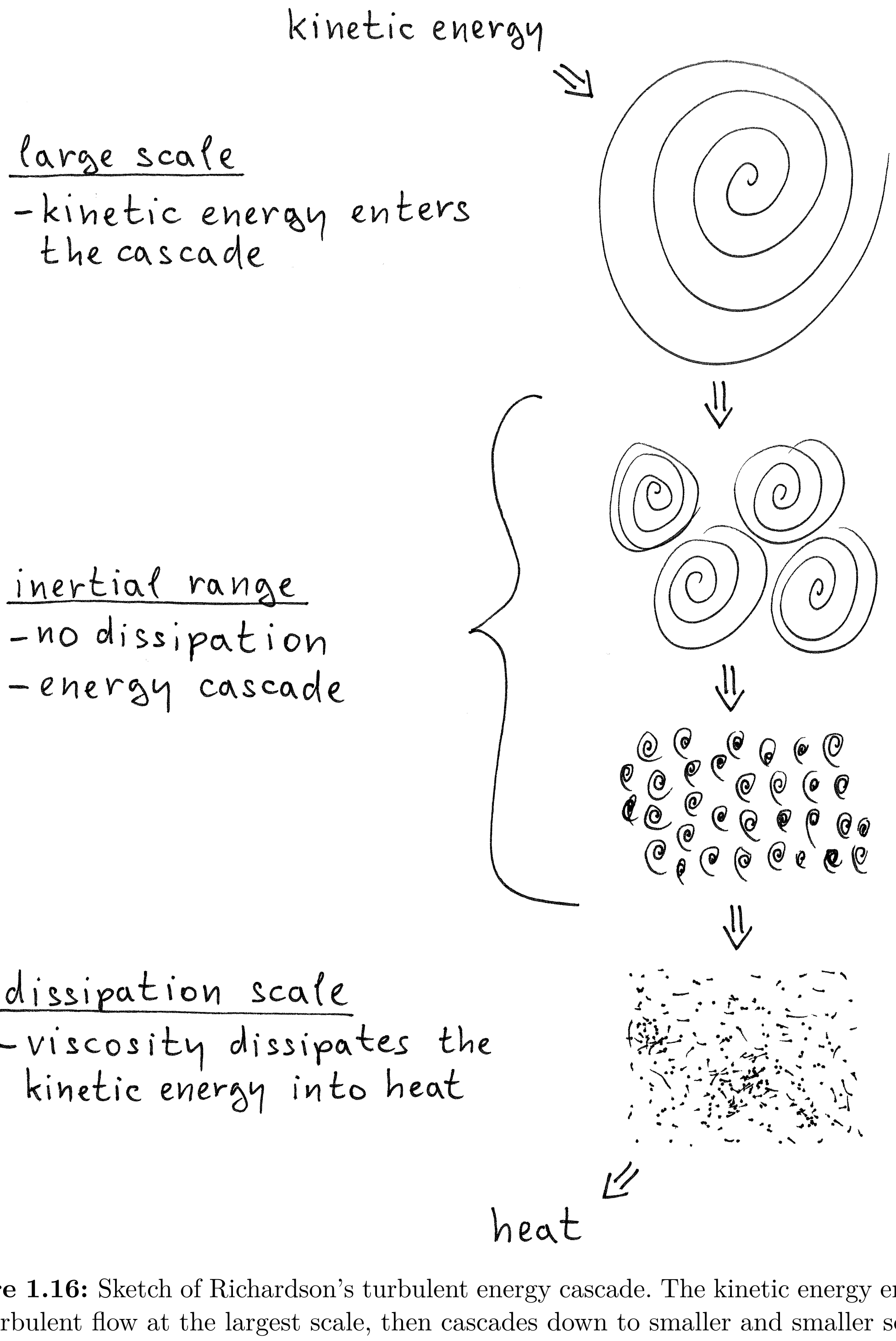

Figure 1.16: Sketch of Richardson's turbulent energy cascade. The kinetic energy enters the turbulent flow at the largest scale, then cascades down to smaller and smaller scales until it reaches the dissipation scale, where it is converted into heat by the fluid viscosity.

1.2.5 Kolmogorov theory

Turbulent flows can be intuitively described as consisting of large eddies[8] that are unstable and break up into smaller eddies. These smaller eddies are also unstable and break up into even smaller eddies and so on. Richardson (1922) stated that (quotation adopted from McDonough, 2007):

> *"Big whorls have little whorls,*
> *Which feed on their velocity;*
> *And little whorls have lesser whorls,*
> *And so on to viscosity."*

In Richardson's view, the turbulent kinetic energy is injected into the system at the largest scale and cascades down to a scale where the fluid viscosity can effectively dissipate it, i.e. convert into heat (Fig. 1.16). We can distinguish three main length scales in a turbulent flow:

1. large scale – where the kinetic energy enters the cascade;
2. inertial range – where the energy cascades from larger to smaller scales, without any additional energy source, and without dissipation; and
3. small scale, also referred to as the Kolmogorov length scale η_{K} – where the viscosity dissipates the kinetic energy into heat.

In 1941, Andrey Kolmogorov published his theory of turbulence, today known as the *K41 theory*. The original papers are in Russian. Here I adopt the description of K41 as given in McDonough (2007) and Benzi & Frisch (2010). An English translation of one of the original papers is available in Kolmogorov (1991).

Kolmogorov used Richardson's idea of the energy cascade. He assumed that at very high finite Reynolds numbers, the small scale turbulence is statistically isotropic and its properties are universally and uniquely determined by the viscosity ν and the rate of energy dissipation ε. He then used the dimensional analysis to derive the following relation for the small scale:

$$\eta_{\mathrm{K}} = \left(\frac{\nu^3}{\varepsilon}\right)^{1/4}. \tag{1.26}$$

Further, assuming that turbulence is self-similar at the inertial range scales, and again employing the dimensional analysis and empirical research, he derived a relation for the mean-square velocity increment

$$\langle(\delta\mathbf{u}(l))^2\rangle = C\varepsilon^{2/3}l^{2/3}, \tag{1.27}$$

---

[8] eddies = coherent patterns of fluctuations in a flow

where C is a universal constant, l is a distance over which the increment is measured, and the mean is the sample mean taken over the whole studied system. The mean-square velocity increment is a second-order structure function[9]. From this equation, he derived the scaling relation for the turbulent energy spectrum

$$E(k) = C_{\mathrm{K}} \varepsilon^{2/3} k^{-5/3}, \tag{1.28}$$

where k is the wavenumber (the length of the wavenumber vector) corresponding to the scale for which the energy is measured, and C_{K} is the Kolmogorov constant. Equations 1.27 and 1.28, also referred to as the "2/3" law and the "5/3" law, are the most widely used and tested results of the K41 theory.

Kolmogorov's conclusions were based on empirical research and strong assumptions of turbulence self-similarity and incompressibility. However, numerical simulations suggest that turbulence is probably not universally self-similar (Benzi & Frisch, 2010). Even though self-similarity may be a reasonable assumption for interstellar turbulence, the ISM is highly compressible, which breaks the other assumption of incompressibility. Moreover the turbulence-driving energy is injected into the ISM at all scales, not only at the largest one (Elmegreen & Scalo, 2004). Nevertheless, the scaling of turbulent quantities as predicted by Kolmogorov is observed in experiments and numerical simulations (McDonough, 2007), as well as in the ISM (Elmegreen & Scalo, 2004; Scalo & Elmegreen, 2004).

To this day, there is no fully deductive theory that would derive Kolmogorov's "2/3" and "5/3" laws from the Navier-Stokes equations.

1.2.6 Magnetised turbulence

Similar to the Reynolds decomposition discussed in Sect. 1.2.2, we can decompose the global magnetic field into the average and fluctuating component: $\mathbf{B} = \mathbf{B}_0 + \delta\mathbf{B}$. Using the Elsasser variables $\mathbf{z}^{\pm} = \mathbf{u} \pm (\mu_0 \varrho)^{-1/2} \delta\mathbf{B}$, based on Elsasser (1950), we can rewrite the MHD momentum and induction Eqs. 1.24 and 1.25 as (adopted from Falceta-Gonçalves et al., 2014)[10]

$$\frac{\partial \mathbf{z}^{\pm}}{\partial t} \mp v_{\mathrm{A}} \nabla_{\|} \mathbf{z}^{\pm} + \mathbf{z}^{\mp} \cdot \nabla \mathbf{z}^{\pm} = -\frac{1}{\varrho} \nabla p + \frac{\nu + \eta_{\mathrm{K}}}{2} \delta \mathbf{z}^{\pm} + \frac{\nu - \eta_{\mathrm{K}}}{2} \delta \mathbf{z}^{\mp} + \frac{\mathbf{f}}{\varrho}, \tag{1.29}$$

where $v_{\mathrm{A}} = B_0 / \sqrt{\mu_0 \varrho}$ is the Alfvén velocity, and $\nabla_{\|}$ is the spatial derivative parallel to the average magnetic field $\mathbf{B}_0$.

---

[9] The structure function of order p for a quantity A is defined as $S_p(\delta r) = \langle |A(\mathbf{r}) - A(\mathbf{r} + \delta \mathbf{r})|^p \rangle$, where $\mathbf{r}$ is the position where the quantity A is measured, and $\delta \mathbf{r}$ is the position increment.

[10] In the paper, Falceta-Gonçalves et al. (2014) do not divide the pressure term on the right hand side of the equation by the fluid density. This is probably an error, because without the $1/\varrho$ factor, the symbol p in the equation would represent the kinematic pressure, i.e. the pressure divided by density. They, however, use the symbol p for true pressure earlier in the paper. Also Falceta-Gonçalves et al. (2014) use the CGS units, while in this thesis I prefer the SI units.

Iroshnikov-Kraichnan model (weak isotropic turbulence of shear Alfvén waves). Iroshnikov (1964) and Kraichnan (1965) considered isotropic MHD turbulence that originates in interactions of wave packets $\mathbf{z}^{\pm}$ travelling in opposite direction with the Alfvén phase velocity $v_{\rm A}$. The interactions between the wave packets are weak, i.e. $|\mathbf{z}^{\pm}| \ll v_{\rm A}$, so a change in the fluid velocity after each interaction is small. The interaction time scale is the Alfvén time $\tau_{\rm A} = l_{\parallel}/v_{\rm A}$, where $l_{\parallel}$ is the characteristic length scale of a wave packet in the direction of the mean field $\mathbf{B}_0$. The assumption of isotropy means that $l_{\parallel} = l$. The assumption of weak Alfvén turbulence means $\tau_{\rm A} \ll \tau_{\rm eddy}$, where $\tau_{\rm eddy} = l/\delta u_l$ is the eddy turnover timescale[11] at the length scale l. The Iroshnikov-Kraichnan model predicts the energy cascade

$$E(k) \propto v_{\rm A}^{1/2} k^{-3/2}. \tag{1.30}$$

Later, Marsch (1991) proposed to use $\tau_{\rm eddy}$ instead of $\tau_{\rm A}$ for the wave packets interactions, and derived a Kolmogorov-like spectrum $E(k) \propto k^{-5/3}$.

Goldreich-Sridhar model (strong anisotropic turbulence of shear Alfvén waves). Goldreich & Sridhar (1995) considered anisotropic, strong turbulence, where $|\mathbf{z}^{\pm}| > v_{\rm A}$. They assumed a critical balance between the wave interaction rate in the parallel direction and the cascade rate in the perpendicular direction such that $k_{\parallel} v_{\rm A} \approx k_{\perp} z_{\perp}$. The resulting energy spectrum is Kolmogorov-like, i.e.

$$E(k) \propto k_{\perp}^{-5/3} \qquad \text{and} \qquad k_{\parallel} \propto k_{\perp}^{2/3}. \tag{1.31}$$

In the model, anisotropy is local, and the large number of eddies with randomly distributed local magnetic fields will yield an isotropic spectrum on average.

What observations and simulations suggest. Numerical experiments suggest that different wave modes can have different energy spectra. While the Alfvén and slow modes follow the Kolmogorov spectrum, fast modes follow the Iroshnikov-Kraichnan spectrum (Cho & Lazarian, 2002, 2003; Kowal & Lazarian, 2010).

The Iroshnikov-Kraichnan spectrum was observed in the solar wind and interplanetary medium (Bamert et al., 2008; Ng et al., 2010). Other observations, however, favour the Kolmogorov spectrum (see references in Falceta-Gonçalves et al., 2014). An analysis of solar wind turbulence by Salem et al. (2009) shows that both types of cascades can be present: The magnetic field fluctuations exhibit the Kolmogorov spectrum, while the velocity field fluctuations exhibit the Iroshnikov-Kraichnan spectrum. Observations also show that the solar wind turbulence is highly anisotropic (Horbury et al., 2008).

---

[11] The eddy turnover timescale is the time taken for a hypothesized turbulent eddy to perform one complete 360° rotation (McDonough, 2007)

It is still not settled which energy cascade describes interstellar MHD turbulence better, or whether it can be adequately described by only a single cascade.

1.2.7 Power sources for interstellar turbulence

The power sources that have been proposed to supply energy for interstellar turbulence include (Elmegreen & Scalo, 2004):

- stars,
- Galactic rotation,
- gas self-gravity,
- fluid instabilities, and
- Galactic gravity.

Stars release energy into the ISM via protostellar and stellar winds, expanding H II regions, and supernova explosions. Galactic rotation releases energy in spiral arms and in the bar by the magnetorotational instability and by the gravitational scattering of clouds. Self-gravity of gas releases energy by gravitational instabilities, e.g. collapse of a cloud. Fluid instabilities include, e.g. the Kelvin-Helmholtz or the Rayleigh-Taylor instability. Galactic gravity releases energy by disk–halo–disk matter circulation (the Galactic fountain), Parker plasma instability, and by interactions of galaxies.

Norman & Ferrara (1996) estimated the contribution of various types of stellar sources and calculated the grand source function of the power for interstellar turbulence (Fig. 1.17). It is dominated by superbubbles and supernovae, followed by winds of massive stars. H II regions play a minor role. How much of the energy released by stars into the ISM is actually converted into turbulence is, however, still uncertain. Assuming an efficiency factor of 0.1, the total contribution from stellar winds and supernovae can be estimated at be of the order of $10^{-26}\,\mathrm{erg\,cm^{-3}\,s^{-1}}$ (van Buren, 1985; Mac Low & Klessen, 2004). The recent numerical simulations done by Fierlinger et al. (2016) suggest that the efficiency factor could be a few percent.

The contribution of power sources inside molecular clouds, before star formation begins, may exceed the global ISM averages up to 10 times (Stone et al., 1998; Basu & Murali, 2001).

Mac Low & Klessen (2004) estimated that magnetorotational instabilities can convert the Galactic rotation into gas motion at a rate of the order of 10^{-29} $\mathrm{erg\,cm^{-3}\,s^{-1}}$. That is about 1000 times less that the contribution of stellar sources. The Galactic rotation may be, however, an important source of energy for turbulence

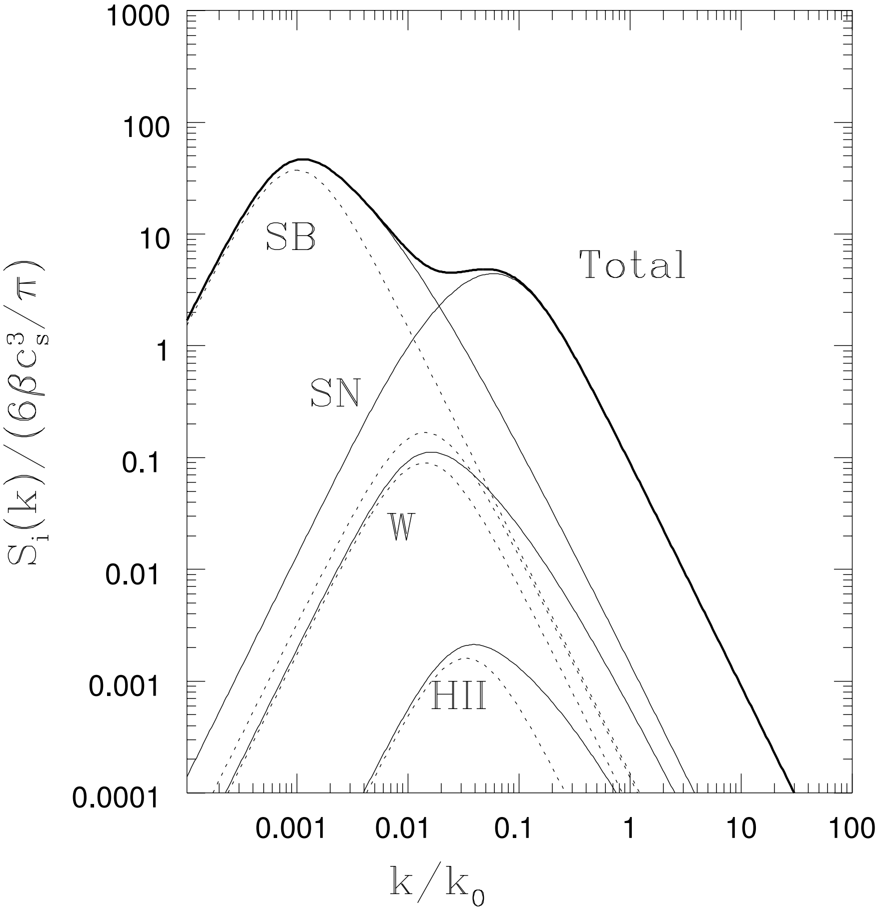

Figure 1.17: Source functions $S_i(k)$ as given by Norman & Ferrara (1996) for stellar sources of power for interstellar turbulence: H II regions (HII), winds of massive stars (W), supernovae (SN), and superbubbles (SB). Dashed lines show the contribution of secondary shocks only – i.e. shocks reflected off interstellar clouds; solid lines show the total contribution of primary and secondary shocks. The thick solid line shows the grand source function, i.e. the total power released into turbulent motions by all four types of stellar sources. (Figure retrieved from arXiv:astro-ph/9602146v1.)

in outer Galactic regions. Extended H I disks in spiral galaxies have a relatively uniform velocity dispersion of about 6 km s^{-1}. Since there are little stellar sources in these regions, Sellwood & Balbus (1999) argue that the power required to maintain such velocity dispersions could be extracted from the disk differential rotation by magnetohydrodynamic instabilities.

The total power that could be converted from the Galactic rotation into turbulence in spiral shocks is about 5×10^{-27} erg cm^{-3} s^{-1}, but the fraction that is actually converted is unknown (Elmegreen & Scalo, 2004).

The gravitational binding energy can be converted into turbulence in the Galactic disk via swing-amplified shear instabilities. The total power available is of the order of 10^{-27} erg cm^{-3} s^{-1}, but the efficiency of conversion is unknown (Elmegreen & Scalo, 2004).

Vishniac (1994) described a kinematic instability that appears in the swept-up layer of decelerating expanding shells. A typical example of such a shell is a supernova remnant or a bubble formed by strong stellar wind. This instability is today referred to as nonlinear thin shell instability (NTSI). Its formation was confirmed by numerical simulations of Blondin & Marks (1996), who also showed it drives supersonic turbulence. Simulations by Walder & Folini (1998) confirmed that supersonic turbulence appears in expanding shells and colliding flows. Klein & Woods (1998) simulated collisions between two interstellar clouds using an adaptive mesh refinement (AMR) code. They found that instabilities like Kelvin-Helmholtz and NTSI appear and create a complex structure of clumpy filaments, similar to what is observed in the ISM. Interactions of shock waves with turbulent flows were numerically studied by Rotman (1991) and Andreopoulos et al. (2000). The studies suggested that a shock wave passing through an already turbulent flow can act as a turbulence booster. Kritsuk & Norman (2002b,a) used numerical simulations to study phase transformations in the ISM stimulated by thermal instabilities. They found that up to 10% of the thermal energy can be converted to gas motions, i.e. turbulence.

It is still an open question how much of the available power of the sources discussed above is converted into turbulence. The dominant sources of turbulence may differ in different regions of the Galaxy, but it seems that in the Galactic disk the dominant sources are superbubbles, supernovae and winds from massive stars.

1.2.8 Simulations

In 1980, Bania & Lyon performed one of the first numerical simulations involving ISM turbulence. The simulation used a grid of 40×40 square cells with the size of each cell of 4.5 pc. They studied the effects of OB stars on the surrounding ISM and found that superposition of expanding H II regions around these stars produced condensations of neutral medium. Some condensations were gravitationally unstable.

Later, hi-resolution simulations of compressible flows in two dimensions (Passot et al., 1988) and three dimensions (Porter et al., 1999, 2002) produced structures with filaments and sheets, similar to what is observed in molecular clouds.

The first simulations of turbulence in the ISM that included self-gravity were done by Leorat et al. (1990). They found that supersonic turbulence is capable of preventing cloud collapse, which can explain why clouds have lifetimes much larger than their free-fall times.

The first simulations of turbulence in a compressible, self-gravitating, magnetic ISM were carried out by Yue et al. (1993). They concluded that turbulence with self-gravity is the mechanism for generating structures like clumps and filaments observed in molecular clouds.

Padoan et al. (1999) compared synthetic ^{13}CO line spectra with observations of the Perseus molecular cloud. They concluded that models of idealised turbulent flows without self-gravity and stellar influence are consistent with the observed statistical properties of molecular clouds like Perseus.

Hydrodynamic simulations of star cluster formation in self-gravitating clouds were able to reproduce many features known from observations like filamentary structures, accretion disks, binaries, runaway stars, or brown dwarfs (e.g. Klessen & Burkert, 2000; Heitsch et al., 2001; Bonnell et al., 2003; Li et al., 2004; Bate, 2009). These simulations also demonstrated that dense cores collapsing into stars develop even if the global collapse of the cloud is suppressed by turbulence (Elmegreen & Scalo, 2004).

Arthur et al. (2011) and Medina et al. (2014) simulated the formation and expansion of H II regions in turbulent molecular clouds. Their simulations included magnetic fields, radiative transfer, and gas heating and cooling. The simulated H II regions featured plenty of structures associated with turbulence – like filaments, pillars, and globules – and were very similar in appearance to H II regions observed in the ISM (see Fig. 1.28 in Sect. 1.3.3). On the other hand, the numerical model did not include self-gravity, thus was unable to reproduce gravitational collapse, i.e. star formation.

Simulations of turbulence in general suffer from the lack of dynamic range. A typical Reynolds number in the ISM is 10^6 to 10^8 (Tielens, 2010) and the number of degrees of freedom scales like $\mathrm{Re}^{9/4}$ for three-dimensional incompressible turbulence (Elmegreen & Scalo, 2004). To cover the full dynamic range we would need a simulation with a resolution of 10^5 to 10^6 zones in each dimension. This is still beyond the capability of today's computers. Nevertheless, the simulations we can afford today are good enough to investigate the cascade in the inertial range, and geometrical and topological properties of turbulence in the ISM (Elmegreen & Scalo, 2004).

1.2.9 Observations

The earliest observations indicating that the ISM is turbulent include the observations of emission lines in the Orion Nebula done by von Hoerner (1951). He found that the root-mean-square radial velocities of those lines increase with projected separation as a power law with an index close to that predicted by Kolmogorov (1/3). Later, observations of the Orion Nebula by Wilson et al. (1959) suggested that the turbulence acting there is incompressible. Another early notion that the ISM is a turbulent environment can be found in the review of the hydrodynamics of the ISM and star formation by von Weizsäcker (1951). In the review, von Weizsäcker mentions that the ISM is turbulent and compressible. He also analyses a model of the ISM of von Hoerner[12], in which clouds are arranged in a hierarchical structure described by the density scaling

$$\frac{\varrho_\nu}{\varrho_{\nu+1}} = \left(\frac{l_\nu}{l_{\nu+1}}\right)^{-3k_\nu}, \tag{1.32}$$

where ν is the hierarchical level, ϱ_ν is the average density at the level ν, l_ν is the length scale of the level ν, and k_ν is the compressibility degree at the level ν. More recent numerical simulations of compressible turbulence suggest $k_\nu \approx 0.15$ (Kritsuk et al., 2007; Kowal & Lazarian, 2007; Falceta-Gonçalves et al., 2014).

However, other observations indicated otherwise: that the ISM is rather a static environment. Interstellar absorption and emission lines looked too smooth (Elmegreen & Scalo, 2004) and observations of dark, round globules by Bok & Reilly (1947), today known as *Bok globules*, suggested force equilibrium. The ISM was therefore considered by the majority of researchers an environment dominated by thermal pressure. It was modelled as several distinct phases in pressure equilibrium (see the paragraph discussing multiphase ISM models in Sect. 1.1.1). Mass was believed to be concentrated in clouds and clumps surrounded by a low density medium. This view of the ISM as a static environment was supported by various studies published in 1960s and 1970s (Elmegreen & Scalo, 2004).

A change came with observations in 1980s. Larson (1981) found that the internal velocity dispersion of clouds correlates well with their sizes and follows a power-law relation with a power-law index of 0.38, close to the prediction of Kolmogorov for the mean velocity increment (1/3, the square root of the "2/3" law, Eq. 1.27). Later, studies of Myers (1983), Dame et al. (1986), and Solomon et al. (1987) confirmed the correlation with a slightly greater power-law index of about -2. In a study of fluctuations of the mean CO velocities, Stenholm (1984) found a power spectrum with an index of -1.67 ± 0.35, also very close to 5/3. Low et al. (1984) described a new type of cloud, *interstellar cirrus*, seen in the Infrared Astronomical Satellite

---

[12] von Weizsäcker (1951) refers to a then-not-yet published work of von Hoerner.

(IRAS) observations at 100 µm. These cirrus clouds featured complex structures of filaments, typical for turbulent flows. And more observations indicating that the ISM is turbulent followed (see references in Elmegreen & Scalo, 2004).

The first in situ observations of interstellar turbulence were presented by Burlaga et al. (2015), who used the data acquired by the space probe Voyager 1. The measurements show that the fluctuations of the interstellar magnetic field in the solar vicinity have a Kolmogorov-like spectrum with a slope of $-5/3$, and that the turbulence acting there is compressible.

Today, the ISM is considered a turbulence-dominated environment, compressible, with Reynolds numbers over 10^6, and energy injected and dissipated over a wide range of scales (Elmegreen & Scalo, 2004; Falceta-Gonçalves et al., 2014).

1.2.10 Effects on the interstellar medium

Turbulence affects the ISM at all scales. Large-scale effects have already been mentioned in preceding sections. In this section I quickly summarise them and add also small-scale effects as described in the review by Scalo & Elmegreen (2004).

The effects of turbulence on the ISM can be divided as follows:

- Large-scale effects
    - affect the morphology,
    - form dense structures, and
    - support clouds against collapse.
- Small-scale effects
    - disperse and mix elements,
    - affect molecular chemistry,
    - scatter and accelerate cosmic rays, and
    - affect radio wave scintillation.

Affect the morphology. Filamentary structures are a typical feature observed in the ISM. Simulations and experiments show that similar structures are often produced by turbulent flows. Turbulence can also be responsible for the creation of some shells (Dib & Burkert, 2005; Hatzidimitriou et al., 2005), as discussed in Sect. 1.2.11. The morphology of the ISM is therefore believed to be strongly affected by turbulence.

Form dense structures. As discussed in Sect. 1.2.9, observations show that molecular clouds are hierarchical (von Weizsäcker, 1951), and their density structures can be represented by dendrograms (Rosolowsky et al., 2008). This hierarchy is believed to be a result of compressible supersonic turbulence (see review by Falceta-Gonçalves et al., 2014).

Support clouds against collapse. Turbulence is believed to be the main force preventing the collapse of gravitationally unstable clouds. Turbulent pressure, a model of how turbulence could support clouds against collapse, was considered in many studies (see references in Elmegreen & Scalo, 2004, Sect. 4.10.). However, it is probably not a model suitable for interstellar turbulence. Turbulent pressure is a reasonable approximation for microturbulence, i.e. turbulence happening at scales much smaller that the studied systems. This is not the case of the ISM, where most of the turbulent energy is injected at the largest scales. Therefore, Elmegreen & Scalo (2004) conclude that rather than by turbulent pressure, cloud collapse is prevented by the transfer of kinetic energy down the cascade to the motions of substructures, namely molecular clumps; and that turbulence prevents global cloud collapse, but not local collapse that occurs in cores produced by turbulence.

Disperse and mix elements. Observations suggest that the ISM is well mixed with fluctuations less than 30%, and that the mixing happens in times $\propto 10^8$ years. This is believed to be a result of turbulence. Turbulence increases the rate of dispersion and mixing of elements produced by supernovae and other stellar sources. The mixing may occur partly in expanding bubbles, partly in the ambient medium.

Affect molecular chemistry. Different chemical species are mixed by turbulent flows inside clouds. Turbulence can also heat the gas in clouds locally and allow temperature-sensitive reactions to happen. This could explain the large abundances of CH^+ and OH molecules found in clouds. Gredel (1997) concluded that CH^+ observations support the idea that the dissipation of the turbulent energy provides the heat needed for the formation of CH^+ molecules in clouds.

Scatter and accelerate cosmic rays. The scattering and acceleration of cosmic rays is caused by turbulent irregularities in the interstellar magnetic field. It is, however, not known if the turbulence interacting with cosmic rays is the same turbulence that acts at large scales. The high isotropy of cosmic rays observed on Earth (>99.95%) suggests that the scattering is very effective and happens frequently (Cutler & Groom, 1991). Cosmic rays are subject to the Fermi acceleration (Fermi, 1949) that happens in shocks and collisions with randomly moving magnetic irregularities. Cosmic rays are also being investigated as possible sources of energy for turbulence.

Affect radio wave scintillation. Radio wave scintillation is an analogue of the scintillation of stars when observed through the Earth's atmosphere. Turbulence in the atmosphere causes stars to blur and twinkle. The scintillation of radio waves from pulsars and other sources was one of the earliest indicators of turbulent ISM. Turbulence in the ISM blurs the pulsar images, spreads out the pulse arrival times, modulates the pulse intensity, or even splits its image. The effects of small-scale turbulence happens on a timescale of minutes, while those of large-scale turbulence happens on a timescale of days to months. Radio wave scintillation is caused by interstellar electron density fluctuations. The observed power spectrum of these fluctuations is usually close to the spectrum predicted by Kolmogorov.

1.2.11 Relation to shell-like structures

Shells and bubbles are not typical features observed in turbulent flows. They are, however, very common in the ISM. In fact, it is still an open question, as formulated by Elmegreen & Scalo (2004): *"Why is the power spectrum of ISM density structure a power law when direct observation shows the ISM to be a collection of shells, bubbles, comets, spiral wave shocks. . . ?"* Yet turbulence and shells are believed to be closely related. Superbubbles, i.e. shells created by winds and supernovae of stellar associations, are thought to be the dominant source of kinetic energy for turbulence in the Galactic disk (see Sect. 1.2.7). An example of a supernova remnant with evident turbulent features is the Crab Nebula shown in Fig. 1.8.

Turbulence, in turn, seems to be able to create shapes similar to shells. This was investigated by Dib & Burkert (2005), who performed numerical simulations with the grid-based code ZEUS-3D[13]. They used a grid of 128^3 cells and included cooling, heating, and self-gravity. With an algorithm for radiative transfer, they built synthetic maps of the H I line emission (Fig. 1.18) and compared those to observations. The structures that appeared in the synthetic maps were similar to the shells and holes observed in the Small and Large Magellanic Clouds, and in Holmberg II. They concluded that some shells in the ISM can be formed as a result of turbulence coupled with thermal and gravitational instabilities.

Hatzidimitriou et al. (2005) came to a similar conclusion based on observations of more than 500 expanding H I shells in the Small Magellanic Cloud. They found that all those shells are young with a dynamical age of a few Myr. They also found that most of the shells do not have any known OB association inside and 59 shells

---

[13] ZEUS-3D: `http://ap.smu.ca/~dclarke/zeus3d`, Stone & Norman (1992a,b); Stone et al. (1992); Clarke (1996, 2010)

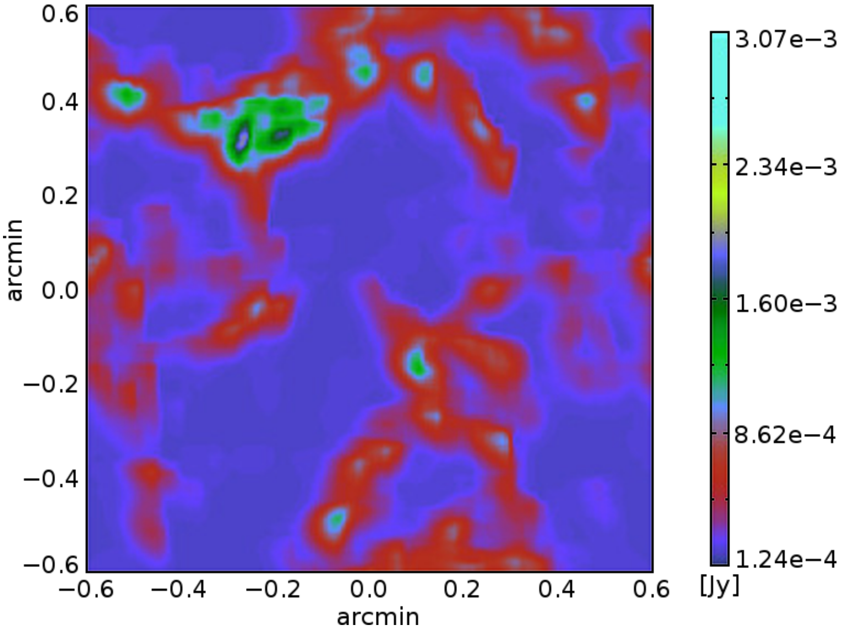

Figure 1.18: Synthetic H I emission map from a numerical simulation of a turbulent medium. It shows structures similar to filaments and shells observed in the ISM. (Dib & Burkert, 2005, retrieved from arXiv:astro-ph/0402593v2, remastered)

are empty – not having a single young stellar object associated with them. However, the properties of the empty and non-empty shells are very similar suggesting they have been created by the same mechanism. After they ruled out massive stars, gamma-ray bursts (GRBs), and high-velocity clouds (HVCs), they concluded that turbulence is the promising mechanism that could be responsible for the formation of those shells.

Thus, turbulence and shell-like structures can be viewed as interacting and closely related features of the ISM.

1.2.12 Summary and conclusion

Today, it is believed that turbulence is ubiquitous in the ISM and affects it at all scales. The observed spectrum of turbulent energy in the ISM is in a good agreement with the "5/3" power-law predicted by Kolmogorov. The predictions of Kolmogorov are based on the assumptions of the Newtonian fluid, flow incompressibility, and turbulence self-similarity. However, these assumptions are unlikely valid in the ISM. Observations indicate that the ISM is highly compressible. Moreover, simulations suggest that turbulence is probably not universally self-similar. Yet the Kolmogorov theory gives reasonable predictions and so far has been the core theory of turbulence on which other more complex theories build.

Magnetic fields bring additional complexity to hydrodynamic turbulence, but seem not to change the slope of the turbulence power spectrum significantly. The Iroshnikov-Kraichnan energy spectrum has the slope of $-3/2$, which is relatively close to Kolmogorov's $-5/3$. Other models of magnetic turbulence predict even a Kolmogorov-like spectrum. Magnetic fields cause, however, that the conducting fluid moves more easily in the direction parallel to the field lines, therefore introduce anisotropy to turbulence.

The dominant energy source for turbulence in the Galactic disk are probably stars; namely stellar winds, expanding H II regions, supernovae, and superbubbles. In outer Galactic regions, where stellar activity is limited, the dominant energy source may be the Galactic rotation.

Turbulence is believed to be responsible for the observed hierarchical structure of the ISM. It is also believed to be a major force preventing the global collapse of molecular clouds, while helping with the formation of local condensations. These local condensations, i.e. cores of molecular clumps, can in turn start forming new stars. The small-scale effects of turbulence include dispersal and mixing of elements, effects on molecular chemistry, scattering and acceleration of cosmic rays, and effects on the radio wave scintillation.

Shell-like structures and turbulence are thought to be closely related and interacting features. Shells of various origins are a major source of turbulent energy. Turbulence can in turn create structures resembling shells observed in the ISM.

It is believed that turbulence is fully described by the Navier-Stokes equations. The existence of a smooth solution to the equations is, however, still one of the unsolved Millennium Prize Problems. The advance in the understanding of interstellar turbulence therefore heavily depends on observation and numerical simulations.

For further reading about interstellar turbulence I recommend the reviews by Elmegreen & Scalo (2004), Scalo & Elmegreen (2004), and Falceta-Gonçalves et al. (2014).

1.3 Shell-like structures in the interstellar medium

The ISM contains abundance of structures that resemble shells, bubbles, arcs, or chimneys. These structures are characterised by a low-density hole surrounded by a denser shell. The shell may enclose the hole fully or only partially. I will refer to these structures collectively as *shell-like structures* or just shortly *shells*.

Some shells are expanding, others are almost static. The largest ones can reach a size over a kiloparsec and make a hole through the galactic disk. Most of them are, however, much smaller, having a typical size of a few parsecs to several hundred parsecs. An example is the Local Bubble – a cavity filled with hot gas with a radius of about 42 pc that surrounds our Solar System. Another example is the dusty bubble N107 with a radius of about 12 pc (Fig. 1.19), studied in Chap. 2.

Most of these shell-like structures are believed to be footprints of the activity of massive stars, while some, especially the largest ones, may result from collisions of HVCs with the Galactic disk. GRBs and turbulence play probably a role in their formation as well. Shells have an extensive impact on the ISM: They make it porous and turbulent, and can affect star formation.

In this review I will deal primarily with shells in our Galaxy. I will describe their basic properties, mention observations, simulations, various theories of their origin, and the impact they have on the ISM and star formation.

I note that these shells should *not* be confused with *shell galaxies*, which result from galaxy mergers.

1.3.1 Observations and catalogues

Large shells, with a size of several hundred parsecs and more, are usually observed in the radio emission of neutral hydrogen as H I shells, while the smaller ones, with a size down to a fraction of a parsec, are usually observed in the infrared emission of dust. In this section I mention the properties of shell-like structures from several selected catalogues (Table 1.5).

H I shells and holes

One of the earliest catalogues of shells include that of Heiles (1979), who analysed the survey of the neutral hydrogen in our Galaxy by Weaver & Williams (1973), and discovered 63 H I shells there. The shells range in radius up to 1.2 kpc, in mass up to $2 \times 10^{7}\,M_{\odot}$, and in the contained kinetic energy up to 10^{53} erg. Of those shells, 17 appear to be expanding with a velocity between $10\,\mathrm{km\,s^{-1}}$ and $22\,\mathrm{km\,s^{-1}}$. Heiles compared the discovered shells with catalogues of other known astronomical objects and concluded that *“the* H I *shells do not seem to be significantly correlated*

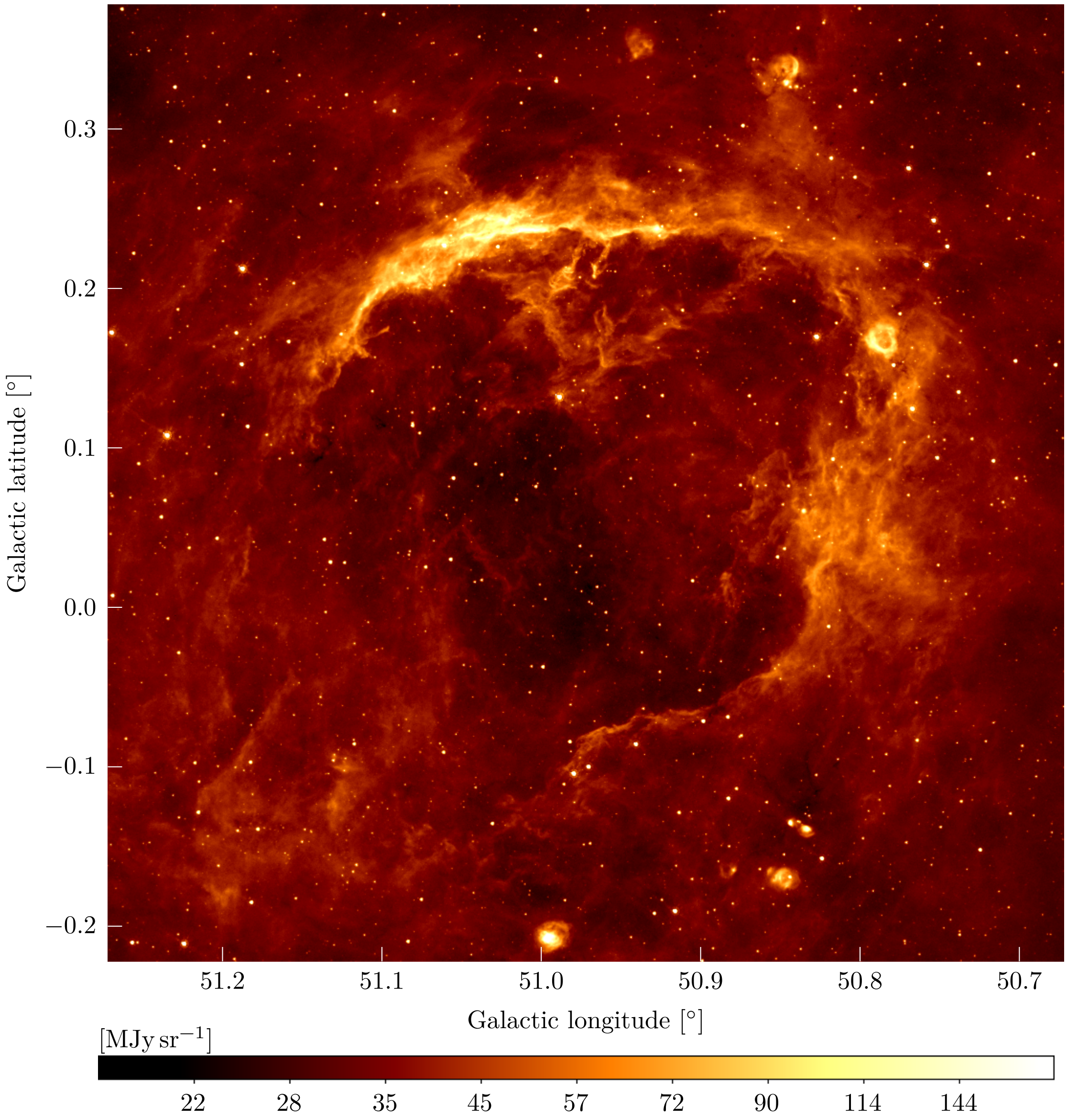

Figure 1.19: GLIMPSE bubble N107 – one of the thousands of dusty bubbles discovered in the disk of our Galaxy – shown here in infrared continuum emission at 8 µm (false colour). The physical radius of the bubble is about 12 pc. This bubble is studied in detail in Chap. 2.

Table 1.5: Selected catalogues of shell-like structures.

Type of objects	Catalogue size	References
In the Milky Way Galaxy		
H I shells	63	Heiles (1979)
H I shells	42	Heiles (1984)
H I shells	628	Ehlerová & Palouš (2005)
H I shells	333	Ehlerová & Palouš (2013)
H I shells	566	Suad et al. (2014)
Far-IR loops	462	Kiss et al. (2004); Könyves et al. (2007)
GLIMPSE bubbles	591	Churchwell et al. (2006, 2007)
GLIMPSE bubbles	5106	Simpson et al. (2012)
In external galaxies		
H I holes	>1000	Bagetakos et al. (2011b)

with any other types of astronomical object, except perhaps young stellar clusters". Later, Heiles (1984) added another 42 H I shells with similar properties discovered in the combined data from the surveys of Weaver & Williams (1973) and Heiles & Habing (1974).

A large catalogue of expanding H I shells was compiled by Ehlerová & Palouš (2005), who used an automated algorithm to search for shells in the Leiden-Dwingeloo H I survey (Hartmann & Burton, 1997). The survey covers almost 80% of the sky. They found 628 H I shells, most of which have an expansion velocity between $5\,\mathrm{km\,s^{-1}}$ and $20\,\mathrm{km\,s^{-1}}$; an estimated energy of 10^{50} erg to 10^{52} erg, with a few that have an estimated energy over 10^{52} erg; a radius of a few hundred parsecs; and an age of 10 Myr to 50 Myr. The catalogue was later revised and extended by Ehlerová & Palouš (2013) with the use of the full-sky data from the Leiden/Argentina/Bonn (LAB) H I survey[14] (Hartmann & Burton, 1997; Arnal et al., 2000; Bajaja et al., 2005; Kalberla et al., 2005). For compiling the revised catalogue, they used an updated version of the original search algorithm. Some shells from the original catalogue were rejected, properties of others were adjusted, and some new shells were added. The revised catalogue contains 333 expanding H I shells with properties similar to those from the original catalogue. Considering shells with radii between 0.1 kpc to 1 kpc, the estimated two- and three-dimensional filling factors (porosities) in the solar neighbourhood are 0.7 and 0.4, respectively. The shells from the revised catalogue are visualised in Fig. 1.20.

Another automated search for expanding H I shells was done by Daigle et al. (2007), who used an algorithm based on artificial neural networks. They searched a

---

[14] LAB H I survey: `https://www.astro.uni-bonn.de/hisurvey`, `ftp://cdsarc.u-strasbg.fr/pub/cats/VIII/76/`

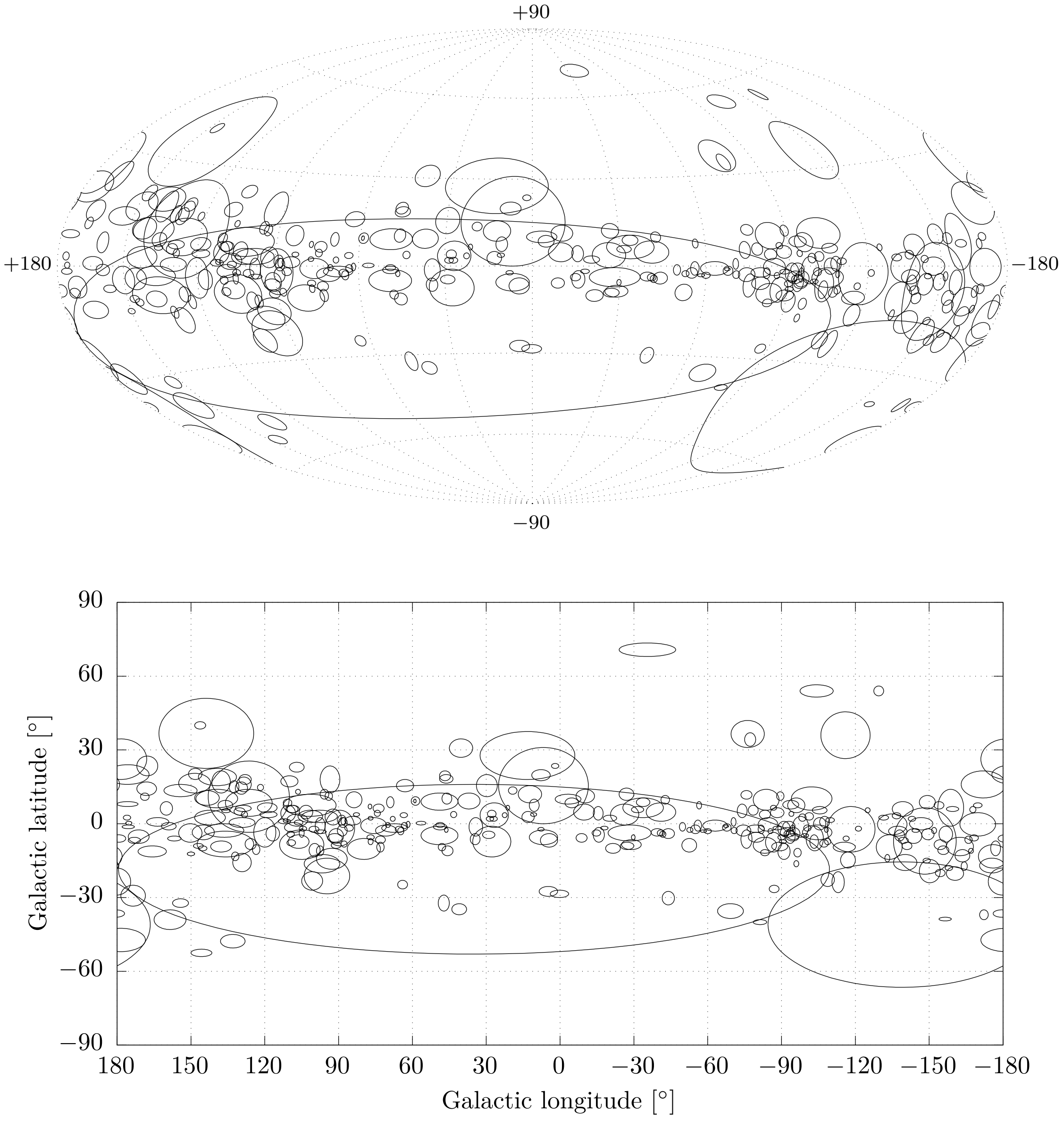

Figure 1.20: H I shells in the Milky Way from the catalogue of Ehlerová & Palouš (2013), plotted here in the Galactic coordinates centred at the Galactic centre. *Top:* Hammer projection. *Bottom:* Equirectangular projection.

region of 48° × 9° in the Perseus arm. The search was restricted to shells with a radius less than 40 pc. They detected over 7000 shell-candidates with expansion velocities ranging from 5 $\mathrm{km\,s^{-1}}$ to 20 $\mathrm{km\,s^{-1}}$.

A catalogue of 566 H I supershells in the second and third Galactic quadrant was compiled by Suad et al. (2014). They combined visual inspection with an automated algorithm to search for shells in the LAB H I survey. The discovered shells range in radius from 100 pc to 2.5 kpc (100 pc was the minimum radius for a shell to be included in the catalogue) and in expansion velocities from 5 $\mathrm{km\,s^{-1}}$ to 40 $\mathrm{km\,s^{-1}}$. The estimated two- and three-dimensional shell filling factors (porosities) in the outer part of the Galaxy are 0.5 and 0.04, respectively.

Regarding shells in external galaxies, Bagetakos et al. (2011b) compiled a catalogue of more than 1000 H I shells (holes) in 20 external galaxies. The identification of shells was done by eye in the high-resolution H I observations provided by The H I Nearby Galaxy Survey (THINGS) (Walter et al., 2008) done with the National Radio Astronomy Observatory (NRAO) Karl G. Jansky Very Large Array (VLA). The shells have sizes from 100 pc (resolution limit) up to 2 kpc, expansion velocities from 4 $\mathrm{km\,s^{-1}}$ to 36 $\mathrm{km\,s^{-1}}$, and estimated ages between 3 Myr and 150 Myr. Bagetakos et al. (2011b) concluded that the observed number and properties of H I shells are in agreement with the hypothesis that they result from stellar feedback. The paper also lists over 20 references to other studies of H I shells in external galaxies.

Far-infrared loops

A catalogue of 462 far-infrared loops based on the IRAS far-infrared full-sky survey was compiled by Kiss et al. (2004) and Könyves et al. (2007). They searched for the loops by eye in the IRAS maps of emission at 60 µm and 100 µm. Most of the loops they discovered have an estimated size between 10 pc and 300 pc. The volume-filling factor of the loops at low Galactic latitudes ($|b| < 30°$) is about 0.3 in the inner region ($-110° < l < 70°$) and about 0.05 in the outer region ($l > 70°$ or $l < -110°$). The volume-filling factor can be used as an estimate of the three-dimensional porosity of the ISM. The loops in the catalogue are represented as ellipses rotated by a position angle. I note that there is an inconsistency in the definition of the position angle.[15] A corrected visualisation of the loops is shown in Fig. 1.21.

---

[15] In both papers that comprise the catalogue (Kiss et al., 2004; Könyves et al., 2007), the position angle is defined as *"the position angle of the major axis to the circle of Galactic latitude at the centre of the ellipse. . . '+' from East to North (or counter-clockwise)"*. However, the Galactic coordinates are usually plotted with the longitude increasing to the left, i.e. with the east on the left. Therefore, the east-to-north direction would appear clockwise. In fact, the position angle of the major axis as given in the catalogue is from the west to the north (counter-clockwise). I verified this by checking the IRAS images of several loops and also by talking personally to Vera Könyves. In the second paper Könyves et al. (2007), Fig. 1 shows the loops rotated in the opposite (wrong) direction.

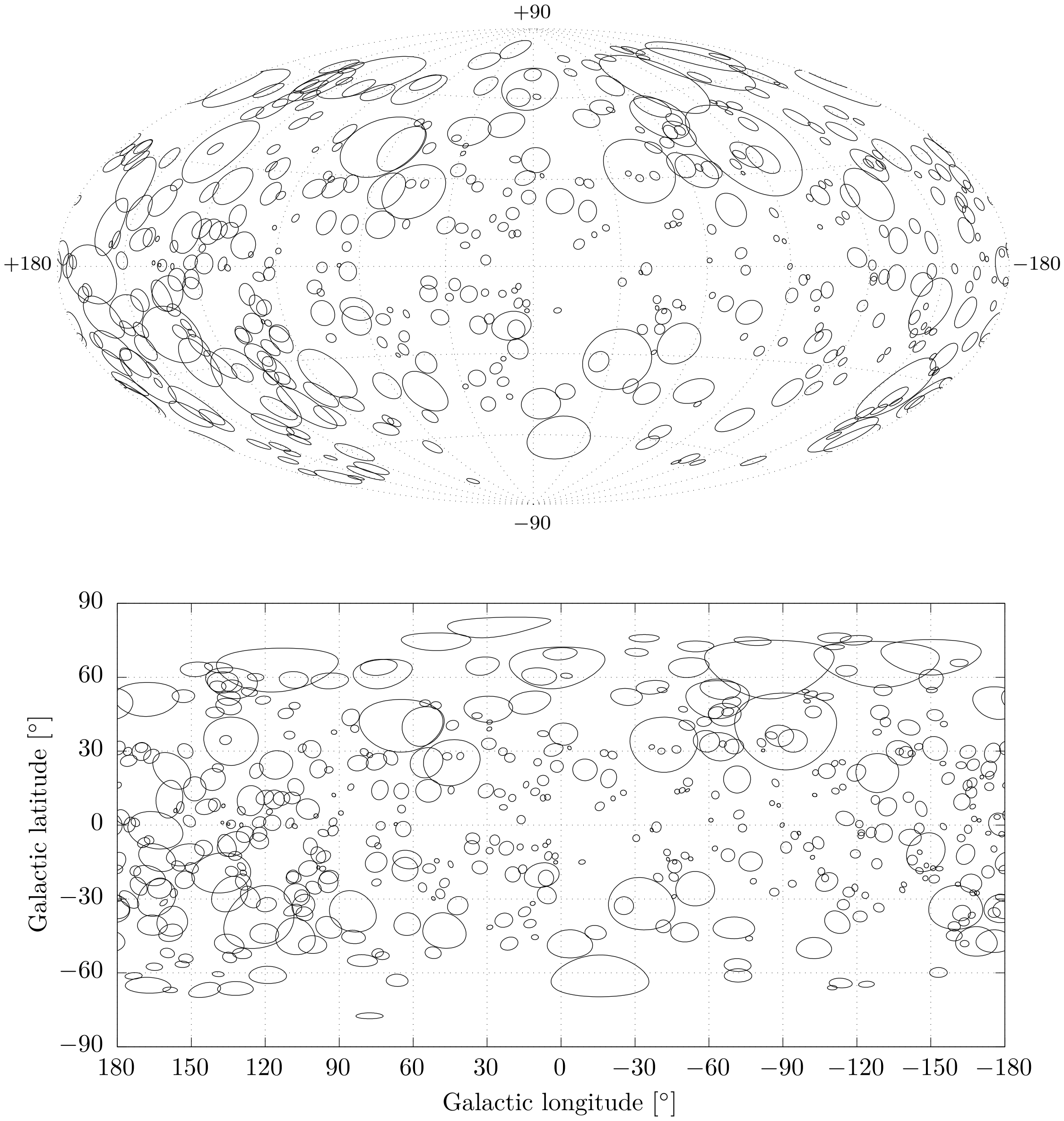

Figure 1.21: Infrared loops in the Milky Way from the catalogue compiled by Kiss et al. (2004) and Könyves et al. (2007), plotted here in the Galactic coordinates centred at the Galactic centre. *Top:* Hammer projection. *Bottom:* Equirectangular projection. I note that these plots show the corrected visualisation of the loops (see Footnote 15 in the text for an explanation).

GLIMPSE bubbles

A catalogue of 591 dusty bubbles in the Galactic disk was compiled by Churchwell et al. (2006, 2007), based on the visual inspection of the infrared observations made with the *Spitzer* Space Telescope. They used the data provided by the Galactic Legacy Infrared Mid-Plane Survey Extraordinaire (GLIMPSE) (Benjamin et al., 2003; Churchwell et al., 2009), hence the name *GLIMPSE bubbles*. Compared to H I shells, GLIMPSE bubbles are rather small objects. They have a typical radius of a few parsecs, with some having a radius over 10 pc. About 20% of the bubbles coincide with a known H II region, and about 13% of the bubbles that lie more than 10° away from the Galactic centre coincide with a known stellar cluster. Churchwell et al. (2006, 2007) concluded that at least 2/3 of the bubbles were probably created by B4–B9 stars, which do not produce a detectable H II region. The remainder, with a few exceptions, were probably created by O–B3 stars. A radio survey of Galactic H II regions later suggested that nearly all GLIMPSE bubbles are H II regions (Bania et al., 2010; Anderson et al., 2011).

The interior of the bubbles is typically filled with 24 µm emission, while 8 µm emission forms a shell delineating the bubbles' borders. The 8 µm emission is dominated by the emission features of PAHs, excited by stellar UV radiation. Since PAHs are unlikely to survive inside the bubbles, the 8 µm emission originates primarily in PDRs, where PAHs can survive and yet be exposed to strong stellar UV radiation (Deharveng et al., 2010). The 24 µm emission is dominated by the continuum emission of hot dust in the vicinity of an exciting star. It can be therefore used to point to the probable location of the star responsible for the creation of a given bubble. Weaker 24 µm emission is also observed in PDRs. It is not clear yet whether the 24 µm emission originates mainly in very small grains or in large grains (Deharveng et al., 2010).

Another catalogue based on GLIMPSE was compiled by Simpson et al. (2012). They engaged a community of over 35 000 volunteers registered in "The Milky Way Project"[16] and with their help identified more than 5000 bubbles.

An example of one of the largest GLIMPSE bubbles is N107, shown in Fig. 1.19, and studied in detail in Chap. 2. A comprehensive multiwavelength study of 102 GLIMPSE bubbles was done by Deharveng et al. (2010).

1.3.2 Origin of shells

The varying sizes, masses, ages, morphologies, and energy requirements of shell-like structures suggest different mechanisms responsible for their creation. These mechanisms, which do not have to act solely, include:

---

[16] `http://www.milkywayproject.org/`

1. feedback from massive (OB) stars: radiation, winds and supernovae;
2. collisions of HVCs with the Galactic disk;
3. energy and mass inserted by GRBs; and
4. turbulence.

Further in this section, I briefly review those mechanisms and describe the characteristics of shells they produce.

Estimated energy requirements for shell formation

The energy requirement is a decisive factor that can favour certain mechanism of the formation of a given shell. The total energy required to create an expanding shell E_{tot} can be estimated from the formula (Chevalier, 1974):

$$\frac{E_{\mathrm{tot}}}{\mathrm{erg}} = 5.3 \times 10^{43} \left(\frac{n_0}{\mathrm{cm}^{-3}}\right)^{1.12} \left(\frac{r_{\mathrm{sh}}}{\mathrm{pc}}\right)^{3.12} \left(\frac{v_{\mathrm{exp}}}{\mathrm{km\,s}^{-1}}\right)^{1.4}, \qquad (1.33)$$

where n_0 is the initial number density of the ambient medium, r_{sh} is the current shell radius, and v_{exp} is the current shell expansion velocity. This equation was originally derived for a spherical shock wave created by a supernova explosion in a homogeneous medium. It therefore assumes abrupt energy input, meaning that it can overestimate the actual energy requirement for a shell created by continuous energy input (see the discussions about continuous versus abrupt energy input in Sect. 1.3.3).

Feedback from massive stars

There are three proposed models of how a massive star can deposit energy into the ISM and create a bubble: an expanding H II region, stellar wind, and a supernova explosion.

The model of an expanding H II region assumes that a massive star or an OB association heats and ionises the hydrogen in its vicinity (e.g. Spitzer, 1978; see also Sect. 1.1.4). This causes a rise in the pressure of the ionised gas and leads to the expansion of the H II region into the surrounding neutral medium. Since this expansion is supersonic with respect to the neutral medium, the medium will be collected in an expanding shell around the H II region. After the massive stars leave the main sequence, the flux of ionising photons decreases and the ionised hydrogen returns to its neutral state. The pressure in the region then drops and no longer drives the shell expansion. What remains is an expanding shell of neutral medium that now expands primarily due to momentum conservation. Figure 1.22 shows a

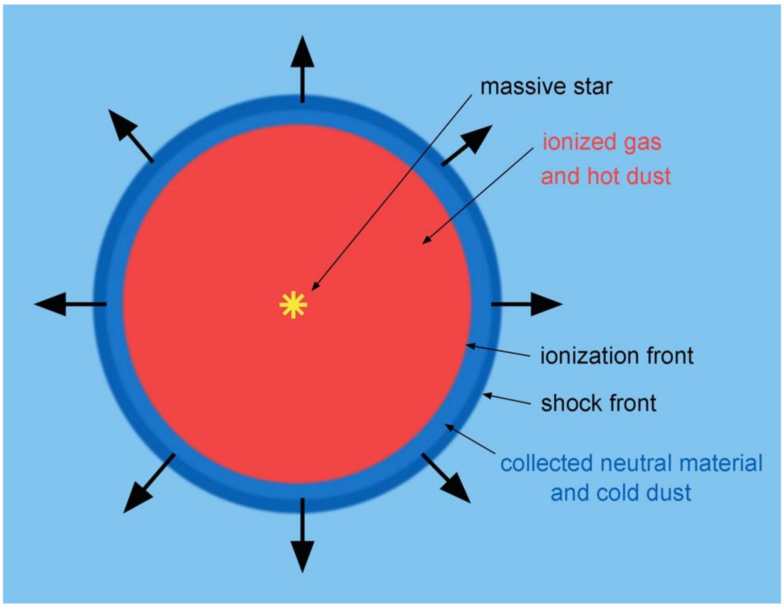

Figure 1.22: Schematic of an expanding H II region formed around a massive star. (Deharveng et al., 2010, Fig. 1, retrieved from arXiv:1008.0926v1 [astro-ph.GA].)

schematic of an expanding H II region in the phase when the driving star is still on the main sequence. Examples of shells created by expanding H II regions can be found among GLIMPSE bubbles (see Sect. 1.3.1).

The model of a wind-blown bubble assumes that the energy driving the expansion is released via stellar wind of a massive star or a group of massive stars (e.g. Castor et al., 1975; Weaver et al., 1977). A wind-blown bubble has several layers. In the innermost layer, the wind is freely expanding up to a layer of shocked stellar wind, where its kinetic energy is thermalised. This layer of shocked wind then expands and sweeps up the ambient ISM into a shell that surrounds the bubble. In later stages of the bubble's evolution the shell is mainly atomic and molecular. A schematic of a possible structure of a wind-blown bubble is shown in Fig. 1.23.

In contrast to the previous two models with continuous energy input, a supernova explosion releases abruptly an energy of about 10^{51} erg (Chevalier, 1974, 1977; Woosley & Weaver, 1986). This creates a low-density cavity in the ISM filled with the HIM and surrounded by an expanding shock. Since the shock expands supersonically with respect to the ambient medium, it collects the medium is an expanding shell. A shell created by a single supernova reaches a typical size of tens of parsecs. But when multiple supernovae explode close to each other, they can create a superbubble with a size of hundreds of parsecs. Shells created by supernovae, with emphasis on multiple explosions and inhomogeneous ambient

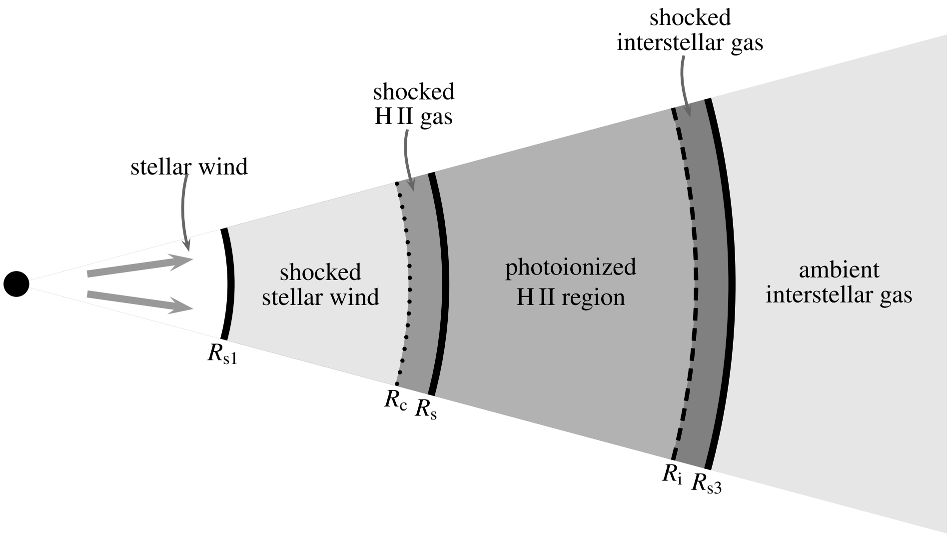

Figure 1.23: Schematic of a possible structure of a wind-blown bubble formed around a massive star. R_{s1} is the stellar wind shock; R_s is the shock in the ionised ambient medium; R_{s3} is the shock in the neutral ambient medium; R_c is the contact discontinuity separating shocked stellar wind and the ambient medium; and R_i is the ionisation front. (Arthur, 2007, Fig. 1, retrieved from arXiv:astro-ph/0605533.)

medium, were studied, e.g., by Bodenheimer et al. (1984); Tenorio-Tagle et al. (1985); Rozyczka et al. (1986); Tenorio-Tagle et al. (1991); Rozyczka et al. (1993).

All these three mechanisms of the formation of stellar-blown shells can act together in an OB association. It is still not settled which mechanism is the dominant one, provided that there is a dominant one. The total energy a typical OB association can release into the ISM is estimated up to 10^{52} erg (Tenorio-Tagle & Bodenheimer, 1988). Most of this energy is, however, thermalised and escapes the shell via radiative cooling. The fraction that is retained in the form of the shell kinetic energy decreases with the shell expansion time. Numerical simulations done by Fierlinger et al. (2016) suggest that this fraction converges to a value of a few percent at the time when the shell expansion decelerates to the sound speed of the ambient medium.[17]

Collisions of high-velocity clouds with the Galactic disk

High-velocity clouds (HVCs) are clouds of the ISM travelling at velocities in excess of about $80\,\mathrm{km\,s^{-1}}$ with respect to the local standard of rest (LSR). They are

---

[17] When the expanding shell decelerates to a subsonic velocity, it is expected to quickly break up and convert its kinetic energy to turbulent motions of the ambient medium (Fierlinger et al., 2016).

found in the Galactic halo and can have masses of up to $10^7\,M_\odot$ (Hulsbosch, 1975; Verschuur, 1975). When an HVC collides with the medium in the Galactic disk, it can release an energy of up to 3×10^{54} erg (Tenorio-Tagle & Bodenheimer, 1988), which is equivalent to more than a thousand of supernova explosions. This is enough energy to create the largest shells that have been observed. Numerical simulations confirm that a collision of an HVC with the Galactic disk can produce an expanding supershell filled with a very hot gas (10^6 K to 10^7 K), similar to what is observed (Tenorio-Tagle, 1980, 1981; Tenorio-Tagle et al., 1986, 1987; Franco et al., 1988).

Energy and mass inserted by gamma-ray bursts

Gamma-ray bursts (GRBs) are the most luminous events observed in the universe (Mészáros, 2006). They have very short duration – typically a few seconds – though a burst lasting about seven hours has been observed (Gendre et al., 2013). GRBs were first detected in late 1960s by a military satellite system, but their discovery was published only in 1973 by Klebesadel et al.. In 1990s, there were two competing theories suggesting the location where these bursts originate. The Galactic hypothesis proposed that GRBs originate in high-velocity neutron stars distributed in a distant Galactic corona (Lamb, 1995). The extragalactic hypothesis, on the other hand, proposed that GRBs originate in cosmological distances (Paczynski, 1995; Waxman, 1997). The Galactic hypothesis was later dismissed in favour of the extragalactic hypothesis, when the observation of GRB 050904 with a high redshift showed that it occurred in a density typical for the ISM (Haislip et al., 2006). Assuming that GRBs indeed occur in the ISM, they should leave behind an expanding remnant. The model in which an expanding shell is created by an abrupt energy input associated with a GRB was studied, e.g., by Efremov et al. (1998, 1999) or Loeb & Perna (1998). The model assumes that a GRB releases an energy of up to 10^{54} erg and could thus create a supershell in the ISM with a radius larger than 1 kpc. However, the energy a GRB releases is probably much smaller, about 5×10^{50} erg (Frail et al., 2001). This is comparable to the amount of energy released by a supernova (about 10^{51} erg). It is the *beaming factor* of GRBs what makes them apparently more luminous than supernovae. The shells created by GRBs would therefore reach sizes comparable to those created by supernovae, i.e. tens of parsecs.

Turbulence

Today, we believe that the ISM is a highly turbulent environment (see Sect. 1.2). Interstellar turbulence appears to be able to create some shells as suggested by numerical simulations (Dib & Burkert, 2005) and observations (Hatzidimitriou et al., 2005). See Sect. 1.2.11 for a more detailed discussion.

Radiation pressure

The largest shells can get additional mechanical energy from the radiation pressure of stars inside the enclosed cavity. The lower gas and dust density in the cavity means also lower extinction of starlight. This may create an anisotropy in the pressure force and result in a net force accelerating the shell expansion (Elmegreen & Chiang, 1982). However, the shell must be large enough and expand with a high-enough velocity for the radiation pressure to boost the expansion significantly. For example, in a medium with a particle number density of $1.2\,\mathrm{cm}^{-3}$, the radiation pressure becomes important for a shell with a radius of 1 kpc and an expansion velocity of three times the sound speed; a smaller shell with a radius of 0.6 kpc would have to be expanding with a velocity of even fifteen times the sound speed (Heiles, 1984; Tenorio-Tagle & Bodenheimer, 1988).

1.3.3 Formation and expansion of shells

Let us first consider the theoretical expansion laws for a spherical isothermal shock associated with shells formed by massive stars. Such a shock will have different expansion characteristics depending on the process of how the stars release energy into the ISM. The shock radius R will evolve with the expansion time t as a power law (Elmegreen, 2011):

- $R \propto t^{4/7}$ for an H II region (continuous energy input, radiative losses due to recombinations),
- $R \propto t^{2/5}$ for a supernova in the Sedov phase (abrupt energy input, energy conserving, non-radiative), and
- $R \propto t^{3/5}$ for stellar wind or continuous multiple supernovae (continuous energy input, non-radiative).

(See Fig. 1.24 for a visual comparison.) These expansion laws assume a constant density of the ambient medium and no external pressure. External pressure is, however, always present and slows down the expansion. Also neglected is the shell momentum that increases its actual expansion speed. This is especially important in later stages when the shell has accumulated a substantial amount of mass. It is the shell momentum that keeps it expanding long after the massive stars stop supplying energy into the central cavity.

External pressure, the shell momentum, and radiative cooling were included in the numerical simulations of Efremov et al. (1999), who compared the properties of shells created by continuous and abrupt energy input. The simulations showed that shells driven by continuous energy input reach greater sizes and expansion velocities in comparison to those driven by abrupt energy input, provided that the

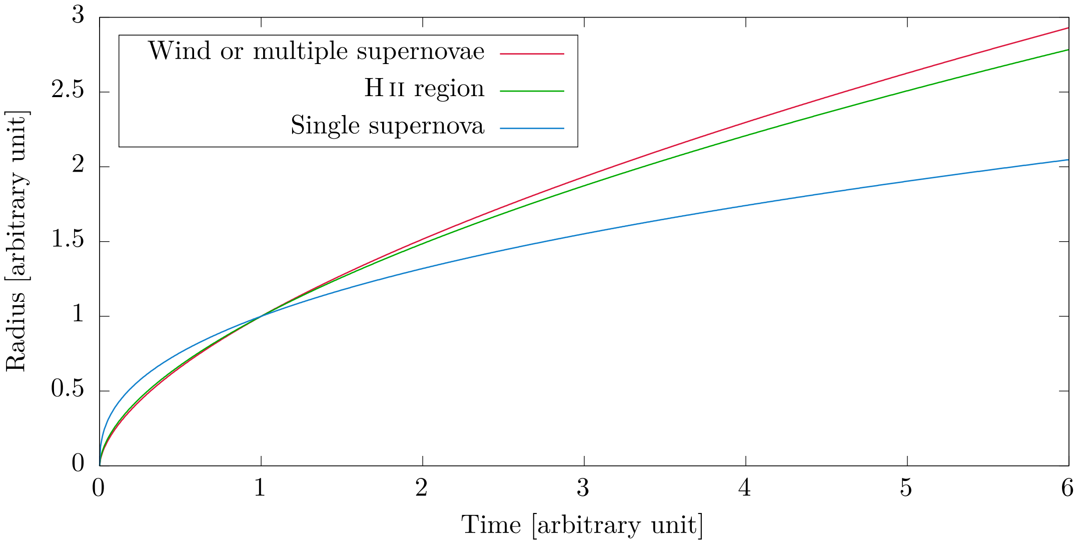

Figure 1.24: Theoretical expansion laws for shells formed around massive stars. The expansion profile describes the radius of an isothermal shock as a function of the expansion time. It depends on the model of how the stars release energy into the ISM. The laws assume a constant density of the ambient medium, no external pressure, and neglect the shell momentum. I note that the graph has arbitrary units to show the shape of the expansion profiles only, meaning the absolute values of the profiles should not be compared.

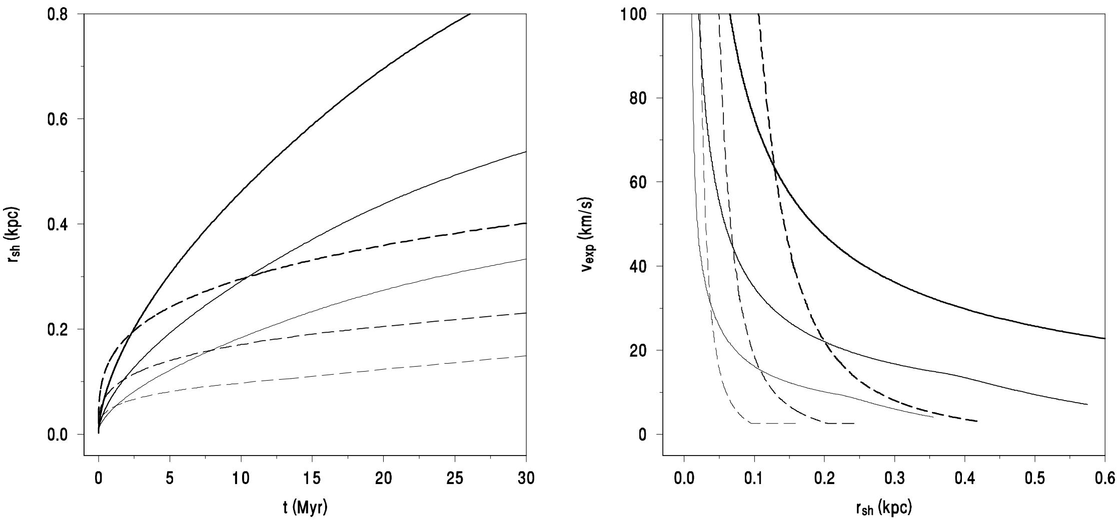

Figure 1.25: Evolution of expanding shells as obtained from numerical simulations. The shells were let expanding in a homogeneous medium with a number density of $1.4\,\mathrm{cm}^{-3}$. Solid lines represent continuous energy input, while dashed lines represent abrupt energy input. The total injected energies were 10^{52} erg (thin lines), 10^{53} erg (medium lines), and 10^{54} erg (thick lines). *Left:* Shell radius as a function of the expansion time. *Right:* Shell expansion velocity as a function of the shell radius. (Efremov et al., 1999, Fig. 1, retrieved from arXiv:astro-ph/9908044)

total amount of energy deposited into the shell is the same (Fig. 1.25). In other words, continuous energy input transforms more of the available energy into the mechanical energy of the shell. Continuous energy input can be provided by H II regions, stellar winds, or multiple supernova explosions, while abrupt energy input can be provided by a single supernova or a GRB.

Earlier simulations of Bodenheimer et al. (1984) gave similar results. They showed that when a secondary supernova explodes inside an already present remnant, and the secondary explosion occurs after a time greater than the cooling time, then the mechanical energy of such a remnant will be larger than the mechanical energy of a remnant created by a single explosion with the combined energy. This suggests that the more the energy input is continuous, the higher the fraction of the total energy that is converted into the shell mechanical energy.

Shells formed in a galactic disk will be distorted by the disk's differential rotation. This was explored with numerical simulations by Palouš et al. (1990) for shells with abrupt energy input. How such a shell is progressively deformed is shown in Fig. 1.26. The simulation setup for the shown shell corresponded to the conditions in the disk of our Galaxy at the location of the Sun; i.e.: the Galactocentric distance of the expansion centre of 8.5 kpc, the mean rotation velocity around the Galactic centre at the location of the expansion centre of $220\,\mathrm{km\,s}^{-1}$, the number density of

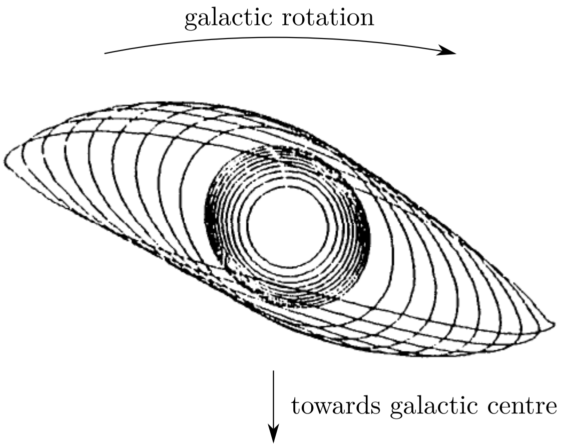

Figure 1.26: Progressive deformation of a shell expanding in a differentially rotating galactic disk as obtained from numerical simulations. Shown is the shell cross-section along the disk. The simulation setup corresponded to the conditions in the disk of our Galaxy at the location of the Sun. First ten contours are drawn at intervals of 10^6 yr, following with contours at intervals of 10^7 yr. (Palouš et al., 1990, Fig. 2b, used with permission of Jan Palouš)

the medium in the central plane of the disk of $1\,\mathrm{cm}^{-3}$, and the disk half-thickness of 100 pc. The total energy that was deposited into the central cavity of the shell at the beginning of the expansion was 5×10^{53} erg.

How the shells expanding in a galactic disk are distorted in the vertical direction was studied by Ehlerová et al. (1997). They performed numerical simulations of shells expanding in a medium with Gaussian stratification in the z-direction

$$n(z) = n_0 \exp\left(-\frac{z^2}{\sigma_z^2}\right), \tag{1.34}$$

where n is the particle number density of the medium in the disk, z is the vertical distance from the central plane of the disk, n_0 is the particle number density of the medium in the central plane of the disk, and σ_z is the Gaussian half-thickness of the disk. The shells were driven by continuous energy input. Their appearance after expanding for 20 Myr in a medium with σ_z of 100 pc, 200 pc, and 500 pc is shown in Figure 1.27.

Apart from the effects mentioned earlier in this section, shells evolving in the ISM are also subject to its magnetic fields, small-scale inhomogeneities, turbulence, and various instabilities like the Taylor or Kelvin-Helmholtz instability (see Fig. 1.8 of the Crab Nebula). More realistic numerical simulations should therefore include those effects. Examples of such simulations include the simulations of the formation and expansion of H II regions in turbulent molecular clouds done by Arthur et al.

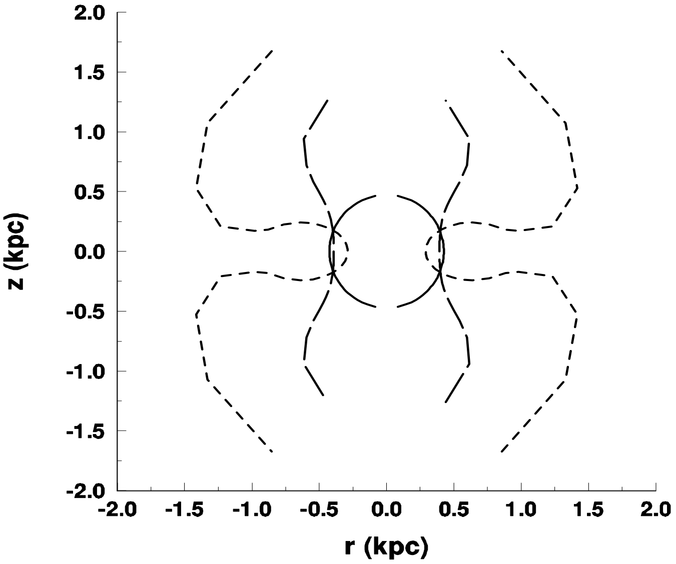

Figure 1.27: Deformation of shells expanding in a stratified medium as obtained from numerical simulations. The medium had Gaussian stratification in the z-direction with a half-thickness σ_z of 500 pc (solid line), 200 pc (long-dashed line), and 100 pc (short-dashed line). (Ehlerová et al., 1997, Fig. 4d, used with permission of Soňa Ehlerová)

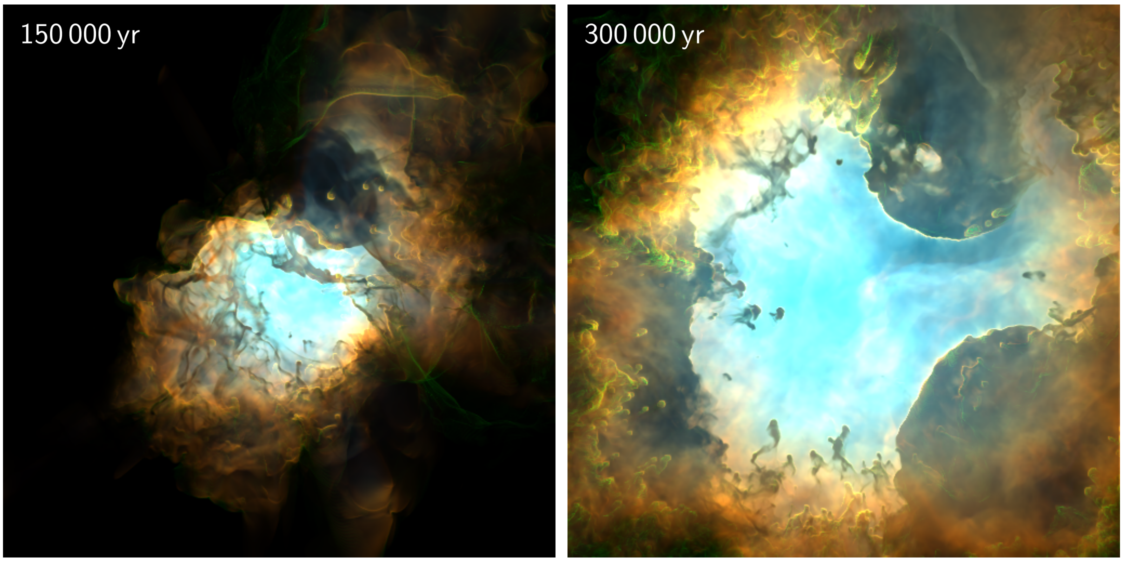

Figure 1.28: Synthetic images of a simulated H II region evolving in a turbulent molecular cloud. The images are false-colour: Red corresponds to the emission line [N II] 6584 Å, green to Hα 6563 Å, and blue to [O III] 5007 Å. Each image is 4 pc × 4 pc in size and indicates the evolution time in the top-left corner. (Medina et al., 2014, Figure 1, retrieved from arXiv:1409.5838v1 [astro-ph.GA], overlaid with the evolution time)

(2011) and Medina et al. (2014). Those simulations were fully three-dimensional and treated the ideal MHD equations (see Sect. 1.2.4), radiative transfer, and gas heating and cooling. The simulations were able to reproduce H II regions with appearance very similar to the appearance of H II regions observed in the ISM (Fig. 1.28).

1.3.4 Impact of shells on the structure and dynamics of the interstellar medium

Expanding shells, regardless of their origin, supply kinetic energy for interstellar turbulence. To give some estimates of how much energy is available: a GRB can release several times 10^{50} erg (Frail et al., 2001); a single supernova explosion can release about 10^{51} erg (Chevalier, 1977; Woosley & Weaver, 1986); a typical OB association as a whole can release up to 10^{52} erg (Tenorio-Tagle & Bodenheimer, 1988); and a collision of a HVC with the Galactic disk can release up to 3×10^{54} erg (Tenorio-Tagle & Bodenheimer, 1988). The fraction of the energy that is actually converted into turbulence is, however, unknown. Though, shells created by massive stars are believed to be the dominant source of energy for turbulence in the Galactic disk (see Sect. 1.2.7).

The large number of shells present in the ISM makes it look like a porous sponge. This is especially obvious in observations of interstellar neutral hydrogen (Fig. 1.3). The quantity that gives the shell filling factor is called *porosity*. It can be two-dimensional (2D) or three-dimensional (3D). For the solar neighbourhood, Ehlerová & Palouš (2013) gave estimates for the 2D porosity of 70% and for the 3D porosity of 40% (based on their catalogue of H I shells, see Sect. 1.3.1). Porosities for a sample of 20 spiral and irregular external galaxies were estimated by Bagetakos et al. (2011b,a) (based on their catalogue of H I holes, see Sect. 1.3.1): The 3D porosities vary from 0.1% to 19.4%, but only four galaxies in the sample have a 3D porosity over 5%. The 2D porosities vary from 0.3% to 12.8%, with a typical value of a few percent. The porosities also depend on the type of the host galaxy: later Hubble types tend to be more porous. Bagetakos et al. (2011b) speculated that *"…the lack of destruction mechanisms in dwarf galaxies contributes to this trend"*. The striking difference between the estimated porosities of the local ISM and those of external galaxies could be explained by the fact that we are able to resolve much smaller shells in the local ISM and include those in the estimates of the local porosity.

Expanding shells with a hot gas in their interiors can in some cases supply that gas into the Galactic halo. When a shell expands near the edge of the Galactic disk, or when it reaches a size comparable to the disk scale height, it can "burst" and release the hot gas into the halo (see Fig. 1.27). The hot gas in the halo can later cool down, condense into clouds, and fall back into the disk as intermediate- or high-velocity clouds (Putman et al., 2012). This model of gas circulation is called *Galactic fountain* (Shapiro & Field, 1976). The collisions of HVCs with the Galactic disk can create new expanding shells (see Sect. 1.3.2).

1.3.5 Star formation triggered by expanding shells

Star formation can happen spontaneously, when a molecular cloud's intrinsic instabilities create gravitationally bounded protostellar cores; or can be "kicked off" by an event like a shock wave passing through the ISM. In the latter case, it is called *triggered* or *induced* star formation. Dale et al. (2015) defines the following three types of triggering:

1. Type I triggering: an increase in the star formation rate.
2. Type II triggering: an increase in the final star formation efficiency.
3. Type III triggering: an increase in the total final number of stars formed.

Type I triggering is also called *weak* triggering, because it only accelerates formation of stars that would form anyway, while type II and III are referred to as *strong* triggering (Dale et al., 2007).

Many shells observed in our Galaxy and in external galaxies expand with velocities up to tens of $\mathrm{km\,s^{-1}}$ (see Sect. 1.3.1). Such velocities are typically supersonic with respect to the medium in which those shells form. This leads to the accumulation of the medium in the expanding shell, where it may become dense and cold enough to condense into molecular clouds, which in turn can start forming new stars. In the context of an expanding H II region, star formation triggered in this way is called *collect-and-collapse* scenario (Elmegreen & Lada, 1977; Whitworth et al., 1994b; Elmegreen, 1994). Another way how an H II region can trigger star formation is *radiation-driven implosion*, which considers the compression of a pre-existing condensation (globule) by the warm gas in the H II region (Duvert et al., 1990; Lefloch & Lazareff, 1994). Further, an H II region can trigger star formation by expanding into a medium shaped by turbulence, or via a small-scale variant of the collect-and-collapse process leading to small-scale gravitational instabilities. The various mechanisms of triggered star formation in an expanding H II region are illustrated in Fig. 1.29.

In the context of larger structures, namely expanding H I shells, triggered star formation may follow a large-scale variant of the collect-and-collapse scenario (Ehlerová et al., 1997; Ehlerová & Palouš, 2002; Palouš & Ehlerová, 2002). Other mechanisms how large expanding shells can trigger star formation include their collisions, or expansion into a pre-existing molecular cloud (Tenorio-Tagle & Bodenheimer, 1988).

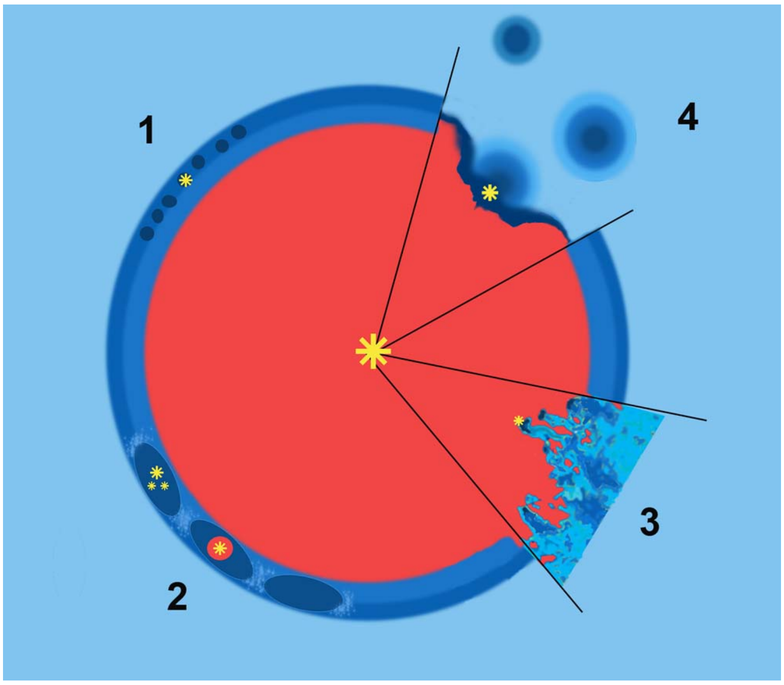

Figure 1.29: Schematic of possible mechanisms of triggered star formation in an expanding H II region. (1) Small-scale gravitational instabilities (e.g. the Jeans instability); (2) large-scale gravitational instabilities leading to the formation of high-mass fragments (collect-and-collapse); (3) ionising radiation acting on a turbulent medium; (4) radiation-driven compression of pre-existing dense clumps. (Deharveng et al., 2010, Fig. 4, retrieved from arXiv:1008.0926v1 [astro-ph.GA].)

Fragmentation of expanding shells

The gravitational fragmentation of expanding shells was studied theoretically in the approximation of an infinitesimally thin shell (*thin-shell approximation*) by, e.g., Vishniac (1983); Whitworth et al. (1994a); Elmegreen (1994); Whitworth et al. (1994b); Wünsch & Palouš (2001); or Parmentier (2004). Let us consider such a thin shell with a local perturbation in its surface density described as $\sigma = \sigma_0 \cos \eta\theta$, where σ_0 is the maximum surface density of the perturbation, η is the perturbation angular wavenumber, and θ is an angular coordinate on the shell surface. The stability of this perturbation can be described by the perturbation growth rate $\omega(\eta)$. It is a dispersion relation that tells whether a perturbation with the wavenumber η will grow, dissolve, or oscillate. For a shell expanding into a uniform medium, the theoretical thin-shell dispersion relation can be written in the form (Elmegreen, 1994):

$$\omega(\eta) = -\frac{3V}{R} + \sqrt{\frac{V^2}{R^2} + \frac{2\pi G \varrho_0 \eta}{3} - \frac{c^2\eta^2}{R^2}}, \tag{1.35}$$

where V and R are the instantaneous shell expansion velocity and radius respectively, G is the gravitational constant, ϱ_0 is the ambient medium density, and c is the velocity dispersion in the shell. A positive ω means the perturbation will grow, a negative ω means it will dissolve, and a complex ω means it will oscillate.

The thin-shell model was later extended to *thick* shells confined by external pressure. In a series of papers Dale et al. (2009), Wünsch et al. (2010), and Dale et al. (2011) studied numerically and analytically the gravitational fragmentation of expanding shells (see example in Fig. 1.30). They introduced the pressure assisted gravitational instability (PAGI) model and derived a corresponding dispersion relation (Wünsch et al., 2010, Eq. 23). The model takes into account the effects of pressure acting on a thick shell. It predicts that the higher the pressure (the thinner the shell), the faster it will fragment, and the smaller the smallest unstable fragments it will produce (Fig. 1.31). For example, a shell expanding into the low-density Galactic halo should fragment slower and form preferentially high-mass fragments when compared with a shell expanding in the Galactic disk.

Doubts about the viability of triggered star formation at the giant-molecular-cloud scale

Many studies interpret observations as evidence of triggered star formation; e.g. Wilking et al. (1984), Karr & Martin (2003), Oey et al. (2005), Zavagno et al. (2006), Deharveng et al. (2007), Maheswar et al. (2007), Zavagno et al. (2007), Deharveng et al. (2008), Deharveng et al. (2010), Kendrew et al. (2012), Cichowolski et al. (2014), or Liu et al. (2015). Most of these studies have been published after 2000. Dale et al. (2015) reviewed a sample of 67 papers that inferred the presence of triggered star

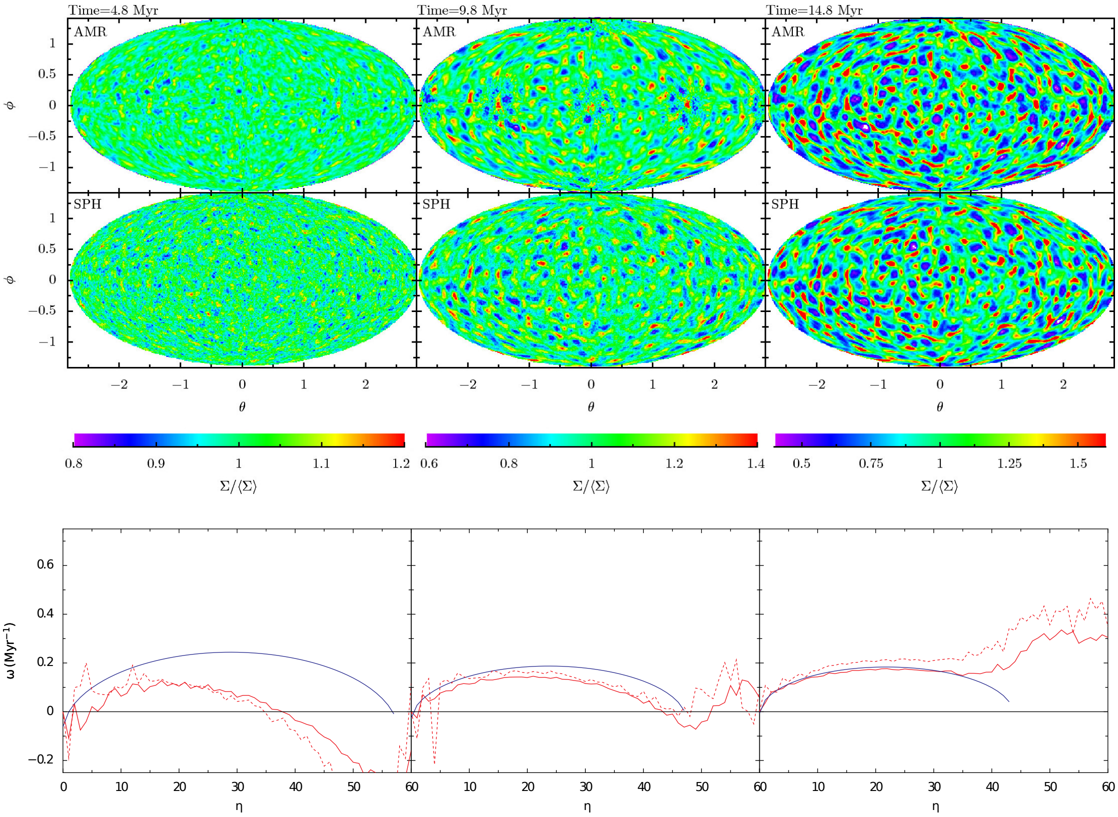

Figure 1.30: Fragmentation of an expanding shell as obtained from numerical simulations done with an adaptive mesh refinement (AMR) and smoothed-particle hydrodynamics (SPH) code. The shell was let expanding in an external pressure of $10^{-13}\,\mathrm{dyn\,cm^{-2}}$, which was chosen so that its thickness remained approximately constant during its evolution. *Top:* Shell in the Hammer projection. $\Sigma/\langle\Sigma\rangle$ gives the relative fluctuation of the surface density. *Bottom:* Plots of the perturbation growth rate ω as a function of the perturbation angular wavenumber η, i.e. the dispersion relation, derived from the AMR (red dotted line) and SPH (red solid line) simulations. The blue line shows the theoretical dispersion relation derived from the thin-shell model. (Dale et al., 2009, Fig. 10, retrieved from arXiv:0906.1670v1 [astro-ph.GA])

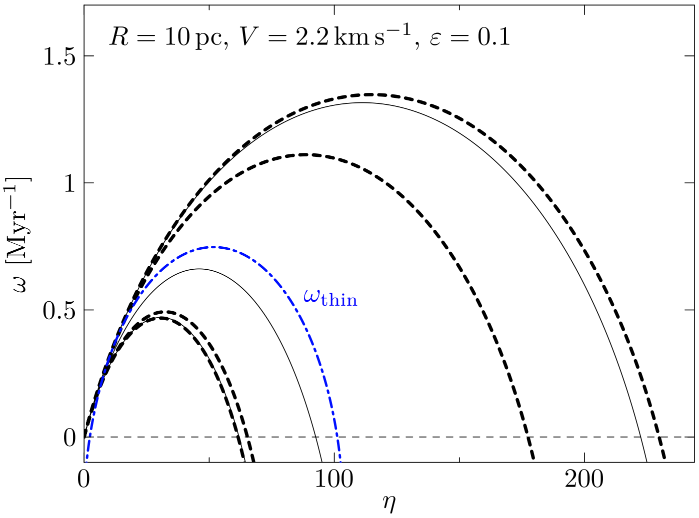

Figure 1.31: PAGI dispersion relation – i.e. the perturbation growth rate ω as a function of the perturbation angular wavenumber η – for different values of external pressure: 0, 10^{-14}, 10^{-13}, 10^{-12}, 10^{-11}, 10^{-10}, and $1\,\mathrm{dyn\,cm^{-2}}$ (given in the order from the lowest to the highest black line). The blue dash-dotted line shows the thin-shell dispersion relation ω_{thin}. R is the shell radius, V is the shell expansion velocity, and ε is a parameter introduced in the PAGI model. (Wünsch et al., 2010, Fig. 5, retrieved from arXiv:1005.4399v1 [astro-ph.GA], edited)

formation in observations. They used a smoothed-particle hydrodynamics (SPH) code to simulate star formation at the giant-molecular-cloud scale. The simulations included stellar feedback and tested the reliability of signposts of triggered star formation cited in those 67 paper. The mostly cited signpost was the proximity of objects to a shell or ionisation front. The statistical analysis suggested that those signposts do not significantly improve the chance of correctly identifying a given star as triggered. The improvement was below a factor of 2 compared to random selection. Therefore they *"... urge caution in interpreting observations of star formation near feedback-driven structures in terms of triggering".*

Another study discussing the viability of star formation triggered by expanding H II regions was done by Beaumont & Williams (2010). They explored the three-dimensional structure of the cold molecular component of 43 GLIMPSE bubbles and found that the cold molecular gas lies in a ring, rather than a sphere, around the bubbles. This indicates that the parental molecular clouds are flattened with a typical thickness of a few parsecs. H II regions formed in such clouds will therefore quickly break out of those clouds and that will limit their influence on star formation in the clouds (Fig. 1.32). Further, the hydrogen column densities of the cold gas associated with the bubbles seem too low for the gas to collapse. Therefore, Beaumont & Williams (2010) hypothesize that *"the flattened molecular clouds are*

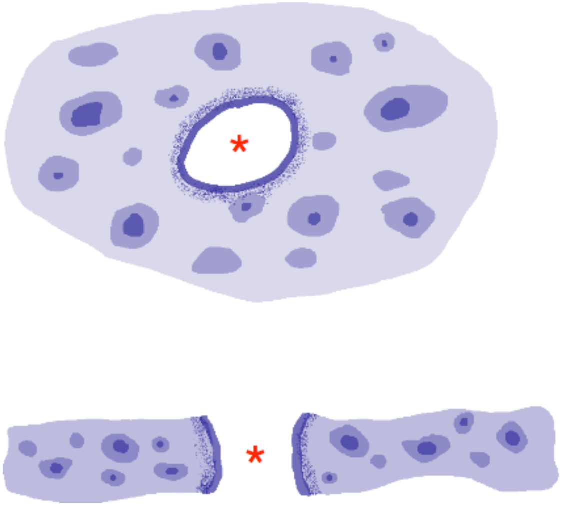

Figure 1.32: Schematic of a ring-like bubble formed around a massive star in a flattened molecular cloud. This cloud morphology allows the bubble (H II region) to quickly break out of the cloud, limiting the bubble's capability of triggering the formation of new stars in the cloud. *Top:* Face-on view. *Bottom:* Edge-on cut. (Beaumont & Williams, 2010, Figure 4, retrieved from arXiv:0912.1852v1 [astro-ph.GA])

not greatly compressed by expanding shock fronts, which may hinder the formation of new stars".

Clearly, triggered star formation is a very active field of research. The extent to which it affects the circulation of matter from the ISM to stars and back is yet to be determined.

1.3.6 Summary and conclusion

Shell-like structures are ubiquitous in the ISM. Thousands have been found in our Galaxy and in other spiral and irregular galaxies. Most shells, especially those with a size up to tens of parsecs, are probably created by massive stars (their radiation, winds, and supernovae). Larger shells, with a size of hundreds of parsecs or more, need either many massive stars to combine their energy, or they can be created by a different mechanism like the collision of a HVC with the Galactic disk. Earlier, GRBs were thought to release enough energy to create the largest shells we observe (up to 10^{54} erg), but recent estimates suggest GRBs release much less energy – comparable to what a supernova explosion releases. Therefore, shells created by GRBs would be expected to reach sizes comparable to the sizes of shells created by supernovae. Turbulent motions in the ISM can possibly create shell-like structures as well.

Inhomogeneities of the ISM distort the shapes of shells. Larger shells, especially those with a size of hundreds of parsecs or more, are strongly affected by the stratification of the Galactic disk. They expand preferentially in the direction towards the low-density Galactic halo, and can thus “burst” and release the hot gas from their interior into the halo. Another distortion of larger shells’ shape is caused by the differential rotation of the Galactic disk.

The turbulent nature of the ISM is reflected in its density and velocity fluctuations at all scales. These inhomogeneities cause that expanding shells sculpt the medium into complex structures – often a mixture of filaments, pillars, and globules. This is very well observed, especially in supernova remnants and in expanding H II regions. Expanding shells are also believed to be an important source of power for interstellar turbulence.

Shells expanding supersonically can trigger star formation: either by the interaction of the shock with pre-existing structures, or by collecting the ambient medium in the shell, where it can cool down, condense and start forming new stars.

Thus, shell-like structures are closely tied to the structure and dynamics of the ISM, and to star formation. A schematic of a possible life cycle of one such shell formed by an OB association is shown in Fig. 1.33.

For further reading about shells, with emphasis on large-scale structures, I recommend the review by Tenorio-Tagle & Bodenheimer (1988). For further reading about various mechanisms of triggered star formation, including small- and large-scale triggering, I recommend the review by Elmegreen (1998).

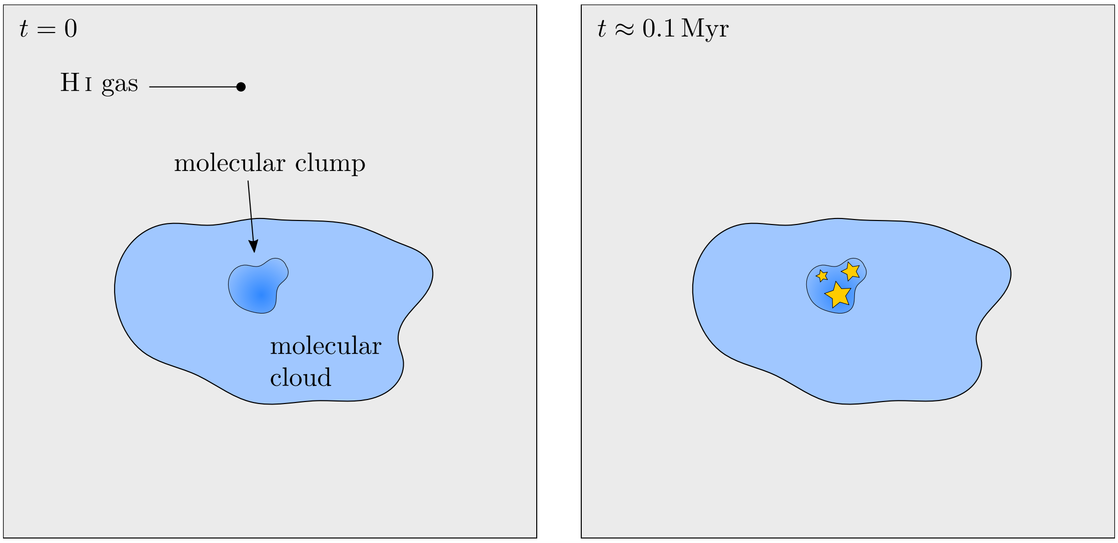

(a) Inside a molecular cloud, which is surrounded by neutral H I gas, a dense and cold molecular clump forms.

(b) An OB association forms in the clump.

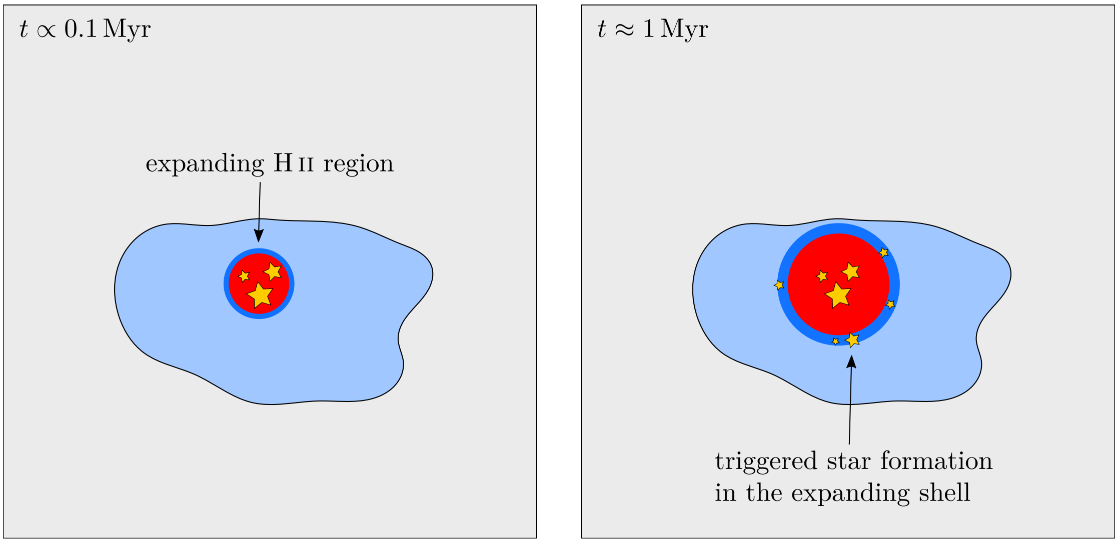

(c) OB stars enter the main sequence and start ionising the gas in their vicinity. An H II region is formed. The pressure of the hot ionised gas drives its expansion. In these early phases, the optical emission of the ionised gas is obscured by the surrounding molecular matter. It can be, however, observed at radio wavelengths.

(d) As the H II region expands supersonically, it collects the ambient medium in a cold and dense shell. This may lead to triggering the formation of additional stars in the cloud.

Figure 1.33: Schematic of a possible life cycle of an expanding shell formed by an OB association. Approximate evolution times are indicated in the pictures. (Continued on the next page.)

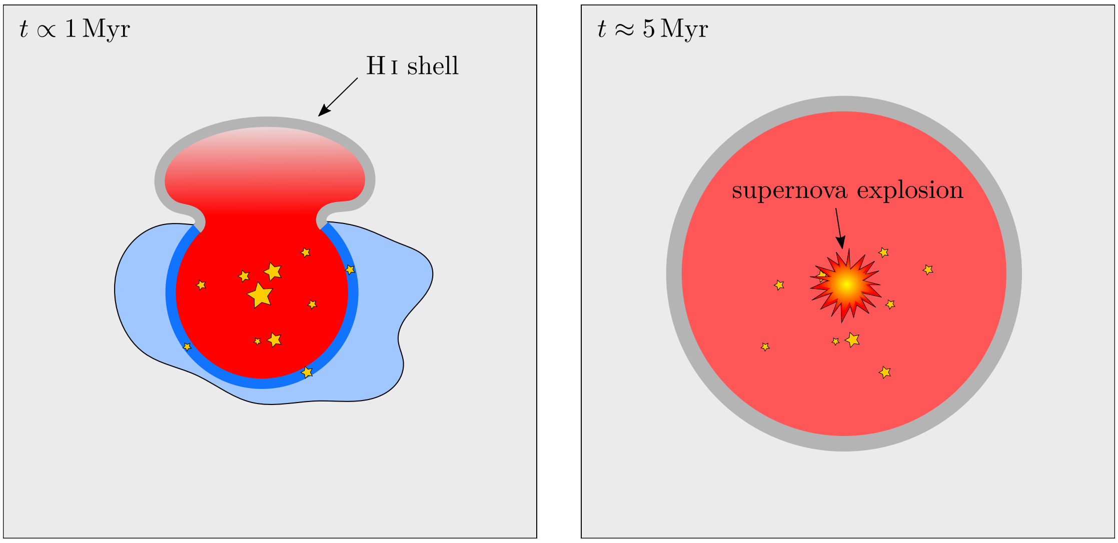

(e) The H II region breaks out of the molecular cloud and starts expanding into the surrounding H I gas. From now on, the H II region may be observed in optical wavelengths. The most massive stars begin to leave the main sequence.

(f) The molecular cloud is completely disrupted by the H II region. The shell continues to expand into the neutral H I medium. Massive stars explode as supernovae and abruptly add energy into the central cavity.

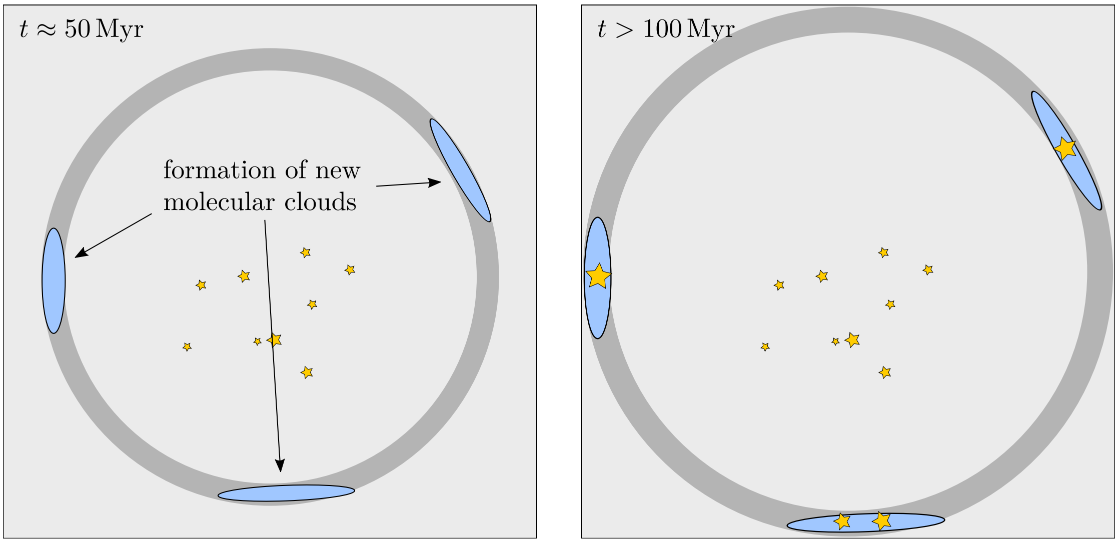

(g) After the massive stars are gone, the gas in the central cavity cools down and recombines. The shell continues to expand due to the momentum it gained earlier. The cold and dense medium in the shell fragments and becomes gravitationally unstable. A new generation of molecular clouds forms.

(h) The molecular clouds start forming new stars. These stars can in turn create new expanding shells, and the whole process can start over again.

Figure 1.33: Continued.

Chapter 2

GLIMPSE bubble N107

This chapter summarises the research into the GLIMPSE bubble N107 that I carried out during my PhD study in collaboration with Kevin Douglas, Jan Palouš, Richard Wünsch, and Soňa Ehlerová. The chapter contains a full reprint of the article Sidorin et al. (2014) (Sect. 2.1) followed by new additional material that was not part of the paper (Sect. 2.2).

I am the principal author of the text, images, and tables, as well as the work described here, with the following exception: Soňa Ehlerová analysed the UKIRT Infrared Deep Sky Survey (UKIDSS) sources, as summarised in Table 2.5; and she wrote the second paragraph of Sect. 2.1.5.3 with the description of her analysis.

2.1 Reprint: *Exploring GLIMPSE bubble N107: Multiwavelength observations and simulations*

Credit: Sidorin, V., Douglas, K. A., Palouš, J., Wünsch, R., Ehlerová, S., 2014, A&A, 565, A6, reproduced with permission © ESO.

For this thesis, I remastered Figs. 2.2, 2.5, 2.7, 2.8, 2.9 and 2.11.

Abstract

Context. The bubble N107 was discovered in the infrared emission of dust in the plane of the Milky Way Galaxy observed by the *Spitzer* Space Telescope (GLIMPSE survey: $l \approx 51\overset{\circ}{.}0$, $b \approx 0\overset{\circ}{.}1$). The bubble represents an example of shell-like structures found all over the Milky Way Galaxy.
Aims. We aim to analyse the atomic and molecular components of N107 as well as its radio continuum emission. With the help of numerical simulations, we aim to estimate the bubble's age and other parameters that cannot be derived directly from observations.
Methods. From the observations of the H I (I-GALFA) and ^{13}CO (GRS) lines we derive the bubble's kinematical distance and masses of the atomic and molecular components. With the algorithm DENDROFIND, we decompose molecular material into individual clumps. From the continuum observations at 1420 MHz (VGPS) and 327 MHz (WSRT), we derive the radio flux density and the spectral index. With the numerical code *ring*, we simulate the evolution of stellar-blown bubbles similar to N107.
Results. The total H I mass associated with N107 is $5.4 \times 10^3\,M_\odot$. The total mass of the molecular component (a mixture of cold gasses of H_2, CO, He, and heavier elements) is $1.3 \times 10^5\,M_\odot$, from which $4.0 \times 10^4\,M_\odot$ is found along the bubble border. We identified 49 molecular clumps distributed along the bubble's border, with the slope of the clump mass function of −1.1. The spectral index of −0.30 of a strong radio source located apparently within the bubble indicates nonthermal emission, hence a component of the flux probably originates in a supernova remnant, not yet catalogued. The numerical simulations suggest N107 is most likely less than 2.25 Myr old. Since the first supernovae explode only after 3 Myr or later, no supernova remnant should be present within the bubble. It may be explained if there is a supernova remnant in the direction towards the bubble, however not associated with it.

Keywords: ISM: bubbles – ISM: clouds – ISM: supernova remnants – H II regions

2.1.1 Introduction

The bubble N107 (SIMBAD: CPA2006 N107[1]) is one of the largest bubbles in the catalogue by Churchwell et al. (2006). This catalogue is based on the infrared observations made with the *Spitzer* Space Telescope (the GLIMPSE survey, Benjamin et al., 2003) and contains more than 300 bubbles found in the interstellar medium (ISM) near the Galactic plane. The catalogue was later expanded by Simpson et al. (2012) to more than 5000 bubbles, which were identified by a community of over 35 000 volunteers. These bubbles, with typical radii less than 10 pc, are examples of shell-like structures, features found in the ISM all over our Galaxy. Other examples are H I shells in catalogues by Heiles (1979, 1984) and Ehlerová & Palouš (2005) with sizes up to 3500 pc, or dusty loops discovered in the Infrared Astronomical Satellite (IRAS) full-sky survey by Kiss et al. (2004) and Könyves et al. (2007).

The varying sizes and masses of these structures suggest different mechanisms responsible for their creation. These mechanisms, which do not have to act solely, include

1. feedback from massive (OB) stars: radiation, winds, and supernovae (see the references in the next paragraph);
2. infall of high-velocity clouds (HVCs) into the Galactic disk (e.g. Heiles, 1984; Tenorio-Tagle & Bodenheimer, 1988; Ehlerová & Palouš, 1996);
3. energy and mass inserted by gamma-ray bursts (GRBs) (e.g. Efremov et al., 1998; Loeb & Perna, 1998; Efremov et al., 1999); and
4. turbulence (Dib & Burkert, 2005; Hatzidimitriou et al., 2005).

The bubble N107, like most of the GLIMPSE bubbles, is probably a result of stellar feedback (Churchwell et al., 2006; Deharveng et al., 2010), which may follow three different models:

1. An expanding H II region, assuming radiative heating and ionisation of hydrogen by ultraviolet (UV) photons from a massive star (Kahn, 1954; Oort & Spitzer, 1955; Spitzer, 1978). The pressure inside the H II region is higher than in the ambient neutral medium, so the H II region expands and collects the neutral material in an expanding shell.
2. A wind-blown bubble, supposing that energy is released via stellar winds (Castor et al., 1975; Weaver et al., 1977). Such a bubble, formed around a massive star, can be divided into several layers: an innermost layer, where the wind is freely expanding up to a layer of shocked stellar wind, where its

---

[1] CPA2006 N107: `http://simbad.u-strasbg.fr/simbad/sim-basic?Ident=CPA2006+N107`

kinetic energy is thermalised. This layer of the shocked wind is followed by a layer of swept up ISM, which in later stages of evolution is mainly atomic and molecular.

3. A supernova explosion, supposing an abrupt energy input into the ISM, producing an expanding shell/remnant (Chevalier, 1974, and references therein).

These different models of stellar feedback were also discussed by Tenorio-Tagle & Bodenheimer (1988), Ehlerová & Palouš (1996), and Efremov et al. (1999).

The shell-like structures can trigger star formation, since they consist of a layer of cold and dense material. In the so-called collect-and-collapse scenario (Elmegreen & Lada, 1977; Elmegreen, 1994; Whitworth et al., 1994b), the shell breaks into fragments and creates a new generation of stars. Radiation driven implosion (Duvert et al., 1990; Lefloch & Lazareff, 1994) considers the compression of pre-existing condensations (globules) by the pressure of the ionised gas. A brief review of these and other triggering mechanisms is given in a study of the GLIMPSE bubbles by Deharveng et al. (2010).

In this paper, we present a multiwavelength study of one of the largest GLIMPSE bubbles, N107, which lies in the central plane of the Galactic disk ($l \approx 51\overset{\circ}{.}0, b \approx 0\overset{\circ}{.}1$). A multiwavelength, colour picture of N107 is shown in Fig. 2.1.

The paper is organised in the following way: In Sect. 2.1.2, we complement the *Spitzer* observations with H I line observations from the Inner-Galaxy ALFA Low-Latitude H I Survey (I-GALFA) (Koo et al., 2010), ^{13}CO ($J = 1{-}0$) line observations from the Galactic Ring Survey (GRS) (Jackson et al., 2006), and radio continuum observations at 1420 MHz and 327 MHz from the VLA Galactic Plane Survey (VGPS) (Stil et al., 2006) and Westerbork Synthesis Radio Telescope (WSRT) (Taylor et al., 1996). From the line observations, we derive the bubble's local standard of rest (LSR) radial velocity, kinematical distance and masses of the molecular and atomic components. From the radio continuum observations, we derive the flux densities and corresponding spectral indices of two radio sources lying apparently inside the bubble. In Sect. 2.1.3, we use the recently published algorithm DENDROFIND (Wünsch et al., 2012) to decompose the molecular gas associated with the bubble into individual clumps and derive the slope of the clump mass function. In Sect. 2.1.4, we use the numerical code *ring* (Palouš, 1990; Ehlerová & Palouš, 1996) to simulate the bubble's expansion in order to estimate its age, energy input, and the size and mass of the molecular cloud from which it evolved. Finally, a discussion and conclusions are presented in Sects. 2.1.5 and 2.1.6.

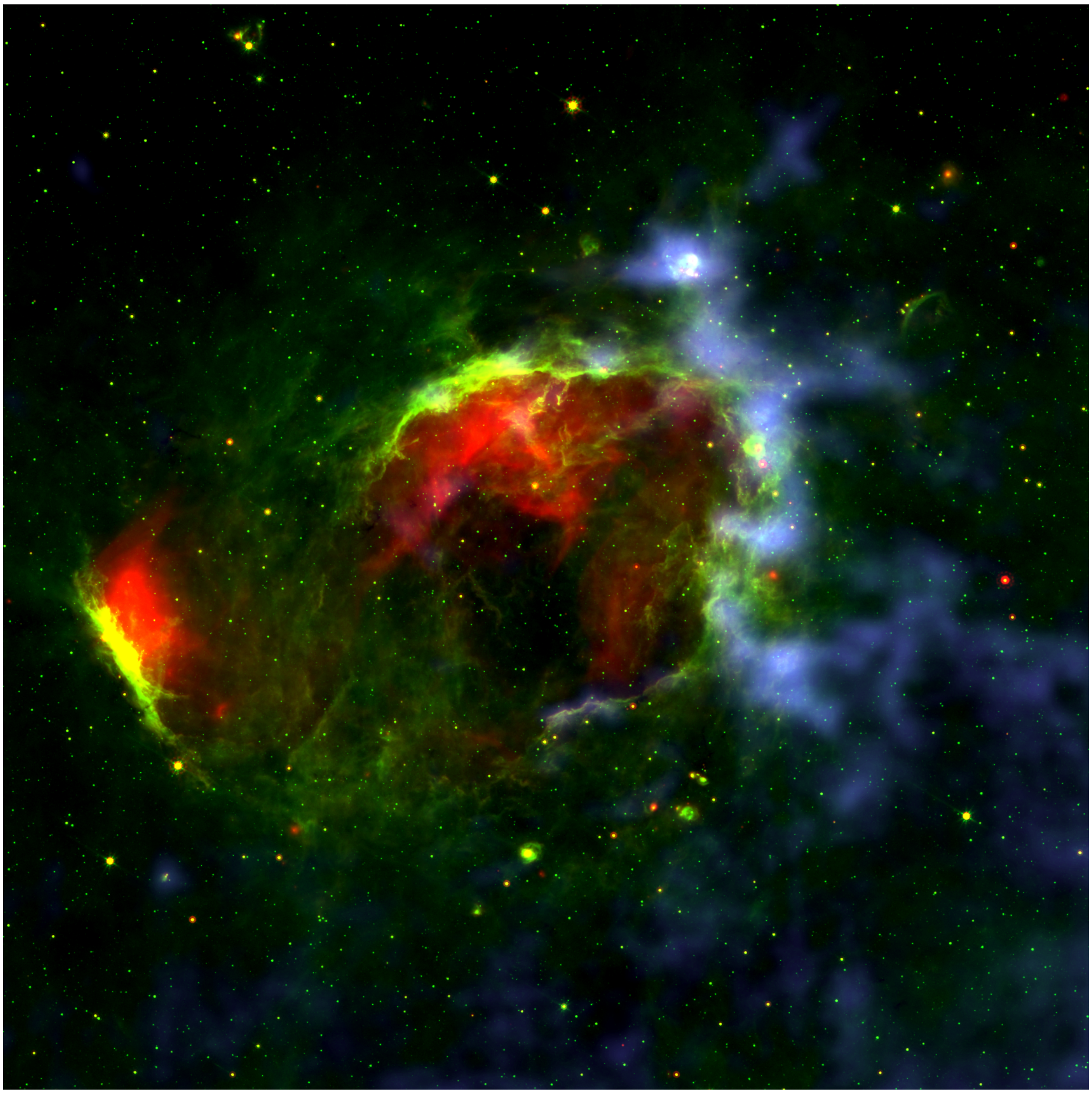

Figure 2.1: Bubble N107 – false colour multiwavelength image. The 24 µm continuum (red) is dominated by the emission of very small dust grains heated by a nearby massive star. The 8 µm continuum (green) is dominated by the emission of polycyclic aromatic hydrocarbons (PAHs), large molecules found within molecular clouds. The CO line (blue) is integrated over the radial velocities between 38.5 $\mathrm{km\,s^{-1}}$ and 47.6 $\mathrm{km\,s^{-1}}$ and traces the cold gas of molecular clouds. The distinct red-green structure seen in the lower-left in the direction of the bubble's opening is probably not related to the bubble, since the radial velocity of the associated molecular material ($\approx$60 $\mathrm{km\,s^{-1}}$) differs significantly from the radial velocity of the N107 complex ($\approx$43 $\mathrm{km\,s^{-1}}$).

2.1.2 Observation of the bubble N107

2.1.2.1 Data sources

The Galactic Legacy Infrared Mid-Plane Survey Extraordinaire (GLIMPSE) (Benjamin et al., 2003) and the 24 and 70 Micron Survey of the Inner Galactic Disk with MIPS (MIPSGAL) (Carey et al., 2009) are two complementary infrared surveys mapping the Galactic disk with the *Spitzer* Space Telescope. GLIMPSE used the Infrared Array Camera (IRAC), which has four channels centred around 3.6 µm, 4.5 µm, 5.8 µm, and 8.0 µm, for which the point response function full width at half maximum (FWHM) is between $1.''7$ and $2.''0$. MIPSGAL used the Multiband Imaging Photometer for *Spitzer* (MIPS) with a broadband channel centred around 24 µm, for which the point spread function FWHM is $6''$.

The Inner-Galaxy ALFA Low-Latitude H I Survey (I-GALFA) (Koo et al., 2010) is part of a large project called GALFA-H I (Peek et al., 2011) that plans to map the entire sky observable by the Arecibo Observatory in the H I line. The FWHM beam size of the Arecibo telescope at 1420 MHz is $3.'35$ with the GALFA-H I radial velocity channel width of $0.184\,\mathrm{km\,s^{-1}}$. The data are provided in Flexible Image Transport System (FITS)[2] datacubes of the brightness temperature T_b. The single-channel standard deviation of the Gaussian noise in the data σ_noise is about 0.25 K.

The Galactic Ring Survey (GRS) (Jackson et al., 2006) is a ^{13}CO ($J = 1{-}0$) survey focused on the Galactic molecular ring. The survey used the FCRAO 14 m telescope, with a FWHM beam size of $46''$ and a radial velocity channel width of $0.21\,\mathrm{km\,s^{-1}}$. The data are provided in FITS cubes of the antenna temperature T_A^*, with a typical noise $\sigma^*_\mathrm{noise} \approx 0.13\,\mathrm{K}$. We converted the data to the main-beam brightness temperature $T_\mathrm{b} = T_\mathrm{A}^*/\eta_\mathrm{MB}$ and $\sigma_\mathrm{noise} = \sigma^*_\mathrm{noise}/\eta_\mathrm{MB}$, where $\eta_\mathrm{MB} = 0.48$ is the main beam efficiency suggested by Jackson et al., 2006.

The VLA Galactic Plane Survey (VGPS) (Stil et al., 2006) is a 1420 MHz continuum and H I line survey of the Galactic disk based on the interferometric observations done with the Karl G. Jansky Very Large Array (VLA). We use only the continuum observations, since H I line observations with a significantly lower noise are available from I-GALFA. The VGPS FWHM beam size is $1'$ and the Gaussian noise is 0.3 K for the continuum observations.

The Westerbork Synthesis Radio Telescope (WSRT) survey (Taylor et al., 1996) is a 327 MHz continuum survey of the Galactic plane that used the WSRT interferometer in the Netherlands. The FWHM resolution is $1' \times (1'/\sin\delta)$ in the right ascension and declination (δ) directions, respectively. This yields for N107 ($\delta \approx 16^\circ$) a FWHM resolution of $1' \times 3.'6$. The median Gaussian noise is 2.5 mJy/beam.

---

[2] For the definition of FITS see Pence et al. (2010)

The UKIRT Infrared Deep Sky Survey (UKIDSS) is defined in Lawrence et al. (2007); UKIDSS uses the United Kingdom Infrared Telescope (UKIRT) Wide Field Camera (WFCAM) (Casali et al., 2007) and a photometric system described in Hewett et al. (2006). The pipeline processing and science archive are described in Irwin et al. (2004) and Hambly et al. (2008). We use data from the 7th data release.

2.1.2.2 Dust component

The bubble's outline is most prominent in the 8 µm maps from the GLIMPSE survey, where it was discovered by Churchwell et al. (2006), who also derived its basic properties: mean position of $l \approx 51\overset{\circ}{.}0$, $b \approx 0\overset{\circ}{.}1$; mean radius of $11\overset{\prime}{.}4$, and mean thickness of $2\overset{\prime}{.}3$. Most emission at 8 µm comes from the bubble edges, forming a ring-like structure. The 8 µm channel is dominated by the emission of PAHs (Draine, 2003; Reach et al., 2006, Fig. 1; Pavlyuchenkov et al., 2013). These PAHs, which are destroyed in the ionised regions, trace the photodissociation regions (PDRs), edges of molecular clouds illuminated by UV radiation from a massive star. The UV radiation pervades the PDRs and excites the PAHs found there.

A counterpart emission at 24 µm was observed in MIPSGAL (Carey et al., 2009). Unlike the 8 µm continuum, emission at 24 µm fills part of the bubble's interior. The 24 µm continuum is dominated by the emission of very small grains – dust grains larger than PAHs – heated by a nearby massive star (Pavlyuchenkov et al., 2013).

A dark hole is present in the south-western part of the bubble's interior. Almost no emission of dust and also no emission of ^{13}CO or H I (see below) is observed there. Figure 2.1 shows a multiwavelength, colour picture of N107 composed of the 8 µm and 24 µm continuum emission and the ^{13}CO line emission integrated over the radial velocities from 38.5 $\mathrm{km\,s^{-1}}$ to 47.6 $\mathrm{km\,s^{-1}}$.

2.1.2.3 Atomic component

We searched the H I datacubes by eye for features possibly associated with the bubble N107. An H I shell, morphologically similar to N107, is located around the central LSR radial velocity of 43 $\mathrm{km\,s^{-1}}$. We note that an incomplete ring of CO clumps is present at similar radial velocities (see Sect. 2.1.2.4). The H I emission is located along the bubble edges, protruding outside farther than the CO emission, forming an atomic envelope of the whole structure. Maps of the H I brightness temperature in several velocity channels are shown in Fig. 2.2.

Figure 2.3 shows a map of the Galactic longitude versus radial velocity (l–v diagram). The front wall is very faint, located at a radial velocity of $\approx$34 $\mathrm{km\,s^{-1}}$. The back wall is more distinct, located at a radial velocity of $\approx$50 $\mathrm{km\,s^{-1}}$. Between

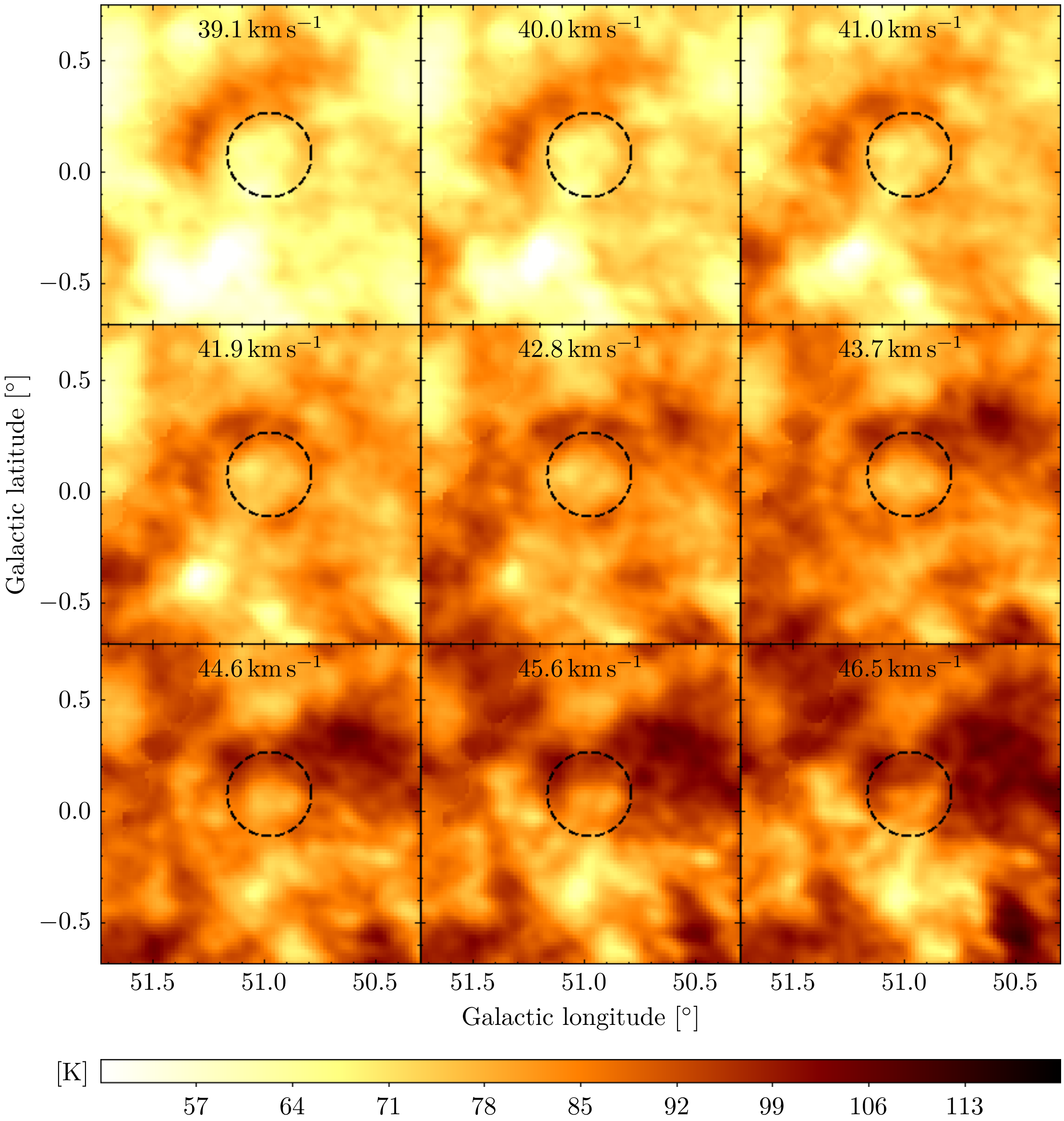

Figure 2.2: Brightness temperature maps of the H I line in several velocity channels. An outline of the bubble N107 as given in the catalogue of Churchwell et al. (2006) is marked with the dashed grey circle. The channels 41.0 km s^{-1} and 41.9 km s^{-1} show morphology very similar to that of the 8 µm emission.

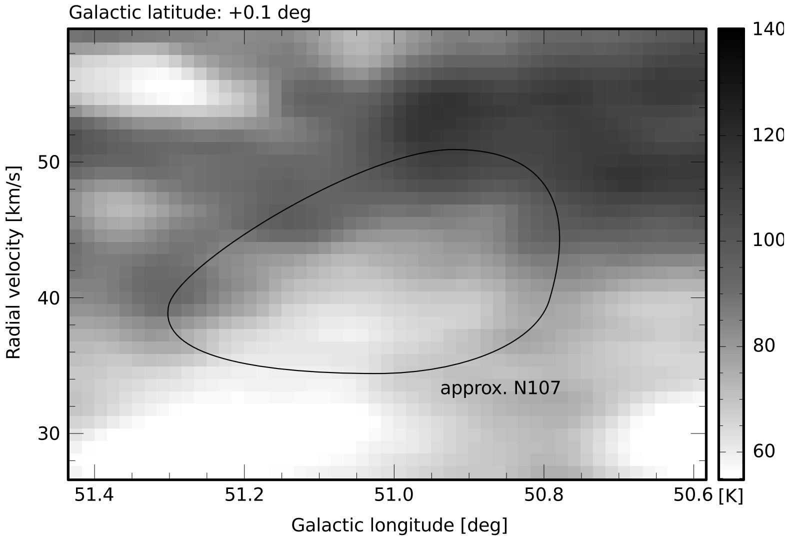

Figure 2.3: Brightness temperature of the H I line in an l–v diagram: a cut through $b = 0\overset{\circ}{.}1$. The black curve marks the approximate extent of the H I shell associated with N107.

these radial velocities, a hole can be seen inside the bubble. The relative expansion velocity of the front versus back wall is $\approx 16\,\mathrm{km\,s^{-1}}$.

In order to measure the H I mass associated with the bubble, we define the following three-dimensional aperture (aperture 1; see also Fig. 2.4, left panel): the radius two times that of N107, $r_{\mathrm{ap1}} = 2 \cdot r_{\mathrm{N107}} = 22\overset{\prime}{.}8$, and the radial velocity channels from $32.7\,\mathrm{km\,s^{-1}}$ to $52.0\,\mathrm{km\,s^{-1}}$ inclusive. All the pixels lying within this aperture contribute to the measured H I mass.

To derive the mass of the neutral hydrogen, we use the optically thin limit of H I line radiative transfer. Then, the H I column density $N_{\mathrm{H\,I}}$ can be computed from the formula (Rohlfs & Wilson, 1996)

$$\frac{N_{\mathrm{H\,I}}}{\mathrm{cm^{-2}}} = 1.8 \times 10^{18} \int \frac{T_{\mathrm{b}}}{\mathrm{K}} \frac{\mathrm{d}v}{\mathrm{km\,s^{-1}}}, \tag{2.1}$$

where T_{b} is the observed brightness temperature of the H I gas and, in our case of an I-GALFA datacube, the integral takes the form of a sum over a set of pixels with $\mathrm{d}v = 0.184\,\mathrm{km\,s^{-1}}$.

The Galactic H I emission has a strong background component. To estimate it, we assume that the bubble's interior is evacuated, so the H I emission observed apparently near the bubble centre is due to this H I background, not associated with the bubble. We define another three-dimensional aperture with a radius half that of N107 and radial velocity channels from $39.1\,\mathrm{km\,s^{-1}}$ to $43.7\,\mathrm{km\,s^{-1}}$ (see Fig. 2.4). This aperture encloses a volume in the central part of the bubble. The mean T_{b}

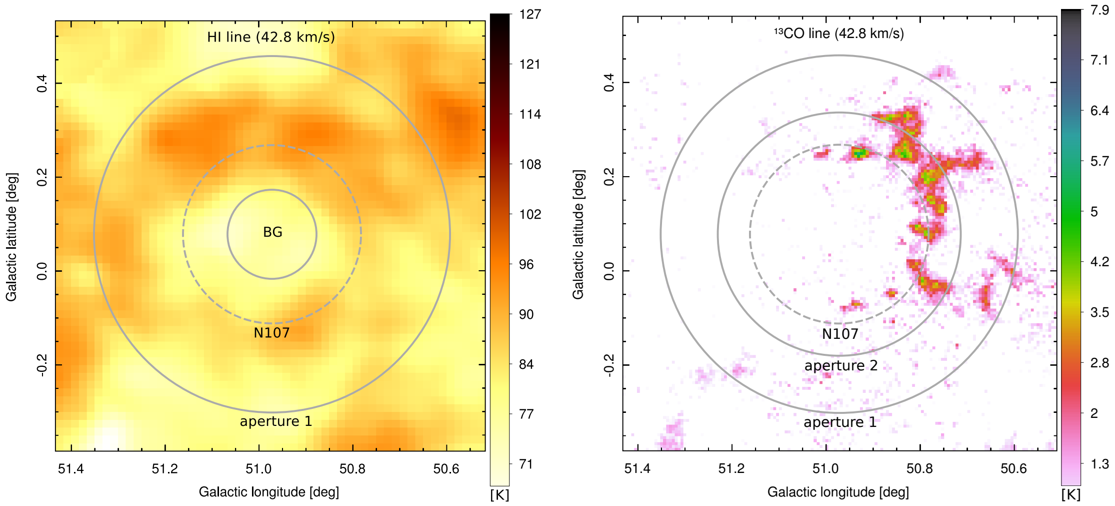

Figure 2.4: Apertures for measuring the mass associated with the bubble N107. The pixels lying within the apertures contribute to the measured masses. The dashed circles mark the bubble N107 as it was identified in the 8 µm emission by Churchwell et al. (2006). *Left:* H I line emission at 42.8 km s^{-1}. The innermost circle (BG) is the region we use to derive the background emission. *Right:* ^{13}CO ($J = 1$–0) line emission at 42.8 km s^{-1}. We used two apertures to measure the molecular mass. Aperture 1 is the same as that for measuring the H I mass, while aperture 2 is smaller and covers only the immediate vicinity of the bubble.

within this region is 72 K, which we adopt as the H I background component and subtract it before computing the mass.

Furthermore, in the process of mass derivation, we need to know the distance to N107. We also consider the ^{13}CO emission (see below) and adopt the central radial velocity of 42.8 km s^{-1}. The Galactic rotation model of Brand & Blitz (1993) gives two kinematical distances for that radial velocity: 3.6 kpc and 7.1 kpc. We adopt the near one of 3.6 kpc, which yields the bubble mean radius of 11.9 pc ($11\overset{\prime}{.}4$). The near distance is favoured by the estimated virial masses of the molecular clumps found along the bubble borders. For the far distance of 7.1 kpc, we got 22 of 49 clumps with supervirial masses, while for the near distance of 3.6 kpc, we got only 2 clumps with virial masses above 1 (clumps 7 and 21 in Table 2.2). We note that Churchwell et al. (2006) suggest distances of 4.7 kpc and 6.0 kpc. They use the same rotation model as we do, but with a less reliable determination of the radial velocity obtained from the observation of coincident H II regions. They also advocate the near kinematical distance.

To estimate the uncertainty of the measured mass, we use the standard Taylor formula,

$$\sigma_f = \sqrt{\sum_i \left(\frac{\partial f}{\partial x_i}\right)^2 \sigma_{x_i}^2}, \tag{2.2}$$

where f is a measured value (in our case the H I mass) and σ_f is its uncertainty, which is derived from uncertainties σ_{x_i} of variables x_i on which f depends.

The resulting H I mass associated with N107, i.e. the total H I mass within aperture 1 after subtracting the background, is $5.4 \times 10^3\,M_\odot$. Major sources of uncertainty are the distance to N107 and the background emission. Assuming a distance uncertainty of 10% (0.36 kpc) and a background uncertainty of 1 K, the total H I mass uncertainty is about 20%, i.e. $1 \times 10^3\,M_\odot$.

2.1.2.4 Molecular component

Around the radial velocity of 43 km s^{-1}, CO emission is present along the bubble borders. Maps of the CO emission (Fig. 2.5) show that CO gas forms clumps, which are distributed in a ring-like structure along the edges of the bubble, protruding outside. Almost no emission comes from the interior. Around the radial velocity of 48 km s^{-1}, the CO emission merges with another complex of molecular clouds, while in the channels below 38 km s^{-1}, the CO emission vanishes.

To measure the associated molecular mass, we use two three-dimensional apertures (see Fig. 2.4, right panel). Aperture 1 is the same as that for measuring the H I mass. Aperture 2 is smaller, with the radius $r_{\mathrm{ap2}} = 1.36 \cdot r_{\mathrm{N107}} = 15\overset{\prime}{.}5$ and radial velocity channels from 38.8 km s^{-1} to 46.9 km s^{-1} inclusive. It covers only the immediate vicinity of the bubble, i.e. only the mass accumulated in the expanding

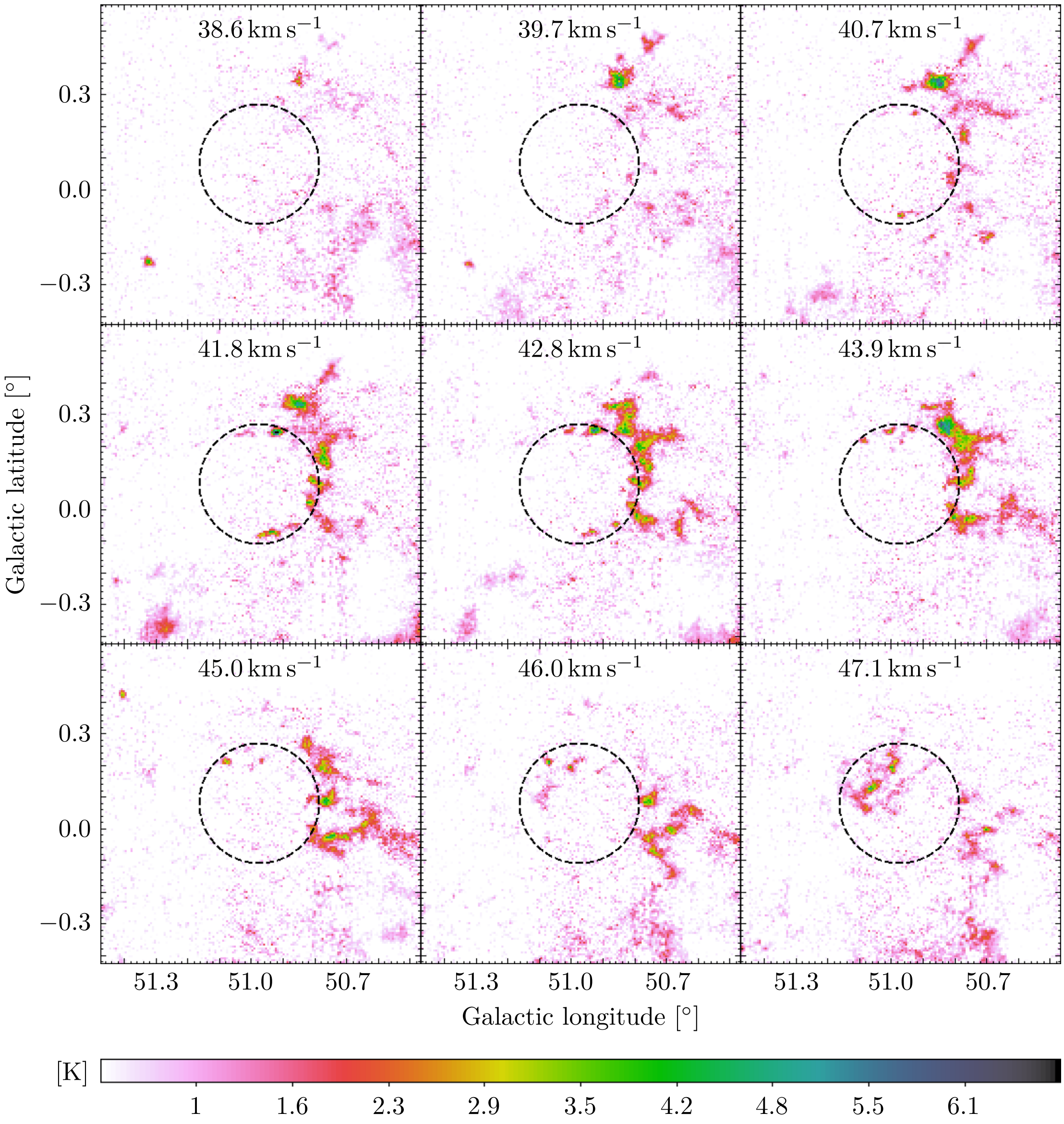

Figure 2.5: Brightness temperature maps of the ^{13}CO ($J = 1{-}0$) emission in several velocity channels in degrees Kelvin. An outline of the bubble N107 as given in the catalogue of Churchwell et al. (2006) is marked with the dashed grey circle.

shell. We note that to compare the observations and simulations (Sect. 2.1.4), we use the molecular mass found within aperture 2. We treat the radiative transfer in the ^{13}CO ($J = 1{-}0$) line as described in Rohlfs & Wilson (1996). First, we derive the optical depth:

$$\tau = -\ln\left[1 - \frac{T_\mathrm{b}}{T_0}\left\{\left[\mathrm{e}^{T_0/T_\mathrm{ex}} - 1\right]^{-1} - \left[\mathrm{e}^{T_0/T_\mathrm{CMB}} - 1\right]^{-1}\right\}^{-1}\right], \tag{2.3}$$

where T_ex is the excitation temperature, which we assume to be 20 K; T_b is the brightness temperature of the CO line; $T_\mathrm{CMB} = 2.7\,\mathrm{K}$ is the temperature of the cosmic microwave background and

$$T_0 = \frac{hf}{k} \approx 5.3\,\mathrm{K}, \tag{2.4}$$

where h is the Planck constant; k is the Boltzmann constant; and $f = 110\,\mathrm{GHz}$ is the ^{13}CO ($J = 1{-}0$) line frequency. Assuming local thermodynamic equilibrium characterised by a single excitation temperature T_ex, we can compute the ^{13}CO column density from the formula (Rohlfs & Wilson, 1996)

$$\frac{N_{^{13}\mathrm{CO}}}{\mathrm{cm}^{-2}} = 2.6 \times 10^{14} \frac{T_\mathrm{ex}}{1 - \mathrm{e}^{-T_0/T_\mathrm{ex}}} \int \tau(v)\,\mathrm{d}v, \tag{2.5}$$

where, in our case of a GRS datacube, $\mathrm{d}v = 0.21\,\mathrm{km\,s^{-1}}$ and the integral becomes a sum over a desired range of pixels. From the ^{13}CO column density, the H_2 column density is derived assuming the abundance $N_{\mathrm{H}_2} = 6.5 \times 10^5 N_{^{13}\mathrm{CO}}$ (Binney & Merrifield, 1998). Finally, the total mass of the molecular matter m_mol is computed using the standard solar hydrogen abundance X,

$$m_\mathrm{mol} = \frac{m_{\mathrm{H}_2}}{X}, \qquad \text{where} \quad X = 0.735, \tag{2.6}$$

and m_{H_2} is the mass in the form of the molecular hydrogen. We note that we use the term *molecular matter* or *molecular mass* to refer to the matter found in molecular clouds, i.e. a mixture of H_2, He, CO, and trace amounts of other molecules, elements, and dust.

The total molecular mass within aperture 1 is $1.3 \times 10^5\,M_\odot$, from which $9.8 \times 10^4\,M_\odot$ is in the form of H_2, the rest being helium and heavier elements. The total molecular mass within aperture 2 (in the expanding shell only) is $4.0 \times 10^4\,M_\odot$, from which $2.9 \times 10^4\,M_\odot$ is in the form of H_2. The major source of uncertainty is the ^{13}CO abundance. We used $N_{\mathrm{H}_2} = 6.5 \times 10^5 N_{^{13}\mathrm{CO}}$ (Binney & Merrifield, 1998). Observations and models show, however, that the abundance varies for different clouds and also depends on the physical conditions inside individual clumps (Wilson, 1999; Sonnentrucker et al., 2007; Visser et al., 2009). Another source of uncertainty is the distance to N107 (3.6 kpc, discussed above in Sect. 2.1.2.3). Using Eq. 2.2, and assuming the ^{13}CO abundance uncertainty of 20% and the distance uncertainty of 10% (0.36 kpc), the uncertainty of the molecular masses given above is about 30%.

2.1.2.5 Radio continuum and spectral index

Since an H II region was identified in the direction of the bubble (Paladini et al., 2003, region 576) and because the 24 µm emission is also present inside the bubble, we expected to observe its radio continuum counterpart.

Indeed, both the VGPS (1420 MHz) and WSRT (327 MHz) surveys show a distinct diffuse radio source in the direction of the bubble (Fig. 2.6). The source is located towards the eastern (left) part of the bubble interior, slightly below the area where the 24 µm emission is strongest. Except for this source, the bubble interior is also filled with much fainter radio emission. Another diffuse radio source is present farther east of the bubble at $l \approx 51.^\circ35$, $b \approx 0^\circ$. This source is associated with a complex of molecular matter found at radial velocities of about 60 km s^{-1}, so it is probably not associated with the bubble. Figure 2.7 shows a comparison of the VGPS radio continuum with the emission at 8 µm and 24 µm. Inside the bubble, the radio continuum follows the bubble outline defined by the PAHs emission at 8 µm. In the northern (top) and western (right) part, the radio continuum is mixed with the emission of very small grains at 24 µm, while in the eastern part (left), the 24 µm emission vanishes and only the radio continuum is observed.

We measured the radio flux densities in four regions: two located towards the bubble interior – defined by apertures A and B – and two located outside the bubble – defined by apertures C and D (Fig. 2.6). Aperture A covers the distinct source in the eastern part of the bubble (source "A"), while aperture B covers the faint emission in its western part (source "B"). Aperture C covers part of the fainter emission outside the bubble (source "C") and aperture D covers the distinct radio source located eastwards outside the bubble (source "D"). We subtracted the background component of the flux estimated from the flux within the aperture BG, which covers a relatively homogeneous region free of visible radio sources (Fig. 2.6). Then we used the fluxes at 1420 MHz and 327 MHz to derive the spectral index α for sources A, B, C, and D,

$$\alpha = \frac{\ln S_1 - \ln S_2}{\ln f_1 - \ln f_2}, \tag{2.7}$$

where S_1 and S_2 are the fluxes at frequencies f_1 and f_2. We note that the theoretical spectral index for a classical H II region in the optically thin limit is -0.1 (Condon & Ransom, 2010), although the usually observed value is around 0 or more (Verschuur & Kellermann, 1988; Rohlfs & Wilson, 1996). In contrast to H II regions, the

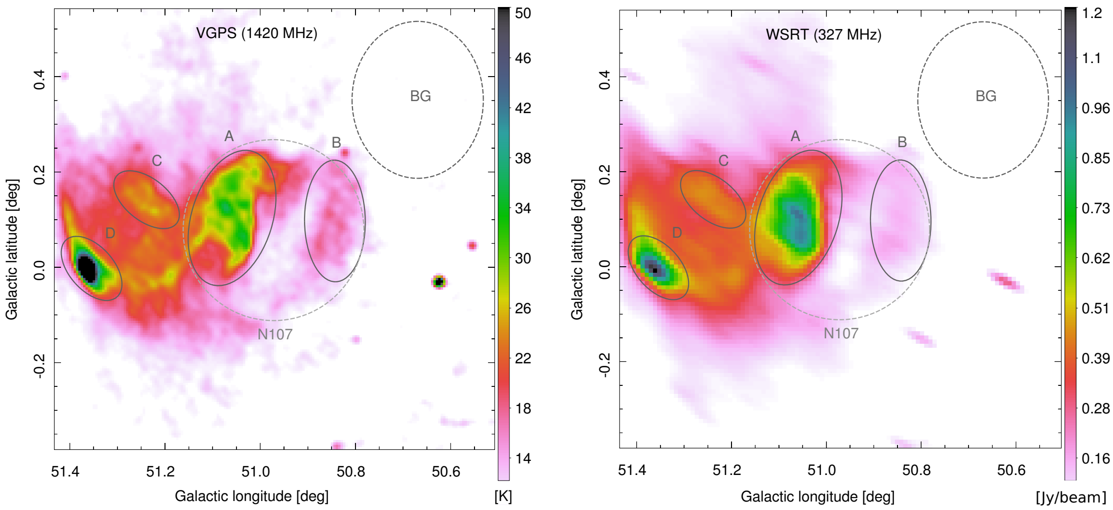

Figure 2.6: Radio continuum emission associated with the bubble N107. The bubble is denoted by the grey dashed circle in the centre. Overlaid are four elliptical apertures (A, B, C, D) used to measure radio continuum fluxes. The grey dashed ellipse in the upper right (BG) is the region used for estimating the background flux. *Left:* Emission at 1420 MHz (21 cm) from the VGPS survey. *Right:* Emission at 327 MHz (92 cm) from the WSRT survey. We note blurring in the direction of declination (top-left–to–bottom-right), caused by the larger beam size (lower resolution) in the declination direction.

mean observed spectral index of supernova remnants is −0.5 (average value in the catalogue of Green, 2009[3]).

The measured flux densities and the derived spectral indices are given in Table 2.1. The spectral index of source A of −0.3 suggests a nonthermal (synchrotron) contribution to the received radio flux: a supernova remnant. No known supernova remnant is associated, yet, with that radio source. For source B, the spectral index of ≈0 suggests a thermal origin of the flux: a classical H II region. The spectral indices of sources C (−0.2) and D (−0.1) suggest that part of their emission is also nonthermal.

2.1.3 Analysis of molecular clumps

We decomposed the molecular ring associated with N107 into individual molecular clumps with the program DENDROFIND, described in the appendix of Wünsch et al. (2012). DENDROFIND processes datacubes, typically position-position-velocity datacubes of the brightness temperature T_b, and outputs a list of molecular clumps

---

[3] An updated version of the catalogue was published by Green (2014). The average value of the spectral index is still −0.5, more precisely −0.48. The catalogue is available online at `http://www.mrao.cam.ac.uk/surveys/snrs/`.

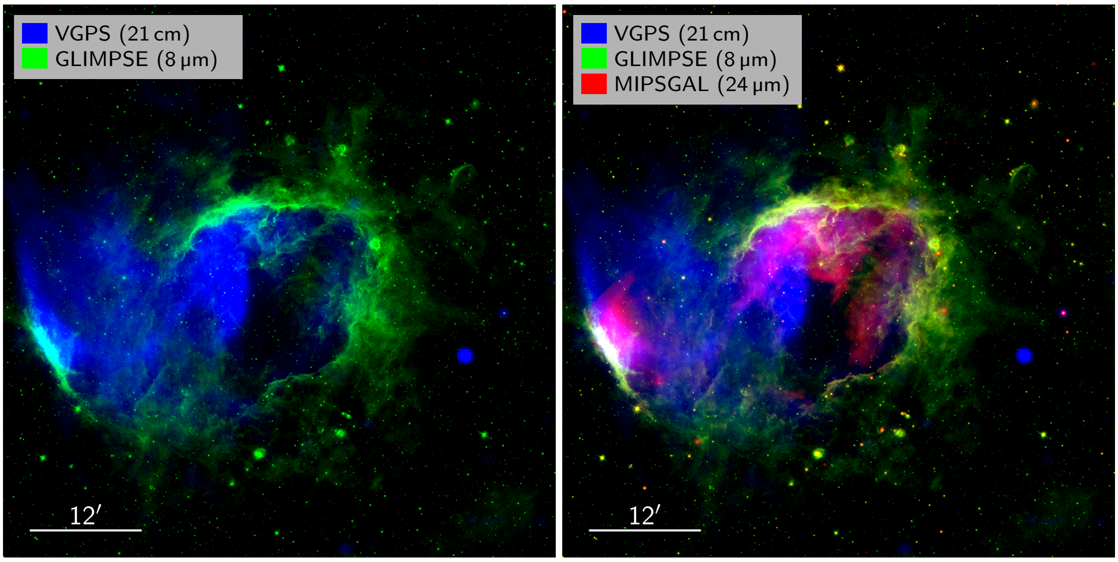

Figure 2.7: Comparison of the VGPS radio continuum emission at 1420 MHz (21 cm) (blue) with 8 μm (green) and 24 μm (red) emission. *Left:* 1420 MHz and 8 μm emission. The radio continuum emission follows the bubble's outline and fills part of its interior. *Right:* Same as left with the 24 μm emission included. Inside the bubble, the radio continuum emission is well correlated with the 24 μm emission, except for the eastern part, where the 24 μm emission is absent and only the radio continuum emission is observed.

Table 2.1: Radio continuum flux densities and spectral indices for apertures A, B, C, and D.

Frequency	S_A	S_B	S_C	S_D
1420 MHz	11.30 Jy	2.81 Jy	2.87 Jy	5.12 Jy
327 MHz	17.55 Jy	2.74 Jy	3.91 Jy	6.19 Jy
Spectral index	−0.30	0.02	−0.21	−0.13

Notes. The flux densities ($S_{\mathrm{A,\,B,\,C,\,D}}$) are background-subtracted.

organised in a hierarchical structure, which can be represented by a dendrogram (Rosolowsky et al., 2008). In our case, the datacube is a cutout of the ^{13}CO GRS data, and has two spatial dimensions (Galactic longitude, Galactic latitude) and one radial velocity dimension. Each clump consists of a dense core surrounded by a less dense molecular envelope. The core is observed as a local T_b peak. DENDROFIND is controlled by four parameters: `Nlevels` sets the number of steps by which it goes through the datacube when searching for clump peaks; `Npxmin` sets the minimal number of pixels which can form a clump; `Tcutoff` sets the minimal T_b which is still considered a signal – pixels with a lower T_b are discarded; `dTleaf` sets the minimal height of a local peak to be considered a clump's core – a higher `dTleaf` will merge more clumps. The parameters `Tcutoff` and `dTleaf` are designed to be set to a value of about three times the noise level. We ran DENDROFIND with the parameters `Nlevels` = 1000, `Npxmin` = 5, and `Tcutoff` = `dTleaf` = $1.0 \approx 3\sigma_\mathrm{noise}$, where $\sigma_\mathrm{noise} \approx 0.34\,\mathrm{K}$ is the estimated standard deviation of the Gaussian noise within our cutout of the ^{13}CO GRS datacube. This value is slightly greater then the typical value for the entire GRS (0.27 K) given by Jackson et al. (2006).

In order to select only the clumps associated with the bubble N107, we took only those clumps whose cores lie within the aperture 2 used for measuring the total molecular mass (Sect. 2.1.2.4). Table 2.2 lists the identified molecular clumps. The meaning of the columns is as follows: N is the number identifying a clump in our list; l_peak, b_peak, and v_peak are the Galactic longitude, Galactic latitude, and LSR radial velocity, respectively, of the brightest pixel of the clump; T_peak is the brightness temperature of the brightest pixel; R is the clump surface-equivalent radius, defined as

$$R = \sqrt{A_\mathrm{cl}/\pi}, \tag{2.8}$$

where A_cl is the clump projected area in the sky; *FWHM* is the clump full width at half maximum computed as

$$FWHM_x = 2\sqrt{2\ln 2}\sqrt{\sigma_x^2 + \left(\frac{\Delta x}{2\sqrt{2\ln 2}}\right)^2}, \tag{2.9}$$

where $x \in \{l,\ b,\ v\}$. The second term under the big square root represents the pixel resolution term and ensures that the *FWHM* will not be smaller than the pixel size. For the GRS datacube, the pixel size Δx is $22''.1 \times 22''.1 \times 0.21\,\mathrm{km\,s^{-1}}$, which corresponds at N107's distance of 3600 pc to $0.39\,\mathrm{pc} \times 0.39\,\mathrm{pc} \times 0.21\,\mathrm{km\,s^{-1}}$. If Δx goes to zero, the *FWHM* approaches the Gaussian *FWHM*. The value of σ_x^2 is the variance weighted by the brightness temperature T_b,

$$\sigma_x^2 = \overline{x^2} - \overline{x}^2 = \sum_\mathrm{pix} \frac{x^2 T_\mathrm{b}}{T_\mathrm{tot}} - \left(\sum_\mathrm{pix} \frac{x T_\mathrm{b}}{T_\mathrm{tot}}\right)^2, \tag{2.10}$$

$$\text{where} \quad T_{\text{tot}} = \sum_{\text{pix}} T_{\text{b}}, \tag{2.11}$$

with the summation taken over all pixels belonging to the clump. The variable M is the clump mass, which is the total mass of pixels belonging to the clump, derived from Eqs. 2.3 to 2.6 (Sect. 2.1.2.4). The error of the clump mass, assuming Gaussian noise and neglecting pixel correlation within the beam, is The error of the clump mass, assuming Gaussian noise and neglecting pixel correlation within the beam, is

$$\Delta M = \sqrt{N_{\text{px}}}\, \Delta M_{\text{px}}, \tag{2.12}$$

where N_{px} is the number of pixels belonging to the clump, and ΔM_{px} is the σ_{noise}-equivalent mass. In our case of the GRS datacube, $\sigma_{\text{noise}} = 0.34\,\text{K}$, which yields $\Delta M_{\text{px}} = 0.21\,M_{\odot}$; M_{vir} is the clump virial mass, estimated as (MacLaren et al., 1988):

$$M_{\text{vir}} = 190 \cdot R \cdot FWHM_v^2. \tag{2.13}$$

The formula above assumes a spherical clump with a density profile $\propto 1/r$. ΔM_{vir} is the virial mass error derived from the first order Taylor expansion of Eq. 2.13, assuming the clump's area and $FWHM_v$ errors of one pixel.

Figure 2.8 shows a histogram of clumps masses.[4] Overlaid is a line representing a fit by a function $\mathrm{d}N/\mathrm{d}M = C(M/M_{\odot})^{\alpha}$, where α is the slope of the clump mass function and C is a constant. We used least-squares fitting on a logarithmic scale, i.e. we fit the log of the bin heights $\log(\mathrm{d}N/\mathrm{d}M)$ by a function $\log(C(M/M_{\odot})^{\alpha})$. The best fitting slope is $\alpha = -1.1$. The bins in the histogram have variable widths, set so that each contains seven clumps. This ensures that all bins have the same significance.

2.1.4 Numerical simulations of bubbles and comparison with N107

We simulated the evolution of bubbles formed in the ISM around massive stars in order to estimate parameters of N107 that cannot be derived directly from observation (especially its age). We used a version of the FORTRAN code *ring* (Palouš, 1990; Ehlerová & Palouš, 1996), which was originally written for simulations of expanding H I shells in the Galactic ISM.

---

[4] An improved analysis of the clump mass spectrum, using a reversed cumulative histogram, is given in Sect. 2.2.4.

Table 2.2: Molecular clumps associated with the bubble N107.

N	$\frac{l_{\mathrm{peak}}}{\mathrm{deg}}$	$\frac{b_{\mathrm{peak}}}{\mathrm{deg}}$	$\frac{v_{\mathrm{peak}}}{\mathrm{km\,s^{-1}}}$	$\frac{T_{\mathrm{peak}}}{\mathrm{K}}$	$\frac{R}{\mathrm{pc}}$	$\frac{FWHM_l}{\mathrm{pc}}$	$\frac{FWHM_b}{\mathrm{pc}}$	$\frac{FWHM_v}{\mathrm{km\,s^{-1}}}$	$\frac{M}{M_\odot}$	$\frac{\Delta M}{M_\odot}$	$\frac{M_{\mathrm{vir}}}{M_\odot}$	$\frac{\Delta M_{\mathrm{vir}}}{M_\odot}$	$\frac{M}{M_{\mathrm{vir}}}$
1	50.919	0.241	41.89	7.0	2.2	2.45	1.62	1.84	1037.1	5.6	1409.9	324.8	0.736
2	50.840	0.266	44.01	5.8	4.0	3.48	3.40	2.83	4082.1	11.5	6050.2	909.0	0.675
3	50.753	−0.029	45.08	4.7	3.2	3.38	2.52	4.63	3119.8	10.8	12847.9	1180.5	0.243
4	51.073	0.204	45.93	4.7	1.2	1.41	0.99	2.57	351.1	3.6	1494.4	247.5	0.235
5	50.766	0.081	45.50	4.6	3.3	3.66	2.21	3.92	3469.1	10.9	9622.4	1044.0	0.361
6	50.938	−0.072	42.31	4.6	1.8	3.06	1.17	1.70	635.2	4.8	1010.1	252.4	0.629
7	50.778	0.192	42.74	4.5	5.0	5.15	5.07	2.76	7365.5	15.9	7259.4	1120.0	1.015
8	50.815	0.020	42.10	4.5	2.3	1.59	2.60	3.91	1206.7	6.8	6597.7	716.4	0.183
9	50.803	−0.029	44.01	4.4	2.3	2.05	2.11	2.26	1059.1	6.1	2272.7	428.0	0.466
10	50.999	0.247	43.59	3.6	1.4	2.08	1.08	2.26	276.5	3.5	1343.3	252.2	0.206
11	50.858	−0.048	42.95	3.3	1.2	1.72	0.86	1.55	169.3	2.8	560.8	154.1	0.302
12	50.796	0.124	44.01	2.5	1.4	1.27	1.41	1.44	149.6	2.7	554.4	164.0	0.270
13	50.784	0.131	46.56	2.3	0.9	0.87	1.09	0.96	45.3	1.5	152.0	67.4	0.298
14	50.870	−0.152	40.83	2.1	1.0	1.22	1.06	1.42	60.9	1.7	366.1	109.3	0.166
15	50.969	−0.128	39.34	2.0	0.8	1.01	0.87	0.58	26.3	1.2	53.4	39.3	0.493
16	50.883	0.297	43.80	1.9	0.5	0.88	0.46	0.47	8.4	0.7	20.0	18.3	0.417
17	50.913	0.180	46.35	1.9	0.9	1.61	0.93	1.09	48.5	1.6	197.8	77.0	0.245
18	50.913	0.155	41.68	1.8	0.6	0.84	0.67	0.46	11.7	0.8	25.2	23.1	0.465
19	50.864	0.210	45.29	1.8	0.5	0.68	0.52	1.11	15.6	0.9	114.0	43.7	0.137
20	50.833	0.210	40.19	1.7	1.0	1.36	1.06	0.81	26.3	1.2	120.1	63.4	0.219
21	50.833	0.057	42.95	1.7	0.5	0.73	0.76	0.21	5.0	0.5	4.6	9.2	1.088
22	50.864	0.260	41.04	1.7	0.4	0.73	0.50	0.41	5.8	0.5	14.2	14.6	0.411
23	50.987	−0.171	41.46	1.6	0.5	0.96	0.58	0.21	4.0	0.5	4.2	8.4	0.950
24	50.956	−0.122	40.40	1.6	0.8	1.27	1.06	0.79	22.7	1.1	99.3	53.6	0.228
25	50.790	0.014	38.91	1.6	0.6	0.85	0.79	0.30	6.2	0.6	9.7	13.8	0.639
26	50.870	−0.042	39.55	1.6	0.8	1.02	1.00	0.59	17.8	1.0	54.8	39.2	0.326
27	50.735	0.051	39.76	1.6	0.6	1.02	0.59	0.41	8.7	0.7	19.3	20.2	0.449
28	50.846	0.192	39.13	1.5	0.4	0.79	0.57	0.31	4.4	0.5	8.0	11.0	0.548
29	50.833	−0.066	41.68	1.5	0.5	0.95	0.57	0.27	4.6	0.5	7.0	10.8	0.661
30	50.889	−0.036	39.76	1.5	0.4	0.59	0.55	0.32	3.8	0.5	7.4	9.8	0.519
31	51.061	−0.042	45.71	1.5	0.5	0.89	0.49	0.48	5.5	0.5	21.5	19.0	0.255
32	50.981	0.026	43.80	1.5	0.5	0.98	0.59	0.21	4.0	0.5	4.2	8.4	0.955
33	50.778	0.032	46.78	1.5	0.6	0.96	0.56	0.48	9.6	0.7	24.9	22.2	0.383
34	50.864	0.087	42.31	1.4	0.5	0.77	0.76	0.21	4.2	0.5	4.2	8.4	0.992
35	50.981	−0.152	46.14	1.4	0.5	0.80	0.59	0.21	3.8	0.5	4.2	8.4	0.899
36	50.987	0.038	46.99	1.4	0.4	0.53	0.81	0.33	3.8	0.5	8.8	11.5	0.426
37	50.864	0.192	42.10	1.4	0.5	0.70	0.71	0.61	8.0	0.7	38.3	26.5	0.210
38	51.006	0.247	45.50	1.4	0.3	0.59	0.39	0.42	3.8	0.5	10.3	10.5	0.370
39	50.969	0.327	46.78	1.3	0.6	1.02	0.59	0.30	5.6	0.6	10.2	14.2	0.554
40	50.956	−0.109	46.35	1.3	0.5	0.52	1.10	0.21	3.5	0.5	4.2	8.4	0.844
41	50.956	−0.091	46.99	1.3	0.5	1.06	0.57	0.21	4.4	0.5	4.6	9.2	0.964
42	50.969	0.327	41.89	1.3	0.4	0.73	0.50	0.32	4.6	0.5	8.5	11.3	0.538
43	50.852	−0.017	45.29	1.3	0.4	0.83	0.53	0.29	3.6	0.5	6.9	10.2	0.521
44	50.741	0.051	42.10	1.3	0.5	0.69	0.78	0.21	3.7	0.5	4.2	8.4	0.892
45	50.821	0.241	39.55	1.3	0.6	0.59	1.11	0.33	7.8	0.7	11.8	15.3	0.665
46	50.815	−0.066	42.95	1.2	0.5	1.15	0.56	0.40	5.7	0.6	16.0	17.1	0.356
47	51.221	0.081	46.78	1.2	0.5	0.71	0.71	0.32	5.6	0.6	10.6	13.9	0.526
48	51.067	0.149	45.93	1.2	0.4	0.53	0.78	0.29	3.5	0.5	6.9	10.1	0.513
49	50.796	0.223	41.04	1.2	0.4	1.01	0.39	0.29	3.4	0.5	7.0	10.2	0.485

Notes. Column 1 gives a number identifying a clump in our list. The meaning of the other columns is explained in Sect. 2.1.3. The clumps are sorted in descending order by T_{peak}.

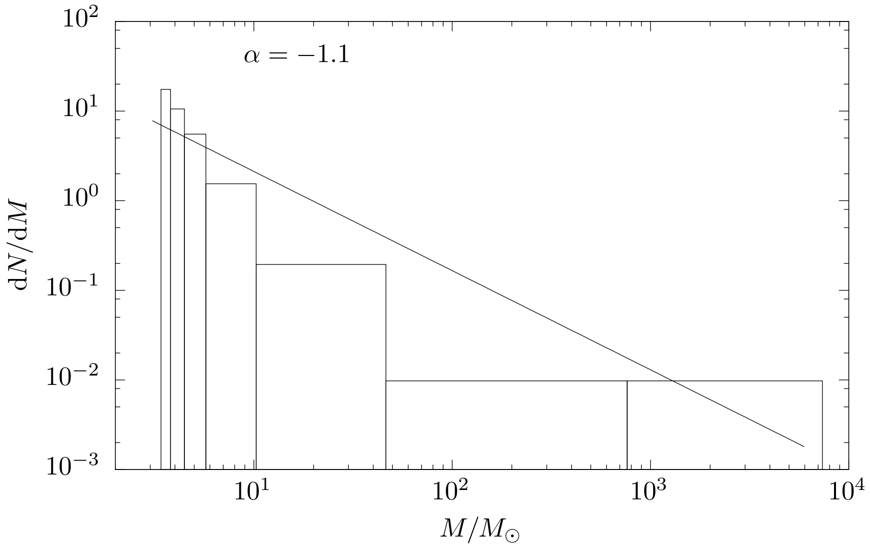

Figure 2.8: Histogram of the masses of molecular clumps associated with the bubble N107. The bin widths are variable, set so that each bin contains seven clumps. The line represents the best fitting power-law function with the index $\alpha = -1.1$.

2.1.4.1 Code description

The simulation starts with a small spherical shell, which is set according to the early stage of the expansion in the wind-blown bubble model (Weaver et al., 1977). The infinitesimally thin shell (thin-shell approximation) is divided into $nl \times np$ elements. We solve the equations of motion including the pressure difference between the shell interior and exterior and the mass accumulation of the ambient medium. We do not include gravity or any other force acting on the shell. The momentum equation for an element of the shell is

$$\frac{\mathrm{d}}{\mathrm{d}t}(m\mathbf{v}) = \mathbf{S}(P_{\mathrm{i}} - P_{\mathrm{e}}), \tag{2.14}$$

where m is the element mass, $\mathbf{v}$ is the element velocity, $\mathbf{S}$ is the element surface, and P_{i} and P_{e} are the interior and exterior pressures respectively. The total number of the shell elements is fixed (we used 30×60), so their surface and mass grow with time. The mass growth of an element is given by the equation

$$\frac{\mathrm{d}m}{\mathrm{d}t} = \rho(\mathbf{v} \cdot \mathbf{S}), \tag{2.15}$$

where ρ is the local density of the ambient medium.

The energy source driving the expansion is represented as a continuous and constant energy input $\dot{E}$. For each time step a corresponding amount of thermal

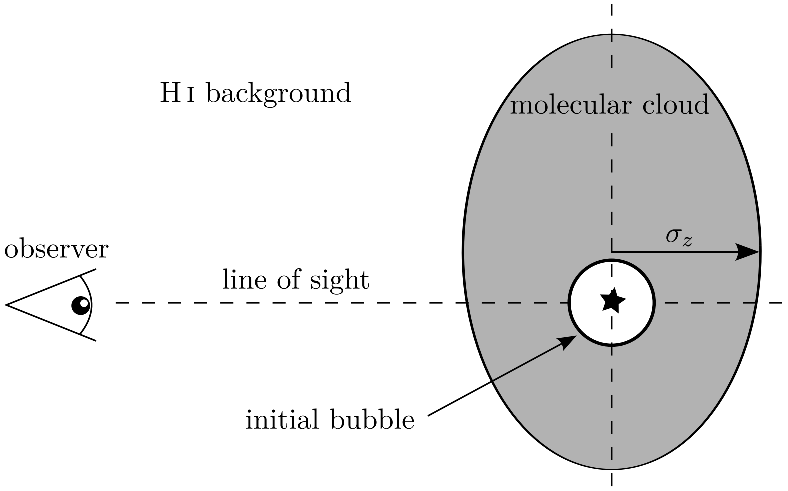

Figure 2.9: Simulation setup for a stellar-blown bubble. The bubble is formed around one or more massive stars inside a molecular cloud that has a three-dimensional Gaussian density profile. The Gaussian thickness σ_x and σ_y in the sky plane is set to 12 pc, while σ_z, which runs parallel to our line of sight, is a parameter we vary. The centre of expansion is dislocated from the centre of the cloud by Δr_0, which is another parameter we vary. The dislocation is towards the $(-x, -y)$ direction, perpendicular to the line of sight. The molecular cloud is overlaid on a background of atomic gas with a particle number density of 4 cm^{-3}

energy is added to the bubble interior and a new value of the interior pressure is computed as

$$P_\mathrm{i} = \frac{2}{3}\frac{E_\mathrm{i}}{V}, \tag{2.16}$$

where E_i is the interior thermal energy and V is the bubble volume. Equation 2.16 assumes that the interior is filled with a monatomic gas. We do not consider radiative cooling and assume that the gas expands adiabatically; i.e. the only way how it can loose energy is through the work done by pushing the bubble's elements.

The motion of the bubble elements is integrated using the fourth-order Runge-Kutta method with adaptive time step.

2.1.4.2 Simulation setup

We assume a bubble expanding in a molecular cloud with a three-dimensional Gaussian density profile (see illustration in Fig. 2.9),

$$n = n_0 \exp\left\{-\frac{1}{2}\left[\left(\frac{x-x_0}{\sigma_x}\right)^2 + \left(\frac{y-y_0}{\sigma_y}\right)^2 + \left(\frac{z-z_0}{\sigma_z}\right)^2\right]\right\}, \tag{2.17}$$

where n is the particle number density; n_0 is the particle number density in the centre of the cloud; σ_x, σ_y, σ_z are the Gaussian thicknesses (standard deviation) in the x, y, z directions respectively; x_0, y_0, z_0 specify the location of the cloud centre.

We also assume the original centre of expansion, i.e. the location of the energy source driving the expansion, is shifted (dislocated) from the centre of the cloud by Δr_0 towards the direction $(-x,\ -y)$. In the coordinates used in the code, the expansion centre (bubble centre) is located at the origin $x = y = z = 0$; we shift the centre of the molecular cloud by Δr_0 in the xy plane:

$$x_0 = y_0 = \Delta r_0/\sqrt{2}, \qquad z_0 = 0. \tag{2.18}$$

We assume a hydrogen abundance of $X = 0.735$, helium abundance of $Y = 0.245$, metallicity of $Z = 0.02$, and a mean relative particle weight of metals of 16.65. We also assume that all hydrogen in the cloud is in the form of H_2. This yields a mean relative particle weight of the molecular matter of $\mu = 2.34$. We further assume that the molecular material of the cloud is isothermal with a temperature set at 20 K. We also consider an atomic gas component, which is represented by a constant density background with 4 hydrogen atoms per cm^3 and a temperature of 6000 K.

The total initial energy of the bubble is set to 1×10^{49} erg and each time step δt the energy is increased by $\dot{E}\,\delta t$.

2.1.4.3 Comparison with observations

We ran a series of simulations in order to find the parameters that produce a bubble with a mass distribution and expansion velocity similar to N107. The input parameters for the code *ring* we varied were the energy input ($\dot{E}$), the shift (dislocation) of the expansion centre from the cloud centre (Δr_0), the Gaussian thickness of the cloud in the direction of our line of sight (σ_z), and the total mass of the parental molecular cloud (M_0). The Gaussian thickness in the sky plane $\sigma_{xy} = \sigma_x = \sigma_y$ was kept constant at 12 pc, which is comparable to the radius of N107. For each set of these parameters, the code evolves a bubble in time and outputs a chain of its snapshots in given time intervals.

Because the bubble is expanding in an inhomogeneous, non-spherical density field, the elements facing a lower density expand faster. This causes the bubble's geometrical centre to move progressively towards the direction of the lower density. To compensate for this drift, we centred each snapshot at the bubble's geometrical centre, which is computed as the mean (x, y, z) coordinates of the bubble elements weighted by their surface. We projected those centred snapshots onto FITS datacubes with two spatial and one radial velocity dimensions with the same pixel size as in the GRS datacube.

The radiation from OB stars illuminating molecular clouds creates a layer of dissociated matter. This layer then shields the radiation and prevents it from penetrating farther inside. The dissociated matter will not contribute to the ^{13}CO line brightness temperature. To account for that, before computing the synthetic ^{13}CO line brightness temperature, we decreased the surface density of each bubble element by $4.35\,M_{\odot}\mathrm{pc}^{-2}$. This value is based on the suggestion for shielding by Krumholz et al. (2009). We assume that the ^{13}CO abundances are the same as we used for measuring the observed molecular mass in Sect. 2.1.2.4. Then for each pixel we derived the corresponding brightness temperature of the ^{13}CO $(J = 1{-}0)$ line. Finally, we applied convolution to simulate the Five College Radio Astronomical Observatory (FCRAO) telescope resolution used in the GRS. The resulting FITS thus represents an image, which would be seen by FCRAO if it observed the simulated bubble at a given evolution time.

We define a goodness-of-fit parameter δ to compare the synthetic datacubes to the observations:

$$\delta = \frac{1}{3}\left[\delta V_{\mathrm{exp}}^2 + \frac{1}{4}\sum_{i=1}^{4}\left(\delta m_i^2 + \delta r_i^2\right)\right]. \tag{2.19}$$

Lower values of δ mean a better fit to (better agreement with) the observed properties of N107. The meaning of the terms is as follows:

$$\delta V_{\mathrm{exp}}^2 = \left(\frac{V_{\mathrm{exp,\,s}} - V_{\mathrm{exp,\,o}}}{V_{\mathrm{exp,\,o}}}\right)^2 \tag{2.20}$$

represents the square of the difference of the bubble expansion velocity between the observed value of N107 ($V_{\mathrm{exp,\,o}}$) and simulated value ($V_{\mathrm{exp,\,s}}$). We adopt the observed bubble expansion velocity of $V_{\mathrm{exp,\,o}} = 8\,\mathrm{km\,s^{-1}}$, which is derived from the H I observations and represents one half of the relative velocity of the shell's front and back wall;

$$\frac{1}{4}\sum_{i=1}^{4}\left(\delta m_i^2 + \delta r_i^2\right) = \frac{1}{4}\sum_{i=1}^{4}\left(\left[\frac{m_{i,\,\mathrm{s}} - m_{i,\,\mathrm{o}}}{m_{i,\,\mathrm{o}}}\right]^2 + \left[\frac{r_{i,\,\mathrm{s}} - r_{i,\,\mathrm{o}}}{r_{i,\,\mathrm{o}}}\right]^2\right) \tag{2.21}$$

is a sum taken over the four circular sectors of aperture 2 used to measure the bubble molecular mass (see Fig. 2.4). This term compares the angular mass distribution between N107 and the simulated bubbles. A visualisation of the sectors is shown in Fig. 2.10. The values $m_{i,\,\mathrm{s}}$ and $m_{i,\,\mathrm{o}}$ are the simulated ("s") and observed ("o") molecular masses in the circular sector i; $r_{i,\,\mathrm{s}}$ and $r_{i,\,\mathrm{o}}$ give the simulated and observed mean radii in the sector i, weighted by the brightness temperature

$$r_i = \langle r_i \rangle_{T_\mathrm{b}} = \frac{\sum\limits_{(\mathrm{px\ in}\ i)} r T_\mathrm{b}}{\sum\limits_{(\mathrm{px\ in}\ i)} T_\mathrm{b}}, \tag{2.22}$$

Table 2.3: Ranges of the input parameters $\dot{E}$, r_0, σ_z, M_0, and the constraints on the evolution time t we used in the numerical simulations of expanding bubbles.

Range of values	Steps
First series (wider parameter ranges)	
$\dot{E} = (0.1 \text{ to } 100) \times 10^{50}\,\mathrm{erg\,Myr^{-1}}$	10 log steps
$r_0 = (0.1 \text{ to } 30)$ pc	10 log steps
$\sigma_z = (1 \text{ to } 30)$ pc	10 log steps
$M_0 = (1 \times 10^5 \text{ to } 1 \times 10^7)\ M_\odot$	10 log steps
$t = (0 \text{ to } 100)$ Myr	0.5 Myr steps
Second series (narrower parameter ranges)	
$\dot{E} = (0.1 \text{ to } 10) \times 10^{50}\,\mathrm{erg\,Myr^{-1}}$	8 log steps
$r_0 = (10 \text{ to } 28)$ pc	10 linear steps
$\sigma_z = (2 \text{ to } 28)$ pc	14 linear steps
$M_0 = (3 \times 10^5 \text{ to } 3 \times 10^6)\ M_\odot$	8 log steps
$t = (0 \text{ to } 8)$ Myr	0.25 Myr steps

where the summations are taken over the pixels in the sector i.

First, we ran a series of simulations with a wider span of the input parameters $\dot{E}$, r_0, σ_z, and M_0, with steps on a logarithmic scale, and the evolution time up to $t = 100$ Myr, with snapshots taken every 0.5 Myr. Then we located a subset of the input parameters with the best fits to the observation (lowest δ) and ran a second series of simulations with finer parameter resolutions. In the second series, we used linear steps for the parameters r_0 and σ_z and logarithmic steps for $\dot{E}$ and M_0. The snapshots were taken every 0.25 Myr up to $t = 8$ Myr. We note that the internal time step of *ring* is controlled dynamically by its Runge-Kutta routines; we only set the snapshot printout interval Δt. The input parameters for both runs are listed in Table 2.3. The ten best fitting runs are shown in Table 2.4.

To conclude, we simulated the evolution of bubbles formed around massive stars in molecular clouds and compared their properties to N107. We got the best agreement for two groups of parameters:

- Group A represents bubbles produced with a lower energy input ($\dot{E} < 0.4 \times 10^{50}\,\mathrm{erg\,Myr^{-1}}$), greater centre-of-expansion dislocation ($r_0 \approx 16$ pc to 22 pc), formed within an oblate molecular cloud with an oblateness of $\sigma_z/\sigma_{xy} = 6/12$, and with a greater evolution time ($t \approx 1.75$ Myr to 2.25 Myr).
- Group B represents bubbles produced with a higher energy input ($\dot{E} = 2.7 \times 10^{50}\,\mathrm{erg\,Myr^{-1}}$), smaller centre-of-expansion dislocation ($r_0 \approx 10$ pc to 12 pc), formed within a prolate molecular cloud ($\sigma_z/\sigma_{xy} \approx [20 \text{ to } 28]/12$), with a smaller evolution time ($t = 1$ Myr).

Table 2.4: First ten sets of parameters best fitting the observations of N107.

$\frac{\dot{E}}{10^{50}\,\mathrm{erg\,Myr^{-1}}}$	$\frac{r_0}{\mathrm{pc}}$	$\frac{\sigma_z}{\mathrm{pc}}$	$\frac{M_0}{10^5\,M_\odot}$	$\frac{t}{\mathrm{Myr}}$	$\frac{V_{\mathrm{exp}}}{\mathrm{km\,s^{-1}}}$	$\frac{m_1/m_2/m_3/m_4}{10^3\,M_\odot}$	$\frac{m_1}{m_3}$	$\frac{\delta}{10^{-2}}$	group
N107 observation									
					8.00	19.0/5.3/2.5/12.6	7.6		
Ten best fitting simulations									
0.2	18	6	5.8	2.25	7.85	14.8/6.8/2.2/6.8	6.7	3.42	A*
0.2	16	6	4.2	2.25	7.90	14.0/6.8/2.5/6.8	5.6	3.44	A
2.7	12	28	15.5	1.00	8.40	16.3/7.4/2.4/7.4	6.8	3.65	B*
2.7	12	20	11.2	1.00	8.55	16.2/7.4/2.4/7.4	6.8	3.73	B
2.7	12	26	15.5	1.00	8.25	16.7/7.8/2.6/7.8	6.4	3.82	B
2.7	10	26	11.2	1.00	8.20	14.5/7.2/2.8/7.2	5.2	3.85	B
2.7	10	28	11.2	1.00	8.35	14.1/6.8/2.5/6.8	5.6	3.88	B
0.4	22	6	15.5	1.75	8.50	17.1/7.6/2.1/7.6	8.1	3.89	A
0.2	20	6	8.0	2.25	8.05	15.8/6.5/1.7/6.5	9.3	3.96	A
2.7	10	20	8.0	1.00	8.50	14.0/6.8/2.6/6.8	5.4	3.96	B

Notes. $m_{1,2,3,4}$ are the masses of the four angular sectors of the bubble (see Fig. 2.10); m_1/m_3 is the ratio of masses from the first and third sector, which quantify the mass contrast between the most and the least massive sector; δ is the goodness-of-fit parameter (lower is better). The simulations are divided into two groups A and B, as discussed in Sect. 2.1.4.3. Further explanation of the table columns is given in Sect. 2.1.4.3. The asterisk (*) marks two simulations – best of their group – which are visualised in Fig. 2.10.

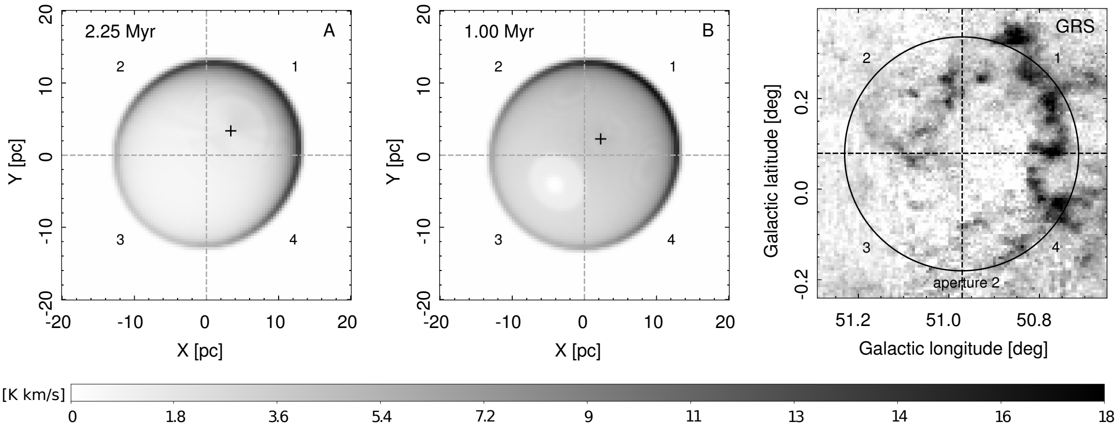

Figure 2.10: Snapshots from the best fitting simulations from group A (left) and B (centre), and the GRS observation of N107 (right). Shown is the brightness temperature of the ^{13}CO line integrated over the radial velocities of $\pm 8\,\mathrm{km\,s^{-1}}$ relative to the radial velocity of the bubble centre. The images also denote the four sectors used to compare the angular mass distribution (see Sect. 2.1.4.3 and Eq. 2.21). The plus sign (+) in pictures A and B marks the original expansion centre. Aperture 2, shown in the GRS picture, marks the region of the observed data we used for comparison with simulations.

Fits show little sensitivity to the parameter M_0, the initial mass of the surrounding molecular cloud ($M_0 \approx 5.8 \times 10^5\,M_\odot$ to $15.5 \times 10^5\,M_\odot$). Both groups of the best-fitting-simulations suggest that the bubble N107 is relatively young ($t \lessapprox 2.25\,\mathrm{Myr}$) and was formed at the very edge of its parental molecular cloud.

Figure 2.10 shows snapshots from the best fitting simulations from both groups A and B, and the GRS observation of the ^{13}CO line.

2.1.5 Discussion

2.1.5.1 Numerical simulation setup, assumptions, and validity of approximations

An important assumption for the simulation setup is the shape and density profile of the parental molecular cloud. In our simulations, we chose the Gaussian density profile and tested different levels of the oblateness (ratio of σ_z to σ_{xy}). The oblate shape of the parental molecular clouds that host bubbles similar to N107 is supported by a study of Beaumont & Williams (2010), who concluded that the *Spitzer* bubbles are formed in oblate, sheet-like, molecular clouds with a thickness of a few parsecs.[5] Our simulations, however, favour neither oblate nor prolate clouds.

---

[5] See also the discussion in Sect. 1.3.5 in this thesis.

The numerical code *ring* assumes the thin-shell approximation, which is applicable so long as the bubble expansion is supersonic, i.e. expanding with a velocity higher than the sound speed of the ambient cold gas: $\approx 0.3\,\mathrm{km\,s^{-1}}$ (for $T = 20\,\mathrm{K}$, $\gamma = 7/5$, $\mu = 2.34$). In our runs, almost all the bubble's elements move faster through the ambient gas during the whole bubble evolution, so the thin-shell approximation is reasonable. Moreover, if the speed of an element decreases below the sound speed, the code stops accumulating mass for that element.

2.1.5.2 Source of radio continuum

The radio continuum emission coming from the direction of the bubble interior has both thermal and nonthermal components. While the strong radio source A is dominated by nonthermal radiation, the fainter source B is emitting thermally (Fig. 2.6 and Table 2.1). The nonthermal source A is brighter than the thermal source B by almost one order of magnitude, so we can expect that the thermal emission is present in the whole bubble volume, only outshone in aperture A by the nonthermal source. The mixing of thermal and nonthermal radiation in aperture A is also suggested by the visual comparison of the radio continuum and the 24 µm emission (Fig. 2.7). The northern part of aperture A features both the radio continuum and the 24 µm emission, while in the southern part only the radio continuum is observed. Furthermore, the merging of thermal and nonthermal radiation in aperture A explains why the measured spectral index (−0.3) is closer to 0 than the typical value for supernova remnants (−0.5, the average value in the supernova remnants catalogue of Green, 2009).

The negative spectral indices of sources C (−0.2) and D (−0.1) suggest that part of their radio continuum is also emitted by a nonthermal source. The nonthermal contribution to the flux is stronger for source C than for source D. This is expected, since aperture D covers a distinct 24 µm (thermal) source, while there is almost no 24 µm emission in aperture C (Figs. 2.6 and 2.7).

Given that first supernovae in an OB association explode only after 3 Myr or later, and considering the bubble evolution time estimated from simulations (<2.25 Myr), no supernova remnant should be present inside the bubble yet. In other words, our analysis suggests that a supernova remnant not associated with the bubble may be present in the direction towards the bubble.

2.1.5.3 Missing OB association

We searched the SIMBAD database and a catalogue of Galactic OB stars by Reed (2003) for sources which could be responsible for the bubble creation. However, no OB star, supernova remnant, or pulsar is known to lie in the direction of the bubble interior or in its vicinity.

Table 2.5: Possible stellar progenitors of the bubble N107 found in the UKIDSS catalogue.

Label	Source ID (UKIDSS)	$\frac{l}{\text{deg}}$	$\frac{b}{\text{deg}}$	$\frac{\text{mass}}{M_\odot}$	$\frac{\text{distance}}{\text{kpc}}$
1	438326491324	51.1461745	+0.0272455	8.00	3.705
2	438326507390	51.0425744	−0.0083589	9.00	4.044
3	438326996219	50.9947238	+0.2626358	9.00	4.112
4	438328069418	50.9462654	−0.0326783	9.00	3.193
5	438328066620	50.8777609	+0.0509439	9.00	3.219
6	438328834208	50.8225691	+0.1274098	9.00	3.232

Notes. Column 1 gives the source label as marked in Fig. 2.11. Column 2 gives the ID from the UKIDSS catalogue. Column 3 and 4 give the Galactic longitude and latitude respectively. Column 5 gives the estimated mass of the source, and Column 6 gives its estimated distance.

We also searched for massive stars possibly related to N107 using the UKIDSS catalogue 7th data release (Lawrence et al., 2007), stellar evolutionary tracks by Bressan et al. (2012), and the standard model of extinction (Rieke & Lebofsky, 1985). We derived the extinction for the massive star candidates in the field of N107 and compared it to the values of extinction given for that direction by Stead & Hoare (2009). The search for massive stars involves many uncertainties, but the comparison of the derived extinctions with independent values is a good test of the credibility of our results. We ended up with six massive star candidates, which lie at distances comparable with the distance of N107 (3.6 kpc). None of these six stars has a measured radial velocity. Three of them lie at the rim of the bubble, so they can hardly be its progenitors, but the others are possible energy sources. The selected massive stars are shown in Fig. 2.11 and are listed in Table 2.5.

2.1.5.4 Molecular clump mass spectrum

The best fitting slope for the mass spectrum of molecular clumps found along the borders of N107 is −1.1 (Fig. 2.8). This is a significantly shallower slope than that of the classical stellar initial mass function (−2.35, Salpeter, 1955) and also shallower than the clump mass function slope from −1.6 to −1.8 derived by Kramer et al. (1998). We note that Kramer et al. (1998) used Gaussian decomposition for clump identification, which is a fundamentally different method than we used;[6] and, moreover, studied different types of clouds, not shell-like as is the case of N107.

The least massive clumps we found have masses of about 3.5 $M_\odot$. This limit is given by the angular resolution and sensitivity of the observations of the ^{13}CO line. With better resolution and sensitivity, we expect that some clumps, especially the

---

[6] See Sect. 3.9 in this thesis for a comparison of several clump-finding algorithms.

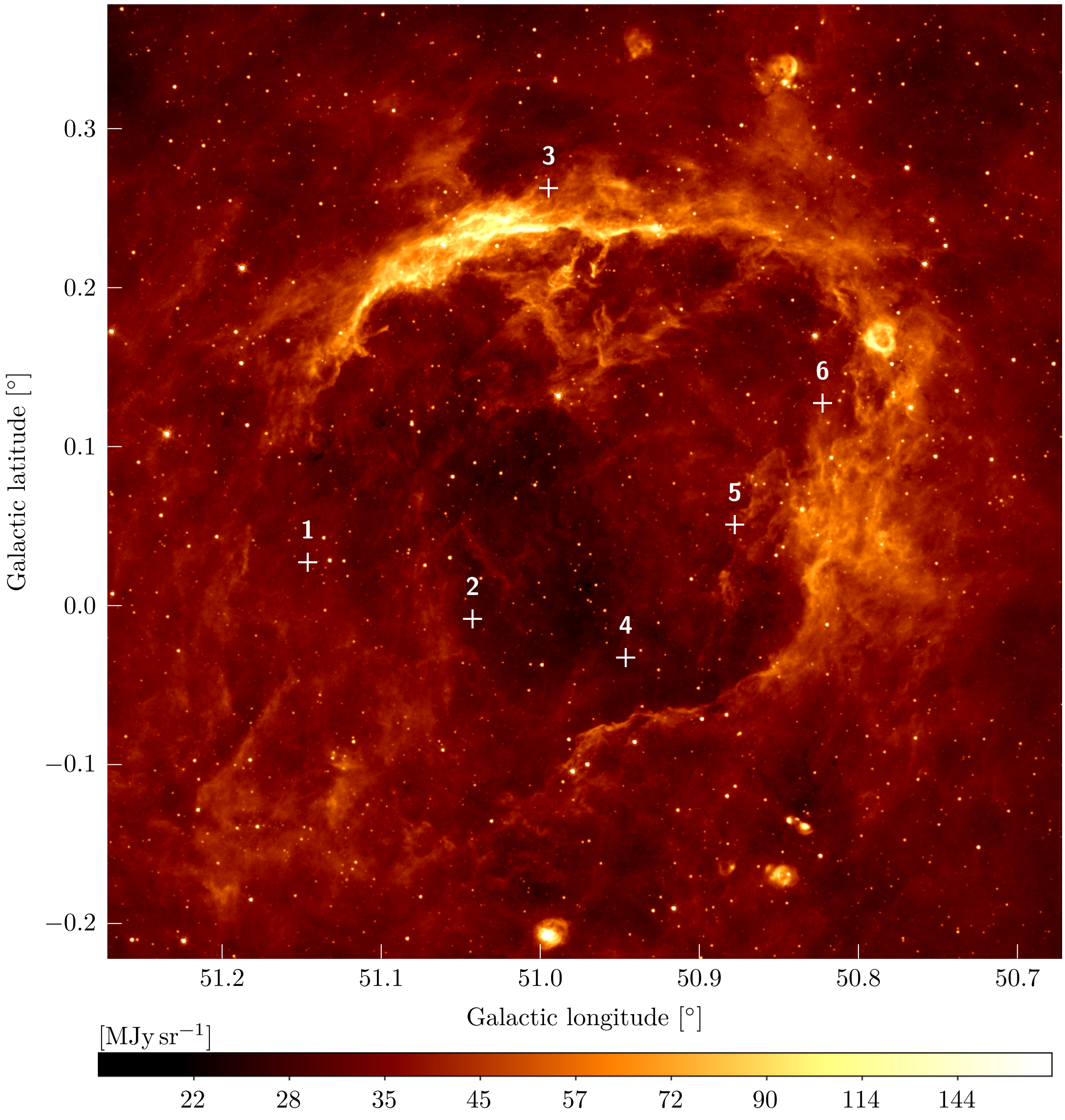

Figure 2.11: Possible stellar progenitors (white cross signs) of the bubble N107 found in the UKIDSS catalogue. The numerical labels of the stars correspond to the labels in Table 2.5. The background is the 8 μm emission taken from GLIMPSE.

most massive ones, would be identified as several less massive clumps. This would alter the shape of the clump mass spectrum, and very likely redistribute the mass of the largest clumps into less massive ones, so that the slope would be steeper.

2.1.6 Conclusion

We studied the dust bubble N107, discovered by Churchwell et al. (2006) in infrared dust emission observed with the *Spitzer* Space Telescope. Radio observations of the H I and ^{13}CO ($J = 1{-}0$) lines revealed its atomic and molecular components, which allowed us to determine the bubble's radial velocity, kinematical distance, and the mass of these components. Using the code DENDROFIND (Wünsch et al., 2012) we decomposed the molecular ring associated with the bubble into 49 individual clumps and found that the clump mass spectrum slope is about -1.1. Radio continuum observations at 1420 MHz and 327 MHz suggest the radio flux coming from the bubble direction has both thermal and nonthermal components; i.e. besides a classical H II region, a supernova remnant contributes to the emission. We simulated the evolution of stellar-blown bubbles within molecular clouds with the numerical code *ring* (Palouš, 1990; Ehlerová & Palouš, 1996). We were able to produce two groups of bubbles with a similar angular mass distribution and expansion velocity to N107: **(A)** bubbles formed within an oblate molecular cloud ($\sigma_z/\sigma_{xy} = 6/12$), with an energy input $\dot{E} < 0.4 \times 10^{50}\,\mathrm{erg\,Myr^{-1}}$, and an evolution time $t \approx 1.75$ Myr to 2.25 Myr; and **(B)** bubbles formed within a prolate molecular cloud ($\sigma_z/\sigma_{xy} = (20$ to $28)/12$), with an energy input $\dot{E} \approx 2.7 \times 10^{50}\,\mathrm{erg\,Myr^{-1}}$, and an evolution time $t = 1$ Myr. Considering the estimated bubble evolution time (<2.25 Myr), no supernova remnant should be present inside the bubble, yet. This may be explained by a supernova remnant present in the direction towards the bubble, but not associated with it.

A summary of the parameters we derived for the bubble N107, together with the parameters given by Churchwell et al. (2006), is presented in Table 2.6.

Acknowledgements

We thank the anonymous referee for multiple constructive suggestions which led to improvements of the paper. This work was supported by the project RVO: 67985815. VS acknowledges support from a Marie Curie fellowship as part of the European Commission FP6 Research Training Network 'Constellation' under contract MCRTN–CT–2006-035890; support from Doctoral grant of the Czech Science Foundation No. 205/09/H033. RW acknowledges support from the project P209/12/1795 of the Czech Science Foundation. The research leading to these results has received funding from the European Community's Seventh Framework Programme under

Table 2.6: Summary of parameters derived for N107.

Property	Value
From catalogue of Churchwell et al. (2006)	
Galactic longitude (central)	$50\overset{\circ}{.}972$
Galactic latitude (central)	$0\overset{\circ}{.}078$
Angular radius (mean)	$11\overset{\prime}{.}39$
Angular thickness (mean)	$2\overset{\prime}{.}26$
Derived from observations	
Radial velocity (central)	$43\,\mathrm{km\,s^{-1}}$
Expansion velocity	$8\,\mathrm{km\,s^{-1}}$
Distance (kinematical)	$3.6\,\mathrm{kpc}$
Radius (mean)	$11.9\,\mathrm{pc}$
Mass in H I (aperture 1)	$(5.4 \pm 1.0) \times 10^3\,M_\odot$
Mass of molecular component (aperture 1)	$(1.3 \pm 0.4) \times 10^5\,M_\odot$
Mass of molecular component (aperture 2)(1)	$(4.0 \pm 1.2) \times 10^4\,M_\odot$
Estimated from simulations	
Energy input rate	$<0.4 \times 10^{50}\,\mathrm{erg\,Myr^{-1}}$(A)
	$\approx 2.7 \times 10^{50}\,\mathrm{erg\,Myr^{-1}}$(B)
Dislocation of expansion centre	$\approx(16$ to $22)\,\mathrm{pc}$(A)
	$\approx(10$ to $12)\,\mathrm{pc}$(B)
Parental cloud thickness in our line of sight	$\approx 6\,\mathrm{pc}$(A)
	$\approx(20$ to $28)\,\mathrm{pc}$(B)
Parental cloud total mass	$\approx(5.8$ to $15.5) \times 10^5\,M_\odot$
Evolution time (age)	$\approx(1.75$ to $2.25)\,\mathrm{Myr}$(A)
	$\approx 1\,\mathrm{Myr}$(B)

Notes. The first section gives the values from the original catalogue of Churchwell et al. (2006). The second section gives the values derived from observation (Sect. 2.1.2). The third section gives the values estimated from simulations (Sect. 2.1.4). (1) Aperture 2 covers only the immediate vicinity of the bubble. See Fig. 2.4 for an illustration. (A) Estimated from simulations from group A. (B) Estimated from simulations from group B.

grant agreement no. PIIF-GA-2008-221289. This research has made use of SAOImage DS9, developed by Smithsonian Astrophysical Observatory (Joye & Mandel, 2003). This research has made use of the SIMBAD database, operated at CDS, Strasbourg, France. This research has made use of NASA's Astrophysics Data System. This research has made use of the NASA/IPAC Infrared Science Archive, which is operated by the Jet Propulsion Laboratory, California Institute of Technology, under contract with the National Aeronautics and Space Administration. This publication has made use of molecular line data from the Boston University-FCRAO Galactic Ring Survey (GRS). The GRS is a joint project of Boston University and Five College Radio Astronomy Observatory, funded by the National Science Foundation under grants AST-9800334, AST-0098562, & AST-0100793.

2.2 Additional material

This section contains additional material that was not published in the paper Sidorin et al. (2014) reprinted in Sect. 2.1.

2.2.1 Notes on the numerical simulations done with the code *ring*

About the code

The code *ring* (Palouš, 1990; Ehlerová & Palouš, 1996) is a Lagrangian 2.5D code written specifically for simulations of expanding shells driven by energy input into their interiors. In the code, a shell is represented by an infinitesimally thin layer (thin-shell approximation) divided into a set of two-dimensional elements. These elements move in a three-dimensional space, hence the title "2.5D code". The shell expansion is driven by the pressure difference between its interior and exterior. As the shell expands, it collects the ambient medium and the mass of its elements grows. The code gives reasonable results only if the expansion is supersonic with respect to the ambient medium. Only then the medium accumulates in a thin shell. When the expansion velocity drops below the sound speed, the thin-shell approximation is not valid any more, and the results given by the code must be interpreted with caution. It can, however, happen that during a simulation only a few shell elements decelerate to a subsonic velocity. The code will then continue to run but will stop accumulating medium into those elements.

The simplicity of the code does not allow its use for general hydrodynamic problems. On the other hand, for simulations of expanding shells, *ring* is much faster than general adaptive mesh refinement (AMR) and smoothed-particle hydrodynamics (SPH) codes. We used *ring* to simulate the evolution of stellar-blown bubbles to estimate the conditions under which the bubble N107 formed. The speed of the code allowed us to explore tens of thousands of combinations of values of the input parameters.

Why did we choose a Gaussian density profile?

We tested several types of the density profile of the parental molecular cloud where our simulated bubbles evolved; namely:

- homogeneous profile,
- sheet-like profile with Gaussian stratification,
- critical Bonnor-Ebert sphere, and
- three-dimensional Gaussian profile.

We were able to produce bubbles similar to N107 with the Bonnor-Ebert and three-dimensional Gaussian profiles. In both cases the resulting bubbles had very similar properties (expansion velocity, total mass, shape), assuming the other input parameters were the same. The differences in the properties at evolution times relevant to N107 (<100 Myr) were insignificant – much smaller than the differences of the properties between individual time steps. Thus, we had no indication that either density profile is better. We therefore opted for the simpler Gaussian profile, which can be described by an explicit formula, in contrast to the Bonnor-Ebert sphere. It is also computationally cheaper to derive the density at a given point in space for an analytical profile.

2.2.2 Gallery of molecular clumps

In Sect. 2.1.3, we identified 49 molecular clumps associated with the bubble N107 (Table 2.2). Below are shown images of those clumps. The images were extracted from the ^{13}CO ($J = 1{-}0$) GRS datacube. Each image represents the sum of the flux from all the pixels belonging to a given clump, projected onto the sky plane. The colour scaling is linear, normalised (stretched) for each clump individually to the minimum and maximum of its projected flux. The first number below each image corresponds to the serial number of the clump in our list (Table 2.2); the second number in parenthesis is the estimated clump mass. The clumps are given in the same order as in Table 2.2, i.e. in descending order of $T_{\rm peak}$.

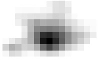
1 (1037.1 $M_\odot$)

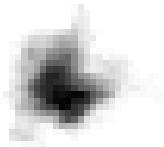
2 (4082.1 $M_\odot$)

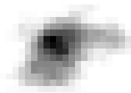
3 (3119.8 $M_\odot$)


4 (351.1 $M_\odot$)

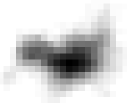
5 (3469.1 $M_\odot$)


6 (635.2 $M_\odot$)

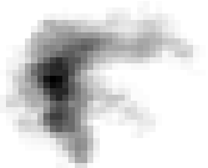
7 (7365.5 $M_\odot$)


8 (1206.7 $M_\odot$)

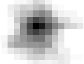
9 (1059.1 $M_\odot$)


10 (276.5 $M_\odot$)


11 (169.3 $M_\odot$)


12 (149.6 $M_\odot$)


13 (45.3 $M_\odot$)


14 (60.9 $M_\odot$)


15 (26.3 $M_\odot$)


16 (8.4 $M_\odot$)

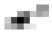
17 (48.5 $M_\odot$)


18 (11.7 $M_\odot$)


19 (15.6 $M_\odot$)


20 (26.3 $M_\odot$)


21 (5.0 $M_\odot$)


22 (5.8 $M_\odot$)


23 (4.0 $M_\odot$)


24 (22.7 $M_\odot$)


25 (6.2 $M_\odot$)


26 (17.8 $M_\odot$)


27 (8.7 $M_\odot$)


28 (4.4 $M_\odot$)


29 (4.6 $M_\odot$)


30 (3.8 $M_\odot$)

31 (5.5 $M_\odot$)

32 (4.0 $M_\odot$)

33 (9.6 $M_\odot$)

34 (4.2 $M_\odot$)

35 (3.8 $M_\odot$)

36 (3.8 $M_\odot$)

37 (8.0 $M_\odot$)

38 (3.8 $M_\odot$)

39 (5.6 $M_\odot$)

40 (3.5 $M_\odot$)

41 (4.4 $M_\odot$)

42 (4.6 $M_\odot$)

43 (3.6 $M_\odot$)

44 (3.7 $M_\odot$)

45 (7.8 $M_\odot$)

46 (5.7 $M_\odot$)

47 (5.6 $M_\odot$)

48 (3.5 $M_\odot$)

49 (3.4 $M_\odot$)

2.2.3 Coloured maps of molecular clumps

Below are shown coloured maps of the molecular clumps associated with the bubble N107 (see Table 2.2 for the list of the clumps). Each slice shows the observed emission in the ^{13}CO ($J = 1{-}0$) line on the left, and a corresponding coloured map of the clumps on the right. The slices cover all radial velocity channels that contain at least one pixel assigned to a clump; i.e. radial velocities from 38.5 km s^{-1} to 48.5 km s^{-1}. The radial velocities are indicated in the slices. I note that only the clumps associated with N107 (as given in Table 2.2) are marked in the maps.

The scaling for the observed ^{13}CO emission is shown in the calibrated greyscale bar. A colour bar matching colours to corresponding clump numbers is also given.

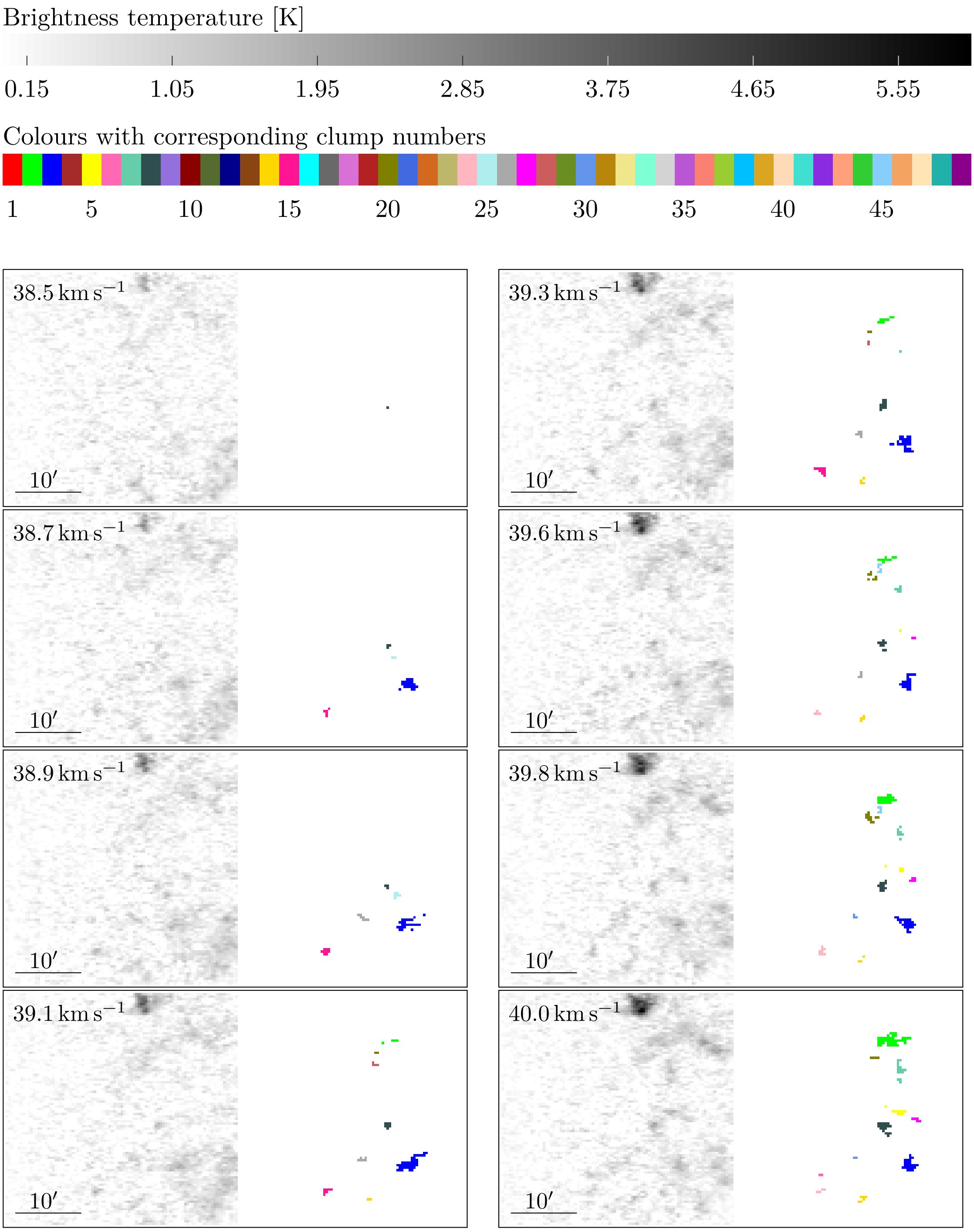
Brightness temperature [K]
0.15
1.05
1.95
2.85
3.75
4.65
5.55
Colours with corresponding clump numbers
1
5
10
15
20
25
30
35
40
45
38.5 km s^{-1}
10′
39.3 km s^{-1}
10′
38.7 km s^{-1}
10′
39.6 km s^{-1}
10′
38.9 km s^{-1}
10′
39.8 km s^{-1}
10′
39.1 km s^{-1}
10′
40.0 km s^{-1}
10′

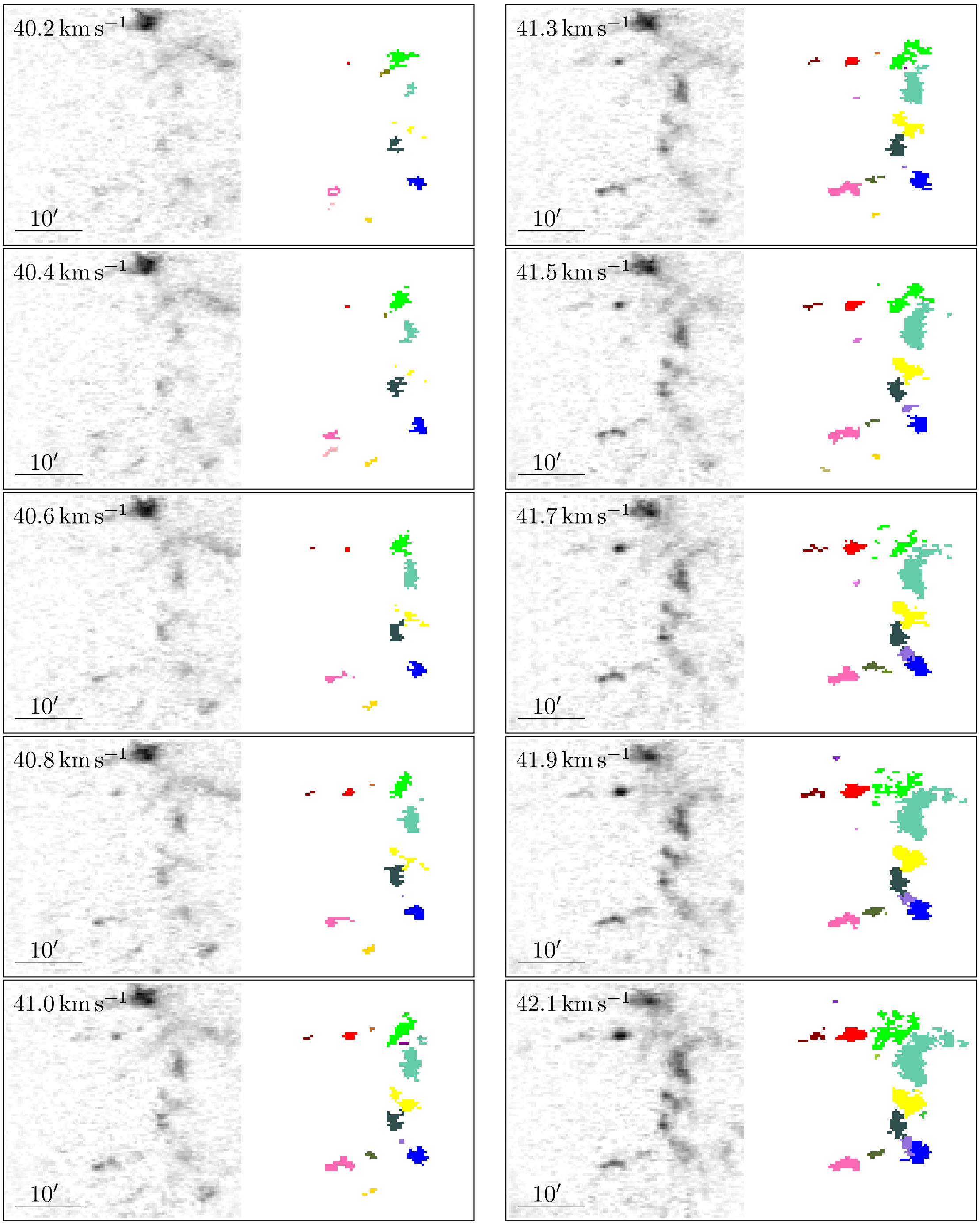
40.2 km s^{-1}
10′
41.3 km s^{-1}
10′
40.4 km s^{-1}
10′
41.5 km s^{-1}
10′
40.6 km s^{-1}
10′
41.7 km s^{-1}
10′
40.8 km s^{-1}
10′
41.9 km s^{-1}
10′
41.0 km s^{-1}
10′
42.1 km s^{-1}
10′

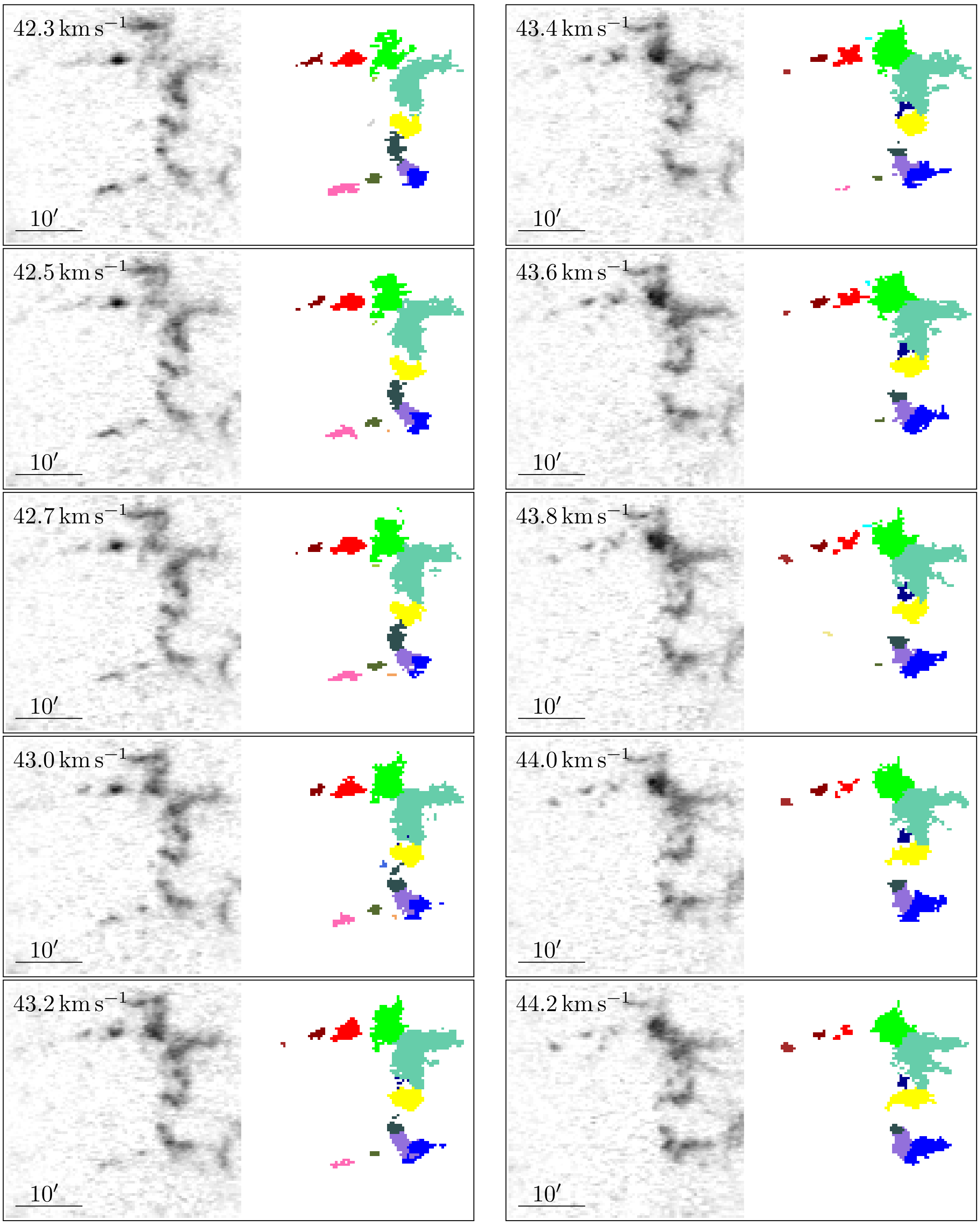
42.3 km s^{-1}
10′
43.4 km s^{-1}
10′
42.5 km s^{-1}
10′
43.6 km s^{-1}
10′
42.7 km s^{-1}
10′
43.8 km s^{-1}
10′
43.0 km s^{-1}
10′
44.0 km s^{-1}
10′
43.2 km s^{-1}
10′
44.2 km s^{-1}
10′

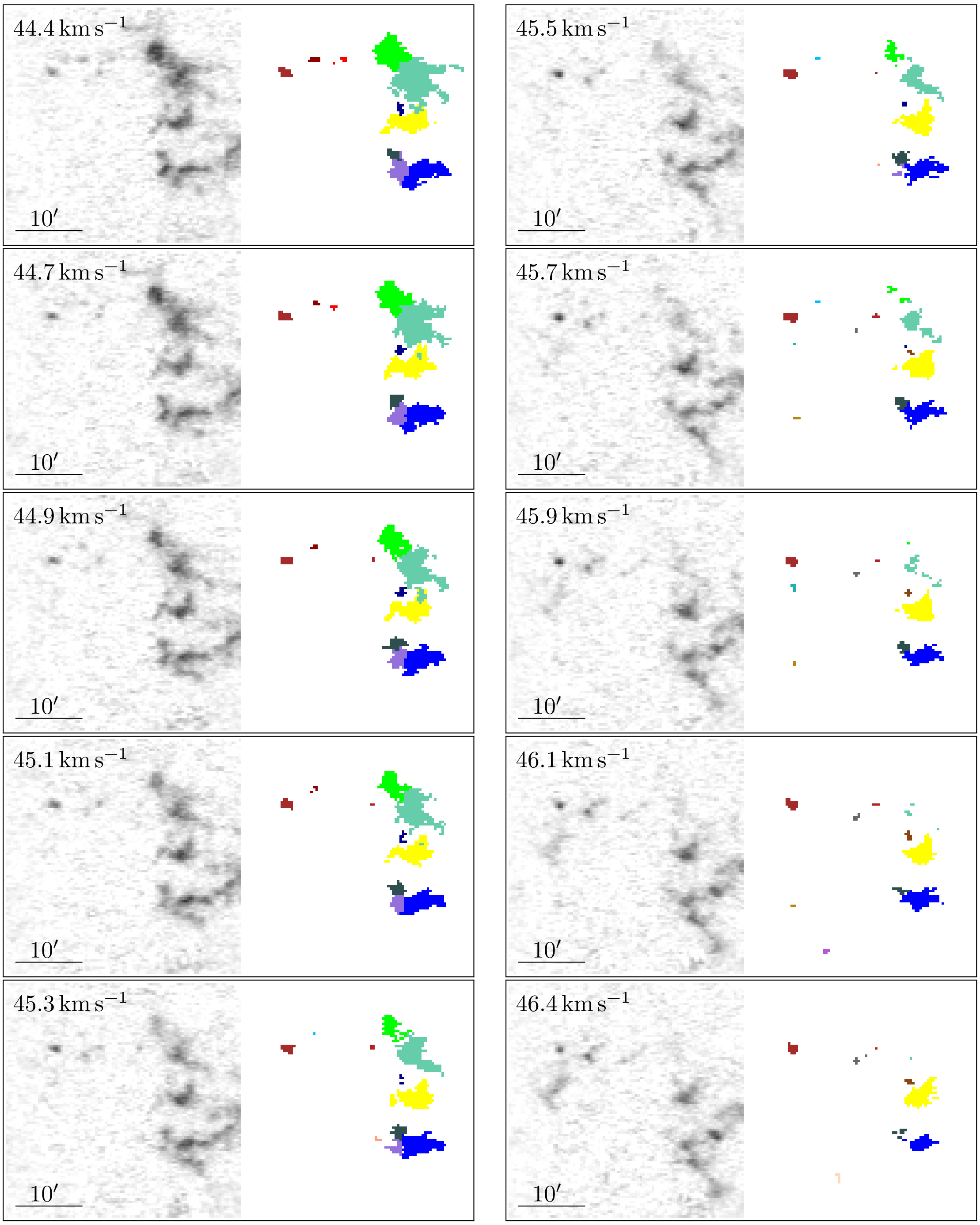
44.4 km s^{-1}
10′
45.5 km s^{-1}
10′
44.7 km s^{-1}
10′
45.7 km s^{-1}
10′
44.9 km s^{-1}
10′
45.9 km s^{-1}
10′
45.1 km s^{-1}
10′
46.1 km s^{-1}
10′
45.3 km s^{-1}
10′
46.4 km s^{-1}
10′

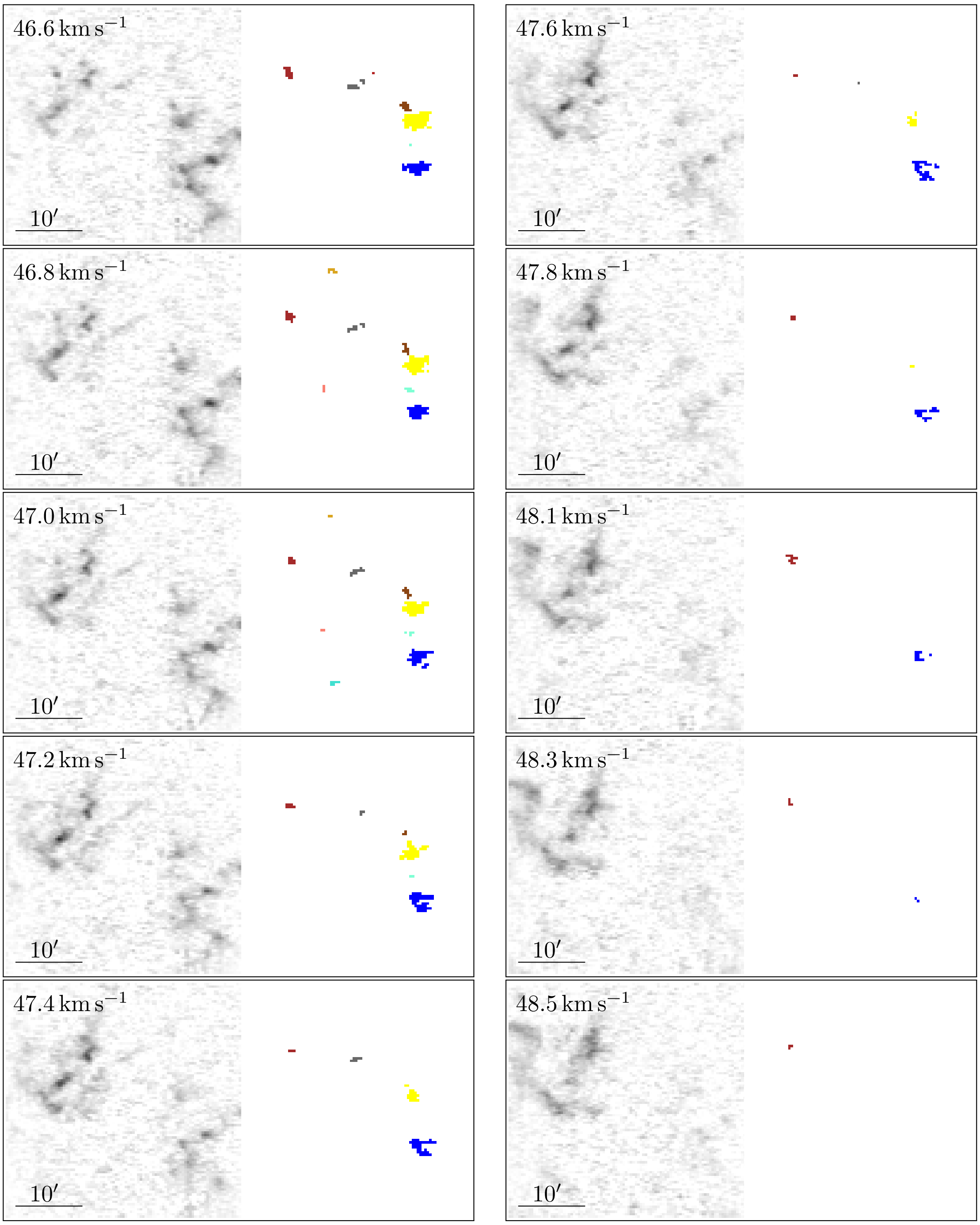
$46.6\,\mathrm{km\,s^{-1}}$
10′
$46.8\,\mathrm{km\,s^{-1}}$
10′
$47.0\,\mathrm{km\,s^{-1}}$
10′
$47.2\,\mathrm{km\,s^{-1}}$
10′
$47.4\,\mathrm{km\,s^{-1}}$
10′
$47.6\,\mathrm{km\,s^{-1}}$
10′
$47.8\,\mathrm{km\,s^{-1}}$
10′
$48.1\,\mathrm{km\,s^{-1}}$
10′
$48.3\,\mathrm{km\,s^{-1}}$
10′
$48.5\,\mathrm{km\,s^{-1}}$
10′

2.2.4 Improved analysis of the clump mass spectrum

In Sect. 2.1.3, we analysed the mass spectrum of clumps associated with the bubble N107. We used a standard histogram for that analysis (Fig. 2.8). It shows the number density of clumps per unit mass interval, i.e. $\mathrm{d}N/\mathrm{d}M$. We fitted it with a power-law function CM^{α} and found the best-fitting slope $\alpha = -1.1$. However, a quick visual inspection clearly shows that the fit is far from satisfactory. We noted that with better resolution and sensitivity of the ^{13}CO observations, we could expect a different shape (and slope) of the clump mass spectrum (Sect. 2.1.5.4). In this section, I present an improved analysis of the clump mass spectrum using a reversed cumulative histogram without data binning – more precisely, each bin contains only one clump. I estimate the slope of the clump mass function α for all clumps and also for the low-, medium-, and high-mass subsets separately.

A reversed cumulative histogram (when treated as a continuous function), giving the total number of clumps with a mass greater than M, can be defined as

$$N(\mathrm{mass} > M) = N(M) = \int\limits_{M}^{M_{\mathrm{max}}} \frac{\mathrm{d}N}{\mathrm{d}M}(M')\mathrm{d}M', \tag{2.23}$$

where M_{max} is the maximum clump mass in the sample, and $\mathrm{d}N/\mathrm{d}M(M')$ gives the number density of clumps with the mass M'. $\mathrm{d}N/\mathrm{d}M$ corresponds to the profile of the standard histogram we used in Fig. 2.8. Assuming that $\mathrm{d}N/\mathrm{d}M$ has the form of a power-law CM^{α}, and substituting this power-law into Eq. 2.23, we get

$$N(M) = A + BM^{\alpha+1}, \tag{2.24}$$

where A and B are constants, and α is the power-law index describing the slope of the clump mass spectrum.

We can estimate the slope α by fitting the functions from Eq. 2.24 to the cumulative histogram of the observed clump masses. The advantage of this approach, in contrast to using a standard histogram, is we do not need to bin data and can therefore fit them using every point (clump) on its own. This eliminates the effects of data binning on the resulting value of α.

The cumulative histogram of the masses of clumps associated with N107, fitted by the functions from Eq. 2.24, is shown in Fig. 2.12. The masses of clumps are taken from Table 2.2. The same as we did in Sect. 2.1.3, I used least-square fitting on a logarithmic scale; i.e. I fitted $\log N(M)$ by $\log(A + BM^{\alpha+1})$.

The best fitting function using all the clumps has the slope $\alpha = -1.3$, which is slightly steeper than the slope of -1.1 estimated from the standard histogram (Fig. 2.8). The subset of the 15 lowest-mass clumps can be fitted by a function with a slope of -4.1, while the subset of the 15 highest-mass clumps can be fitted by a function with a slope of -1.0. The middle part with 19 medium-mass clumps can

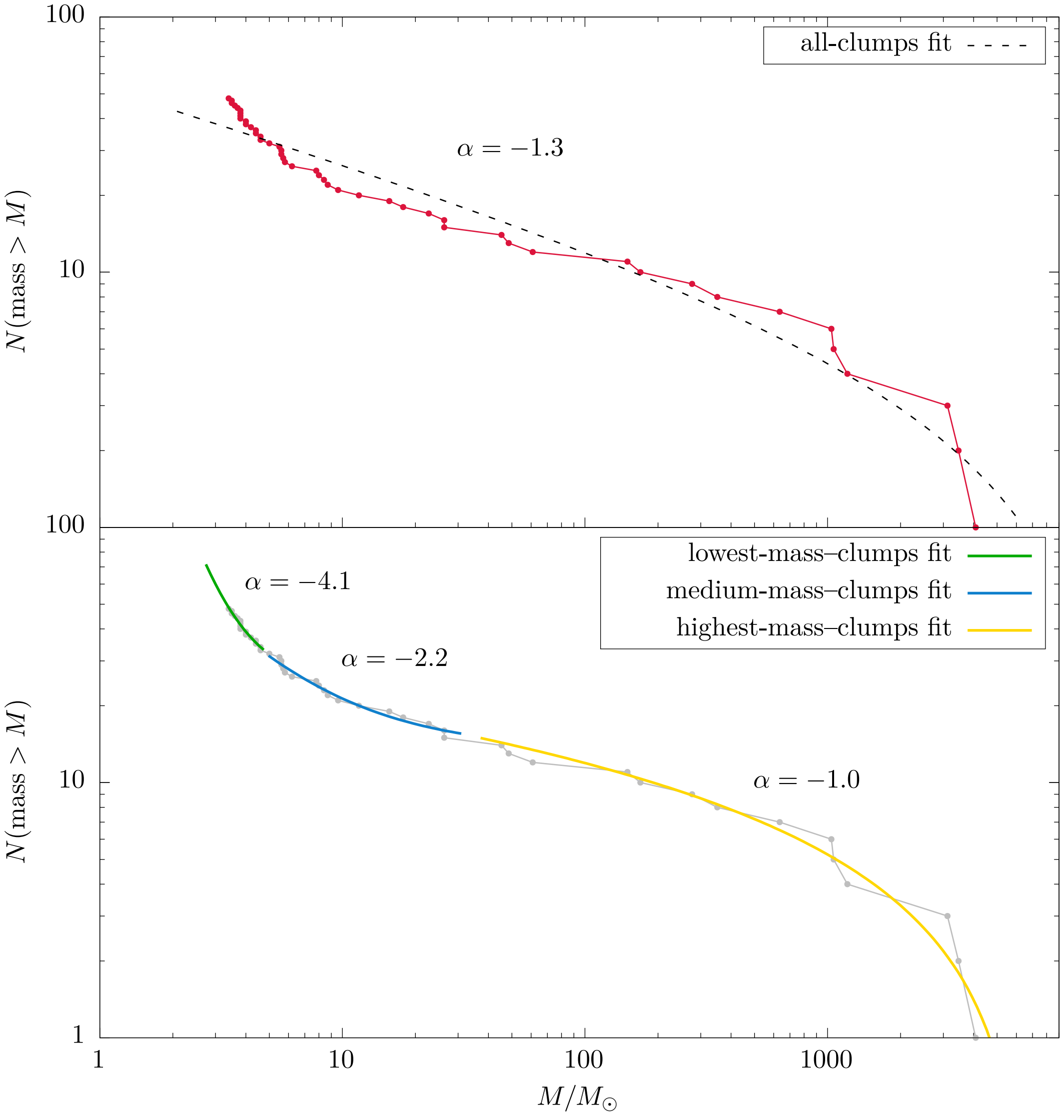

Figure 2.12: Distribution of the masses of molecular clumps associated with N107, shown here in a reversed cumulative histogram. The histogram is plotted as a piecewise linear curve with points, where each point corresponds to a change in the profile by one clump. The vertical axis gives the total number of clumps with a mass greater then M. The histogram is fitted by functions of the type $N(M) = A + BM^{\alpha+1}$ (see text for explanation). *Top:* Histogram (red) fitted by a single function with the power-law index $\alpha = -1.3$ (black dashed line). *Bottom:* Histogram (grey) fitted in three regions independently: 15 lowest-mass clumps ($\alpha = -4.1$), 19 medium-mass clumps ($\alpha = -2.2$), and 15 highest-mass clumps ($\alpha = -1.01$).

be fitted by a function with a slope of −2.2. This is interestingly close to the slope of Salpeter's classical initial mass function of −2.35 (Salpeter, 1955).

We can expect the low- and high-mass ends of the observed clump mass spectrum to be distorted most. Therefore, the slope of −2.2 derived from the middle part of the histogram (medium-mass clumps) should be considered the most reliable estimate.

2.2.5 Internal velocity variation versus clump size

The observation of Larson (1981) that the internal velocity dispersions of molecular clouds are well correlated with the sizes of the clumps was one of the convincing indicators suggesting that turbulence plays an important role in the dynamics of the ISM (see Sect. 1.2.9). Larson (1981) found that the internal velocity dispersion scales with the region size as a power-law with an index of 0.38. This is close to the value of 1/3 derived from Kolmogorov's "2/3" law (Eq. 1.27).

Here I investigate the correlation between the internal velocity variations and sizes of the clumps associated with the bubble N107. The data are taken from Table 2.2. In the scatter plot in Fig. 2.13, I compare $FWHM_{\mathrm{v}}$ and the radius R of those clumps (see Sect. 2.1.3 for the definitions of the quantities). The scatter plot can be fitted by a power-law function with the index $\alpha = 1.2$. This is a markedly steeper slope than that of 0.38 derived by Larson (1981), or 1/3 predicted by the Kolmogorov theory of turbulence. One reason behind this discrepancy could be that Larson (1981) included thermal speeds in the total internal velocity dispersions. Adding a constant value to the velocity dispersions would make the slope shallower. Another reason could be the difference in the type of objects used for the analysis. I study only molecular clumps (found by an automated algorithm) with masses up to 7000 $M_{\odot}$, while Larson (1981) included also much larger objects with masses up to $3 \times 10^5\,M_{\odot}$. And finally, I take the surface-equivalent radius R of the clumps as their "size", while Larson (1981) considered their maximum linear dimension. The radius R, as defined in Sect. 2.1.3, will always be less than or equal to the maximum linear dimension. However, in most cases it will be notably smaller. Using R as the region "size" can thus make the slope steeper.

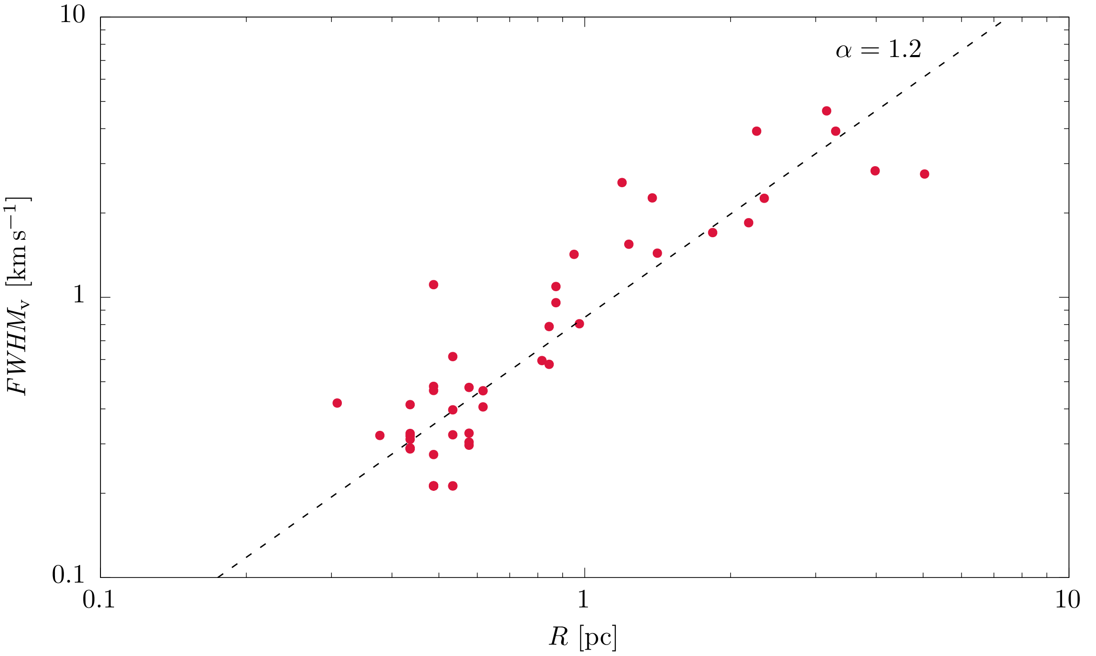

Figure 2.13: Relation of the internal velocity differences $FWHM_\mathrm{v}$ and radii R of the molecular clumps associated with the bubble N107. The scatter plot is fitted by a power-law function with the index $\alpha = 1.2$.

Chapter 3

Quickclump

This chapter describes the computer program Quickclump **version 1.3**. It is an automated clump-finding tool that I wrote during my PhD study. The chapter has the form of software documentation and is targeted at users as well as developers.

Note about terminology. Quickclump works with three-dimensional data. Although the proper term for an element in a three-dimensional grid is *voxel*, I use the term *pixel* in this text.

3.1 What is Quickclump?

Quickclump is a fast and accurate Python program that identifies clumps in three-dimensional Flexible Image Transport System (FITS) datacubes. It is primarily intended for decomposing interstellar clouds into individual clumps. Quickclump was inspired by another clump-finding code called DENDROFIND, first conceived by Richard Wünsch and described in the appendix of Wünsch et al. (2012).

3.2 Quick start guide

To find clumps in your datacube `my_datacube.fits`, type

```
python qc.py my_datacube.fits
```

This will find clumps within the datacube using the default settings. A list of the clumps will be saved into the text file `my_datacube.clumps.txt`, and a map of the clumps (clump mask) will be saved into the FITS file `my_datacube.clumps.fits`.

3.3 What is a clump?

A clump, in the context of the interstellar medium (ISM), is the intermediate structure in the hierarchy of cloud–clump–core (Bergin & Tafalla, 2007). The density structure of a molecular cloud could be imagined as a hilly island in the sea, where the altitude of the terrain corresponds to the density in the cloud. Individual hills then correspond to clumps, and the hill peaks correspond to cores (the densest places in molecular clouds). Some hills are small and low, others are high and huge. Some hills stand solitary on the ground, while others merge into complexes where they touch each other and are separated by valleys with different depths. Such patterns, translated from altitude to density, can be found in molecular clouds. Indeed, the internal structure of molecular clouds appears hierarchical, with lots of clumps and filaments (e.g. Larson, 1981; Ferrière, 2001; Bergin & Tafalla, 2007). For an overview of the observed properties of molecular clouds, clumps, and cores, see Table 1.4.

The human brain and eyes are naturally capable of analysing structures and can see individual clumps in clouds without much effort. We need, however, a basic definition of what clump is to develop software that would be able to "see" clumps similarly as humans can see them. All the clump-finding algorithms I describe in this chapter, including Quickclump, use the same basic definition of clump that could be expressed as:

> *A clump consists of a local density peak (core) surrounded by an envelope of less dense material.*

The definition given above, yet simple, seems to be a good starting point for developing an effective clump-finding algorithm. Further details have to be specified, of course; e.g. how the envelope should be found, or how to deal with touching clumps. It is those details where individual algorithms differ. GaussClumps, for example, identifies the envelopes by fitting the source data with a multi-dimensional Gaussian profile, thus assuming clumps have Gaussian shapes. On the other hand, Clumpfind draws contours around peaks and does not assume anything about the clump profile. Quickclump also does not assume anything about the clump profile; it starts at a peak and expands the clump pixel by pixel until the background level is reached, or until another clump is touched.

3.4 How Quickclump came to live

During our analysis of radio observations of molecular clouds in the Carina Flare supershell (later published as Wünsch et al., 2012), we needed a code that would reliably identify individual molecular clumps. We experimented with Clumpfind, but soon realised it has certain limitations. Primarily that it cannot utilise the differences in data values of pixels that fall into the same interval between two contour levels. Richard Wünsch then came with the idea of DENDROFIND, where individual clumps would be regarded as leaves in a dendrogram. The dendrogram would also represent the hierarchical structure of clumps in a cloud. The criterion deciding whether two touching clumps will be merged would be given by the length of their leaves, i.e. the difference between their peak data value and the data value in the valley separating them.

Richard Wünsch wrote the first implementation of DENDROFIND in Python, later rewrote it in C. DENDROFIND proved to be more accurate in finding clumps than Clumpfind and provided the information about the hierarchical structure of clumps. We then used DENDROFIND to analyse the molecular component of the Carina Flare supershell (Wünsch et al., 2012), and later to analyse the molecular component of the bubble N107 (Sidorin et al., 2014; Chap. 2 in this thesis).

DENDROFIND was developed with the aim of having an accurate clump-finding code for relatively small datacubes, like that with the observation of the Carina Flare supershell. Accuracy was preferred over speed. DENDROFIND was, however, unsuitable for analysing bigger datacubes with more than a few hundred clumps. Even the implementation in C, which is more than ten times faster than the implementation in Python, ran for several days with datacubes of the order of 100^3 pixels. During my analysis of the molecular component of the bubble N107, I realised that a possibly-faster algorithm could be developed to produce results as accurate as those of DENDROFIND's. The main idea of the algorithm would be to sort pixels by their data values and then process them one by one, starting with the pixel with the highest data value. Such an algorithm would be even more accurate then DENDROFIND, in fact as accurate as DENDROFIND run with the number of steps `Nlevels` set to infinity. Moreover, the need of the purely-technical parameter `Nlevels` would be naturally eliminated. I then tried to implement the algorithm from scratch. The result is Quickclump.

3.5 Description of the Quickclump algorithm

Quickclump assumes that the input data is a three-dimensional rectangular array. It further assumes the definition of clump as expressed in Sect. 3.3. Each clump starts as a single pixel representing the clump's core. Such pixel appears in the input array as a local peak. The clump is then progressively expanded to neighbouring pixels representing the core's envelope. The core together with its envelope comprise the clump.

From the technical point of view, the main idea of the Quickclump algorithm is to sort the pixels in the input array by their data values and then process them one by one, starting with the pixel with the highest data value. The complete algorithm can be described in the following steps:

1. Load the input datacube and add a boundary (padding) to it so that each pixel has a well-defined neighbourhood.

   The current code implementation uses a neighbourhood of plus-minus one pixel in every direction along the main coordinate axes. The neighbourhood is represented in the code as a constant, so can be easily redefined if needed.

   The boundary pixels are filled with the lowest possible value, e.g. `-inf` for Python's `float`. This ensures that when the array with input data will be sorted by value, the boundary pixels will come last.

2. Initialise an integer array for the pixel mask (map of clumps).

   The array is of the same size as the input datacube. The numbers in the array will tell to which clump a given pixel belongs. This array can be imagined as a blank canvas ready for drawing a map of clumps.

3. Sort the references to pixels in the input datacube by the pixels' data value.

   It is the array keys that is sorted here, not the input datacube itself. The pixels must stay at their places. The sorted references to pixels are stored in a separate array.

   This sorting will allow the main loop to process the pixels in the order determined by their data values.

4. **Main loop:** Process pixels in the input datacube, one at a time, in the order given by the array of sorted keys from Step 3.

   The main loop starts at the pixel with the highest data value, then moves to the pixel with the second highest data value, etc., down to a limit given by the parameter `Tcutoff`. When the value of `Tcutoff` is reached, the loop terminates. For the algorithm to work correctly, `Tcutoff` must be greater than the data value assigned to the boundary pixels (Step 1). In the implementation described here, `Tcutoff` is required to be greater than zero.

   In each iteration of the main loop, Quickclump scans the current pixel's neighbourhood. It looks into the pixel mask array (Step 2) and retrieves all clumps whose pixels are found in the neighbourhood. Here, the effort we put into the addition of the boundary to the datacube pays off. We can be sure that the current pixel has a well-defined neighbourhood, so we do not need special logic to handle pixels at borders.

There are three possible scenarios what to do next, based on the number of neighbours of the current pixel. The current pixel can have (1) no neighbouring clump; (2) only one neighbouring clump; or (3) more neighbouring clumps.

(1) If the pixel has no neighbouring clump, it must be a local peak, so a new clump is created. Remember that pixels are processed in the descending order given by their data values. Therefore if the current pixel had another pixel with a higher data value in its neighbourhood, than that neighbouring pixel would have to be already processed and assigned to a clump earlier. The new clump's label (integer) is recorded to the mask array, to the location corresponding to the current pixel.

(2) If the current pixel has only one neighbouring clump, it is added to that clump and the mask array is updated accordingly.

(3) A more complex situation is when the current pixel has more neighbouring clumps. This in fact means that more clumps are claiming the pixel, or in other words the pixel represents a point where those clumps touch. First, the nearest clump with a high-enough peak is found between the neighbours. How the pixel-clump distance is defined is described in a note below. A high-enough peak is a peak that lies at least `dTleaf` above the current pixel's data value. If such a clump cannot be found, i.e. all the neighbouring clumps have too low peaks, the clump with the highest peak will be taken instead. The current pixel is then added to this clump, the mask array is updated, and clumps with too low peaks are merged to this clump. Now, the current pixel represents a point where clumps that survived the merging connect. This information is saved and is later contained in the output text file with the list of clumps.

5. Merge or delete small clumps.

   Clumps that have too little pixels (<`Npxmin`) are either merged to the nearest clump in their neighbourhood, or deleted if they are solitary.

6. Save the list of clumps and the pixel mask to output files.

   The list of clumps is saved to a text file compatible with the output of DENDROFIND. The pixel mask array (map of clumps) is saved to a FITS file with the same dimension as the input FITS file.

How the pixel-clump distance is defined. The distance between a pixel and a clump in the datacube is defined as

$$\Delta r = \sqrt{(x_{\rm px} - x_{\rm cl})^2 + (y_{\rm px} - y_{\rm cl})^2 + (z_{\rm px} - z_{\rm cl})^2}, \tag{3.1}$$

where $(x_{\mathrm{px}},\ y_{\mathrm{px}},\ z_{\mathrm{px}})$ is the position of the pixel, and $(x_{\mathrm{cl}},\ y_{\mathrm{cl}},\ z_{\mathrm{cl}})$ is the position of the clump. The position of a clump is defined as the mean position of its pixels weighted by their data values d_i, e.g.

$$x_{\mathrm{cl}} = \frac{\sum_i d_i x_i}{\sum_i d_i}, \tag{3.2}$$

where the summations are taken over all pixels belonging to the clump. I note that the position of a clump varies (drifts) as new pixels are progressively added to it, or when another clump is merged to it.

3.6 Obtaining Quickclump

GitHub

`https://github.com/vojtech-sidorin/quickclump`

GitHub (direct download link)

`https://github.com/vojtech-sidorin/quickclump/archive/master.zip`

Web

`http://galaxy.asu.cas.cz/~vosidorin/quickclump.html`

3.7 Usage

```
python qc.py [-h] [--version] [--dTleaf DTLEAF] [--Tcutoff TCUTOFF]
[--Npxmin NPXMIN] [--ofits OFITS] [--otext OTEXT] [--verbose]
[--silent] ifits
```

3.7.1 Positional (mandatory) arguments

`ifits`

Filename of the input FITS datacube.

3.7.2 Optional arguments

`-h, --help`

Show the help message and exit.

`--version`

Show the program's version number and exit.

`--dTleaf DTLEAF`
Minimal depth of the valley separating adjacent clumps. Clumps separated by a valley that is shallower than this will be merged together. The value must be >0. The default value is $3 \times \sigma_{\mathrm{noise}}$, where σ_{noise} is estimated from the data. See *How the noise standard deviation is estimated* below.

`--Tcutoff TCUTOFF`
Minimal data value to consider. Pixels with lower values will not be processed. The value must be >0. The default value is $3 \times \sigma_{\mathrm{noise}}$, where σ_{noise} is estimated from the data. See *How the noise standard deviation is estimated* below.

`--Npxmin NPXMIN`
Minimal size of a clump in pixels. Smaller clumps will be either merged to an adjacent clump or deleted. The default value is `5`.

`--ofits OFITS`
FITS file where the found clumps will be saved. If `OFITS` exists, it will be overwritten. If set to "`None`" (case insensitive), `OFITS` file will not be written. The default value is `ifits` with the modified extension `.clumps.fits`.

`--otext OTEXT`
Text file where the found clumps will be saved in a human-readable form. If `OTEXT` exists, it will be overwritten. If set to "`None`" (case insensitive), `OTEXT` file will not be written. This will speed up the program's execution. On the other hand, the `OTEXT` file is needed for the construction of a dendrogram. The default value is `ifits` with the modified extension `.clumps.txt`.

`--verbose, -v`
Increase verbosity.

`--silent`
Suppress output to stdout; i.e. set verbosity to a minimum.

How the noise standard deviation is estimated. First, the uncorrected sample standard deviation is computed as

$$s = \sqrt{\frac{1}{N} \sum_{\text{all px}} (d_{\mathrm{px}} - \overline{d})^2}, \tag{3.3}$$

where N is the total number of pixels in the datacube, d_{px} is the pixel's data value, $\overline{d}$ is the mean data value, and the summation is taken over all pixels in the datacube. Then, pixels with data values greater than or equal to $3s$ are excluded from the sample. Those pixels are regarded as dominated by signal, and the pixels remaining in the sample are regarded as dominated by noise. The noise standard deviation σ_{noise} is then estimated as the uncorrected sample standard deviation of those “noisy” pixels, i.e.

$$\sigma_{\text{noise}} \overset{\text{est.}}{=} s_{\text{noise}} = \sqrt{\frac{1}{N_{\text{noise}}} \sum_{\text{noise px}} (d_{\text{px}} - \overline{d}_{\text{noise}})^2}, \tag{3.4}$$

where N_{noise} is the total number of “noisy” pixels, $\overline{d}_{\text{noise}}$ is the mean data value of “noisy” pixels, and the summation is taken over all “noisy” pixels.

3.8 Supportive tools and additional software

Quickclump does not assume anything about the physical units of input data; it works directly with the values provided in the input FITS datacube. If you need to somehow preprocess your data, e.g. convert units or trim the input datacube, you can use the supportive scripts shipped with DENDROFIND, or the plethora of other tools like Starlink[1], GILDAS[2], Miriad[3], or any from the list at `http://www.atnf.csiro.au/computing/software`.

To visualise (not only) FITS datacubes, including the maps of clumps produced by Quickclump, I highly recommend SAOImage DS9[4].

3.9 Other clump-finding codes

In this section I describe several other clump-finding codes, including DENDROFIND – the code that inspired me to develop Quickclump.

3.9.1 DENDROFIND

DENDROFIND was originally conceived by Richard Wünsch and described in the appendix of Wünsch et al. (2012). It was itself inspired by algorithm Clumpfind, and was developed with the aim of having a more accurate clump-finding code. The first implementation was published in Python, later rewritten in C for performance reasons. I contributed with a set of supportive Python scripts for data preprocessing and statistical analysis of the resulting clumps. DENDROFIND can be downloaded from `http://galaxy.asu.cas.cz/~richard/dendrofind/`. Besides a list of identified clumps, DENDROFIND also provides valuable information about

---

[1] Starlink: `http://starlink.eao.hawaii.edu`

[2] GILDAS: `https://www.iram.fr/IRAMFR/GILDAS/`

[3] Miriad: `http://www.atnf.csiro.au/computing/software/miriad/`

[4] SAOImage DS9: `http://ds9.si.edu`

the hierarchical structure of clumps. This hierarchical structure can be visualised in a dendrogram (Rosolowsky et al., 2008).

Algorithm description

DENDROFIND does not assume anything about the physical units or the coordinate system of the input data. It only requires the input data to be three-dimensional. DENDROFIND was, however, developed and tested on datacubes with radio observations of molecular lines. These datacubes have typically position-position-velocity coordinates and contain observations of the brightness temperature of a molecular line. For the purpose of the algorithm description, let us assume we have such a datacube with observation of a molecular cloud in a CO line, with the unit of the brightness temperature T_b.

The algorithm can be imagined as if we observed decreasing water level in the case of an archipelago. First, all isles are underwater. As the water level starts to decline, the highest peaks of hills on the isles appear, followed by those less elevated. As the water level continues to decline, the hills grow in size as more and more land around them is exposed. Some hills and isles will remain isolated, while others will merge at a certain level and create larger islands with rugged terrains. The decision when two touching hills should be merged, i.e. considered a single hill, depends on the depth of the shallowest valley that separates them. The minimum depth is given by the parameter `dTleaf`. Hills, i.e. clumps, separated by a shallower valley will be merged.

DENDROFIND processes the input datacube in a loop over decreasing T_b levels. The number of T_b levels is given by the parameter `Nlevels`. It starts at the highest level, corresponding to the maximum value in the input data, and proceeds down to a level given by the parameter `Tcutoff`. At each level, the code processes all pixels with a data value greater than or equal to the current T_b level. Pixels corresponding to local peaks are marked as cores of new clumps. Pixels not-yet-assigned to a clump are attached to the clump they touch. Here I note that all not-yet-assigned pixels at and above the current T_b level must either touch a clump, which must have been discovered at a higher level, or they must represent a local maximum (peak) in the data. If a pixel touches more than one adjacent clump, it is assigned to the clump whose peak (pixel with maximum T_b) lies nearest. Then, clumps that are touching and have too shallow valleys between them (<`dTleaf`) are merged. In the merger, the master clump is the one with the highest peak. Clumps that are touching, but are not merged together because they are separated by a valley that is deep enough, provide important information about the hierarchical structure in the cloud. The information about their connections is preserved and can be later used to construct a dendrogram. When all the pixels with a data value greater than or equal to the current T_b are assigned to clumps, the main loop moves down to the next T_b level. When the main loop reaches the minimum level given by `Tcutoff`, it terminates. Then, before returning a list of clumps to the user, the clumps are reviewed. Those with too little pixels (<`Npxmin`) are either merged to a neighbouring clump, or discarded if they are solitary. Finally, a list of found clumps is saved to a text file.

To summarise, DENDROFIND is controlled by four parameters that can be passed at the command line:

- `Nlevels` gives the number of levels that the main loop steps through when processing the datacube.
- `Npxmin` gives the minimum number of pixels that can form a clump; clumps with less pixels are either merged or deleted.
- `Tcutoff` gives the lowest considered data value; only pixels with a higher data value are processed.
- `dTleaf` gives the minimum height for a local peak to create a separate clump. The height is measured from the shallowest valley separating a neighbouring clump. Clumps that are too short are merged to a neighbouring clump.

Compared to Clumpfind, DENDROFIND is more accurate and provides the information about the hierarchical structure of clumps. This was, however, achieved at the expense of higher computational complexity and memory requirements. The code was originally written and is suitable for analysing relatively small datacubes with only tens of clumps. It is too slow to handle larger datacubes. The performance issue is successfully addressed by Quickclump, which runs much faster, consumes less system memory, and eliminates the need of the purely-technical parameter `Nlevels`, while reaching the same or better accuracy in identifying clumps (Sect. 3.10.1).

A practical use of DENDROFIND was demonstrated in the study of the Carina Flare supershell by Wünsch et al. (2012), which is also the paper where the algorithm was first described. DENDROFIND was also used for the analysis of the molecular component of the bubble N107 (Sidorin et al., 2014; Chap. 2 in this thesis).

3.9.2 Starlink/CUPID

CUPID[5] is a package that allows the identification and analysis of clumps. It is part of the Starlink Project software distribution[6]. Starlink, started in 1980, was originally a UK project that provided software, hardware, and know-how to UK

---

[5] CUPID: `http://starlink.eao.hawaii.edu/starlink/CUPID`, Berry et al. (2007); Berry (2013)

[6] Starlink: `http://starlink.eao.hawaii.edu`, Disney & Wallace (1982)

astronomical institutes. The Project was shut down in 2005. Currently, as of July 2016, the software is maintained by the East Asian Observatory[7].

CUPID implements four different clump-finding algorithms described further in this chapter; they are: Clumpfind, GaussClumps, FellWalker, and Reinhold.

3.9.3 Clumpfind

This algorithm was developed by Williams et al. (1994), who also published its first implementation in FORTRAN, later rewritten in Interactive Data Language (IDL). Today, it is available as a stand-alone program[8], as part of the CUPID package, or as the task `clfind` in the Miriad package[9]. Clumpfind is the algorithm that inspired Richard Wünsch to develop DENDROFIND, which in turn inspired myself to develop Quickclump.

Clumpfind divides the datacube into a given number of contour levels. Then starts at the highest level and walks down to a given minimum, typically $3\sigma_{\text{noise}}$. At each contour level, pixels that have data values above that level are processed. They are grouped into contiguous sets, or “islands”. If such an “island” contains pixels that have already been assigned to a clump, and all those already-assigned pixels belong to a single clump, then all the pixels in the group are attached to that clump. If the “island” contains pixels of more than a single clump, then each not-yet-assigned pixel is attached to the clump whose pixels are nearest. If the “island” contains no pixels that have already been assigned to a clump, then a new clump is formed.

An advantage of the algorithm is that it does not assume anything about the shape of clumps, in contrast to, e.g. GaussClumps. One shortcoming, which is inherited by DENDROFIND, is that it requires a purely technical parameter to set the number of contour levels. Quickclump eliminates the need of such a parameter. Another shortcoming, which both DENDROFIND and Quickclump solved, is that Clumpfind processes pixels in the input data in chunks given by contours. It does not utilise the differences in data values of pixels within a given interval separated by two adjacent contour levels. One more shortcoming is that Clumpfind can in extreme cases produce noncontiguous clumps (Wünsch et al., 2012). This, however, happens rarely. Both DENDROFIND and Quickclump produce always contiguous clumps.

---

[7] East Asian Observatory: `http://www.eaobservatory.org/`

[8] Clumpfind (IDL implementation): `http://www.ifa.hawaii.edu/users/jpw/clumpfind.shtml`

[9] Miriad: `http://www.atnf.csiro.au/computing/software/miriad/`

3.9.4 GaussClumps

This algorithm was described in the appendix of Stutzki & Guesten (1990). Today, it is available as part of the CUPID package, or in the GILDAS package[10].

GaussClumps starts by locating the brightest pixel in the input data. Then it fits a multi-dimensional Gaussian profile to the peak and its surroundings. The fit is then subtracted from the data, added to the list of clumps, and the algorithm moves to the next brightest pixel in the residual data. This is repeated until one of the termination criteria is met. In the CUPID implementation, the termination criteria are, e.g.: the total data sum extracted from the input data being greater or equal to the total sum in the input data; or the number of found clumps reaching the value given by the parameter `MaxClumps`.

An advantage of the algorithm is that it can handle overlapping clumps, because a single pixel can be shared between several clumps. A disadvantage of the algorithm is that is assumes clumps have Gaussian shapes. This can lead to identification of clumps that are not really present in the data. Such clumps may emerge in the residual data after a Gaussian profile, fitted on a non-Gaussian clump, has been subtracted from the data.

3.9.5 FellWalker

This algorithm was developed by Berry (2015) to address some of Clumpfind's issues; namely the dependence of the resulting identified clumps on the input parameter that sets the number and width of the contour levels. FellWalker is part of the CUPID package.

FellWalker considers all pixels with a data value above a given level as a possible start point for an uphill walk. Such a walk starts at a not-yet-visited pixel. The algorithm searches its immediate neighbourhood and follows the uphill path of the steepest ascent. When it reaches a pixel that has already been assigned to a clump, all the pixels that were visited during the ascent are assigned to that clump. Alternatively, when a local maximum is reached without going through an already-assigned pixel, then a new clump is created, and all the pixels visited during the ascent are assigned to that new clump. However, there may be false local maxima in the data as a result of noise. To deal with those, when a local maximum is found, the algorithm searches an extended neighbourhood. If pixels with a higher data values are found in this neighbourhood, the walk continues to the pixel with the highest data value. The size of the extended neighbourhood can be set with an input parameter. Further, neighbouring clumps that are separated by too shallow dips are merged. The minimal dip allowed between clumps is another

---

[10] GILDAS: `https://www.iram.fr/IRAMFR/GILDAS`

input parameter. The merging of adjacent clumps can be optionally followed by smoothing their borders with a cellular automaton.

The comparison of FellWalker and Clumpfind on synthetic data done by Berry (2015) showed that Clumpfind tends to split actual Gaussian clumps into several parts, thus identifying more clumps than there is really present in the data. On the other hand, FellWalker tends to merge some overlapping clumps that can be otherwise seen by eye, thus identifying less clumps than there is present.

An advantage of the algorithm is that it does not assume anything about the shape of clumps.

3.9.6 Reinhold

The Reinhold algorithm was developed by Kim Reinhold at the Joint Astronomy Centre in Hilo, Hawaii. It is part of the CUPID package.

First, the algorithm finds edges and peaks in one-dimensional profiles through the data array. A peak in a profile is simply the highest not-yet-used value. Each peak is then followed down to edges in both directions. An edge is defined by any of the four criteria: (1) a pixel that touch an already-assigned pixel, (2) when two adjacent pixels have data values below the background level, (3) when the slope of the profile falls below a given limit, or (4) when the end of the profile is reached. All profiles parallel to the main axes plus all possible diagonal profiles are scanned. Then, all the discovered peaks are reviewed. Only true local maxima, i.e. peaks that appear as peaks from all directions, are retained. The edges are then cleaned by cellular automata. First, they are thickened, then thinned again. In three dimensions, the edges resemble shells around peaks. The volume of these shells is then filled, i.e. the pixels inside each shell form a clump. The filling spreads from the peak to the pixels lying within its shell. The filling algorithm cannot, however, deal with certain nonconvex shapes. For example an S-shaped clump will not be completely filled, and will lose some pixels. The edges can have holes. In such a case, the filling algorithm will not cause large scale leakage. It may only claim the pixels in profiles parallel to the main axes and going through the hole. Finally, the discovered clumps are cleaned with another cellular automaton.

An advantage is that the algorithm does not assume anything about the shape of clumps. A disadvantage is that is cannot handle some nonconvex shapes of clumps.

3.10 Tests of Quickclump

3.10.1 Quickclump versus DENDROFIND

Quickclump and DENDROFIND should produce almost identical results. Although their algorithms are very different, they use the same technical definition of clump. The minor differences in the results could originate in the following two differences of the codes (see Sects. 3.5 and 3.9.1 for detailed descriptions of the algorithms):

1. Quickclump reaches the same accuracy as DENDROFIND run with the parameter `Nlevels` set to infinity. This results from the fact that Quickclump processes all pixels, which are sorted by their data values, one by one.

2. When two clumps are claiming the same pixel, Quickclump first attempts to assign that pixel to the nearest clump with a peak higher that `dTleaf` above the pixel's data value. If such a clump cannot be found, the pixel is assigned to the clump with the highest peak. A clump's position is computed as the mean position of its pixels weighted by the pixels' data values.

   On the other hand, DENDROFIND assigns the pixel to the clump whose peak lies nearest.

I performed a series of tests to compare the results and performance of Quickclump and DENDROFIND. The tests were run on a four-core CPU Intel i5-750. During the testing, no other demanding tasks were running, so the codes could use the full power of one CPU core in the turbo mode at 3.2 GHz. The input datacube used in the tests was a cutout from the Galactic Ring Survey (GRS) (Jackson et al., 2006): a datacube of $125 \times 125 \times 57$ pixels in the l–b–v space, where $l = (50\overset{\circ}{.}59$ to $51\overset{\circ}{.}35)$, $b = (0\overset{\circ}{.}30$ to $0\overset{\circ}{.}46)$, and $v = (37.0\,\mathrm{km\,s^{-1}}$ to $48.9\,\mathrm{km\,s^{-1}})$; centred at the bubble N107 ($l = 51\overset{\circ}{.}0$, $b = 0\overset{\circ}{.}1$, $v = 43\,\mathrm{km\,s^{-1}}$). The datacube contained observations of the brightness temperature of the ^{13}CO ($J = 1{-}0$) line. It was the very same datacube that was used in the study of the molecular component of the bubble N107 (Sidorin et al., 2014; Chap. 2 in this thesis). I performed two test runs with each code:

- Run 1 with the parameters `Tcutoff` = `dTleaf` = 1.0, and `Npxmin` = 5. In this run I used both the C and Python implementations of DENDROFIND.

- Run 2 with the parameters `Tcutoff` = `dTleaf` = 0.8, and `Npxmin` = 5. In this run I used only the C implementation of DENDROFIND. The Python implementation ran for too long to finish. (I stopped it after it ran over 100 days.)

Table 3.1: Comparison of the performance of the codes Quickclump and DENDROFIND. The columns are: the program name (and implementation variant), the total running time, the peak memory usage, and the total number of identified clumps. These results are for Run 1 with the parameters `Tcutoff` $=$ `dTleaf` $= 1.0$, and `Npxmin` $= 5$. In this run, both the C and Python implementations of DENDROFIND are compared.

Program	Running time	Peak memory	Clumps found
Quickclump	13.6 seconds	51 MiB	217
DENDROFIND (Python)	10.9 days	463 MiB	218
DENDROFIND (C)	8.00 hours	339 MiB	218

Table 3.2: Same as Table 3.1 for Run 2 with the parameters `Tcutoff` $=$ `dTleaf` $= 0.8$, and `Npxmin` $= 5$. In this run, only the C implementation of DENDROFIND is compared.

Program	Running time	Peak memory	Clumps found
Quickclump	19.2 seconds	68 MiB	457
DENDROFIND (C)	69.2 hours	668 MiB	465

DENDROFIND was run in both cases with the parameter `Nlevels` $= 1000$. This parameter is not used by Quickclump.

The performance of the codes is compared in Tables 3.1 and 3.2. In Run 1, Quickclump is more than 2000 times faster than the C implementation of DENDROFIND, and almost 70 000 times faster than the Python implementation of DENDROFIND. In Run 2, Quickclump is almost 13 000 faster than the C implementation of DENDROFIND. This suggests that Quickclump scales better with the complexity of the data analysis.[11] The peak memory usage of Quickclump is roughly one order of magnitude smaller that that of DENDROFIND in both runs.

A visual comparison of clumps found by the two codes in Run 1 is shown in Fig. 3.1. The codes produce almost identical results.

The distribution of the “sizes” of the clumps discovered by Quickclump and DENDROFIND is compared in Fig. 3.2. In this context, the term “size” means the sum of data values of the pixels that belong to a given clump. Quickclump and DENDROFIND are in a good agreement.

The observed differences in the results of Quickclump and DENDROFIND include the differences in the total number of identified clumps, several pixels with a different colour (i.e. assigned to a different clump), and the differences in the histograms of clump “sizes”. These differences are, however, very minor and could be attributed to the differences in the algorithms (accuracy and pixel-assignment logic) mentioned at the beginning of this section.

---

[11] The data in both test runs are the same, but the lower values of the parameters `Tcutoff` and `dTleaf` in Run 2 increase the complexity of the analysis.

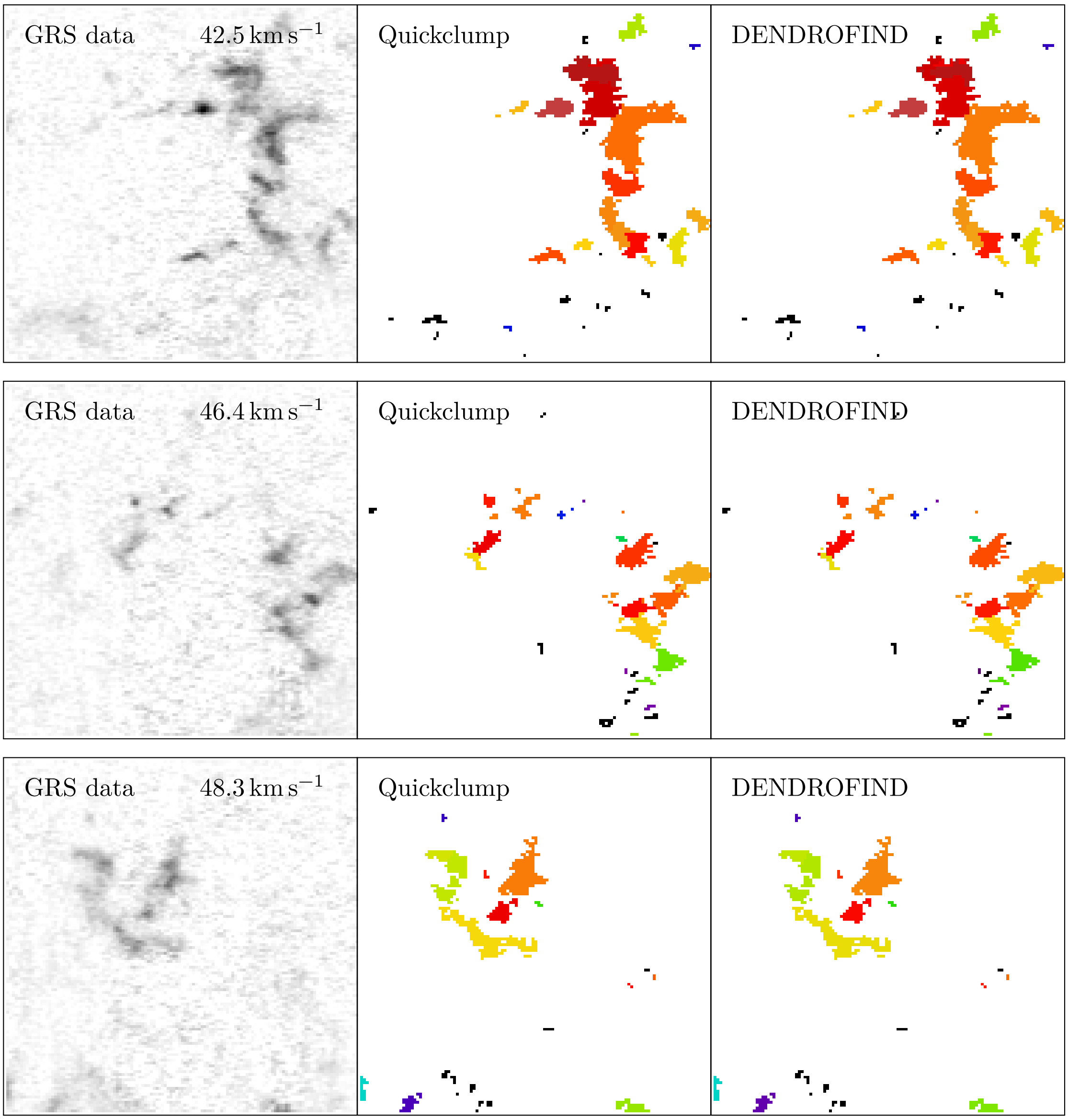

Figure 3.1: Visual comparison of clumps found by Quickclump and DENDROFIND in Run 1. *Left column:* Slices from the GRS datacube of 125 × 125 × 57 pixels with observations of the ^{13}CO ($J = 1{-}0$) line. The datacube is centred at the bubble N107 ($l = 51\overset{\circ}{.}0$, $b = 0\overset{\circ}{.}1$, $v = 43\,\mathrm{km\,s^{-1}}$). The radial velocity is indicated in the slices. *Middle column:* Maps of clumps identified by Quickclump. *Right column:* Maps of clumps identified by DENDROFIND.

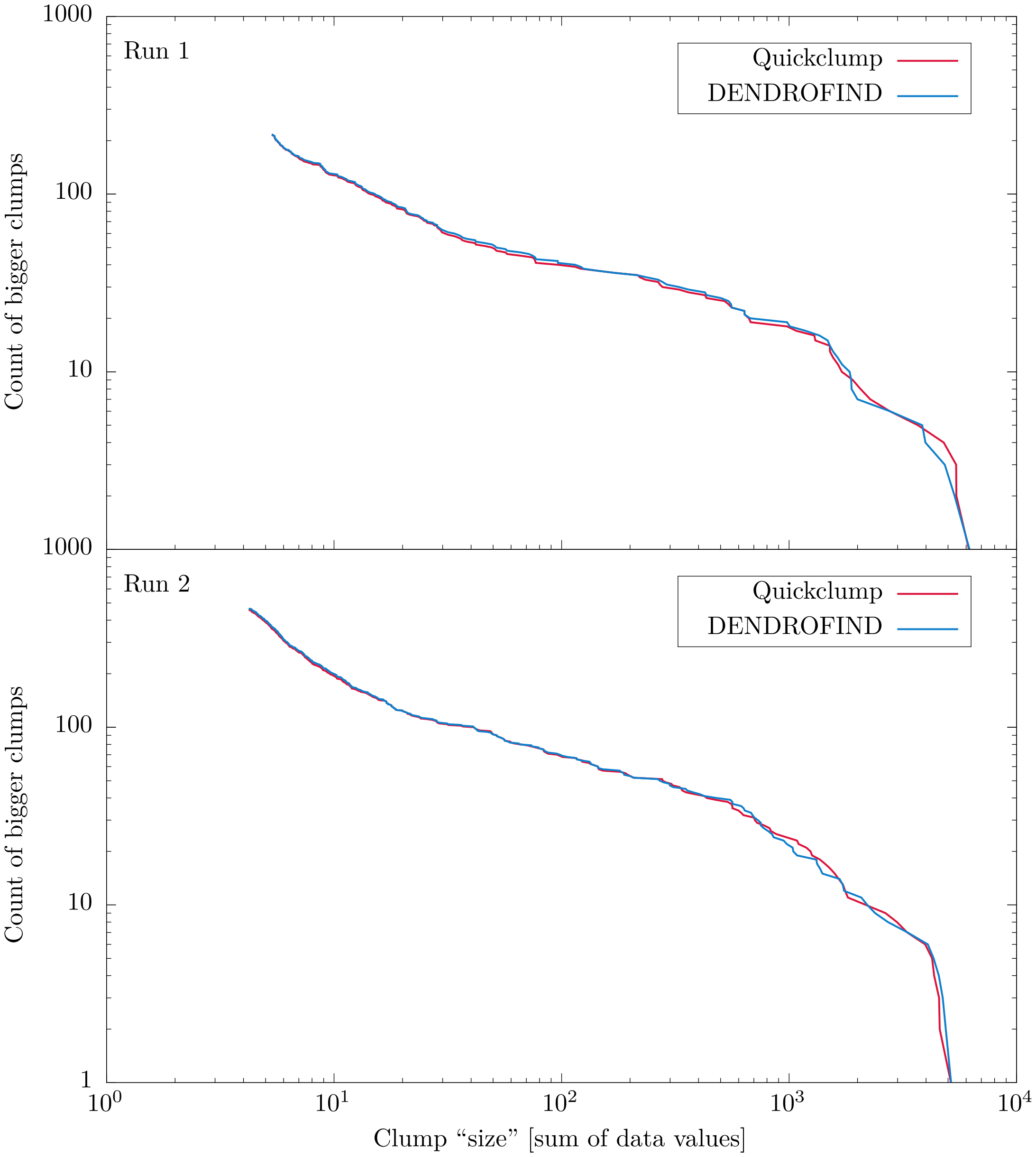

Figure 3.2: Comparison of the distribution of "sizes" of clumps found by Quickclump and DENDROFIND in Run 1 and Run 2. Here, the term "size" means the sum of data values of the pixels that belong to a given clump. The graphs show a reversed cumulative histogram. The vertical axis gives the total number of clumps with a "size" greater than the value given on the horizontal axis.

To conclude, the tests confirm that Quickclump gives results consistent with those of DENDROFIND, but runs significantly faster, and consumes less system memory.

3.10.2 Scaling with the input datacube size

To test how Quickclump scales with the size of the input datacube, I performed a series of tests with synthetic data. I generated three sets of datacubes of various sizes with the following random data distributions:

- normal, with $\mu = 1$ and $\sigma = 0.25$;
- lognormal, with the underlying normal distribution with $\mu = 0$ and $\sigma = 0.25$; and
- uniform, with values in the interval $[0,\ 1]$;

where μ is the mean value, also called expected value, and σ is the standard deviation. The datacubes had sizes from 20^3 pixels to 150^3 pixels, and the data were generated by the NumPy[12] random sampling methods (`numpy.random`[13]).

Then I ran Quickclump with the parameters `dTleaf` $= 0.75$, `Tcutoff` $= 0.75$, `Npxmin` $= 5$, `ofits` $=$ `None`, and `otext` $=$ `None` on each datacube. The FITS and textual outputs were suppressed to test only the performance of the clump-finding algorithm. Especially the generation of the textual output takes significantly more time than the clump-finding algorithm itself for cubes with more than about 1000 clumps. To measure the running time and the peak memory usage, I used the standard Unix program GNU `time` (version 1.7).

Example slices of the sample datacubes, together with slices of the maps of the identified clumps, are shown in Figs. 3.3 to 3.5. The results of measuring the running time and the peak memory usage are shown in Table 3.3 and graphs in Fig. 3.6.

To conclude, the scaling tests show that Quickclump scales approximately linearly with the input datacube size in both the running time and the peak memory usage.

3.10.3 Automated unit and regression testing

The Quickclump code distribution includes automated unit and regression tests. Unit tests test individual program units – typically subroutines. Regression tests test whether a program as a whole gives correct results, e.g. by comparing the

---

[12] NumPy: http://www.numpy.org

[13] `numpy.random`: http://docs.scipy.org/doc/numpy/reference/routines.random.html

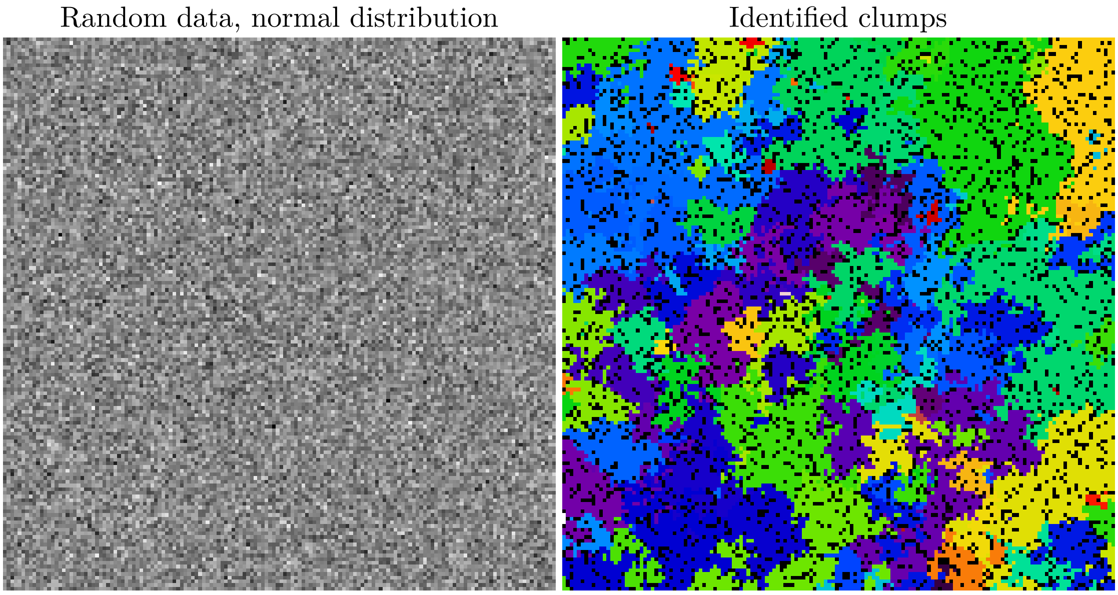

Random data, normal distribution

Identified clumps

Figure 3.3: Slice from a sample datacube of 150^3 pixels with random data used in the scaling tests of Quickclump. These data were generated with a normal distribution. *Left:* The data. *Right:* Map of clumps identified by Quickclump. Each clump is represented by a different colour, similarly to how political maps of states are sometimes coloured.

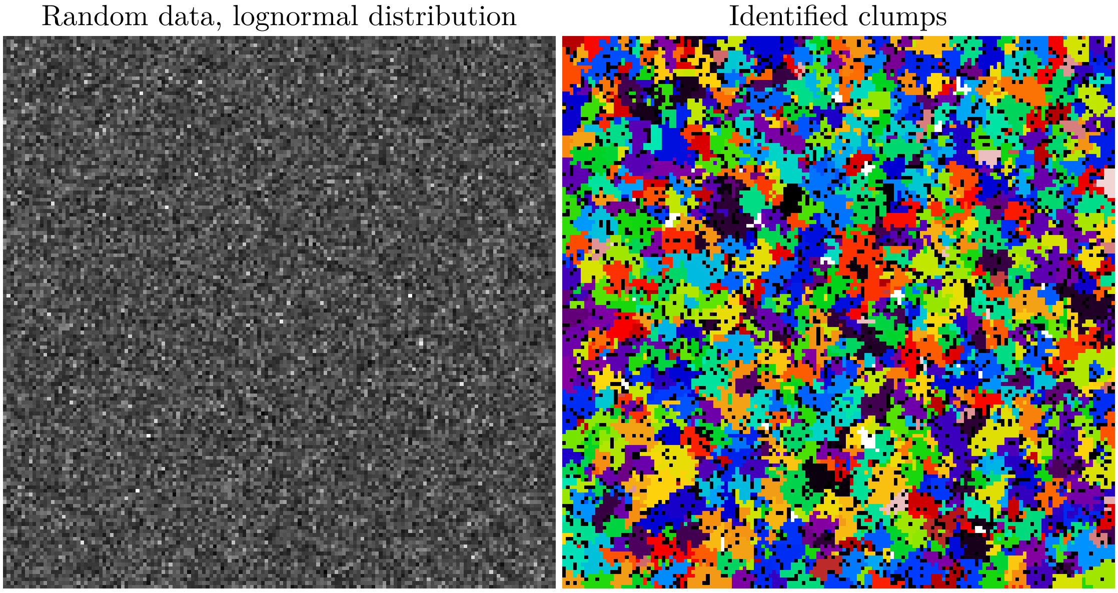

Random data, lognormal distribution

Identified clumps

Figure 3.4: Same as Fig. 3.3 for lognormal distribution.

Table 3.3: Results of the scaling tests of Quickclump done with synthetic data. The sample datacubes contained random data generated with normal, lognormal, and uniform distributions. The results are visualised in Fig. 3.6.

Datacube size	Clumps found	Running time	Peak memory
		second	MiB
Normal distribution			
20^3	2	1.25	18
60^3	97	33.90	126
80^3	182	78.45	278
90^3	260	114.03	390
100^3	356	156.47	530
110^3	497	213.62	700
120^3	642	279.08	904
130^3	848	355.37	1145
140^3	1009	460.19	1424
150^3	1234	575.75	1749
Lognormal distribution			
20^3	50	1.37	18
60^3	1282	35.86	128
80^3	2961	87.85	284
90^3	4326	123.02	399
100^3	5896	170.72	542
110^3	7879	229.14	716
120^3	10018	300.01	923
130^3	12837	385.62	1171
140^3	15927	488.87	1460
150^3	19738	603.19	1791
Uniform distribution			
20^3	100	0.45	16
60^3	2570	10.50	80
80^3	5908	24.10	169
90^3	8410	34.76	235
100^3	11757	47.75	317
110^3	15390	63.45	417
120^3	20230	83.38	537
130^3	25690	109.20	677
140^3	32025	136.29	843
150^3	39188	169.28	1034

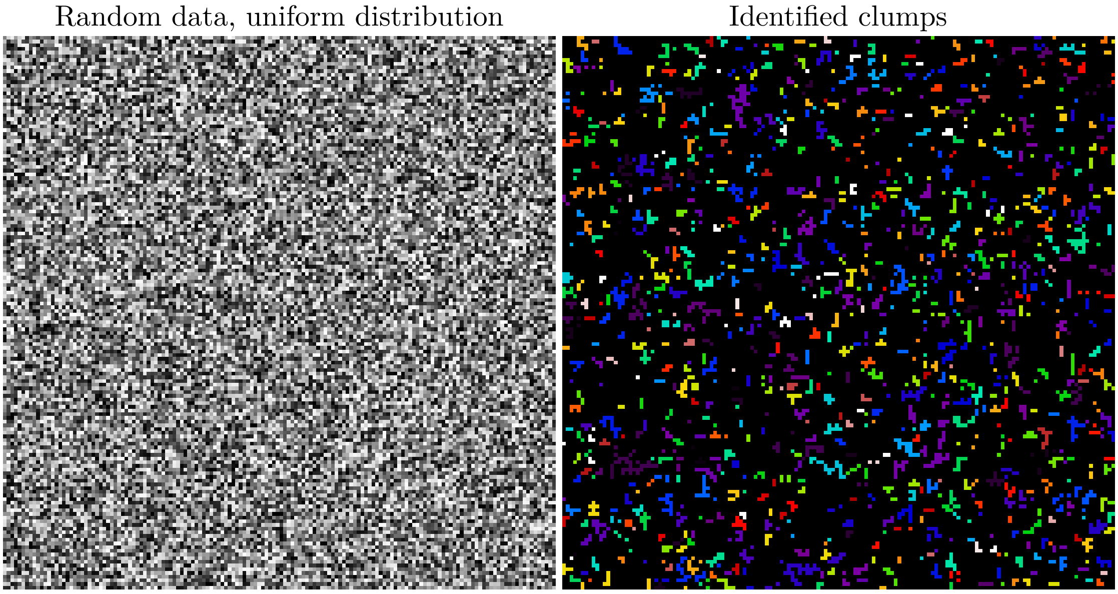

Figure 3.5: Same as Fig. 3.3 for uniform distribution.

program's output with an expected output. The tests can be found in the module `test_qc.py`. Sample files for the tests are located in the directory `test_samples`. The tests are fast, intended to be run before every commit of code changes. To run the tests, type

```
python test_qc.py
```

By default, all available tests will be run.

3.11 Licensing

Quickclump is released under the GNU General Public License version 3, or (at your option) any later version. The full text of the license can be found at `http://www.gnu.org/licenses/`. In brief:

> Quickclump is free software: you can redistribute it and/or modify it under the terms of the GNU General Public License as published by the Free Software Foundation, either version 3 of the License, or (at your option) any later version.
>
> Quickclump is distributed in the hope that it will be useful, but without any warranty; without even the implied warranty of merchantability or fitness for a particular purpose. See the GNU General Public License for more details.

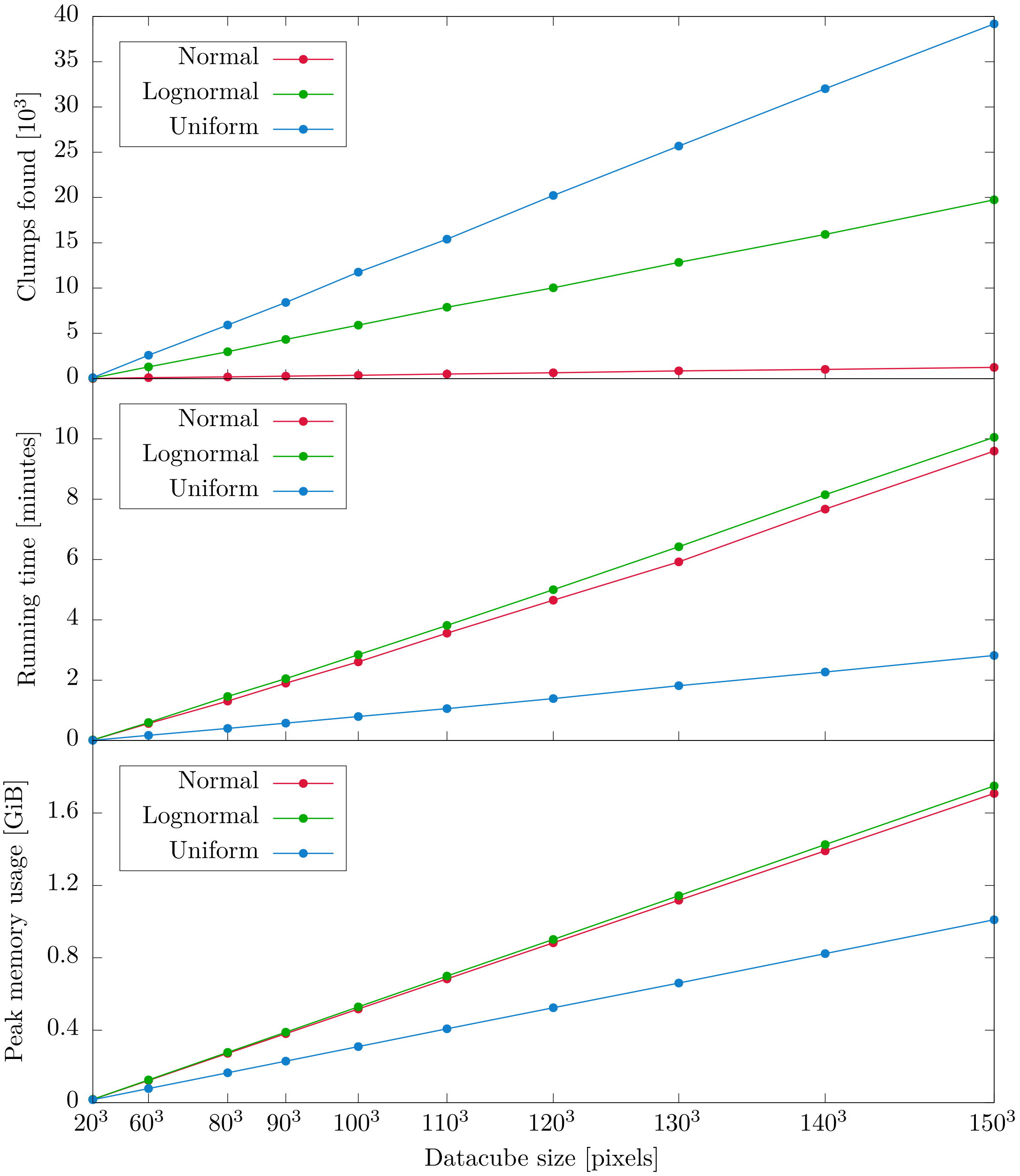

Figure 3.6: Results of the scaling tests of Quickclump taken from Table 3.3 showing the total number of identified clumps (top), running time (middle), and the peak memory usage (bottom) as a function of the datacube size. The sample datacubes contained synthetic data generated with normal, lognormal, and uniform random distributions. I note that the scaling of the running time and peak memory usage is approximately linear for all three types of random data.

3.11.1 Third-party modules

Quickclump uses the following third-party modules that are not part of the Python standard library:

NumPy
Large, multi-dimensional arrays, high-level mathematical functions, matrix operations.
http://www.numpy.org

Astropy/PyFITS
Python interface to FITS files. Originally a separate module, PyFITS was merged into the Astropy library as `astropy.io.fits`.
http://www.stsci.edu/institute/software_hardware/pyfits
http://www.astropy.org/

Appendix A

Publications related to this thesis

A.1 Reviewed papers

Sidorin, V., Douglas, K. A., Palouš, J., Wünsch, R., Ehlerová, S. 2014, *Exploring GLIMPSE bubble N107: Multiwavelength observations and simulations*, A&A, 565, A6, reprinted in this thesis in Sect. 2.1 with permission © ESO

Wünsch, R., Jáchym, P., **Sidorin, V.**, Ehlerová, S., Palouš, J., Dale, J., Dawson, J. R., Fukui, Y. 2012, *The Carina Flare. What can fragments in the wall tell us?*, A&A, 539, A116

Palouš, J., Wünsch, R., Dale, J. E., **Sidorin, V.**, Whitworth, A. 2010, *Stellar feedback and triggered star formation*, in Proceedings of the International Astronomical Union, IAU Symposium, Volume 266, p. 41-45

Sidorin, V., Palouš, J. 2009, *Shell-Like Structures in the ISM: Observation Versus Simulations*, in Proceedings of the 18th Annual Conference of Doctoral Students, ed. Jana Šafránková & Jiří Pavlů, MATFYZPRESS (ISBN 978-80-7378-103-3)

A.2 Posters

Sidorin, V., Douglas, K., Palouš, J. 2010, *Bubble N107*, at conference CONSTELLATION – The Origin of Stellar Masses, Tenerife, Canary Islands, Spain, October 18–22, 2010

Sidorin, V., Douglas, K. 2010, *Bubbles in our Galaxy*, at ESOF 2010 – Marie Curie Conference, Turin, Italy, June 30–July 2, 2010

A.3 Talks

Sidorin, V., Palouš, J. 2009, *Shell-Like Structures in the ISM*, at RAGtime 11 – Workshop on Black Holes and Neutron Stars, Opava, September 22, 2009

Sidorin, V., Palouš, J. 2009, *Dusty* H I *Shells*, at Constellation Work Package 2 Interim Meeting: The Birth and Influence of Massive Stars, Prague, September 15, 2009

Sidorin, V., Palouš, J. 2009, *Shell-Like Structures in the ISM: Observation Versus Simulations*, at University of Exeter, Exeter, July 23, 2009

Sidorin, V., Palouš, J. 2009, *Shell-Like Structures in the ISM: Observation Versus Simulations*, at 18th Annual Conference of Doctoral Students, Charles University, Prague, June 3, 2009

A.4 Theses

Sidorin, V. 2008, *IR, optical and X-ray counterparts of* H I *shells in the Milky Way*, Master's thesis, defended on June 5, 2008

A.5 Software

Quickclump – fast and accurate clump-finding code, described in Chap. 3, GitHub: `https://github.com/vojtech-sidorin/quickclump`, Web: `http://galaxy.asu.cas.cz/~vosidorin/quickclump.html`

Acknowledgements

This research has made use of the following software: Linux (https://kernel.org); Debian (https://debian.org); Kubuntu (http://kubuntu.org); gnuplot (http://gnuplot.info); GIMP (http://gimp.org); Inkscape (https://inkscape.org); Python (https://python.org); SAOImage DS9 (http://ds9.si.edu, Joye & Mandel, 2003); LaTeX 2ε(https://latex-project.org); TeX Live (https://www.tug.org/texlive); pdfTeX(https://www.tug.org/applications/pdftex).

This research has made use of NASA's Astrophysics Data System. (http://adsabs.harvard.edu/)

This research made use of Montage. It is funded by the National Science Foundation under Grant Number ACI-1440620, and was previously funded by the National Aeronautics and Space Administration's Earth Science Technology Office, Computation Technologies Project, under Cooperative Agreement Number NCC5-626 between NASA and the California Institute of Technology. (http://montage.ipac.caltech.edu/)

This research has made use of the SIMBAD database, operated at CDS, Strasbourg, France. (http://simbad.u-strasbg.fr/, Wenger et al., 2000)

This research has made use of the data provided by the Virginia Tech Spectral-Line Survey (VTSS), which is supported by the National Science Foundation.

References

Anderson, L. D., Bania, T. M., Balser, D. S., & Rood, R. T. 2011, ApJS, 194, 32

Andreopoulos, Y., Agui, J. H., & Briassulis, G. 2000, Annual Review of Fluid Mechanics, 32, 309

Aragón, J. L., Naumis, G. G., Bai, M., Torres, M., & Maini, P. K. 2006, ArXiv Physics e-prints

Arnal, E. M., Bajaja, E., Larrarte, J. J., Morras, R., & Pöppel, W. G. L. 2000, A&AS, 142, 35

Arthur, S. J. 2007, Wind-Blown Bubbles around Evolved Stars, ed. T. W. Hartquist, J. M. Pittard, & S. A. E. G. Falle, 183

Arthur, S. J., Henney, W. J., Mellema, G., de Colle, F., & Vázquez-Semadeni, E. 2011, MNRAS, 414, 1747

Bagetakos, I., Brinks, E., Walter, F., et al. 2011a, in EAS Publications Series, Vol. 52, EAS Publications Series, ed. M. Röllig, R. Simon, V. Ossenkopf, & J. Stutzki, 103–106

Bagetakos, I., Brinks, E., Walter, F., et al. 2011b, AJ, 141, 23

Bajaja, E., Arnal, E. M., Larrarte, J. J., et al. 2005, A&A, 440, 767

Bamert, K., Kallenbach, R., le Roux, J. A., et al. 2008, ApJ, 675, L45

Bania, T. M., Anderson, L. D., Balser, D. S., & Rood, R. T. 2010, ApJ, 718, L106

Bania, T. M. & Lyon, J. G. 1980, ApJ, 239, 173

Basu, S. & Murali, C. 2001, ApJ, 551, 743

Bate, M. R. 2009, MNRAS, 392, 590

Beaumont, C. N. & Williams, J. P. 2010, ApJ, 709, 791

Benjamin, R. A., Churchwell, E., Babler, B. L., et al. 2003, PASP, 115, 953

Benzi, R. & Frisch, U. 2010, Scholarpedia, 5, 3439, revision 137205

Berezhko, E. G. & Völk, H. J. 2004, A&A, 427, 525

Bergin, E. A. & Tafalla, M. 2007, ARA&A, 45, 339

Berry, D. S. 2013, Starlink User Note, 255

Berry, D. S. 2015, Astronomy and Computing, 10, 22

Berry, D. S., Reinhold, K., Jenness, T., & Economou, F. 2007, in Astronomical Society of the Pacific Conference Series, Vol. 376, Astronomical Data Analysis Software and Systems XVI, ed. R. A. Shaw, F. Hill, & D. J. Bell, 425

Bertoldi, F., Carilli, C. L., Cox, P., et al. 2003, A&A, 406, L55

Bhattacharjee, P. 2000, Phys. Rep., 327, 109

Binney, J. & Merrifield, M. 1998, Galactic Astronomy, ed. Binney, J. & Merrifield, M.

Bland-Hawthorn, J. & Gerhard, O. 2016, ArXiv e-prints

Blondin, J. M. & Marks, B. S. 1996, New A, 1, 235

Bodenheimer, P., Yorke, H. W., & Tenorio-Tagle, G. 1984, A&A, 138, 215

Bok, B. J. & Reilly, E. F. 1947, ApJ, 105, 255

Bonnell, I. A., Bate, M. R., & Vine, S. G. 2003, MNRAS, 343, 413

Bouchet, P., Dwek, E., Danziger, J., et al. 2006, ApJ, 650, 212

Brand, J. & Blitz, L. 1993, A&A, 275, 67

Bressan, A., Marigo, P., Girardi, L., et al. 2012, MNRAS, 427, 127

Bronfman, L., Cohen, R. S., Alvarez, H., May, J., & Thaddeus, P. 1988, ApJ, 324, 248

Burlaga, L. F., Florinski, V., & Ness, N. F. 2015, ApJ, 804, L31

Cappellaro, E. & Turatto, M. 2001, in Astrophysics and Space Science Library, Vol. 264, The Influence of Binaries on Stellar Population Studies, ed. D. Vanbeveren, 199

Cappellaro, E., Turatto, M., Tsvetkov, D. Y., et al. 1997, A&A, 322, 431

Carey, S. J., Noriega-Crespo, A., Mizuno, D. R., et al. 2009, PASP, 121, 76

Carruthers, G. R. 1970, ApJ, 161, L81

Casali, M., Adamson, A., Alves de Oliveira, C., et al. 2007, A&A, 467, 777

Castor, J., McCray, R., & Weaver, R. 1975, ApJ, 200, L107

Chevalier, R. A. 1974, ApJ, 188, 501

Chevalier, R. A. 1977, ARA&A, 15, 175

Cho, J. & Lazarian, A. 2002, Physical Review Letters, 88, 245001

Cho, J. & Lazarian, A. 2003, MNRAS, 345, 325

Churchwell, E., Babler, B. L., Meade, M. R., et al. 2009, PASP, 121, 213

Churchwell, E., Povich, M. S., Allen, D., et al. 2006, ApJ, 649, 759

Churchwell, E., Watson, D. F., Povich, M. S., et al. 2007, ApJ, 670, 428

Cichowolski, S., Pineault, S., Gamen, R., et al. 2014, MNRAS, 438, 1089

Clarke, D. A. 1996, ApJ, 457, 291

Clarke, D. A. 2010, ApJS, 187, 119

Clemens, D. P., Sanders, D. B., & Scoville, N. Z. 1988, ApJ, 327, 139

Compiègne, M., Verstraete, L., Jones, A., et al. 2011, A&A, 525, A103

Condon, J. J. & Ransom, S. M. 2010, Essential Radio Astronomy (National Radio Astronomy Observatory), [online; http://www.cv.nrao.edu/course/astr534/ERA.shtml]

Cox, D. P. & Reynolds, R. J. 1987, ARA&A, 25, 303

Cutler, D. J. & Groom, D. E. 1991, ApJ, 376, 322

Daigle, A., Joncas, G., & Parizeau, M. 2007, ApJ, 661, 285

Dale, J. E., Clark, P. C., & Bonnell, I. A. 2007, MNRAS, 377, 535

Dale, J. E., Haworth, T. J., & Bressert, E. 2015, MNRAS, 450, 1199

Dale, J. E., Wünsch, R., Smith, R. J., Whitworth, A., & Palouš, J. 2011, MNRAS, 411, 2230

Dale, J. E., Wünsch, R., Whitworth, A., & Palouš, J. 2009, MNRAS, 398, 1537

Dame, T. M., Elmegreen, B. G., Cohen, R. S., & Thaddeus, P. 1986, ApJ, 305, 892

Dame, T. M., Hartmann, D., & Thaddeus, P. 2001, ApJ, 547, 792

Davis, Jr., L. & Greenstein, J. L. 1951, ApJ, 114, 206

Deharveng, L., Lefloch, B., Kurtz, S., et al. 2008, A&A, 482, 585

Deharveng, L., Schuller, F., Anderson, L. D., et al. 2010, A&A, 523, A6

Deharveng, L., Zavagno, A., Lefloch, B., Caplan, J., & Pomarès, M. 2007, in IAU Symposium, Vol. 237, IAU Symposium, ed. B. G. Elmegreen & J. Palouš, 212–216

Dib, S. & Burkert, A. 2005, ApJ, 630, 238

Dickey, J. M. & Lockman, F. J. 1990, ARA&A, 28, 215

Disney, M. J. & Wallace, P. T. 1982, QJRAS, 23, 485

Draine, B. T. 2003, ARA&A, 41, 241

Drew, J. E., Greimel, R., Irwin, M. J., et al. 2005, MNRAS, 362, 753

Duvert, G., Cernicharo, J., Bachiller, R., & Gomez-Gonzalez, J. 1990, A&A, 233, 190

Efremov, Y. N., Ehlerová, S., & Palouš , J. 1999, A&A, 350, 457

Efremov, Y. N., Elmegreen, B. G., & Hodge, P. W. 1998, ApJ, 501, L163+

Ehlerová, S. & Palouš, J. 1996, A&A, 313, 478

Ehlerová, S. & Palouš, J. 2002, MNRAS, 330, 1022

Ehlerová, S. & Palouš, J. 2005, A&A, 437, 101

Ehlerová, S. & Palouš, J. 2013, A&A, 550, A23

Ehlerová, S., Palouš, J., Theis, C., & Hensler, G. 1997, A&A, 328, 121

Elmegreen, B. G. 1994, ApJ, 427, 384

Elmegreen, B. G. 1998, in Astronomical Society of the Pacific Conference Series, Vol. 148, Origins, ed. C. E. Woodward, J. M. Shull, & H. A. Thronson, Jr., 150

Elmegreen, B. G. 2000, ApJ, 530, 277

Elmegreen, B. G. 2011, in EAS Publications Series, Vol. 51, EAS Publications Series, ed. C. Charbonnel & T. Montmerle, 45–58

Elmegreen, B. G. & Chiang, W.-H. 1982, ApJ, 253, 666

Elmegreen, B. G. & Lada, C. J. 1977, ApJ, 214, 725

Elmegreen, B. G. & Scalo, J. 2004, ARA&A, 42, 211

Elsasser, W. M. 1950, Physical Review, 79, 183

Ewen, H. I. & Purcell, E. M. 1951, Nature, 168, 356

Falceta-Gonçalves, D., Kowal, G., Falgarone, E., & Chian, A. C.-L. 2014, Nonlinear Processes in Geophysics, 21, 587

Fermi, E. 1949, Physical Review, 75, 1169

Ferrière, K. 1998, ApJ, 497, 759

Ferrière, K. M. 2001, Reviews of Modern Physics, 73, 1031

Field, G. B., Goldsmith, D. W., & Habing, H. J. 1969, ApJ, 155, L149

Fierlinger, K. M., Burkert, A., Ntormousi, E., et al. 2016, MNRAS, 456, 710

Finkbeiner, D. P. 2003, ApJS, 146, 407

Fitzpatrick, E. L. 1999, PASP, 111, 63

Fitzpatrick, R. 2012, Fluid Mechanics

Frail, D. A., Kulkarni, S. R., Sari, R., et al. 2001, ApJ, 562, L55

Franco, J., Tenorio-Tagle, G., Bodenheimer, P., Rozyczka, M., & Mirabel, I. F. 1988, ApJ, 333, 826

Gaustad, J. E., McCullough, P. R., Rosing, W., & Van Buren, D. 2001, PASP, 113, 1326

Gendre, B., Stratta, G., Atteia, J. L., et al. 2013, ApJ, 766, 30

Goldreich, P. & Sridhar, S. 1995, ApJ, 438, 763

Goldsmith, D. W., Habing, H. J., & Field, G. B. 1969, ApJ, 158, 173

Gredel, R. 1997, A&A, 320, 929

Green, D. A. 2009, VizieR Online Data Catalog, 7253, 0

Green, D. A. 2014, Bulletin of the Astronomical Society of India, 42, 47

Gurnett, D. A., Kurth, W. S., Burlaga, L. F., & Ness, N. F. 2013, Science, 341, 1489

Gvaramadze, V. V., Kniazev, A. Y., & Fabrika, S. 2010, MNRAS, 405, 1047

Haislip, J. B., Nysewander, M. C., Reichart, D. E., et al. 2006, Nature, 440, 181

Hall, J. S. 1949, Science, 109, 166

Hambly, N. C., Collins, R. S., Cross, N. J. G., et al. 2008, MNRAS, 384, 637

Hartmann, D. & Burton, W. B. 1997, Atlas of Galactic Neutral Hydrogen

Hartmann, J. 1904, ApJ, 19, 268

Hatzidimitriou, D., Stanimirovic, S., Maragoudaki, F., et al. 2005, MNRAS, 360, 1171

Heger, A., Fryer, C. L., Woosley, S. E., Langer, N., & Hartmann, D. H. 2003, ApJ, 591, 288

Heiles, C. 1979, ApJ, 229, 533

Heiles, C. 1984, ApJS, 55, 585

Heiles, C. & Habing, H. J. 1974, A&AS, 14, 1

Heitsch, F., Mac Low, M.-M., & Klessen, R. S. 2001, ApJ, 547, 280

Hewett, P. C., Warren, S. J., Leggett, S. K., & Hodgkin, S. T. 2006, MNRAS, 367, 454

Hiltner, W. A. 1949a, ApJ, 109, 471

Hiltner, W. A. 1949b, Science, 109, 165

Hollenbach, D. & Salpeter, E. E. 1971, ApJ, 163, 155

Hörandel, J. R. 2008, Advances in Space Research, 41, 442
Horbury, T. S., Forman, M., & Oughton, S. 2008, Physical Review Letters, 101, 175005
Hulsbosch, A. N. M. 1975, A&A, 40, 1
Indebetouw, R., Matsuura, M., Dwek, E., et al. 2014, ApJ, 782, L2
Iroshnikov, P. S. 1964, Soviet Ast., 7, 566
Irwin, M. J., Lewis, J., Hodgkin, S., et al. 2004, in Society of Photo-Optical Instrumentation Engineers (SPIE) Conference Series, Vol. 5493, Optimizing Scientific Return for Astronomy through Information Technologies, ed. P. J. Quinn & A. Bridger, 411–422
Jackson, J. M., Rathborne, J. M., Shah, R. Y., et al. 2006, ApJS, 163, 145
Jenkins, E. B., Drake, J. F., Morton, D. C., et al. 1973, ApJ, 181, L122
Jenkins, E. B. & Meloy, D. A. 1974, ApJ, 193, L121
Jokipii, J. R. 1976, ApJ, 208, 900
Joye, W. A. & Mandel, E. 2003, in Astronomical Society of the Pacific Conference Series, Vol. 295, Astronomical Data Analysis Software and Systems XII, ed. H. E. Payne, R. I. Jedrzejewski, & R. N. Hook, 489
Kahn, F. D. 1954, Bull. Astron. Inst. Netherlands, 12, 187
Kalberla, P. M. W., Burton, W. B., Hartmann, D., et al. 2005, A&A, 440, 775
Karr, J. L. & Martin, P. G. 2003, ApJ, 595, 900
Karttunen, H., Kroeger, P., Oja, H., Poutanen, M., & Donner, K. J. 2007, Fundamental astronomy
Kendrew, S., Simpson, R., Bressert, E., et al. 2012, ApJ, 755, 71
Kiss, C., Moór, A., & Tóth, L. V. 2004, A&A, 418, 131
Klebesadel, R. W., Strong, I. B., & Olson, R. A. 1973, ApJ, 182, L85
Klein, R. I. & Woods, D. T. 1998, ApJ, 497, 777
Klessen, R. S. & Burkert, A. 2000, ApJS, 128, 287
Kolmogorov, A. N. 1991, Royal Society of London Proceedings Series A, 434, 9
Könyves, V., Kiss, C., Moór, A., Kiss, Z. T., & Tóth, L. V. 2007, A&A, 463, 1227
Koo, B.-C., Gibson, S. J., Kang, J.-h., et al. 2010, Highlights of Astronomy, 15, 788
Kowal, G. & Lazarian, A. 2007, ApJ, 666, L69
Kowal, G. & Lazarian, A. 2010, ApJ, 720, 742
Kraichnan, R. H. 1965, Physics of Fluids, 8, 1385
Kramer, C., Stutzki, J., Rohrig, R., & Corneliussen, U. 1998, A&A, 329, 249
Kritsuk, A. G. & Norman, M. L. 2002a, ApJ, 580, L51
Kritsuk, A. G. & Norman, M. L. 2002b, ApJ, 569, L127
Kritsuk, A. G., Norman, M. L., Padoan, P., & Wagner, R. 2007, ApJ, 665, 416
Krumholz, M. R., McKee, C. F., & Tumlinson, J. 2009, ApJ, 693, 216
Kuiper, G. P., Struve, O., & Strömgren, B. 1937, ApJ, 86, 570
Lamb, D. Q. 1995, PASP, 107, 1152

Larson, R. B. 1981, MNRAS, 194, 809
Lawrence, A., Warren, S. J., Almaini, O., et al. 2007, MNRAS, 379, 1599
Lefloch, B. & Lazareff, B. 1994, A&A, 289, 559
Leorat, J., Passot, T., & Pouquet, A. 1990, MNRAS, 243, 293
Li, P. S., Norman, M. L., Mac Low, M.-M., & Heitsch, F. 2004, ApJ, 605, 800
Liu, H.-L., Wu, Y., Li, J., et al. 2015, ApJ, 798, 30
Loeb, A. & Perna, R. 1998, ApJ, 503, L35+
Low, F. J., Young, E., Beintema, D. A., et al. 1984, ApJ, 278, L19
Mac Low, M.-M. & Klessen, R. S. 2004, Reviews of Modern Physics, 76, 125
Maciel, W. J., Costa, R. D. D., & Idiart, T. E. P. 2009, Rev. Mexicana Astron. Astrofis., 45, 127
MacLaren, I., Richardson, K. M., & Wolfendale, A. W. 1988, ApJ, 333, 821
Maheswar, G., Sharma, S., Biman, J. M., Pandey, A. K., & Bhatt, H. C. 2007, MNRAS, 379, 1237
Marsch, E. 1991, in Reviews in Modern Astronomy, Vol. 4, Reviews in Modern Astronomy, ed. G. Klare, 145–156
Mathewson, D. S. & Ford, V. L. 1970, MmRAS, 74, 139
Mazzali, P. A., Röpke, F. K., Benetti, S., & Hillebrandt, W. 2007, Science, 315, 825
McCray, R. & Kafatos, M. 1987, ApJ, 317, 190
McDonough, J. M. 2007, Introductory lectures on turbulence: Physics, Mathematics and Modeling, `http://www.engr.uky.edu/~acfd/lctr-notes634.pdf`
McKee, C. F. 1995, in Astronomical Society of the Pacific Conference Series, Vol. 80, The Physics of the Interstellar Medium and Intergalactic Medium, ed. A. Ferrara, C. F. McKee, C. Heiles, & P. R. Shapiro, 292
McKee, C. F. & Ostriker, J. P. 1977, ApJ, 218, 148
Medina, S.-N. X., Arthur, S. J., Henney, W. J., Mellema, G., & Gazol, A. 2014, MNRAS, 445, 1797
Mészáros, P. 2006, Reports on Progress in Physics, 69, 2259
Meyer, J.-P. 1985, ApJS, 57, 173
Miville-Deschênes, M.-A. & Lagache, G. 2005, ApJS, 157, 302
Morrison, F. A. 2013, An Introduction to Fluid Mechanics (Cambridge University Press)
Muller, C. A. & Oort, J. H. 1951, Nature, 168, 357
Myers, P. C. 1983, ApJ, 270, 105
NASA, ESA, J. Hester and A. Loll, Arizona State University. 2005, A Giant Hubble Mosaic of the Crab Nebula, `http://hubblesite.org/newscenter/archive/releases/2005/37/`
Neugebauer, G., Habing, H. J., van Duinen, R., et al. 1984, ApJ, 278, L1
Ng, C. S., Bhattacharjee, A., Munsi, D., Isenberg, P. A., & Smith, C. W. 2010, Journal of Geophysical Research (Space Physics), 115, 2101

Norman, C. A. & Ferrara, A. 1996, ApJ, 467, 280
Nozawa, T., Kozasa, T., Umeda, H., Maeda, K., & Nomoto, K. 2003, ApJ, 598, 785
Oey, M. S., Watson, A. M., Kern, K., & Walth, G. L. 2005, AJ, 129, 393
Oort, J. H. & Spitzer, Jr., L. 1955, ApJ, 121, 6
Paczynski, B. 1995, PASP, 107, 1167
Padoan, P., Bally, J., Billawala, Y., Juvela, M., & Nordlund, Å. 1999, ApJ, 525, 318
Paladini, R., Burigana, C., Davies, R. D., et al. 2003, A&A, 397, 213
Palouš, J. 1990, in IAU Symposium, Vol. 144, IAU Symposium, 101P
Palouš, J. & Ehlerová, S. 2002, in Revista Mexicana de Astronomia y Astrofisica Conference Series, Vol. 12, Revista Mexicana de Astronomia y Astrofisica Conference Series, ed. W. J. Henney, J. Franco, & M. Martos, 35–36
Palouš, J., Franco, J., & Tenorio-Tagle, G. 1990, A&A, 227, 175
Palouš, J., Wünsch, R., Dale, J. E., Sidorin, V., & Whitworth, A. 2010, in IAU Symposium, Vol. 266, IAU Symposium, ed. R. de Grijs & J. R. D. Lépine, 41–45
Parmentier, G. 2004, MNRAS, 351, 585
Passot, T., Pouquet, A., & Woodward, P. 1988, A&A, 197, 228
Pavlyuchenkov, Y. N., Kirsanova, M. S., & Wiebe, D. S. 2013, Astronomy Reports, 57, 573
Peek, J. E. G., Heiles, C., Douglas, K. A., et al. 2011, ApJS, 194, 20
Pence, W. D., Chiappetti, L., Page, C. G., Shaw, R. A., & Stobie, E. 2010, A&A, 524, A42
Planck Collaboration, Ade, P. A. R., Aghanim, N., et al. 2015, A&A, 576, A105
Porter, D., Pouquet, A., Sytine, I., & Woodward, P. 1999, Physica A Statistical Mechanics and its Applications, 263, 263
Porter, D., Pouquet, A., & Woodward, P. 2002, Phys. Rev. E, 66, 026301
Putman, M. E., Peek, J. E. G., & Joung, M. R. 2012, ARA&A, 50, 491
Rasmussen, I. L. & Peters, B. 1975, Nature, 258, 412
Reach, W. T., Rho, J., Tappe, A., et al. 2006, AJ, 131, 1479
Reed, B. C. 2003, AJ, 125, 2531
Reynolds, O. 1895, Royal Society of London Philosophical Transactions Series A, 186, 123
Reynolds, R. J. 1984, ApJ, 282, 191
Reynolds, R. J. 1985, ApJ, 294, 256
Reynolds, R. J. 1991, in IAU Symposium, Vol. 144, The Interstellar Disk-Halo Connection in Galaxies, ed. H. Bloemen, 67–76
Reynolds, R. J., Haffner, L. M., & Madsen, G. J. 2002, in Astronomical Society of the Pacific Conference Series, Vol. 282, Galaxies: the Third Dimension, ed. M. Rosada, L. Binette, & L. Arias, 31
Reynolds, S. P. 2008, ARA&A, 46, 89

Richardson, L. F. 1922, Quarterly Journal of the Royal Meteorological Society, 48, 282

Rieke, G. H. & Lebofsky, M. J. 1985, ApJ, 288, 618

Rohlfs, K. & Wilson, T. L. 1996, Tools of Radio Astronomy, ed. Rohlfs, K. & Wilson, T. L.

Rohlfs, K. & Wilson, T. L. 2004, Tools of radio astronomy

Rosolowsky, E. W., Pineda, J. E., Kauffmann, J., & Goodman, A. A. 2008, ApJ, 679, 1338

Rotman, D. 1991, Physics of Fluids, 3, 1792

Rozyczka, M., Tenorio-Tagle, G., & Bodenheimer, P. 1986, A&A, 167, 120

Rozyczka, M., Tenorio-Tagle, G., Franco, J., & Bodenheimer, P. 1993, MNRAS, 261, 674

Salem, C., Mangeney, A., Bale, S. D., & Veltri, P. 2009, ApJ, 702, 537

Salpeter, E. E. 1955, ApJ, 121, 161

Scalo, J. & Elmegreen, B. G. 2004, ARA&A, 42, 275

Schawinski, K., Justham, S., Wolf, C., et al. 2008, Science, 321, 223

Schlegel, D. J., Finkbeiner, D. P., & Davis, M. 1998, ApJ, 500, 525

Scoville, N. Z., Yun, M. S., Sanders, D. B., Clemens, D. P., & Waller, W. H. 1987, ApJS, 63, 821

Sellwood, J. A. & Balbus, S. A. 1999, ApJ, 511, 660

Shapiro, P. R. & Field, G. B. 1976, ApJ, 205, 762

Sidorin, V. 2008, Master's thesis, Charles University in Prague, `https://is.cuni.cz/webapps/zzp/detail/47390/`, `http://galaxy.asu.cas.cz/~vosidorin/download/Sidorin2008_MSc_Thesis_4screen.pdf`

Sidorin, V., Douglas, K. A., Palouš, J., Wünsch, R., & Ehlerová, S. 2014, A&A, 565, A6

Sidorin, V. & Palouš, J. 2009, in Proceedings of the 18th Annual Conference of Doctoral Students – WDS 2009, ed. J. Šafránková & J. Pavlů, 52–58

Simpson, J. A. 1983, Annual Review of Nuclear and Particle Science, 33, 323

Simpson, J. A. & Garcia-Munoz, M. 1988, Space Sci. Rev., 46, 205

Simpson, R. J., Povich, M. S., Kendrew, S., et al. 2012, MNRAS, 424, 2442

Snowden, S. L., Egger, R., Freyberg, M. J., et al. 1997, ApJ, 485, 125

Solomon, P. M., Rivolo, A. R., Barrett, J., & Yahil, A. 1987, ApJ, 319, 730

Sonnentrucker, P., Welty, D. E., Thorburn, J. A., & York, D. G. 2007, ApJS, 168, 58

Spitzer, L. 1978, Physical processes in the interstellar medium

Spitzer, Jr., L. 1956, ApJ, 124, 20

Stead, J. J. & Hoare, M. G. 2009, MNRAS, 400, 731

Stenholm, L. G. 1984, A&A, 137, 133

Stil, J. M., Taylor, A. R., Dickey, J. M., et al. 2006, AJ, 132, 1158

Stone, J. M., Mihalas, D., & Norman, M. L. 1992, ApJS, 80, 819

Stone, J. M. & Norman, M. L. 1992a, ApJS, 80, 753

Stone, J. M. & Norman, M. L. 1992b, ApJS, 80, 791

Stone, J. M., Ostriker, E. C., & Gammie, C. F. 1998, ApJ, 508, L99

Strömgren, B. 1939, ApJ, 89, 526

Stutzki, J. & Guesten, R. 1990, ApJ, 356, 513

Suad, L. A., Caiafa, C. F., Arnal, E. M., & Cichowolski, S. 2014, A&A, 564, A116

Tammann, G. A., Loeffler, W., & Schroeder, A. 1994, ApJS, 92, 487

Taylor, A. R., Goss, W. M., Coleman, P. H., van Leeuwen, J., & Wallace, B. J. 1996, ApJS, 107, 239

Tenorio-Tagle, G. 1980, A&A, 88, 61

Tenorio-Tagle, G. 1981, A&A, 94, 338

Tenorio-Tagle, G. & Bodenheimer, P. 1988, ARA&A, 26, 145

Tenorio-Tagle, G., Bodenheimer, P., Rozyczka, M., & Franco, J. 1986, A&A, 170, 107

Tenorio-Tagle, G., Bodenheimer, P., & Yorke, H. W. 1985, A&A, 145, 70

Tenorio-Tagle, G., Franco, J., Bodenheimer, P., & Rozyczka, M. 1987, A&A, 179, 219

Tenorio-Tagle, G., Rozyczka, M., Franco, J., & Bodenheimer, P. 1991, MNRAS, 251, 318

Tielens, A. G. G. M. 2010, The Physics and Chemistry of the Interstellar Medium

Trumpler, R. J. 1930a, PASP, 42, 214

Trumpler, R. J. 1930b, Lick Observatory Bulletin, 14, 154

van Buren, D. 1985, ApJ, 294, 567

Verschuur, G. L. 1975, ARA&A, 13, 257

Verschuur, G. L. & Kellermann, K. I. 1988, Galactic and Extragalactic Radio Astronomy

Vincent van Gogh. 1889, The Starry Night, painting, `https://www.google.com/culturalinstitute/asset-viewer/the-starry-night/bgEuwDxel93-Pg`

Vishniac, E. T. 1983, ApJ, 274, 152

Vishniac, E. T. 1994, ApJ, 428, 186

Visser, R., van Dishoeck, E. F., & Black, J. H. 2009, A&A, 503, 323

von Hoerner, S. 1951, ZAp, 30, 17

von Weizsäcker, C. F. 1951, ApJ, 114, 165

Wachter, S., Mauerhan, J. C., Van Dyk, S. D., et al. 2010, AJ, 139, 2330

Walder, R. & Folini, D. 1998, A&A, 330, L21

Walter, F., Brinks, E., de Blok, W. J. G., et al. 2008, AJ, 136, 2563

Watson, D., Christensen, L., Knudsen, K. K., et al. 2015, Nature, 519, 327

Waxman, E. 1997, ApJ, 489, L33

Weaver, H. & Williams, D. R. W. 1973, A&AS, 8, 1

Weaver, R., McCray, R., Castor, J., Shapiro, P., & Moore, R. 1977, ApJ, 218, 377

Weiler, K. W. & Sramek, R. A. 1988, ARA&A, 26, 295

Wenger, M., Ochsenbein, F., Egret, D., et al. 2000, A&AS, 143, 9

Whitworth, A. P., Bhattal, A. S., Chapman, S. J., Disney, M. J., & Turner, J. A. 1994a, A&A, 290

Whitworth, A. P., Bhattal, A. S., Chapman, S. J., Disney, M. J., & Turner, J. A. 1994b, MNRAS, 268, 291

Wilking, B. A., Harvey, P. M., Lada, C. J., Joy, M., & Doering, C. R. 1984, ApJ, 279, 291

Williams, J. P., de Geus, E. J., & Blitz, L. 1994, ApJ, 428, 693

Williamson, F. O., Sanders, W. T., Kraushaar, W. L., et al. 1974, ApJ, 193, L133

Wilson, O. C., Minich, G., Flather, E., & Coffeen, M. F. 1959, ApJS, 4, 199

Wilson, T. L. 1999, Reports on Progress in Physics, 62, 143

Wolfire, M. G., Hollenbach, D., McKee, C. F., Tielens, A. G. G. M., & Bakes, E. L. O. 1995, ApJ, 443, 152

Woosley, S. E. & Weaver, T. A. 1986, ARA&A, 24, 205

Wünsch, R., Dale, J. E., Palouš, J., & Whitworth, A. P. 2010, MNRAS, 407, 1963

Wünsch, R., Jáchym, P., Sidorin, V., et al. 2012, A&A, 539, A116

Wünsch, R. & Palouš, J. 2001, A&A, 374, 746

York, D. G. 1977, ApJ, 213, 43

Yue, Z. Y., Zhang, B., Winnewisser, G., & Stutzki, J. 1993, Annalen der Physik, 505, 9

Zavagno, A., Deharveng, L., Comerón, F., et al. 2006, A&A, 446, 171

Zavagno, A., Pomarès, M., Deharveng, L., et al. 2007, A&A, 472, 835

List of Figures

List of Tables

Acronyms

AMR adaptive mesh refinement. 50, 78, 116

CNM cold neutral medium. 18, 19, 22, 23

FCRAO Five College Radio Astronomical Observatory. 107

FITS Flexible Image Transport System. 90, 106, 107, 129, 133–136, 146, 151

FWHM full width at half maximum. 90

GLIMPSE Galactic Legacy Infrared Mid-Plane Survey Extraordinaire. 7, 59, 60, 64, 66, 79, 85–88, 90, 91, 100, 113, 167

GRB gamma-ray burst. 7, 13, 56, 58, 65, 68, 71, 74, 80, 87

GRS Galactic Ring Survey. 86, 88, 90, 97, 101, 102, 106, 107, 110, 117, 142, 144

HIM hot ionised medium. 18, 19, 26–28, 33, 66

HVC high-velocity cloud. 7, 56, 58, 65, 67, 68, 74, 75, 80, 87

I-GALFA Inner-Galaxy ALFA Low-Latitude H I Survey. 86, 88, 90, 93

IDL Interactive Data Language. 139

IRAC Infrared Array Camera. 90

IRAS Infrared Astronomical Satellite. 38, 52, 62, 87

IRIS Improved Reprocessing of the IRAS Survey. 38

ISM interstellar medium. 7, 13, 15, 16, 18–20, 22–24, 28, 31, 33, 35, 37, 46, 48, 50–58, 62, 65–70, 72, 74, 75, 80, 81, 87, 88, 102, 127, 130, 169

LAB Leiden/Argentina/Bonn. 60, 62

LSR local standard of rest. 67, 88, 91, 101

MHD magnetohydrodynamics. 43, 46–48, 74

MIPS Multiband Imaging Photometer for *Spitzer*. 90

MIPSGAL 24 and 70 Micron Survey of the Inner Galactic Disk with MIPS. 90, 100

NRAO National Radio Astronomy Observatory. 62

NTSI nonlinear thin shell instability. 50

PAGI pressure assisted gravitational instability. 77, 79, 167

PAH polycyclic aromatic hydrocarbon. 36, 64, 89, 91, 98

PDR photodissociation region. 36, 64, 91

RANS Reynolds-averaged Navier-Stokes equations. 42

SPH smoothed-particle hydrodynamics. 78, 79, 116

THINGS The H I Nearby Galaxy Survey. 62

UKIDSS UKIRT Infrared Deep Sky Survey. 85, 91, 112, 113

UKIRT United Kingdom Infrared Telescope. 91

UV ultraviolet. 20, 23, 27, 36, 64, 87, 91

VGPS VLA Galactic Plane Survey. 86, 88, 90, 98–100

VLA Karl G. Jansky Very Large Array. 62, 90

WFCAM Wide Field Camera. 91

WIM warm ionised medium. 18, 19, 23, 24, 26

WNM warm neutral medium. 18, 19, 22, 23

WSRT Westerbork Synthesis Radio Telescope. 86, 88, 90, 98, 99

This document was typeset with pdfTeX/LaTeX 2_{ε}.

Date of compilation: October 10, 2016.